Cardiovascular Applications of Magnetic Resonance Imaging

Sandra Bovens

ISBN:
Lay-out: www.wenziD.nl || Wendy Schoneveld
Printed by: Gildeprint drukkerijen, Enschede

Cardiovascular Applications of Magnetic Resonance Imaging

Cardiovasculaire applicaties van beeldvorming op basis van magnetische resonantie

(met een samenvatting in het Nederlands)

PROEFSCHRIFT

ter verkrijging van de graad van doctor aan de Universiteit Utrecht op gezag van de rector magnificus, prof.dr. G.J. van der Zwaan, ingevolge het besluit van het college voor promoties in het openbaar te verdedigen op vrijdag 3 februari 2012 des middags te 2.30 uur

door

Sandra Margaretha Bovens

geboren op 30 mei 1984 te Utrecht

Promotoren: Prof. dr. G. Pasterkamp
Prof. dr. C. J. A. van Echteld

Financial support by the Dutch Heart Foundation for the publication of this thesis is gratefully acknowledged. The research described in this thesis was supported by a grant of the Dutch Heart Foundation (DHF-2006T06)

CONTENTS

1

INTRODUCTION

Magnetic resonance imaging (MRI) is one of the most applied imaging techniques in the medical world. This non-invasive technique is widely implemented in almost every medical specialty as well as in their respective fields of research, such as oncology, neurology, orthopedics, psychiatry, and cardiology, due to for example its ability to differentiate between several types of soft tissues and provide functional analysis of specific organs, like the brain and the heart.[1-6] Cardiac MRI (CMR) has many applications. It can be used to assess general cardiac function, for the left as well as the right ventricle, in which the heart is imaged by stacking a number of slices to cover the entire atrium and create cine images per slice with ECG triggering to calculate volumes.[6] The study of the right ventricle can be challenging due to the complex shape, however, some CMR sequences can be performed to create a 3D reconstruction, that facilitates a more accurate evaluation of right ventricular function and morphology.[7] Recently, several studies have been performed to visualize the geometry of the coronary arteries also by the use of 3D MRI.[8, 9]

The last decade there have been major developments in a different field of cardiovascular MRI, the imaging of atherosclerotic plaques. With the ability of MRI to distinguish types of soft tissue it is also possible to detect different components of the atherosclerotic plaque. The limiting factor in atherosclerotic MRI is the resolution that can be reached by the MRI scanner. However, large components, such as calcifications, lipid rich necrotic cores (LRNC), and large thrombi/intra-plaque hemorrhages could be detected with specific sequences or combinations of sequences.[10-13] Efforts have been made to detect plaque components which reach the resolution limits of clinical MRI but do play an important role in the progression of plaque development and onset of clinical symptoms. Direct thrombus imaging can be applied when the area of interest contains methemoglobin and thereby identify only thrombi or intra-plaque hemorrhage.[14] This gives the opportunity to distinguish plaque bleeding from LRNC, which is problematic when using only standard T1W and T2W sequences.[15, 16] Neovascularization in the plaque is also one of the plaque components that is beyond the limit of resolution of currently clinically available MRI systems. However, the rate of uptake of a contrast agent in the plaque, such as Gadolinium (Gd), could be a surrogate marker for the presence of plaque microvessels.[17] Important cellular components that reflect local inflammatory responses in the plaque, such as macrophages, could be imaged with the use of a different contrast agent. (ultra)Small particles of iron oxide ((U)SPIO) are taken up by macrophages residing in the plaque and can be visualized with T2W (T2*W) sequences.[18, 19]

With the increase in availability of MR scanners with higher magnetic fields, such as the 3 Tesla, and more recently the 7 Tesla, the potential of this imaging modality could be increasingly appreciated since a higher magnetic field gives the opportunity to measure faster or with a higher spatial resolution.

Murine atherosclerotic plaque imaging

The last couple of years MRI has been applied in basic cardiovascular research with a specific focus on molecular imaging. Imaging of characteristics of the atherosclerotic plaque has been a major challenge in the field of vascular biology and there was an urgent need for imaging modules that were capable to detect 'vulnerable' atherosclerotic plaques. These so-called vulnerable plaques are plaques which are prone to rupture, have high inflammatory cell infiltrates, a thin fibrous cap, a high plaque vessel density, and a large lipid-rich necrotic core.[20] Several human studies have shown that these vulnerable/

inflammatory atherosclerotic plaques are related to cardiovascular events such as myocardial infarcts, strokes and transient ischemic attacks (TIA). The use of contrast agents which are specifically targeted to components of these vulnerable atherosclerotic plaques would facilitate the non invasive monitoring of the vascular stability within patients which would accelerate the search for pharmaceutical interventions that stabilizes plaques. There are several contrast agents available, each having their own pros and cons. Micelles and liposomes are lipid-based contrast agents which have been used in the field of oncology, since they have an empty core which could be used to encapsulate medications.[21, 22] Micelles consist of a single lipid layer and liposomes have a lipid bilayer giving the option to encapsulate hydrophobic as well as hydrophilic drugs, respectively. Additionally, a gadolinium lipid is incorporated which facilitates tracing with specific MR sequences as well as the incorporation of a fluorescent lipid for evaluation of histological sections. Due to their small size, in the nm to µm range, these can enter areas with a enhanced permeability and retention effect (EPR) such as inflamed areas or areas with newly formed vasculature (tumors).[23] Several murine studies have been performed using micelles or liposomes, which were coated with ligands to facilitate specific detection of a target of interest.[24-26] Alternatively, (ultra) small particles of iron oxide ((U)SPIO) could also be used, either targeted or untargeted. The untargeted (U)SPIOs are taken up by macrophages and accumulate in atherosclerotic plaques[27] and lymph nodes[28], however these contrast agents do not have the ability to incorporate drugs and have shorter circulatory times *in vivo*.

Murine cardiac imaging

Genetically modified mice have frequently been used as models of cardiovascular disease (e.g. myocardial infarction[29] and cardiac ischemia/reperfusion injury[30]. However, the average heart rate in mice is ~7 times higher compared to humans and the length of a healthy murine heart is about 1 cm. This small size makes cardiac imaging challenging, but several methods have been developed to accurately study cardiac function in small rodents, even without the use of ECG-electrodes.[31, 32] The ability to assess cardiac function non-invasively has also created the possibility to perform follow-up studies. The main use of murine MRI in the field of cardiovascular research has been the study on ventricular remodeling after the induction of a myocardial infarction or cardiac ischemia/reperfusion injury. For example, studies in our lab have shown the involvement of the immune system in ventricular remodeling after myocardial infarction.[29] In addition, MRI has revealed that experimental pharmacological studies (e.g. stem cell treatments) resulted in improved cardiac function.[33] Additionally, some studies have reported specific MR sequences which could be applied to examine diastolic cardiac function, in models of heart failure or cardiac hypertrophy.[34]

MRI is now widely used in experimental and clinical research. For specific applications in cardiovascular studies the technology is well standardized. However, for other research purposes the technology is still in an experimental phase. For instance, the visualization of atherosclerotic plaque is performed using non standardized settings and at present molecular plaque imaging is still in its infancy.

This thesis will address new applications of (pre)clinical cardiovascular (molecular) magnetic resonance imaging, in mice and men.

OUTLINE OF THIS THESIS

Part I of this thesis will focus on atherosclerosis and (molecular) imaging; **chapter 2** gives an overview of the current status of magnetic resonance imaging (MRI) of human carotid atherosclerotic lesions. We executed a literature search on experimental atherosclerotic MRI validation studies and conclude that this type of research still is in a preclinical experimental phase. **Chapter 3** describes the pharmacokinetic (and pharmacodynamic) study of untargeted and agonist-coated micelles in a murine atherosclerosis model. **Chapter 4** describes the association between neutrophil gelatinase-associated lipocalin (NGAL) and inflamed human carotid plaques from the Athero-Express study. This biomarker was validated in a murine atherosclerosis model with NGAL targeted antibody-coated micelles to detect inflamed 'unstable' plaques. One of the benefits of micelles is that drugs can be incorporated and thereby create the possibility to target drug delivery.
We also studied the use of MRI in human atherosclerotic lesions, in **chapter 5** we examined ^{1}H-NMR spectroscopy images to detect lactate levels as a marker of plaque hypoxia and thereby a possible predictive (non-invasively detectable) biomarker of plaque rupture. To stratify patients with carotid atherosclerotic plaque burden more accurately, including inflammatory status and not only hemodynamic significant stenosis, we started a study to scan patients scheduled for a carotid endarterectomy (CEA) with a 7 Tesla MRI scanner. Brain and carotid plaque are scanned and histology of the atherosclerotic plaque evaluated and correlated to brain damage. The preliminary results of the first patients are discussed in **chapter 6**.
All chapters describe positive contrast agents (T1 contrast agents) or non-contrast MRI, in **chapter 7** we evaluate a negative contrast agent; ultra-small particles of iron oxide (USPIO), a particle which could enter the plaque either passively or actively via monocyte/macrophage uptake in the blood and subsequent infiltration into the plaque. However, MRI evaluation of plaque uptake is hampered by strong blooming effects due to the higher presence of USPIOs in the lymph nodes surrounding the vessels.

In part II of this thesis the focus is on cardiac imaging in murine models. In **chapter 8** a new MRI method for the determination of cardiac function is evaluated. This self-gating method makes ECG electrodes obsolete and increases the quality of the images or reduces scan time. The method is evaluated in healthy mice as well as mice suffering from a myocardial infarction. This same method can also be used to study diastolic heart function, reconstructing an image every 3ms leading to a frame rate of up to 90 frames per heart beat. In **chapter 9** a diabetic mouse model is used to study diastolic cardiac function in time; from early/mild dysfunction to cardiac hypertrophy. **Chapter 10** describes the first results of a study which is aimed at the reduction of infarct size in mice suffering from a myocardial infarction after permanent LAD ligation. Mice are treated with a BLT1 receptor antagonist to prevent binding of LTB4 and subsequent neutrophil/macrophage infiltration into the myocardium.

Lastly, in **chapter 11** the results obtained in the research described in parts I and II is discussed and recommendations for future research are formulated.

1. Lebel RM, Eissa A, Seres P, Blevins G, Wilman AH. Quantitative high field imaging of sub-cortical gray matter in multiple sclerosis. Mult Scler 2011 October 27.

2. Fernandez-Seara MA, Mengual E, Vidorreta M, znarez-Sanado M, Loayza FR, Villagra F, Irigoyen J, Pastor MA. Cortical hypoperfusion in Parkinson's disease assessed using arterial spin labeled perfusion MRI. Neuroimage 2011 October 18.

3. Krivitzky LS, Roebuck-Spencer TM, Roth RM, Blackstone K, Johnson CP, Gioia G. Functional Magnetic Resonance Imaging of Working Memory and Response Inhibition in Children with Mild Traumatic Brain Injury. J Int Neuropsychol Soc 2011 October 12;1-10.

4. Chou D, Samartzis D, Bellabarba C, Patel A, Luk KD, Kisser JM, Skelly AC. Degenerative magnetic resonance imaging changes in patients with chronic low back pain: a systematic review. Spine (Phila Pa 1976) 2011 October 1;36(21 Suppl):S43-S53.

5. Budge LP, Salerno M. The role of cardiac magnetic resonance in the evaluation of patients presenting with suspected or confirmed acute coronary syndrome. Cardiol Res Pract 2011;2011:605785.

6. Nacif MS, Zavodni A, Kawel N, Choi EY, Lima JA, Bluemke DA. Cardiac magnetic resonance imaging and its electrocardiographs (ECG): tips and tricks. Int J Cardiovasc Imaging 2011 October 28.

7. Sheehan FH, Ge S, Vick GW, III, Urnes K, Kerwin WS, Bolson EL, Chung T, Kovalchin JP, Sahn DJ, Jerosch-Herold M, Stolpen AH. Three-dimensional shape analysis of right ventricular remodeling in repaired tetralogy of Fallot. Am J Cardiol 2008 January 1;101(1):107-13.

8. Chiribiri A, Ishida M, Nagel E, Botnar RM. Coronary imaging with cardiovascular magnetic resonance: current state of the art. Prog Cardiovasc Dis 2011 November;54(3):240-52.

9. Boffano C, Chiribiri A, Cesarani F. Native whole-heart coronary imaging for the identification of anomalous origin of the coronary arteries. Int J Cardiol 2009 September 11;137(1):e27-e28.

10. Alizadeh DR, Doornbos J, Tamsma JT, Stuber M, Putter H, van der Geest RJ, Lamb HJ, de RA. Assessment of the carotid artery by MRI at 3T: a study on reproducibility. J Magn Reson Imaging 2007 May;25(5):1035-43.

11. Kerwin W, Xu D, Liu F, Saam T, Underhill H, Takaya N, Chu B, Hatsukami T, Yuan C. Magnetic resonance imaging of carotid atherosclerosis: plaque analysis. Top Magn Reson Imaging 2007 October;18(5):371-8.

12. Ota H, Yu W, Underhill HR, Oikawa M, Dong L, Zhao X, Polissar NL, Neradilek B, Gao T, Zhang Z, Yan Z, Guo M, Zhang Z, Hatsukami TS, Yuan C. Hemorrhage and large lipid-rich necrotic cores are independently associated with thin or ruptured fibrous caps: an in vivo 3T MRI study. Arterioscler Thromb Vasc Biol 2009 October;29(10):1696-701.

13. Cappendijk VC, Cleutjens KB, Kessels AG, Heeneman S, Schurink GW, Welten RJ, Mess WH, Daemen MJ, van Engelshoven JM, Kooi ME. Assessment of human atherosclerotic carotid plaque components with multisequence MR imaging: initial experience. Radiology 2005 February;234(2):487-92.

14. Moody AR, Murphy RE, Morgan PS, Martel AL, Delay GS, Allder S, MacSweeney ST, Tennant WG, Gladman J, Lowe J, Hunt BJ. Characterization of complicated carotid plaque with magnetic resonance direct thrombus imaging in patients with cerebral ischemia. Circulation 2003 June 24;107(24):3047-52.

15. Cai JM, Hatsukami TS, Ferguson MS, Small R, Polissar NL, Yuan C. Classification of human carotid atherosclerotic lesions with in vivo multicontrast magnetic resonance imaging. Circulation 2002 September 10;106(11):1368-73.

16. Yuan C, Mitsumori LM, Ferguson MS, Polissar NL, Echelard D, Ortiz G, Small R, Davies JW, Kerwin WS, Hatsukami TS. In vivo accuracy of multispectral magnetic resonance imaging for identifying lipid-rich necrotic cores and intraplaque hemorrhage in advanced human carotid plaques. Circulation 2001 October 23;104(17):2051-6.

17. Kerwin W, Hooker A, Spilker M, Vicini P, Ferguson M, Hatsukami T, Yuan C. Quantitative magnetic resonance imaging analysis of neovasculature volume in carotid atherosclerotic plaque. Circulation 2003 February 18;107(6):851-6.

18. Howarth S, Li ZY, Trivedi RA, King-Im JM, Graves MJ, Kirkpatrick PJ, Gillard JH. Correlation of macrophage location and plaque stress distribution using USPIO-enhanced MRI in a patient with symptomatic severe carotid stenosis: a new insight into risk stratification. Br J Neurosurg 2007 August;21(4):396-8.

19. Tang TY, Howarth SP, Miller SR, Graves MJ, King-Im JM, Trivedi RA, Li ZY, Walsh SR, Brown AP, Kirkpatrick PJ, Gaunt ME, Gillard JH. Comparison of the inflammatory burden of truly asymptomatic carotid atheroma with atherosclerotic plaques contralateral to symptomatic carotid stenosis: an ultra small superparamagnetic iron oxide enhanced magnetic resonance study. J Neurol Neurosurg Psychiatry 2007 December;78(12):1337-43.

20. Yla-Herttuala S, Bentzon JF, Daemen M, Falk E, Garcia-Garcia HM, Herrmann J, Hoefer I, Jukema JW, Krams R, Kwak BR, Marx N, Naruszewicz M, Newby A, Pasterkamp G, Serruys PW, Waltenberger J, Weber C, Tokgozoglu L. Stabilisation of atherosclerotic plaques. Position paper of the European Society of Cardiology (ESC) Working Group on atherosclerosis and vascular biology. Thromb Haemost 2011 July 4;106(1):1-19.

21. Dane KY, Nembrini C, Tomei AA, Eby JK, O'Neil CP, Velluto D, Swartz MA, Inverardi L, Hubbell JA. Nano-sized drug-loaded micelles deliver payload to lymph node immune cells and prolong allograft survival. J Control Release 2011 August 12.

22. Zucker D, Andrianov A, Steiner A, Raviv U, Barenholz Y. In-vitro and in-vivocharacterization of PEGylated nanoliposomes co-remotely loaded with topotecan and vincristine. J Control Release 2011 October 12.

23. Maeda H. Tumor-selective delivery of macromolecular drugs via the EPR effect: background and future prospects. Bioconjug Chem 2010 May 19;21(5):797-802.

24. Briley-Saebo KC, Cho YS, Tsimikas S. Imaging of Oxidation-Specific Epitopes in Atherosclerosis and Macrophage-Rich Vulnerable Plaques. Curr Cardiovasc Imaging Rep 2011 February;4(1):4-16.

25. van Bochove GS, Paulis LE, Segers D, Mulder WJ, Krams R, Nicolay K, Strijkers GJ. Contrast enhancement by differently sized paramagnetic MRI contrast agents in mice with two phenotypes of atherosclerotic plaque. Contrast Media Mol Imaging 2011 January;6(1):35-45.

26. te Boekhorst BC, Bovens SM, Hellings WE, van der Kraak PH, van de Kolk KW, Vink A, Moll FL, van Oosterhout MF, de Vries JP, Doevendans PA, Goumans MJ, de Kleijn DP, van Echteld CJ, Pasterkamp G, Sluijter JP. Molecular MRI of murine atherosclerotic plaque targeting NGAL: a protein associated with unstable human plaque characteristics. Cardiovasc Res 2011 February 15;89(3):680-8.

27. Sigovan M, Boussel L, Sulaiman A, Sappey-Marinier D, Alsaid H, sbleds-Mansard C, Ibarrola D, Gamondes D, Corot C, Lancelot E, Raynaud JS, Vives V, Lacledere C, Violas X, Douek PC, Canet-Soulas E. Rapid-clearance iron nanoparticles for inflammation imaging of atherosclerotic plaque: initial experience in animal model. Radiology 2009 August;252(2):401-9.

28. te Boekhorst BC, Bovens SM, Nederhoff MG, van de Kolk KW, Cramer MJ, van Oosterhout MF, Ten HM, Doevendans PA, Pasterkamp G, van Echteld CJ. Negative MR contrast caused by USPIO uptake in lymph nodes may lead to false positive observations with in vivo visualization of murine atherosclerotic plaque. Atherosclerosis 2010 May;210(1):122-9.

29. Timmers L, van Keulen JK, Hoefer IE, Meijs MF, van MB, den OK, van Echteld CJ, Pasterkamp G, de Kleijn DP. Targeted deletion of nuclear factor kappaB p50 enhances cardiac remodeling and dysfunction following myocardial infarction. Circ Res 2009 March 13;104(5):699-706.

30. Arslan F, Smeets MB, O'Neill LA, Keogh B, McGuirk P, Timmers L, Tersteeg C, Hoefer IE, Doevendans PA, Pasterkamp G, de Kleijn DP. Myocardial ischemia/reperfusion injury is mediated by leukocytic toll-like receptor-2 and reduced by systemic administration of a novel anti-toll-like receptor-2 antibody. Circulation 2010 January 5;121(1):80-90.

31. Bovens SM, te Boekhorst BC, den OK, van de Kolk KW, Nauerth A, Nederhoff MG, Pasterkamp G, Ten HM, van Echteld CJ. Evaluation of infarcted murine heart function: comparison of prospectively triggered with self-gated MRI. NMR Biomed 2011 April;24(3):307-15.

32. Heijman E, de GW, Niessen P, Nauerth A, van EG, de GL, Nicolay K, Strijkers GJ. Comparison between prospective and retrospective triggering for mouse cardiac MRI. NMR Biomed 2007 June;20(4):439-47.

33. van Laake LW, Passier R, den OK, Schreurs C, Monshouwer-Kloots J, Ward-van OD, van Echteld CJ, Doevendans PA, Mummery CL. Improvement of mouse cardiac function by hESC-derived cardiomyocytes correlates with vascularity but not graft size. Stem Cell Res 2009 September;3(2-3):106-12.

34. Stuckey DJ, Carr CA, Tyler DJ, Aasum E, Clarke K. Novel MRI method to detect altered left ventricular ejection and filling patterns in rodent models of disease. Magn Reson Med 2008 September;60(3):582-7.

PART I

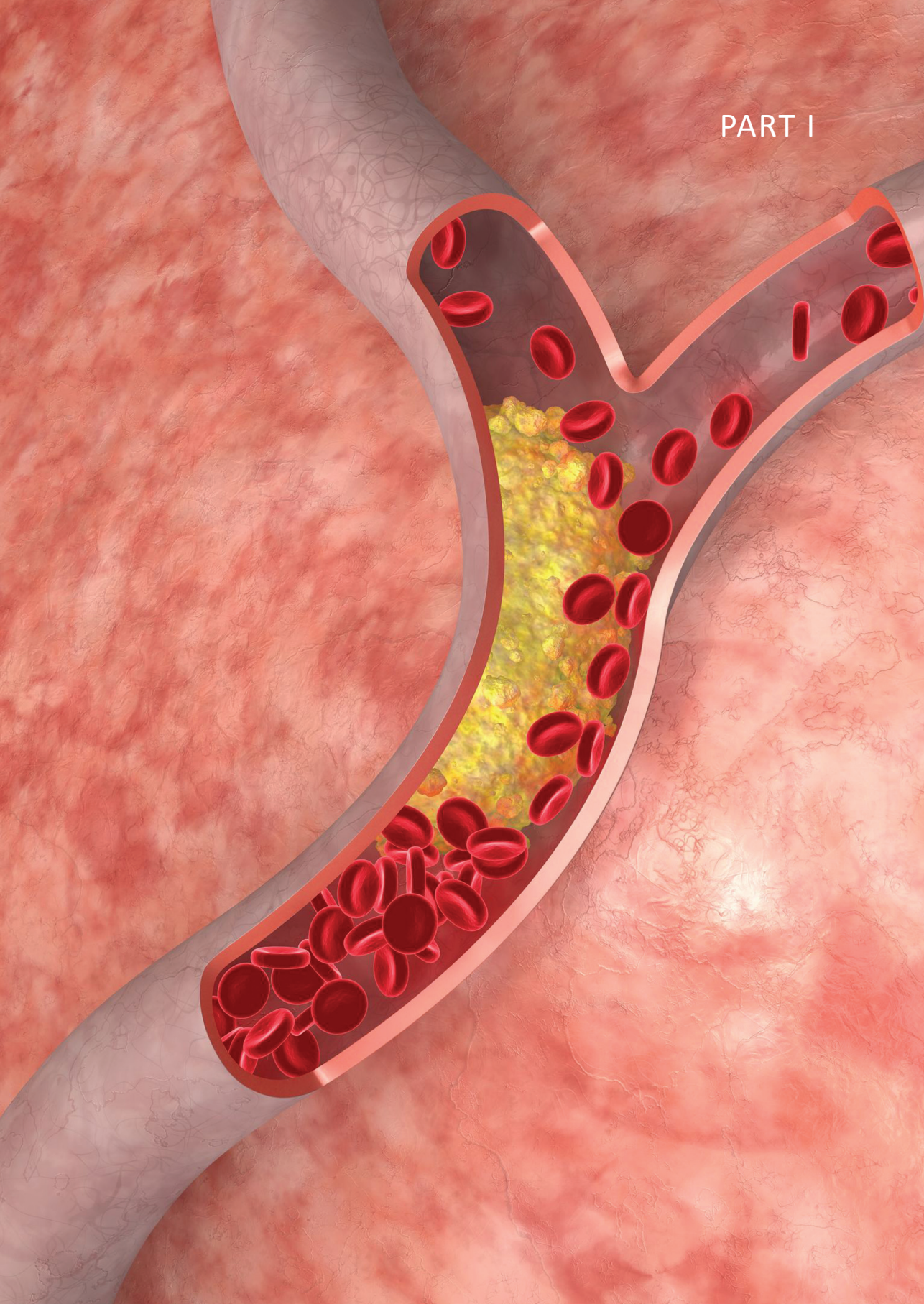

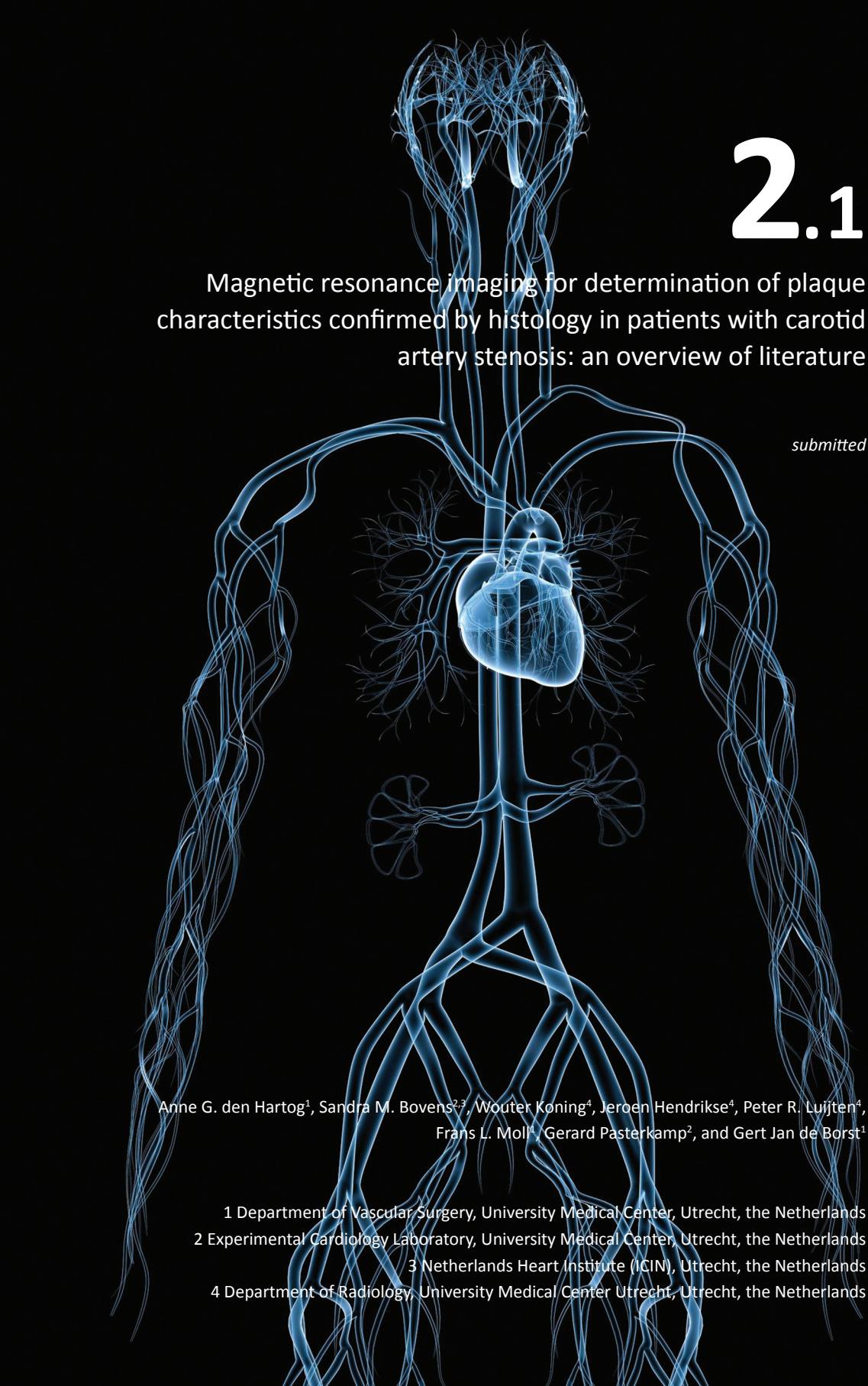

2.1

Magnetic resonance imaging for determination of plaque characteristics confirmed by histology in patients with carotid artery stenosis: an overview of literature

submitted

Anne G. den Hartog[1], Sandra M. Bovens[2,3], Wouter Koning[4], Jeroen Hendrikse[4], Peter R. Luijten[4], Frans L. Moll[1], Gerard Pasterkamp[2], and Gert Jan de Borst[1]

1 Department of Vascular Surgery, University Medical Center, Utrecht, the Netherlands
2 Experimental Cardiology Laboratory, University Medical Center, Utrecht, the Netherlands
3 Netherlands Heart Institute (ICIN), Utrecht, the Netherlands
4 Department of Radiology, University Medical Center Utrecht, Utrecht, the Netherlands

ABSTRACT

Introduction

Implementation of high-resolution MRI (hrMRI) in the diagnostic workup is one of the most promising techniques to identify plaque morphology and vessel wall structure more precisely.

Original research articles and several reviews report on carotid imaging in general or compare different imaging modalities. Fibrous cap (FC), intraplaque hemorrhage (IPH), Lipid Rich Necrotic Core (LRNC), and less calcification are already well known important factors for plaque vulnerability and visualization of these components with MRI is important for clinical MR imaging. This review provides an overview of the recent literature on MRI as a diagnostic tool for the determination of the major components of the carotid plaque with histology as a reference test.

Methods

A systematic search strategy with synonyms for 'carotid artery stenosis' and 'MRI' and 'histology' was conducted in MEDLINE and EMBASE databases. This resulted in 1211 articles, after careful selection 19 papers fulfilled our in and exclusion criteria. Studies varied too much in presentation, especially on the applied MRI and histology methods, therefore a pooled analysis could not be performed.

Results

One study was performed on a 3.0-Tesla MRI scanner; all other studies were performed on a 1.5-Tesla scanner. Most performed sequences were 2-dimensional (2D) and 3D T1-weighted (T1W) and all histology protocols varied slightly. Our results indicate that calcification, FC, IPH, and LRNC can be identified with moderate to good sensitivity and specificity. A good comparison of all studies was impossible due to the heterogeneity in all MRI and histology protocols.

Conclusions

MRI still holds a promise, clinical application for plaque characterization would require consensus regarding MRI settings and confirmation by histology. For this reason, which is based on current literature, it may be too early to routinely apply MRI as an imaging modality to assess plaque characteristics that have been associated with plaque vulnerability. Predefined protocols for histology and imaging must be established to reliably conclude from outcomes and become useful for the clinic.

INTRODUCTION

Large randomized trials for symptomatic[1, 2] and asymptomatic[3, 4] patients with high-grade (>70%) carotid artery stenosis have confirmed the benefit of carotid endarterectomy (CEA) above medical treatment alone. Currently, patient selection for CEA still merely depends on symptoms and the degree of stenosis.[5] Several studies, however, have suggested the relative importance of plaque characteristics, rather than stenosis, with the future risk for stroke on both short-term and long-term varying, depending on carotid plaque composition.[6-8] Furthermore, local atherosclerotic plaque composition in patients undergoing CEA is an independent predictor of future cardiovascular events.[9]

Radiologic imaging has become increasingly important for identifying plaque characteristics in vivo. In clinical practice, duplex ultrasound (DUS) imaging combined with computed tomography angiography (CTA) or magnetic resonance angiography (MRA) of the carotid arteries creates the ideal workup to demonstrate the presence, location, and extent of carotid narrowing.[10, 11] These modalities can help determine the degree of stenosis and the presence of calcifications. However for example, CTA often overestimates the degree of these calcifications and overshadows other plaque components that might be important for determining plaque vulnerability.[12, 13] Validated histologic markers for vulnerability of plaques are a thin fibrous cap (FC), a lipid-rich necrotic core (LRNC), intraplaque hemorrhage (IPH) or thrombus, or both, and of less importance, calcification.[14] These are the major components of an atherosclerotic carotid plaque. In addition, intraplaque vessel density is related to events after surgery.[9] Owing to the small size of these neovessels and the limiting spatial resolution of magnetic resonance imaging (MRI), it is not yet possible to image these neovessels precisely. An alternative could be to use gadolinium and assess the rate of gadolinium uptake in the plaque: fast uptake would mean a relatively high plaque vessel density.[15] Furthermore, inflammation and, therefore, the presence of macrophages in the carotid plaque, have been associated with plaque rupture but must be visualized with ultrasmall super-paramagnetic iron oxide (USPIO)–enhanced MRI.[16, 17] However, the addition of contrast agents or USPIO agents in imaging makes MRI less noninvasive since a second MRI scan is necessary (upto 24 hours later) and therefore a little less attractive for clinical use. For noninvasive imaging, it is of eminent importance that the major characteristics associated with vulnerability, and especially clinical outcome, are identified. Currently, DUS, MRA, and CTA are observer-dependent and not capable of identifying all of the specific plaque characteristics. Development of new imaging modalities to visualize carotid atherosclerotic plaque characteristics more distinctively and in more detail is still in progress.

Implementation of high-resolution MRI (hrMRI) in the diagnostic workup is one of the most promising techniques to identify plaque morphology and vessel wall structure more precisely.[18] HrMRI can potentially be used for different purposes: First, hrMRI has been suggested for the identification of patients with vulnerable plaques at risk for embolic events and who are therefore appropriate candidates for surgery. Second, due to good soft tissue contrast, the degree of stenosis can be reliably determined.[18-21] Third, MRI can be potentially used to monitor the response to medications e.g. statin therapy over time, for example, in asymptomatic patients with atherosclerosis who are not yet eligible for revascularization.[22]

Carotid imaging has been investigated extensively. Original research articles and several reviews report on carotid imaging in general or compare different imaging modalities.[23-27] Owing to this enormous number of articles, we believe it is important to provide an overview of current MRI of the major carotid plaque characteristics specifically. We believe that FC, IPH, LRNC, and less calcification are already well known important factors for vulnerability, which have been investigated for several years, and

visualization of these with MRI might represent the current state of clinical MR imaging. This review provides an overview of the recent literature on MRI as a diagnostic tool for the determination of the major components of the carotid plaque with histology as a reference test.

METHODS

A systematic literature search on all studies relating carotid artery stenosis, MRI, and endarterectomy-derived plaque histology was conducted in August 2011 according to the search strategy and data collection guidelines of the Preferred Reporting Items for Systematic Reviews and Meta-analyses (PRISMA) statement.[28]

Search strategy

MedLine and EMBASE databases were searched in August 2011, using the combination of synonyms for "carotid artery stenosis" and "MRI" and "histology" to include all possible eligible studies. A manual search of the Cochrane Library yielded no relevant articles. We restricted our query to articles only from 2000 and later, because the progress and the technical development of the MRI scan in these last 10 years can provide us with the most realistic overview of studies on carotid plaque imaging.

Study selection

After discarding duplicates, the title and abstract of the remaining articles were screened independently by two observers (A.H. and S.B.) according to the following predefined criteria. Inclusion criteria were (1) presenting data about patients with carotid artery stenosis, (2) reporting the diagnostic accuracy of the MRI scanner, and (3) histology as a reference test. Subsequently, the full text of the included articles was read, and the article was excluded if one or more of the following criteria were applicable: (1) no comparison with a reference test, (2) *ex vivo* imaging, (3) irrelevant study design (e.g., case report, review), (4) nonhuman study, (5) not written in English, and (6) unavailable full-text report after all efforts were taken to retrieve the report, including contacting the authors. Reference lists of the included articles were searched manually and yielded no relevant new articles. Disagreements between the reviewers were resolved by consensus. A flowchart of the applied search strategy and selection process is presented in Figure 1.

Data collection and items

The included articles were grouped by subheadings of the specific major plaque components: calcifications, FC, IPH, and LRNC. Thrombus is not mentioned separately because IPH consists of similar components; in addition, these terms are interchangeably used with the addition of luminal or intraplaque thrombus.

MRI sequences, histology protocol, and outcome measures for diagnostic research from the included studies were also collected. Studies varied too much in presentation, especially on the applied MRI and histology methods, therefore a pooled analysis could not be performed.

Primary outcome measures were the diagnostic accuracy parameters, including sensitivity, specificity, positive predictive value, negative predictive value, and κ value for comparison of histology and MRI results. These quantitative results were not always reported in the studies but could occasionally be calculated from the given data. A κ value of >0.7 indicated good agreement.

Data presentation

All included articles were presented per individual study in a descriptive manner and are summarized systematically in the Tables.

Results

Our search resulted in 1211 articles. After removing the duplicates, applying inclusion and exclusion criteria, and screening references, 19 articles were considered valid for inclusion. Calcification was reported in 4 studies,[29-32] FC in 6,[29, 31, 33-36] IPH in 14,[20, 29, 31-33, 36-44] and LRNC in 6 studies[30-32, 40, 44, 45] (Figure 1 & Table 1).

MRI sequences

MRI protocols were specified in all studies, and slightly different sequences or settings were used in the different studies (Table 2). One study was performed on a 3.0-Tesla MRI scanner[20], all other studies were performed on a 1.5-Tesla scanner. Mostly 2-dimensional (2D) and 3D T1-weighted (T1W) sequences were performed.

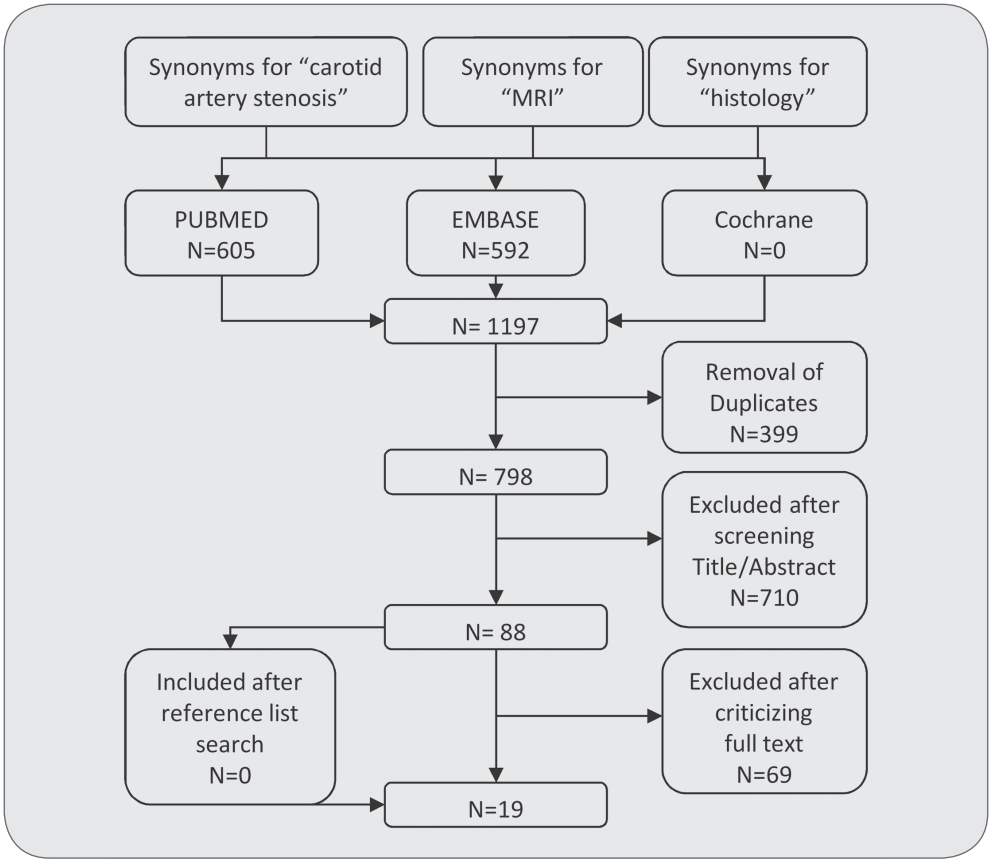

Figure 1 | *Flowchart included papers*

Table 1 | Magnetic resonance sequences of all included studies[a]

First author	Year	Type MRI	T1W	T2W	PDW	TOF	OTHER
Hatsukami[33]	2000	1.5T SIGNA, GE Health care	NA	NA	NA	NA	3D MOTSA
Yuan[43]	2001	1.5T SIGNA, GE Health care	DIR 2D FSE	Cardiac gated, Shared echo FSE	Cardiac gated, Shared echo FSE	NA	NA
Cai[28]	2002	1.5T SIGNA, GE Health care	DIR 2D FSE	Cardiac gated, Shared echo FSE	Cardiac gated, Shared echo FSE	NA	NA
Mitsumori[34]	2003	1.5T SIGNA, GE Health care	DIR 2D FSE	Cardiac gated, Shared echo FSE (SHARE)	Cardiac gated, Shared echo FSE (SHARE)	NA	NA
Moody[41]	2003	1.5T Siemens	3D GE (MRDTI)	NA	NA	NA	NA
Cappendijk[37]	2004	1.5T Intera, Philips 8.1.2	3D TFE 2D DIR TSE	NA	NA	3D TFE	NA
Chu[38]	2004	1.5T SIGNA, GE Health care	BB 2D FSE (fat suppression)	Cardiac gated, FSE	Cardiac gated, FSE (fat suppression)	3D	NA
Kamp-schulte[40]	2004	1.5T SIGNA, GE Health care	Yes, not specified	Yes, not specified	Yes, not specified	Yes, not specified	NA
Cappendijk[29]	2005	1.5T Intera, Philips 8.1.2	2D TSE 3D TFE	ECG- gated, TSE ECG gated partial T2 weighted TSE	NA	NA Scout 3D TFE	NA
Saam[31]	2005		FSE	Yes, not specified	Yes, not specified	Yes, not specified	NA
Honda[39]	2006	1.5T SIGNA, GE Health care	2D FSE (fat suppression)	Shared FSE BB DIR (fat suppression)	FSE BB DIR(fat suppression) Shared DIR FSE FS	2D MRA	NA
Puppini[30]	2006	1.5T Siemens	TSE	TSE (shared)	TSE (shared)	3D	NA
Albuquer-que[32]	2007	1.5T Siemens	FS 3D GE	No	No	3D MRA	NA
Watanabe[20]	2008	1.5T Philips	Localizing images gated FS	Gated FS TSE	No	3D	NA
Cappendijk[44]	2008	1.5T Intera, Philips 8.1.2	3D TFE 2D TSE	2D TSE, ECG gated	2D TSE, ECG gated	NA	NA
Yim[42]	2008	1.5T SIGNA, GE Health care	FSE FSE with FS CE FSE after gado	FSE	Yes, not specified	3D TOF MR angio	NA
Yoshida[35]	2008	1.5T Philips Gyroscan	3D IR TSE(FS) 2D DIR TSE	2D DIR TSE	No	No	NA
Bitar[36]	2008	1.5T SIGNA, GE Health care	3D FS GE (IPH)	No	No	No	NA
Ota[19]	2010	3.0T SIGNA Ex-cite, GE Health Care & Achieva,Philips	2D FSE 3D TOF 3D MP-RAGE	No	No	No	No cardiac gaiting

MRI, magnetic resonance imaging; T1W, T1-weighted; T2W, T2-weighted; PDW, proton density weighted; TOF, time of flight; MOTSA, multiple overlapping thin slab angiography; NA, not available; T, Tesla; DIR, double inversion recovery; 2D, two-dimensional; CE, contrast enhancent; FS, fat suppressed; FSE, fast spin echo; 3D, three-dimensional; SHARE, shared echo-FSE ; BB, black blood; MRDTI, magnetic resonance direct thrombus imaging; GE, gradient echo; TFE, turbo field echo; TSE, turbo spin echo; IPH, intraplaque hemorrhage; MP, magnetization prepared; RAGE, rapid acquisition gradient echo; gado, gadolinium; IR, inversion recovery

a TSE and FSE are comparable sequences but dependent of the manufacturer of the MRI scanner used

Histological analysis

Histology protocols were described in all studies. In general, all protocols varied slightly, and in most studies, these were only roughly documented (Table 3). When investigators used qualified protocols to perform histologic analysis, the American Heart Association (AHA) classification was often chosen.[29, 31, 32, 41, 44, 45] This is a numeric classification of eight histologically defined lesion types.[46, 47]

1. Calcifications

Four studies described the detection of calcification by MRI confirmed with histology.[29-32] Calcifications are usually detected by hypointense areas on all contrast weightings or by hypointense areas on two of four sequences (T1W, T2W, proton-density weighted [PDW], and time of flight [TOF]). However, no standardized protocols are used for the detection. Independent of the sequence (or combination of sequences) used, MRI often underestimates the extend of the calcified areas. To maintain morphology in the histologic slide, the plaques are decalcified.

The AHA classification was used by Cai *et al.*[29] to assess plaque status, and calcified plaques are scaled in class VII. Saam *et al.*[32] determined the areas of calcifications with a hypointense signal on all four weightings, and considering all areas of calcifications, the sensitivity was 76% and specificity was 86%. A higher sensitivity and specificity were achieved when only areas >2 mm^2 were considered. These last data might be slightly biased, because only 21% of all calcification areas in this study were >2 mm^2. A good correlation of MRI and histology (R = 0.74; P < .001) for calcification was calculated.

Cappendijk *et al.*[30] used a random combination of two weightings (T1W, T2W, intermediate and partial T2W) to assess calcification and identified 18 of 18 regions of interest. A standard examination protocol with four different weightings (TOF, T1, PDW, T2) was used by Puppini *et al.*[31] to identify calcification in 40 of 56 sections, whereas MRI detected them in 32 of 40.

2. Fibrous cap

Five[29, 31, 33-36] studies reported the appearance of the intact or ruptured FC, and only one study[33] stated that the MRI protocol was not suitable for detecting FC structure. Due to the limiting resolution of MRI and the (usually) thin FCs several different methods have been evaluated and therefore there was no consistency in the protocols between the different studies yet.

Hatsukami *et al.*[34] used a 3D multiple overlapping thin-slab angiography sequence to investigate whether MRI was capable of identifying FC thickness in patients with carotid artery disease *in vivo*. In this sequence, a thick FC appeared as a dark band between the bright lumen and grey plaque components. The absence of this dark band indicated a thin FC or a ruptured FC when a bright grey region was seen directly adjacent to the lumen. Although the case numbers were small, the observed sensitivity and specificity for the identification of FC rupture were promising; however, the 95% confidence intervals (CIs) for data in this study were wide.[34] In contrast, Albuquerque *et al.*[33] did not find a significant association between the presence of a hyperintense signal on MRI and semiquantitative evaluation of FC thickness (P = .38). Probably the semiquantitative analysis of FC thickness by histology, according to Hatsukami *et al.*[33], limited their results. Their T1W images did not allow for evaluation of FC structure, and these were only based on FC thickness. Cai *et al.*[29] also used the TOF images to determine whether the FC was thick (>0.25 mm) or ruptured. The analysis used a modified AHA classification that differentiated ruptured from intact FC.[46, 47] The modified AHA class IV/V indicates a thick or thin intact FC, whereas AHA class VI indicates a FC rupture. Mitsumori *et al.*[35] evaluated the accuracy of in vivo multisequence MRI in identifying the unstable FC. Four different contrast-weighted axial images were

Table 2 | Accuracy of magnetic resonance imaging of all included studies

	Year	Patients		Sensitivity	Specificity	Kappa (κ)
Calcifications						
Cai[28]	2002	60	Type VII45	80%	94%	κ=0.74 (0.67-0.82) Weighted κ=0.79
Saam[31]	2005	40	All areas	76%	86%	
			Areas >2 mm^2	84%	91%	κ=0.75(0.66-0.84)
Cappendijk[29]	2005	11		NA	NA	NA
Puppini[30]	2006	19		80%	94%	κ=0.65
FC						
Hatsukami[33]	2000	22	FC rupture	89%	96%	κ=0.83(0.67-1.0) weighted κ=0.87
Cai[28]	2002	60	Type IV/V45	84%	90%	κ=0.74 (0.67-0.82)
			Type VI45	82%	91%	Weighted κ=0.79
Mitsumori[34]	2003	18	Unstable FC	81%	90%	NA
Puppini[30]	2006	19	Disrupted FC	100%	80%	NA
Albuquerque[32]	2007	72		NA	NA	NA
Yoshida[35]	2008	70		NA	NA	NA
IPH						
Yuan[43]	2001	18	IPH alone	NA	NA	NA
			IPH + LRNC	85% (78-92)	92% (86-98)	κ=0.69 (0.16)
Cai[28]	2002	60	Type VI45	82%	91%	κ=0.74
Moody[41]	2003	63	Type VI45	84%	84%	κ=0.75 (interobsever) κ=0.90 (intraobserver)
Cappendijk[37]	2004	11		NA	NA	NA
Chu[38]	2004	27		90%	74%	κ=0.74 (reader 1) κ=0.52 (reader 2)
Kampschulte[40]	2004	26		96%	82%	κ=0.91
Saam[31]	2005	40	All areas	82%	77%	
			Areas >2 mm^2	87%	84%	κ=0.71 (0.61-0.80)
Honda[39]	2006	18	TOF imaging	100%	100%	
			T1W	100%	44.4%	
			PDW	44.4%	42.9%	
			T2W	44.4%	100%	
Puppini[30]	2006	19		92%	100%	κ=0.95
Albuquerque[32]	2007	72		96%	96%	κ=0.91 (0.81-1.00)
Yoshida[35]	2008	70		NA	NA	NA
Yim[42]	2008	135	Halo alone	91%	83%	
			Multisequence	93%	85%	0.79 (0.60-0.95)
Bitar[36]	2008	11	Reader 1	100%	80%	0.73 (0.59-0.86)
			Reader 2	94%	88%	0.77 (0.64-0.91)
			Mean measures	97%	84%	NA
Ota[19]	2010	38	Overall RAGE	31%		0.53 (0.68 >3pixels)
			Overall TOF	17%		0.33
			Overall FSE	28%		0.42
			RAGE (IPH>2.81 mm^2)	80%	97%	0.80
			FSE (IPH>2.81 mm^2)	70%	92%	0.63
			TOF (IPH>2.81 mm^2)	56%	96%	0.57
LRNC						
Yuan[43]	2001	18		98%(96-100)	100%(92-100)	κ=0.98 (0.93-100)
Saam[31]	2005	40	All areas	92%	65%	
			Areas >2 mm^2	95%	76%	κ=0.73 (0.62-0.82)
Cappendijk[29]	2005	11	Qualitative	93% (77-99)	96% (86-100)	NA
Puppini[30]	2006	19		92%	95%	κ=0.85
Cappendijk[44]	2008	50	Multisequence*	69-100%	69-100%	NA
Honda[39]	2006	18		NA	NA	

obtained at each slice location. A strong relation was found between the presence and intactness of the FC. On the TOF images, a stable FC is identified as a relatively thick, intact band of low signal seen adjacent to the lumen. For identification of an unstable FC in vivo, good sensitivity (81%) and specificity (90%) were found. Flow artifacts or intimal calcifications sometimes obscured the lumen surface; still, owing to the availability of different contrast weightings images, the FC could be correctly interpreted.[35]

3. Intraplaque hemorrhage

IPH was mostly positively associated with imaging profiles. However, there was no consistency in protocols used between all studies. Twelve studies investigated the presence of IPH in the carotid plaque in patients with carotid artery stenosis documented by 1.5-Tesla MRI.[20, 29, 31-33, 36-44] Only one study investigated the accuracy of 3.0-Tesla MRI in identifying IPH.[20]

IPH is often diffuse and located in the LRNC, making it difficult to distinguish between these two. Several studies report the use of multicontrast MRI to solve this problem. Yuan *et al.*[44] showed the use of the TOF sequence combined with a T1W sequence in which the IPH and LRNC were both seen as hyperintense, compared with the signal intensity (SI) of muscle tissue, on the T1W images, whereas on the TOF images, IPH was hyperintense but the LRNC was isointense.[44] Because only 16 patients showed isolated IPH, no accurate assessment of MRI for IPH alone could be made.

Other authors also looked at a combined detection method of TOF and T1W sequences, sometimes with the addition of T2W and PDW sequences.[29, 31, 32, 36, 39-41, 43] Chu *et al.*[38] subdivided the IPH into fresh (<1 week), recent (1-6 weeks), or old (>6 weeks) hemorrhage. To distinguish between the different stages, they used all four contrast weightings. In the fresh hemorrhage the IPH was hyperintense in the T1W and TOF images and hypointense or isointense on the T2W and PDW images. Recent IPH was hyperintense on all contrast weightings and old IPH was hypointense on all contrast weightings. Furthermore Saam *et al.*[31] identified IPH according to the protocol of Chu *et al.*[38] There was a moderate to strong correlation between MRI and histology ($R = 0.66$, $P < .001$).

Kampschulte *et al.*[40] and Cai *et al.*[28] identified several plaque characteristics according to the AHA classification. Recent hemorrhage appeared as high SI in both T1W and TOF images. Yet, Yim *et al.*[43] used a slightly different approach: they investigated the value of the high SI halo sign as a new marker of a fresh or recent IPH on specifically the TOF sequence. A high SI halo sign around the carotid artery on MIP images of TOF MRA, compared with the surgical and histopathologic findings, demonstrated a slightly lower sensitivity and specificity when compared with the multisequence approach. Honda *et al.*[39] investigated the instability of the plaques by combining a TOF and T2W sequence, and a high signal intensity was observed at both sequences. The TOF sequence was very sensitive to the detection of IPH.

Table 2 | *RAGE, rapid acquisition gradient echo; TOF, time of flight; FSE, fast spin echo; IPH, intraplaque hemorrhage; FC, fibrous cap; LRNC, lipid-rich-necrotic-core; T1W, T1-weighted; PDW, proton density weighted; T2W, T2-weighted*

[a] all histological cutoff points

Table 3 | Histology protocols of all included studies

First author	Year	Observers	Blinded for MRI results	Time between CEA and histology	Direct after CEA	Sectioning	Staining	Outcome recorded
Hatsukami[33]	2000	2 readers	Yes	NA	Intact excised formalin-fixed decalcified paraffin embedded	Sectioned every 0.5mm-1.0mm	Stained as previously described52	FC thickness Intact thick/intact thin/ruptured
Yuan[43]	2001	1 reviewer	Yes	Directly	Fixed in formalin decalcified embedded in paraffin	10-µm sections every 0.5-1.0mm	H&E Mallory's trichome	AHA classification
Cai[28]	2002	1 reviewer	Yes	NA	Fixed in formalin decalcified embedded in paraffin	Sections every 0.5-1.0-mm throughout length	H&E Mallory's trichome	AHA classification
Mitsumori[34]	2003	1 reviewer	Yes	Directly	Fixed in formalin decalcified in 10% formic acid paraffin-embedded en bloc	10-µm sections every 1.0 mm in CCA and every 0.5 mm in ACI	H&E Mallory's trichome V&G	unstable FC: ulcerated, fissured, disrupted or min thickness <0.25mm
Moody[41]	2003	2 observers	Yes	Directly	10% formalin 5-mm blocks paraffin embedding	4-µm serial sections	HE	complicated plaque vs non-complicated
Cappendijk[37]	2004	2 biologists 2 pathologists (IPH age)	Yes	NA	Intact lateral/ventral ink fixed in formalin embedded in paraffin	4-µm sections in 3-mm intervals	HE	plaque components
Chu[38]	2004	1 investigator	Yes	NA	Fixed in formalin decalcified embedded in paraffin	10-µm slices every 0.5-1 mm	H&E Mallory's trichome	fresh/recent/old hemorrhage
Kampschulte[40]	2004	1 reviewer	Yes	Directly	Fixed in formalin decalcified embedded in paraffin	10-µm slices every 0.5-1 mm	H&E Mallory's trichome	AHA classification/ hemorrhage and cap thickness/rupture
Cappendijk[29]	2005	2 vascular biologists 1 pathologist	Yes	Directly	Lateral/ventral ink formalin 3 mm sections embedded in paraffin	4-µm sections	H&E EvG	plaque components : fibrous tissue lipid core calcifications IPH
Saam[31]	2005	1 reviewer	Yes	NA	Fixed in 10% formalin decalcified embedded en bloc in paraffin	10-µm slices every 1 mm common and 0.5 mm internal	H&E mallory's trichome	AHA classification

Honda[39]	2006			NA	NA	NA	H&E	plaque components
Puppini[30]	2006	1 pathologist	Yes	NA	Fixed in formaldehyde decalcified embedded in paraffin	3-mm sections 5-µm thick	H&E	AHA classification
Albuquerque[32]	2007	1 experienced pathologist	Yes	NA	Posterior/cranial ink/ decalcification inclusion in paraffin	10-µm sections every 3.0 mm	H&E Mallory trichromic	IPH: acute, recent, old
Watanabe[20]	2008	NA	Yes	NA	Mark laterally/ventrally fixed with formalin 2mm sections embedded in paraffin	NA	H&E EvG	plaque components & soft vs fibrous
Cappendijk[44]	2008	2 investigators	Yes	Directly	formalin 3-mm transverse embedded in paraffin	4-µm slices of each section	HE EvG	AHA classification ROIs of: fibrous tissue, LC, calcification, IPH
Yim[42]	2008	1 pathologist	Blinded	NA	fixed in formalin embedded in paraffin	Every 1 mm, 10-µm sections	HE	plaque components: IPH, fibrous tissue LC, calcifications
Yoshida[35]	2008	1 observer	Yes	NA	intact fixed in formalin demineralized embedded in paraffin	2-mm intervals, 5-µm sections	HE Masson trichrome EvG	ROIs of: FC, fibrosis, LC, IPH, calcifications, myxomateus tissue
Bitar[36]	2008	1 vascular pathologist	Yes	NA	10% formaldehyde decalcified embedded in paraffin	500-µm intervals from CCA-ICA 5-µm slice thickness	H&E	IPH
Ota[19]	2010	1 experienced pathologist	Yes	NA	formalin decalcified embedded in paraffin en bloc	10 µm every 1.0 mm in CCA every 0.5 mm in ICA through length of specimen	H&E mallory trichome	presence/absence/size IPH

MRI, magnetic resonance imaging; CEA, carotid endarterectomy; NA, not available; FC, fibrous cap; H&E, Hematoxylin and Eosin; EvG, Verhoeff Elastic von Gieson; ; AHA, American Heart Association; CCA, common carotid artery; ICA, internal carotid artery; IPH, intraplaque hemorrhage; LC, lipid core; vs, versus

Other studies also showed specific IPH detection with MRI; however, they only used one sequence. A T1W sequence, MR direct thrombus imaging, dedicated to detect the methemoglobin in IPH, was introduced by Moody *et al.*[42], with good performance. Albuquerque *et al.*[33], using a similar sequence, showed excellent agreement between the histologic finding of acute or recent hemorrhage and the MRI findings (correlation coefficient, 0.91; 95% CI, 0.81-1.00). The most commonly used double-inversion recovery (DIR) T1W turbo spin echo (TSE) was replaced by a T1W turbo field echo (TFE) in the study of Cappendijk *et al.*[38] A high interobserver agreement was found, and >80% of the IPH areas could be detected. Fibrous tissue within the thickened vessel wall, but outside of the main plaque area, was sometimes falsely detected as IPH.

Only one study[20] compared histology with 3.0-Tesla MRI. They found calcifications influenced their ability to visualize IPH, and these 15 sections were excluded from analysis. On different T1W images, IPH had a variable appearance, and on the 3D magnetization-prepared rapid acquisition gradient-echo (RAGE), the signal was more hyperintense. They processed 231 MRI sections and found a moderate agreement between MRI and histology when using the RAGE or fast spin echo (FSE) sequences. A lower agreement was found when using the TOF sequence. An improvement of the outcome measures was seen when excluding MRI areas that were <3 pixels (2.81 mm^2).

4. Lipid-rich necrotic core

We identified six studies that reported the imaging of LRNC and performed histology as a reference standard.[30-32, 40, 44, 45] Mostly, T1W sequences are used to identify LRNC, however the sequences used by the several research groups differ slightly amongst each other.

In LRNC with and without IPH, the LRNC overall accuracy improved when no IPH was present.[44] To identify LRNC, T1W and TOF sequences were used, and when necessary, T2W and PDW. The LRNC appeared hyperintense on the T1W scans and isointense on the TOF scans. Saam *et al.*[31], used comparable sequences when considering LRNC areas >2 mm^2, and the sensitivity and specificity increased, with a good correlation between MRI and histology ($R = 0.75$, $P < .001$).[32] However, Cappendijk *et al.*[30] showed a high sensitivity and specificity for the qualitative detection of LRNC or IPH, or both. In a further analysis, differentiation between LRNC with or without IPH was tried by using a multisequence algorithm (T1, T2, partial T2, PDW TSE, and T1W TFE sequences) as well as a single sequence (T1W TFE).[45] This showed an inter-reader agreement for semiquantitative analysis of LRNC of 0.86% (95% CI, 0.77%-0.94%) and 0.91% (95% CI, 0.85%-0.95%) for multisequence and single-sequence images, respectively. A large LRNC area was often overestimated by MRI. Puppini *et al.*[31] showed that MRI could detect LRNC without IPH in 34 of 56 regions vs 36 of 56 sections at histology. Honda *et al.*[40] stated that the T1W, T2W, and PDW sequences detected the lipid-rich components (high signal intensity) with a lower sensitivity then IPH.

DISCUSSION

This review provides an overview of the existing literature reporting noninvasive carotid plaque characterization by in vivo MRI with histology as a reference standard and indicates MRI is a valuable diagnostic tool in the preoperative workup to detect the major carotid plaque components in patients with carotid artery stenosis. However, although many studies have been published on hrMRI, we were unable to perform meta-analysis due to significant heterogeneity in study methods. Therefore, proportions for the specific plaque characteristics remain unclear.

MRI as a valuable diagnostic tool in carotid artery disease is not a new finding. Several studies have investigated the function of MRI in plaque imaging, and most indicate MRI is a valuable tool.[27, 48] Our review, based on *in vivo* imaging and histology, confirms this hypothesis and therefore we believe it might be valuable to implement hrMRI in the diagnostic work-up for patients with mild to moderate carotid artery stenosis. In contrast to patients with severe symptomatic carotid artery stenosis, patients with mild to moderate carotid stenosis remain an unclassified group.[1, 2] The benefit for these patients probably must be found in an extensive diagnostic workup to learn whether this less severe stenosis might be prone to cause any more symptoms. According to available literature, hrMRI might be contributive in this evaluation.

Our results indicate that calcification, FC, IPH, and LRNC can be identified with moderate to good sensitivity and specificity. Calcification is easily detected by MRI on all contrast weightings, and might be easiest on a bright-blood TOF sequence. Overall sensitivity ranged from 76% to 92% and sensitivity from 86% to 95%. For precise FC evaluation, the combination of bright-blood MRI and other sequences are necessary. According to the included studies, FC can be evaluated by MRI and confirmed by histology with a good sensitivity (range, 81%-100%) and a good specificity (range, 80-96%). Furthermore, the reported κ values of 0.74 to 0.85 were considered good.

In the literature, IPH is one of the most investigated plaque components with MRI. However, it is difficult to distinguish IPH and LRNC; and therefore, several studies identified IPH in a small number of plaques or in combination with LRNC. Literature is conflicting about the clinical impact of the differentiation between these two components. For example, one study showed that the presence of these components indicated a higher risk for vulnerability of the carotid plaque and therefore might result in more clinical events.[49] Although, in a larger cohort Hellings *et al.*[9] showed that patients whose excised carotid plaque revealed plaque hemorrhage or marked intraplaque vessel formation demonstrated an increased risk of a vascular event in follow-up after CEA, in contrast to large lipid core which was not associated with clinical outcome. Due to these conflicting results in literature and their supposed clinical impact we believe it might be valuable to distinguish these two components more precisely with MRI.

Studies that performed a multisequence protocol, detected IPH with a sensitivity ranging from 82% to 96% and a specificity of 74% to 100%. In studies where only one similar sequence was used, IPH was identified with a sensitivity of 84% to 100% and specificity of 84% to 96%. The detection of LRNC by MRI varied from 69% to 100% and the sensitivity from 95% to 100%. When IPH was not present in LRNC, the sensitivity and specificity often improved slightly. Reviewing images with multicontrast weightings provided the most comprehensive evaluation.[44]

Imaging of specific characteristics, such as thrombus and microvessels, must be improved to establish imaging of plaque composition more precisely and thereby predict the more hazardous plaques in patients. Thrombus is still merely investigated in concordance with the IPH component, and contrast agents are necessary for the detection of microvessels.[50] Unfortunately in our literature search, we

were not able to identify studies specifically focusing on thrombus or microvessels that reported outcome in diagnostic parameters and used histology as a reference. Furthermore, possibly imaging techniques like USPIO-enhanced MRI might be valuable in imaging vascularity or plaque inflammation *in vivo*. Currently this technique is often subject of research, however this imaging modality was not the scope of our review.

Our study had a few limitations. First, we chose *in vivo* imaging for the scope of this review because we believe this is relevant for clinical use of MRI. In *ex vivo* imaging, the radiofrequency coil is placed very close to the plaque, creating higher signal intensities and is performed without blood flow and the possibility of swallowing; therefore, no triggering is needed and no flow artefacts are seen.

Second, we believe it is necessary to use histology as a reference test to make conclusions on the function of MRI more valuable. Studies that perform histology can report their findings in diagnostic outcome parameters, making it possible to compare and extrapolate to the clinical setting. By retaining these conditions, a lot of studies on MRI had to be excluded. These studies might be valuable for contributing to the development in MRI research but did not fulfill our inclusion criteria. Furthermore, plaque composition, which may predict future events, and degree of stenosis must both be part of the decision for a specific treatment. For example, Zhao *et al.*[51, 52] showed that the presence of IPH in all categories of stenosis and plaque burden suggests that direct characterization of plaque composition and surface status is necessary to fully discriminate disease severity.

In our opinion for a good comparison, it is necessary that authors use predefined histological analysis and MR sequences in studies investigating the accuracy of MRI in patients with carotid artery stenosis. In a review performed by Lovett *et al.*[53], 73 eligible carotid imaging studies were included, of which 30 were about MRI. There was great variation in preparation of the plaque for histological assessment. Our review found incomparable or poorly reported histological or imaging protocols, creating a potential interpretational error. To standardize future reporting, it is advisable to use comparison with a validated histological protocol. Despite these limitations, we believe it is still valuable to provide this overview of articles investigating histological verified MRI of the carotid plaque to evaluate the current state of MRI clinically. Besides, this review can serve as "the wake-up call" for all investigators to use standardized imaging and histology protocols to allow comparison and pooling of studies investigating the diagnostic accuracy of MRI in identifying carotid plaque characteristics.

Future perspectives

This current review might contribute to the recent knowledge of *in vivo* carotid MRI and comparison with histology for identification of the more "vulnerable" plaque. For future research concerning carotid artery imaging, it is very important that predefined, validated histological and imaging protocols will be used to make clinical interpretation of these studies more reliable. At least it is valuable to define outcome in established diagnostic accuracy measurements, because these are comparable. Furthermore, future research using 3.0-Tesla MRI and the even more advanced 7.0-Tesla MRI will possibly create an additional imaging protocol that is totally capable of identifying the more hazardous and complicated plaques.[54, 55]

Conclusion

MRI appears to be effective in identifying specific plaque components and therefore might be valuable in diagnostic workup of patients with carotid artery stenosis in addition to stenosis grade. However, although MRI still holds a promise, clinical application for plaque characterization would require

consensus regarding MRI settings. For this reason and based on current literature it may be too early to routinely apply MRI as an imaging modality to assess plaque characteristics that have been associated with plaque vulnerability. Predefined protocols for histology and imaging must be established to make outcomes more comparable and clinically useful.

Author Contributions

Conception and design: AH, SB, WK, JH, PL, FM, GP, GB
Analysis and interpretation: AH, SB
Data collection: AH, SB
Writing the article: AH, SB
Critical revision of the article: AH, SB, WK, JH, PL, FM, GP, GB
Final approval of the article: AH, SB, WK, JH, PL, FM, GP, GB
Statistical analysis: AH, SB
Obtained funding: Not applicable
Overall responsibility: GB

The first part of this chapter described the current status of human carotid artery atherosclerotic plaque MRI studies, validated with histology. The next part of this chapter will focus on the development of molecular MRI, for the detection of atherosclerotic lesion in animal models. The focus lies on the correct evaluation with histology to accurate interpretation of the results from the animal experiments.

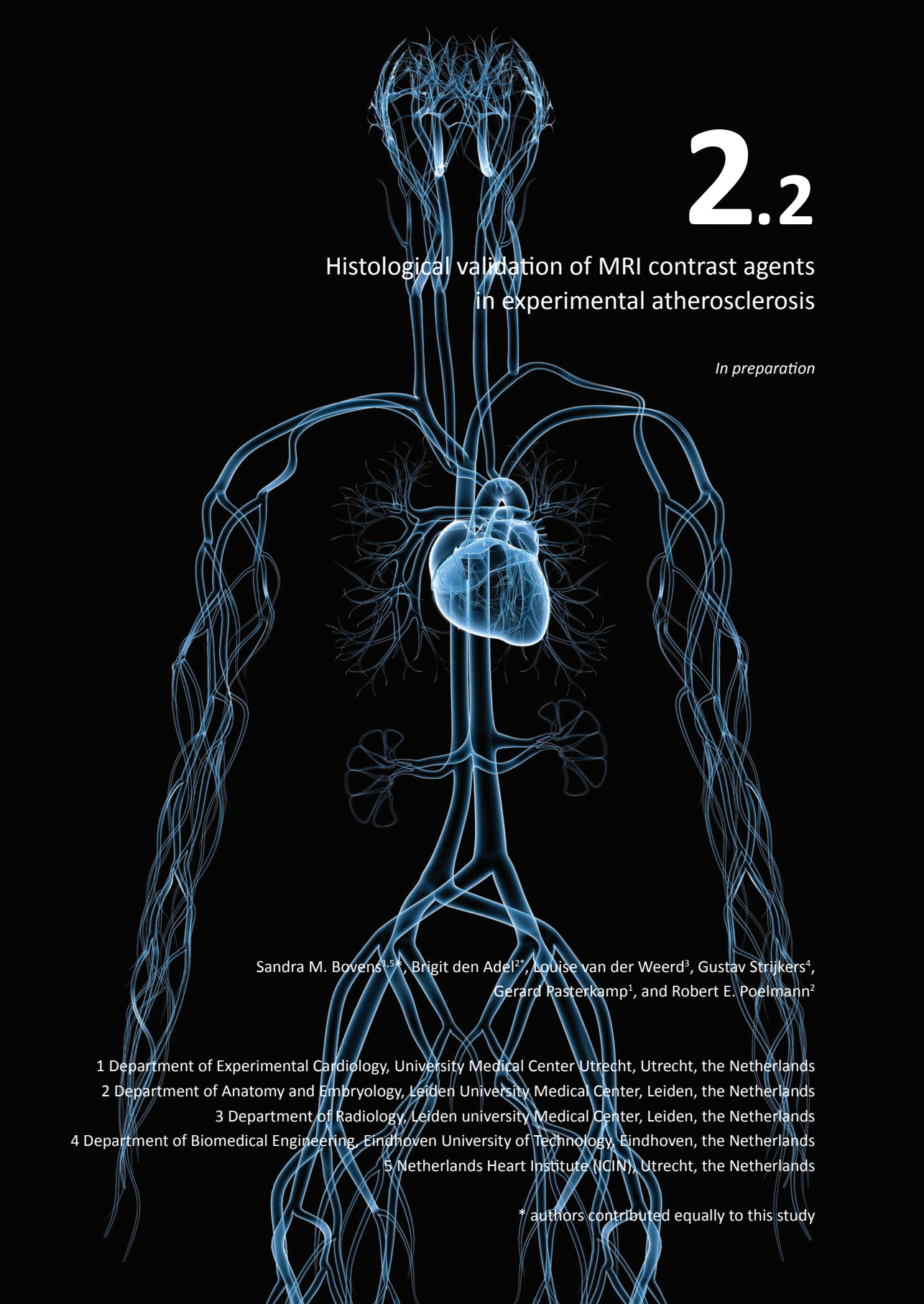

2.2

Histological validation of MRI contrast agents in experimental atherosclerosis

In preparation

Sandra M. Bovens[1,5*], Brigit den Adel[2*], Louise van der Weerd[3], Gustav Strijkers[4], Gerard Pasterkamp[1], and Robert E. Poelmann[2]

1 Department of Experimental Cardiology, University Medical Center Utrecht, Utrecht, the Netherlands
2 Department of Anatomy and Embryology, Leiden University Medical Center, Leiden, the Netherlands
3 Department of Radiology, Leiden university Medical Center, Leiden, the Netherlands
4 Department of Biomedical Engineering, Eindhoven University of Technology, Eindhoven, the Netherlands
5 Netherlands Heart Institute (ICIN), Utrecht, the Netherlands

* authors contributed equally to this study

ABSTRACT

MRI and MRI contrast agents (CA) have emerged as the most promising technique to study atherothrombotic disease *in vivo*.

Nowadays it becomes more and more apparent that post-processing techniques of tissues determine to a large extent whether one can validate CA accumulation in atherosclerotic plaques; lipid-based nanoparticles generally wash out during embedding in paraffin, however any incorporated peptide/antibody remains attached to its ligand. In verifying ligand binding, embedding in paraffin and subsequent, staining of the antibody-antigen complex is suitable. However, to determine whether the nanoparticles entered the vessel, cryopreservation is required to either stain for presence of DTPA or to visualize a fluorophore incorporated in the nanoparticle.

Conclusions

Understanding histological validation methods is of utmost importance for proper application and testing validation of MR contrast agents in animal models of atherosclerosis. Correct characterization possibilities of contrast agent accumulation may ultimately further contrast agent applications in the clinic.

INTRODUCTION

Atherosclerosis and its thrombotic complications are the major cause of morbidity and mortality in the industrialized countries, despite the clinical advances that have been made over the past 20 years in the prevention and treatment of this disease.[56] The main components of the atherothrombotic plaques are: (i) connective tissue extracellular matrix, including collagen, proteoglycans, fibronectin, and elastic fibres; (ii) crystalline cholesterol, cholesteryl esters, and phospholipids; (iii) cells including monocyte-derived macrophages, T-lymphocytes, and smooth muscle cells, and eventually (iv) thrombotic material with platelets and fibrin. Varying proportions of these components are present in different plaques, thus giving rise to heterogeneity of lesions.[46, 57, 58] Since the composition of the 'vulnerable' plaques, which are prone to rupture, contain a high frequency of inflammatory cells and may cause clinically manifest problems, varies depending on their anatomical site, with striking heterogeneity even within the same individual. Therefore reliable non-invasive imaging modalities able to detect and characterize atherothrombotic disease in its various stages and their different anatomical regions are desirable for clinical use.[59] An ideal clinical imaging modality for atherosclerotic vascular disease is safe, inexpensive, non- or minimally invasive, accurate, and reproducible while the results should correlate with the extent of atherosclerotic disease and have high predictive value for the occurrence of future clinical events.[60, 61]

Although not in compliance with all of the afore mentioned factors, high-resolution magnetic resonance imaging (MRI) has excellent soft tissue contrast and has emerged as the most promising technique to study atherothrombotic disease *in vivo*.[62] Magnetic resonance imaging does not involve ionizing radiation and provides high-resolution images of various vascular regions. An MR image is based on radiofrequency signal, typically from water protons, following administration of a radiofrequency pulse, while the subject is placed in a strong magnetic field. The emitted signal varies according to the water concentration and the relaxation times (T1 and T2). Using combined analysis of different tissue signal intensities generated by the application of T1-weigted (T1W), T2-weigted (T2W), and proton-density-weighted (PDW) images, it is possible to determine plaque anatomy. As magnetic resonance imaging provides imaging without ionizing radiation it can be repeated sequentially over time. Detailed analysis of atherosclerotic plaques is hampered by an inherent lack of sensitivity of MRI, which can be overcome by the use of contrast agents.

In the past decade, development of MRI contrast agents increased tremendously. T1 and T2 contrast agents (CA), with and without molecular targeting, are nowadays widely applied in animal models of human atherosclerosis.[63] Currently, there are no clinically established methods to non-invasively differentiate between stable and vulnerable plaques and to identify rupture prone plaques. As a result, there has been much activity in this field with the development of molecularly targeted MRI contrast agents.[64] Validation of the MR molecular images in pre-clinical atherosclerosis models by comparison with "gold standard" histology images is at these stages of utmost importance. In many cases histological validation is difficult or even flawed because of 1; lack of secondary detection methods (for e.g. Gd), 2; interaction of the contrast agent with the histological staining and 3; autofluorescence of tissue.

This review will focus on several strategies and validated histological methods of T1 as well as T2 contrast agents in different atherosclerotic mouse models, which have been used over the past few years and can help to validate the in vivo application and thereby further the introduction of contrast agents in the clinic.

T1 contrast agents

The most widely (clinically) applied positive contrast agents are based on Gd^{3+}-DTPA or –DOTA chelates. Due to the relatively low relaxivity of one Gd-DTPA molecule, Gd is also often incorporated into nanoparticles, such as micelles or liposomes which can harbor much larger payloads of gadolinium. So far, no methods have been developed for direct detection of Gd^{3+} on histological slides. Indirectly, Gd can be detected in situ using Europium (Eu) analogues.[65] Inductively coupled plasma mass spectroscopy (ICP-MS) of tissue homogenates can also be used to trace Gd in tissues, however, the exact cellular localization of the CA is lost with this method.[66] Recently several commercially available anti-DOTA and anti-DTPA antibodies have been developed which allow detection of Gd-chelates in their anatomical environment.[67] Of course this requires the presence of a stable and accessible chelate (without spherical hindrance) in the applied contrast agent. To our knowledge histological validation using these antibodies has not been published. We were able to histologically detect Gd-DTPA in atherosclerotic plaques (unpublished data). We used cryosections of carotid arteries from $ApoE^{-/-}$ mice with atherosclerotic plaques that were injected with Gd-DTPA containing micelles. DAB positive areas in the large arteries were detected in areas where positive signal enhancement could be observed using MRI (Figure 1). However, this method may not be suitable to tissues that underwent paraformaldehyde fixation and paraffin embedding as both Gd-DOTA and DTPA will wash out during this procedure.

Micelles or liposomes usually have a lipid-bound fluorochrome incorporated in the membrane for detection by fluorescence microscopy. Originally, rhodamine-PE was the fluorochrome of choice[68], however, rhodamine-PE fails to be detected in atherosclerotic plaques in $ApoE^{-/-}$ mice due to autofluorescence of elastic lamellae round the same emission wavelength (580 nm) leading to images that are difficult to interpret.[69] In $ApoE^{-/-}$ mice with extensive intimal thickening this problem could elegantly be circumvented by incorporation of a lipid-bound near infrared fluorophore like NIR664 in nanoparticles as described by van Bochove *et al*.[70] Advantage could then be taken of the autofluorescence of elastic lamellae without the need for additional staining procedures. An example is shown in Figure 2 where the elastic lamellae are depicted in green and the micelles with a NIR664 lipid in red.

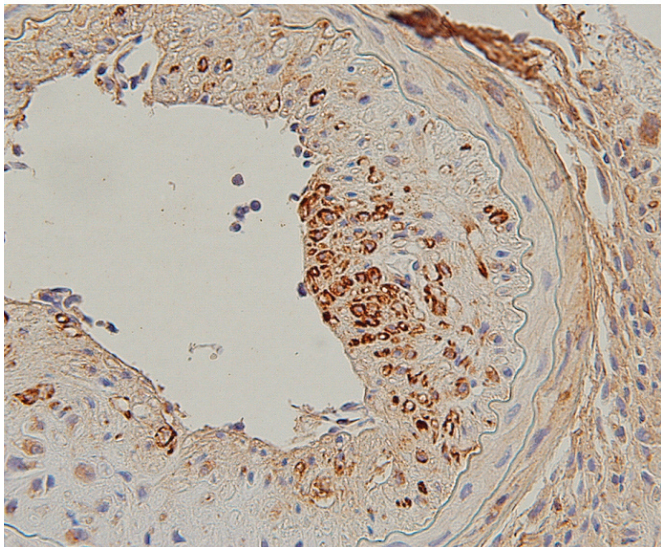

Figure 1 | *Staining of Gd-DTPA in an atherosclerotic plaque of an $ApoE^{-/-}$ mouse*
Gd-DTPA positive areas are depicted in brown (DAB).

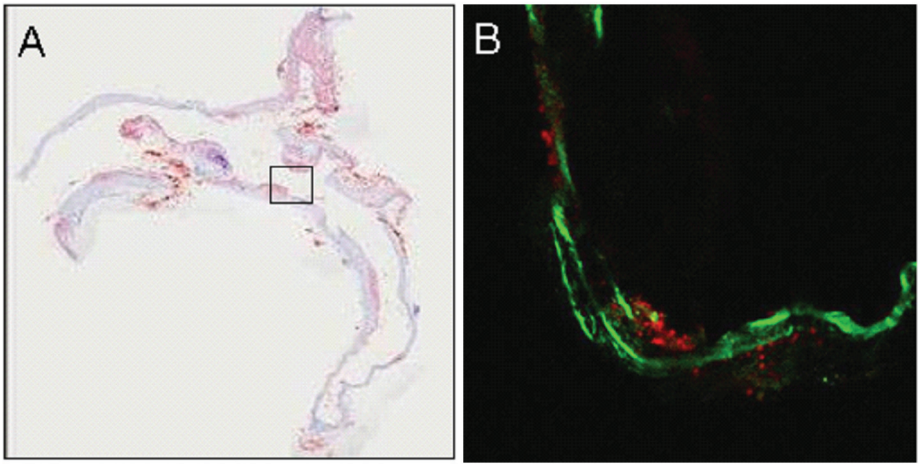

Figure 2 | *Detection of NIR664 lipid in an atherosclerotic plaque of an ApoE$^{-/-}$ mouse*
A: overview of aortic arch. B: zoomed frame of A, depicting the elastic lamellae in green and the micelles with a NIR664 lipid in red.

When using a different atherosclerotic mouse model (ApoE$^{-/-}$/eNOS$^{-/-}$ double knockout mice[71]) in which intra-plaque hemorrhage and the spontaneous development of aneurysms (in males) can be observed, erythrocytes cause additional autofluorescence, especially in the near infrared wavelength; in this mouse model NIR and other fluorochromes cannot be applied.

To circumvent flawed histological validation due to autofluorescence overlapping with the fluorescent spectrum of fluorochromes incorporated in nanoparticles, a different approach could be used to detect micelles/liposomes indirectly with a secondary histological staining. This brings other challenges: this approach could only be used with an antibody attached to the particle. For *in vivo* applications utmost consideration must be made using this approach due to known possible adverse immunological reactions against antibodies.
By processing tissue to obtain paraffin slides, micelles or liposomes are be washed away, however, the bound antibodies remain *in situ*. A secondary antibody can then be used directly on the paraffin slides, after which a DAB or AF step can visualize the bound antibodies and reveal the locations of the specific *in vivo* bound micelles.[72] An example of this staining is shown in Figure 3, NGAL staining showing the large distribution (Figure 3A) and the antibody staining to detect bound antibodies which were coupled to micelles (Figure 3B). A partial overlap in AF signal can be observed, all micelles were specifically bound to NGAL, yet more available NGAL (not bound by the micelles) was present and detected by the histological staining.

Van Tilborg *et al*.[73] used this approach with micelles or liposomes containing lipids conjugated to biotin (or streptavidin). An avidin chaser was used *in vivo* to increase the clearance rate of unbound particles. However, when these particles were used for histological evaluation using an avidin method it gives rise to severe background staining. Normally the aspecific background biotin will be blocked in any staining (cryo or paraffin sections), yet this is of course not possible when a particle contains biotin labeled lipids. So though this method may be very useful *in vivo* in experimental animals it cannot be used for histological validation of contrast agents.

Yet another promising approach to circumvent hindrance by autofluorescence in atherosclerotic vessels may be the development of dual histology/MRI contrast agents in which an optical histological stain is tagged with MRI contrast agents. Thus far this has only been described for brain MRI contrast agents.[74] Luxol Fast Blue (LFB), a classical staining for myelin, was modified such that it contained cupper. Both the macroscopic and microscopic distributions of LFB were found to mimic those of traditional histological preparations and the *in vivo* use of the compound allowed for detailed co-registration of histology and MRI. One could hypothesize that a similar approach could be used with a modified Oil Red O stain or classical collagen staining to detect atherosclerotic plaques.

An emerging new class of reporter genes encodes for proteins with affinity for radioisotopes or positron emitter probes. These receptors, transporters or enzymes can provide quantitative images on administration of suitable radiolabeled probes.[75] MRI reporter genes are unique among all reporter genes used with the various imaging modalities because they can provide information on gene expression that can be co-registered with anatomic/histological and functional information.[76]

An enzyme that was exploited as an MRI reporter gene is β-galactosidase (β-gal). β-gal is an enzyme encoded by the LacZ gene of Escherichia coli; it catalyzes hydrolysis of β-d-galactosides and is widely used in microscopy because of its large variety of substrates. The use of β-gal in MRI was demonstrated by its effect on (1-(2-(β-galactopyranosyloxy)propyl)-4,7,10-tris(carboxymethyl)-1,4,7,10-tetraazacyclododecane)gadolinium(III) (EgadMe).[77] Once EgadMe was cleaved by β-gal and its free coordination site of gadolinium was exposed, it altered the relaxation time of water and created contrast. β-gal was also used in spectroscopic and histological imaging.[78]

T2 contrast agents

USPIO (18-30 nm) and SPIO (100-200 nm) are superparamagnetic particles made of an iron crystalline core. These particles become ferromagnetic in the presence of a strong magnetic field (e.g. an MR imager) but lose their magnetization in the absence of the field. All iron oxides are T2-contrast agents and exhibit a "blooming" effect, creating negative, i.e. black, contrast beyond the regions where they are localized.[79] This blooming effect stresses the need to histologically validate the cellular localization of the contrast agent as the side of contrast agent accumulation does not literally reflect the area that is visualized using

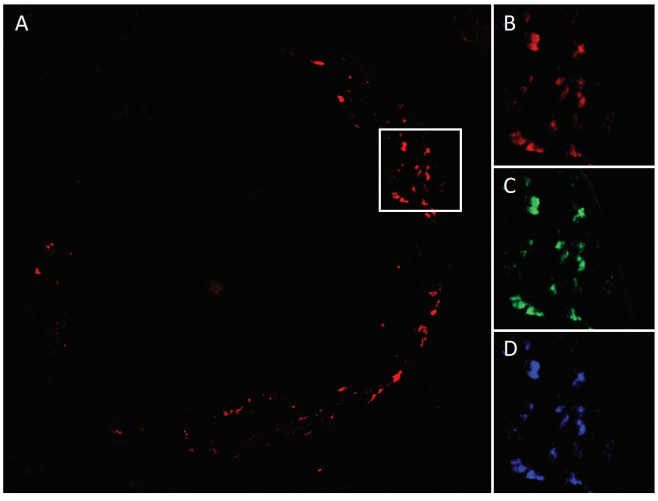

Figure 3 | *Autofluorescence in an atherosclerotic plaque from an ApoE$^{-/-}$/eNOS$^{-/-}$ mouse*
Autofluorescence can be observed in several wavelengths: red (A: ex543, em590), green (B: ex488, em518), and far red (C: depicted in blue; em633, em670)
Ex: excitation; em: emission

MRI. The inherent DAB reactivity of most USPIOs implies that staining a molecular marker besides the iron particle requires the use of different development methods. Iron oxide nanoparticles are typically classified according to their size which impacts their magnetic and biological properties. The coating is often dextran, citrate, or a polymer such as polyethylene glycol or polyvinyl alcohol.

Iron oxide-based contrast agents can be reliably detected using a Prussian blue staining, if needed with an amplification step. When using molecular targeted iron oxides it is difficult to discriminate specific binding from aspecific cellular uptake. Therefore one would like to combine the widely applied Prussian blue staining to detect iron with a secondary staining for the molecular target of the CA. In literature, staining with 3,3'-diaminobenzidine (DAB), a commonly used chromogen for immunohistochemical stainings, are widely applied as secondary detection method for iron oxides.[80] Development of a DAB staining requires a redox reaction to obtain its typical brown color. The redox reaction is performed with a peroxidase enzyme, yet iron oxides may also act as a reducing agent. We tested this hypothesis on aortic arch tissue of ApoE$^{-/-}$ mice that were injected with USPIOs and subsequently sacrificed.

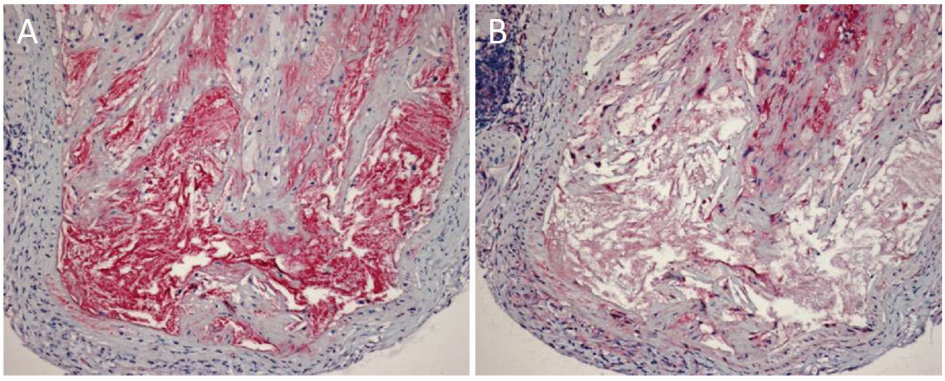

Figure 4 | *NGAL and micelle staining in an atherosclerotic plaque from an ApoE$^{-/-}$/eNOS$^{-/-}$ mouse*
A: NGAL staining depicted in red (AF); B: micelle staining depicted in red (AF). Some overlap between the staining can be observed, with more NGAL present than micelles.
NGAL: neutrophil gelatinase-associated lipocalin; AF: alkaline phosphatase

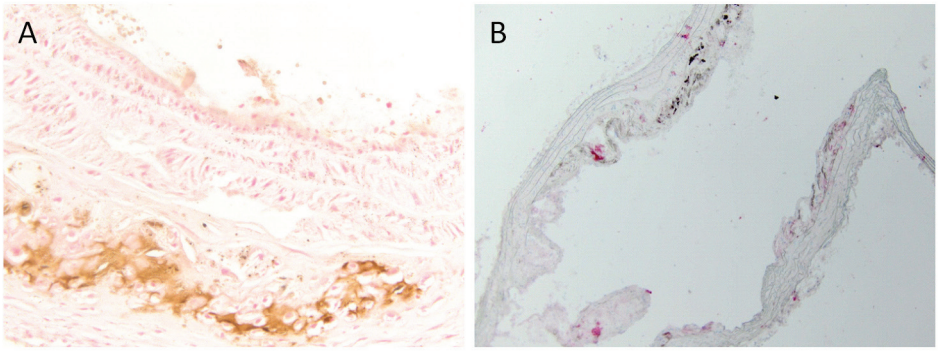

Figure 5 | *Staining of USPIO in an atherosclerotic plaque from an ApoE$^{-/-}$ mouse*
A: false positive double staining due to reactivity of USPIO and DAB. B: double staining of USPIO with Prussian Blue and secondary target with AF. USPIO: ultra-small particle of iron oxide; AF: alkaline phosphatase

We found that a DAB step in the presence of iron oxide nanoparticles leads to false-positive results for the secondary staining and difficulties to discriminate between the molecular target and the iron particle (Figure 4A). To circumvent this problem, we tested several other classical staining methods. Double staining of iron oxide particles with Prussian blue and a molecular target with alkaline phosphatase substrate turned out most suitable for detection of multiple targets without interference of iron oxides with the secondary staining (Figure 4B).

DISCUSSION

Histological validation of contrast agent accumulation is a necessary hurdle to take in the validation process of a contrast agent.

Evaluation of the specificity of targeted contrast agent accumulation to detect atherosclerotic lesions is difficult due to the occurrence of time-dependent both passive and active uptake in areas with EPR. To discriminate between these effects the timing of imaging and tissue harvesting after contrast agent is of utmost importance to assure the interpretation of MRI data is not obscured by changes in contrast agent accumulation over time or ambiguity in the histology.

It becomes more and more apparent that post-processing techniques of harvested tissues determine to a large extent whether one can validate CA accumulation; lipid-based nanoparticles generally wash out during embedding in paraffin, however any incorporated peptide/antibody remains attached to its ligand. If one wishes to verify ligand binding, embedding in paraffin and subsequent staining of the antibody-antigen complex is suitable. However, to verify whether the same nanoparticles entered the vessel, cryopreservation is required to either stain for presence of DTPA or to visualize an incorporated fluorophore in the nanoparticle.

Different mouse models of atherosclerosis ask for different validation solutions. Although this overview is written in the context of atherosclerosis one can of course extrapolate these findings to other fields as autofluorescence, washing out of particles and chemical interferences are general challenges one encounters working with MRI contrast agents.

The use of contrast agents, both targeted and non-targeted, for the detection of plaques has, so far, not reached the clinic. However, molecular MRI is one of the most promising non-invasive screening tools for identification of patients at risk of a clinical event. To foresee clinical implications of molecular imaging of atherosclerosis two main aspects need to be considered: i.e. technical constraints that currently hamper clinical applications, in particular for imaging of the coronary arteries, and the potential clinical impact in terms of managing strategies to ultimately reduce the occurrence of cardiac events. Even more importantly, once technical progress will make molecular imaging ready for large clinical use, substantial research will be needed to verify which category of subjects or patients will benefit the most from this evaluation. The opportunity to identify the vulnerable patients and the vulnerable plaques noninvasively is of tremendous clinical interest and from available pathophysiological and clinical studies some potential applications of molecular imaging may be hypothesized. Both sensitivity and specificity of contrast agents will need to be high to allow future clinical applications.

In theory, evaluation of asymptomatic patients classified at intermediate risk by current risk stratification algorithms may be useful to reclassify those with elevated coronary inflammatory activity in whom treatment would be desired. Prognostic value and cost-effectiveness will need to be compared to other currently applied techniques.

The potential to monitor therapeutic efficiency of anti-atherosclerotic drugs or lifestyle changes using molecular imaging is attractive and worth being tested in clinical studies. This potential, together with ongoing rapid technical improvements underlines the importance of early validation of novel contrast agents.

Several research groups are involved in the solution of technical problems, while others are involved in contrast-enhanced MRI, which allows lower SNR because of increased contrast between targets of interest and their background. Equally important, the possibility to use vehicles carrying not only (super) paramagnetic agents but also antibodies, peptides or receptor agonists, provides a technique which is capable of targeting vulnerable plaque markers which are more specific and/or sensitive for prediction of plaque disruption than the classical morphologic features.

Conclusion

To successfully implement molecular MRI as a clinical screening tool, it is of utmost importance for the *ex vivo* validation methods to be as efficient and transparent as possible. Keeping this in mind, in the near future treatment may be tailored to the individual patient.

1. Randomised trial of endarterectomy for recently symptomatic carotid stenosis: final results of the MRC European Carotid Surgery Trial (ECST). Lancet 1998 May 9;351(9113):1379-87.

2. Barnett HJ, Taylor DW, Eliasziw M, Fox AJ, Ferguson GG, Haynes RB, Rankin RN, Clagett GP, Hachinski VC, Sackett DL, Thorpe KE, Meldrum HE, Spence JD. Benefit of carotid endarterectomy in patients with symptomatic moderate or severe stenosis. North American Symptomatic Carotid Endarterectomy Trial Collaborators. N Engl J Med 1998 November 12;339(20):1415-25.

3. Endarterectomy for asymptomatic carotid artery stenosis. Executive Committee for the Asymptomatic Carotid Atherosclerosis Study. JAMA 1995 May 10;273(18):1421-8.

4. Halliday A, Harrison M, Hayter E, Kong X, Mansfield A, Marro J, Pan H, Peto R, Potter J, Rahimi K, Rau A, Robertson S, Streifler J, Thomas D. 10-year stroke prevention after successful carotid endarterectomy for asymptomatic stenosis (ACST-1): a multicentre randomised trial. Lancet 2010 September 25;376(9746):1074-84.

5. Rothwell PM, Eliasziw M, Gutnikov SA, Fox AJ, Taylor DW, Mayberg MR, Warlow CP, Barnett HJ. Analysis of pooled data from the randomised controlled trials of endarterectomy for symptomatic carotid stenosis. Lancet 2003 January 11;361(9352):107-16.

6. Dawkins AA, Evans AL, Wattam J, Romanowski CA, Connolly DJ, Hodgson TJ, Coley SC. Complications of cerebral angiography: a prospective analysis of 2,924 consecutive procedures. Neuroradiology 2007 September;49(9):753-9.

7. Rothwell PM, Gibson R, Warlow CP. Interrelation between plaque surface morphology and degree of stenosis on carotid angiograms and the risk of ischemic stroke in patients with symptomatic carotid stenosis. On behalf of the European Carotid Surgery Trialists' Collaborative Group. Stroke 2000 March;31(3):615-21.

8. Verhoeven B, Hellings WE, Moll FL, de Vries JP, de Kleijn DP, de BP, Busser E, Schoneveld AH, Pasterkamp G. Carotid atherosclerotic plaques in patients with transient ischemic attacks and stroke have unstable characteristics compared with plaques in asymptomatic and amaurosis fugax patients. J Vasc Surg 2005 December;42(6):1075-81.

9. Hellings WE, Peeters W, Moll FL, Piers SR, van SJ, Van der Spek PJ, de Vries JP, Seldenrijk KA, De Bruin PC, Vink A, Velema E, de Kleijn DP, Pasterkamp G. Composition of carotid atherosclerotic plaque is associated with cardiovascular outcome: a prognostic study. Circulation 2010 May 4;121(17):1941-50.

10. Koelemay MJ, Nederkoorn PJ, Reitsma JB, Majoie CB. Systematic review of computed tomographic angiography for assessment of carotid artery disease. Stroke 2004 October;35(10):2306-12.

11. Nandalur KR, Hardie AD, Raghavan P, Schipper MJ, Baskurt E, Kramer CM. Composition of the stable carotid plaque: insights from a multidetector computed tomography study of plaque volume. Stroke 2007 March;38(3):935-40.

12. Gronholdt ML, Wagner A, Wiebe BM, Hansen JU, Schroeder TV, Wilhjelm JE, Nowak M, Sillesen H. Spiral computed tomographic imaging related to computerized ultrasonographic images of carotid plaque morphology and histology. J Ultrasound Med 2001 May;20(5):451-8.

13. Walker LJ, Ismail A, McMeekin W, Lambert D, Mendelow AD, Birchall D. Computed tomography angiography for the evaluation of carotid atherosclerotic plaque: correlation with histopathology of endarterectomy specimens. Stroke 2002 April;33(4):977-81.

14. Naghavi M, Libby P, Falk E, Casscells SW, Litovsky S, Rumberger J, Badimon JJ, Stefanadis C, Moreno P, Pasterkamp G, Fayad Z, Stone PH, Waxman S, Raggi P, Madjid M, Zarrabi A, Burke A, Yuan C, Fitzgerald PJ, Siscovick DS, de Korte CL, Aikawa M, Juhani Airaksinen KE, Assmann G, Becker CR, Chesebro JH, Farb A, Galis ZS, Jackson C, Jang IK, Koenig W, Lodder RA, March K, Demirovic J, Navab M, Priori SG, Rekhter MD, Bahr R, Grundy SM, Mehran R, Colombo A, Boerwinkle E, Ballantyne C, Insull W, Jr., Schwartz RS, Vogel R, Serruys PW, Hansson GK, Faxon DP, Kaul S, Drexler H, Greenland P, Muller JE, Virmani R, Ridker PM, Zipes DP, Shah PK, Willerson JT. From vulnerable plaque to vulnerable patient: a call for new definitions and risk assessment strategies: Part I. Circulation 2003 October 7;108(14):1664-72.

15. Kerwin W, Hooker A, Spilker M, Vicini P, Ferguson M, Hatsukami T, Yuan C. Quantitative magnetic resonance imaging analysis of neovasculature volume in carotid atherosclerotic plaque. Circulation 2003 February 18;107(6):851-6.

16. Kerwin W, Hooker A, Spilker M, Vicini P, Ferguson M, Hatsukami T, Yuan C. Quantitative magnetic resonance imaging analysis of neovasculature volume in carotid atherosclerotic plaque. Circulation 2003 February 18;107(6):851-6.

17. Metz S, Beer AJ, Settles M, Pelisek J, Botnar RM, Rummeny EJ, Heider P. Characterization of carotid artery plaques with USPIO-enhanced MRI: assessment of inflammation and vascularity as in vivo imaging biomarkers for plaque vulnerability. Int J Cardiovasc Imaging 2011 July;27(6):901-12.

18. Yuan C, Mitsumori LM, Beach KW, Maravilla KR. Carotid atherosclerotic plaque: noninvasive MR characterization and identification of vulnerable lesions. Radiology 2001 November;221(2):285-99.

19. Hayes CE, Mathis CM, Yuan C. Surface coil phased arrays for high-resolution imaging of the carotid arteries. J Magn Reson Imaging 1996 January;6(1):109-12.

20. Ota H, Yarnykh VL, Ferguson MS, Underhill HR, DeMarco JK, Zhu DC, Oikawa M, Dong L, Zhao X, Collar A, Hatsukami TS, Yuan C. Carotid intraplaque hemorrhage imaging at 3.0-T MR imaging: comparison of the diagnostic performance of three T1-weighted sequences. Radiology 2010 February;254(2):551-63.

21. Watanabe Y, Nagayama M, Suga T, Yoshida K, Yamagata S, Okumura A, Amoh Y, Nakashita S, Van CM, Dodo Y. Characterization of atherosclerotic plaque of carotid arteries with histopathological correlation: vascular wall MR imaging vs. color Doppler ultrasonography (US). J Magn Reson Imaging 2008 August;28(2):478-85.

22. Corti R, Fayad ZA, Fuster V, Worthley SG, Helft G, Chesebro J, Mercuri M, Badimon JJ. Effects of lipid-lowering by simvastatin on human atherosclerotic lesions: a longitudinal study by high-resolution, noninvasive magnetic resonance imaging. Circulation 2001 July 17;104(3):249-52.

23. Hatsukami TS, Yuan C. MRI in the early identification and classification of high-risk atherosclerotic carotid plaques. Imaging Med 2010 February 1;2(1):63-75.

24. Hermus L, van Dam GM, Zeebregts CJ. Advanced carotid plaque imaging. Eur J Vasc Endovasc Surg 2010 February;39(2):125-33.

25. Leiner T, Gerretsen S, Botnar R, Lutgens E, Cappendijk V, Kooi E, van EJ. Magnetic resonance imaging of atherosclerosis. Eur Radiol 2005 June;15(6):1087-99.

26. Watanabe Y, Nagayama M. MR plaque imaging of the carotid artery. Neuroradiology 2010 April;52(4):253-74.

27. Yuan C, Kerwin WS. MRI of atherosclerosis. J Magn Reson Imaging 2004 June;19(6):710-9.

28. Liberati A, Altman DG, Tetzlaff J, Mulrow C, Gotzsche PC, Ioannidis JP, Clarke M, Devereaux PJ, Kleijnen J, Moher D. The PRISMA statement for reporting systematic reviews and meta-analyses of studies that evaluate healthcare interventions: explanation and elaboration. BMJ 2009;339:b2700.

29. Cai JM, Hatsukami TS, Ferguson MS, Small R, Polissar NL, Yuan C. Classification of human carotid atherosclerotic lesions with in vivo multicontrast magnetic resonance imaging. Circulation 2002 September 10;106(11):1368-73.

30. Cappendijk VC, Cleutjens KB, Kessels AG, Heeneman S, Schurink GW, Welten RJ, Mess WH, Daemen MJ, van Engelshoven JM, Kooi ME. Assessment of human atherosclerotic carotid plaque components with multisequence MR imaging: initial experience. Radiology 2005 February;234(2):487-92.

31. Puppini G, Furlan F, Cirota N, Veraldi G, Piubello Q, Montemezzi S, Gortenuti G. Characterisation of carotid atherosclerotic plaque: comparison between magnetic resonance imaging and histology. Radiol Med 2006 October;111(7):921-30.

32. Saam T, Ferguson MS, Yarnykh VL, Takaya N, Xu D, Polissar NL, Hatsukami TS, Yuan C. Quantitative evaluation of carotid plaque composition by in vivo MRI. Arterioscler Thromb Vasc Biol 2005 January;25(1):234-9.

33. Albuquerque LC, Narvaes LB, Maciel AA, Staub H, Friedrich M, Filho JRH, Marques MB, Rohde LE. Intraplaque hemorrhage assessed by high-resolution magnetic resonance imaging and C-reactive protein in carotid atherosclerosis. Journal of Vascular Surgery 2007;46(6):1130-7.

34. Hatsukami TS, Ross R, Polissar NL, Yuan C. Visualization of fibrous cap thickness and rupture in human atherosclerotic carotid plaque in vivo with high-resolution magnetic resonance imaging. Circulation 2000 August 29;102(9):959-64.

35. Mitsumori LM, Hatsukami TS, Ferguson MS, Kerwin WS, Cai J, Yuan C. In vivo accuracy of multisequence MR imaging for identifying unstable fibrous caps in advanced human carotid plaques. J Magn Reson Imaging 2003;17(4):410-20.

36. Yoshida K, Narumi O, Chin M, Inoue K, Tabuchi T, Oda K, Nagayama M, Egawa N, Hojo M, Goto Y, Watanabe Y, Yamagata S. Characterization of carotid atherosclerosis and detection of soft plaque with use of black-blood MR imaging. Am J Neuroradiol 2008;29(5):868-74.

37. Bitar R, Moody AR, Leung G, Symons S, Crisp S, Butany J, Rowsell C, Kiss A, Nelson A, Maggisano R. In vivo 3D high-spatial-resolution MR imaging of intraplaque hemorrhage. Radiology 2008 October;249(1):259-67.

38. Cappendijk VC, Cleutjens KB, Heeneman S, Schurink GW, Welten RJ, Kessels AG, Van Suylen RJ, Daemen MJ, van Engelshoven JM, Kooi ME. In vivo detection of hemorrhage in human atherosclerotic plaques with magnetic resonance imaging. J Magn Reson Imaging 2004 July;20(1):105-10.

39. Chu B, Kampschulte A, Ferguson MS, Kerwin WS, Yarnykh VL, O'Brien KD, Polissar NL, Hatsukami TS, Yuan C. Hemorrhage in the atherosclerotic carotid plaque: a high-resolution MRI study. Stroke 2004 May;35(5):1079-84.

40. Honda M, Kitagawa N, Tsutsumi K, Nagata I, Morikawa M, Hayashi T. High-resolution magnetic resonance imaging for detection of carotid plaques. Neurosurgery 2006 February;58(2):338-46.

41. Kampschulte A, Ferguson MS, Kerwin WS, Polissar NL, Chu B, Saam T, Hatsukami TS, Yuan C. Differentiation of intraplaque versus juxtaluminal hemorrhage/thrombus in advanced human carotid atherosclerotic lesions by in vivo magnetic resonance imaging. Circulation 2004 November 16;110(20):3239-44.

42. Moody AR, Murphy RE, Morgan PS, Martel AL, Delay GS, Allder S, MacSweeney ST, Tennant WG, Gladman J, Lowe J, Hunt BJ. Characterization of complicated carotid plaque with magnetic resonance direct thrombus imaging in patients with cerebral ischemia. Circulation 2003;107(24):3047-52.

43. Yim YJ, Choe YH, Ko Y, Kim ST, Kim KH, Jeon P, Byun HS, Kim DI. High signal intensity halo around the carotid artery on maximum intensity projection images of time-of-flight MR angiography: a new sign for intraplaque hemorrhage. J Magn Reson Imaging 2008 June;27(6):1341-6.

44. Yuan C, Mitsumori LM, Ferguson MS, Polissar NL, Echelard D, Ortiz G, Small R, Davies JW, Kerwin WS, Hatsukami TS. In vivo accuracy of multispectral magnetic resonance imaging for identifying lipid-rich necrotic cores and intraplaque hemorrhage in advanced human carotid plaques. Circulation 2001;104(17):2051-6.

45. Cappendijk VC, Kessels AGH, Heeneman S, Cleutjens KBJM, Schurink GWH, Welten RJT, Mess WH, Van Suylen RJ, Leiner T, Daemen MJAP, van Engelshoven JMA, Kooi ME. Comparison of lipid-rich necrotic core size in symptomatic and asymptomatic carotid atherosclerotic plaque: Initial results. J Magn Reson Imaging 2008;27(6):1356-61.

46. Stary HC, Chandler AB, Dinsmore RE, Fuster V, Glagov S, Insull W, Jr., Rosenfeld ME, Schwartz CJ, Wagner WD, Wissler RW. A definition of advanced types of atherosclerotic lesions and a histological classification of atherosclerosis. A report from the Committee on Vascular Lesions of the Council on Arteriosclerosis, American Heart Association. Circulation 1995 September 1;92(5):1355-74.

47. Stary HC. Natural history and histological classification of atherosclerotic lesions: an update. Arterioscler Thromb Vasc Biol 2000 May;20(5):1177-8.

48. Watanabe Y, Nagayama M. MR plaque imaging of the carotid artery. Neuroradiology 2010 April;52(4):253-74.

49. Takaya N, Yuan C, Chu B, Saam T, Underhill H, Cai J, Tran N, Polissar NL, Isaac C, Ferguson MS, Garden GA, Cramer SC, Maravilla KR, Hashimoto B, Hatsukami TS. Association between carotid plaque characteristics and subsequent ischemic cerebrovascular events: a prospective assessment with MRI--initial results. Stroke 2006 March;37(3):818-23.

50. Kerwin W, Hooker A, Spilker M, Vicini P, Ferguson M, Hatsukami T, Yuan C. Quantitative magnetic resonance imaging analysis of neovasculature volume in carotid atherosclerotic plaque. Circulation 2003 February 18;107(6):851-6.

51. Kerwin W, Hooker A, Spilker M, Vicini P, Ferguson M, Hatsukami T, Yuan C. Quantitative magnetic resonance imaging analysis of neovasculature volume in carotid atherosclerotic plaque. Circulation 2003 February 18;107(6):851-6.

52. Zhao X, Underhill HR, Zhao Q, Cai J, Li F, Oikawa M, Dong L, Ota H, Hatsukami TS, Chu B, Yuan C. Discriminating carotid atherosclerotic lesion severity by luminal stenosis and plaque burden: a comparison utilizing high-resolution magnetic resonance imaging at 3.0 Tesla. Stroke 2011 February;42(2):347-53.

53. Lovett JK, Redgrave JN, Rothwell PM. A critical appraisal of the performance, reporting, and interpretation of studies comparing carotid plaque imaging with histology. Stroke 2005 May;36(5):1091-7.

54. Hinton-Yates DP, Cury RC, Wald LL, Wiggins GC, Keil B, Seethmaraju R, Gangadharamurthy D, Ogilvy CS, Dai G, Houser SL, Stone JR, Furie KL. 3.0 T plaque imaging. Top Magn Reson Imaging 2007 October;18(5):389-400.

55. van der Kolk AG, Hendrikse J, Zwanenburg JJ, Visser F, Luijten PR. Clinical applications of 7T MRI in the brain. Eur J Radiol 2011 September 19.

56. Libby P, Ridker PM, Hansson GK. Inflammation in atherosclerosis: from pathophysiology to practice. J Am Coll Cardiol 2009 December 1;54(23):2129-38.

57. Davies MJ. Stability and instability: two faces of coronary atherosclerosis. The Paul Dudley White Lecture 1995. Circulation 1996 October 15;94(8):2013-20.

58. Libby P, Ridker PM, Maseri A. Inflammation and atherosclerosis. Circulation 2002 March 5;105(9):1135-43.

59. Corti R, Fuster V, Badimon JJ, Hutter R, Fayad ZA. New understanding of atherosclerosis (clinically and experimentally) with evolving MRI technology in vivo. Ann N Y Acad Sci 2001 December;947:181-95.

60. Corti R, Fuster V, Badimon JJ, Hutter R, Fayad ZA. New understanding of atherosclerosis (clinically and experimentally) with evolving MRI technology in vivo. Ann N Y Acad Sci 2001 December;947:181-95.

61. Matter CM, Stuber M, Nahrendorf M. Imaging of the unstable plaque: how far have we got? Eur Heart J 2009 November;30(21):2566-74.

62. Saraste A, Nekolla SG, Schwaiger M. Cardiovascular molecular imaging: an overview. Cardiovasc Res 2009 September 1;83(4):643-52.

63. Saraste A, Nekolla SG, Schwaiger M. Cardiovascular molecular imaging: an overview. Cardiovasc Res 2009 September 1;83(4):643-52.

64. Te Boekhorst BC, Cramer MJ, Pasterkamp G, van Echteld CJ, Doevendans PA. Recent developments and new perspectives on imaging of atherosclerotic plaque: role of anatomical, cellular and molecular MRI Part I and II. Int J Cardiovasc Imaging 2010 April;26(4):433-45.

65. Elster AD, Jackels SC, Allen NS, Marrache RC. Dyke Award. Europium-DTPA: a gadolinium analogue traceable by fluorescence microscopy. AJNR Am J Neuroradiol 1989 November;10(6):1137-44.

66. Frame EM, Uzgiris EE. Gadolinium determination in tissue samples by inductively coupled plasma mass spectrometry and inductively coupled plasma atomic emission spectrometry in evaluation of the action of magnetic resonance imaging contrast agents. Analyst 1998 April;123(4):675-9.

67. Frame EM, Uzgiris EE. Gadolinium determination in tissue samples by inductively coupled plasma mass spectrometry and inductively coupled plasma atomic emission spectrometry in evaluation of the action of magnetic resonance imaging contrast agents. Analyst 1998 April;123(4):675-9.

68. van Bochove GS, Paulis LE, Segers D, Mulder WJ, Krams R, Nicolay K, Strijkers GJ. Contrast enhancement by differently sized paramagnetic MRI contrast agents in mice with two phenotypes of atherosclerotic plaque. Contrast Media Mol Imaging 2011 January;6(1):35-45.

69. Mulder WJ, Strijkers GJ, van Tilborg GA, Griffioen AW, Nicolay K. Lipid-based nanoparticles for contrast-enhanced MRI and molecular imaging. NMR Biomed 2006 February;19(1):142-64.

70. van Bochove GS, Paulis LE, Segers D, Mulder WJ, Krams R, Nicolay K, Strijkers GJ. Contrast enhancement by differently sized paramagnetic MRI contrast agents in mice with two phenotypes of atherosclerotic plaque. Contrast Media Mol Imaging 2011 January;6(1):35-45.

71. Kuhlencordt PJ, Gyurko R, Han F, Scherrer-Crosbie M, Aretz TH, Hajjar R, Picard MH, Huang PL. Accelerated atherosclerosis, aortic aneurysm formation, and ischemic heart disease in apolipoprotein E/endothelial nitric oxide synthase double-knockout mice. Circulation 2001 July 24;104(4):448-54.

72. Te Boekhorst BC, Bovens SM, Hellings WE, van der Kraak PH, van de Kolk KW, Vink A, Moll FL, van Oosterhout MF, de Vries JP, Doevendans PA, Goumans MJ, de Kleijn DP, van Echteld CJ, Pasterkamp G, Sluijter JP. Molecular MRI of murine atherosclerotic plaque targeting NGAL: a protein associated with unstable human plaque characteristics. Cardiovasc Res 2011 February 15;89(3):680-8.

73. van Tilborg GA, Mulder WJ, van der Schaft DW, Reutelingsperger CP, Griffioen AW, Strijkers GJ, Nicolay K. Improved magnetic resonance molecular imaging of tumor angiogenesis by avidin-induced clearance of nonbound bimodal liposomes. Neoplasia 2008 December;10(12):1459-69.

74. Blackwell ML, Farrar CT, Fischl B, Rosen BR. Target-specific contrast agents for magnetic resonance microscopy. Neuroimage 2009 June;46(2):382-93.

75. Serganova I, Ponomarev V, Blasberg R. Human reporter genes: potential use in clinical studies. Nucl Med Biol 2007 October;34(7):791-807.

76. Gilad AA, Winnard PT, Jr., van Zijl PC, Bulte JW. Developing MR reporter genes: promises and pitfalls. NMR Biomed 2007 May;20(3):275-90.

77. Louie AY, Huber MM, Ahrens ET, Rothbacher U, Moats R, Jacobs RE, Fraser SE, Meade TJ. In vivo visualization of gene expression using magnetic resonance imaging. Nat Biotechnol 2000 March;18(3):321-5.

78. Kodibagkar VD, Yu J, Liu L, Hetherington HP, Mason RP. Imaging beta-galactosidase activity using 19F chemical shift imaging of LacZ gene-reporter molecule 2-fluoro-4-nitrophenol-beta-D-galactopyranoside. Magn Reson Imaging 2006 September;24(7):959-62.

79. Schmitz SA. [Iron-oxide-enhanced MR imaging of inflammatory atherosclerotic lesions: overview of experimental and initial clinical results]. Rofo 2003 April;175(4):469-76.

80. Jaffer FA, Libby P, Weissleder R. Molecular imaging of cardiovascular disease. Circulation 2007 August 28;116(9):1052-61.

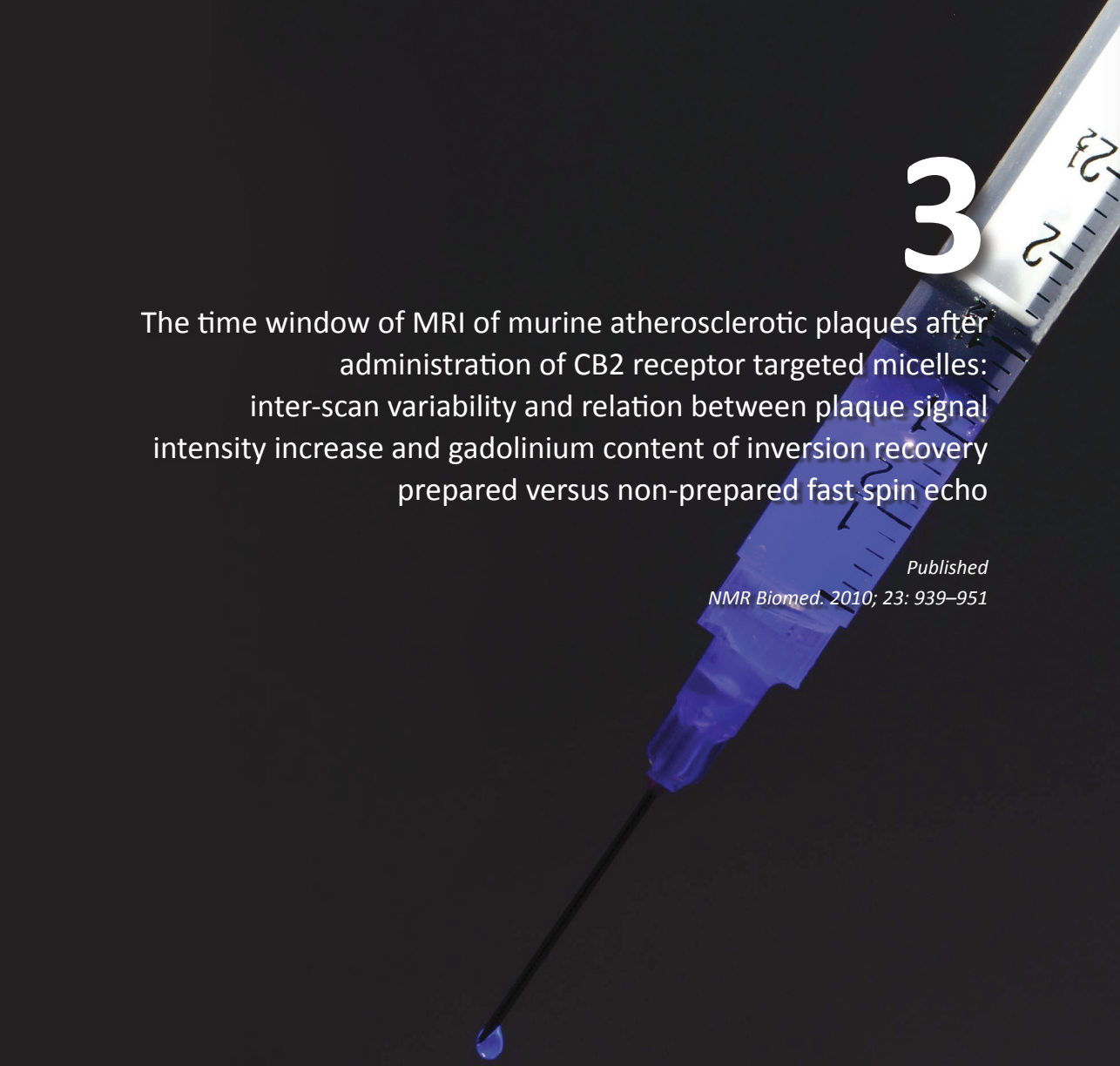

3

The time window of MRI of murine atherosclerotic plaques after administration of CB2 receptor targeted micelles: inter-scan variability and relation between plaque signal intensity increase and gadolinium content of inversion recovery prepared versus non-prepared fast spin echo

Published
NMR Biomed. 2010; 23: 939–951

Bernard C.M. te Boekhorst[1,2], Sandra M. Bovens[1,2], Kees W.A. van de Kolk[1], Maarten J.M. Cramer[1], Pieter A.F.M. Doevendans[1], Michiel ten Hove[1], Louise van der Weerd[3], Rob E. Poelmann[4], Gustav J. Strijkers[5], Gerard Pasterkamp[1], and Cees J.A. van Echteld[1]

1 Department of Cardiology, University Medical Center Utrecht, Utrecht, the Netherlands
2 Netherlands Heart Institute (ICIN), Utrecht, the Netherlands
3 Department of Radiology, Leiden University Medical Center, Leiden, the Netherlands
4 Department of Anatomy and Embryology, Leiden University Medical Center, Leiden, the Netherlands
5 Department of Biomedical Engineering, Eindhoven University of Technology, Eindhoven, the Netherlands

ABSTRACT

Background

Single fast spin echo scans covering limited time frames are mostly used for contrast-enhanced MRI of atherosclerotic plaque biomarkers. Knowledge on inter-scan variability of the Normalized Enhancement Ratio of plaque (NER_{plaque}) and relation between NER_{plaque} and gadolinium content for inversion-recovery fast spin echo is limited. Study aims were: evaluation of 1. timing of MRI after intravenous injection of Cannabinoid-2 receptor (CB2-R) (expressed by human and mouse plaque macrophages) targeted micelles, 2. inter-scan variability of inversion-recovery fast spin echo and fast spin echo, 3. relation between NER_{plaque} and gadolinium content for inversion-recovery fast spin echo and fast spin echo.

Methods and Results

Inversion-recovery fast spin echo/fast spin echo imaging was performed before and every 15 minutes up to 48 hours after injection of CB2-R targeted or control micelles using several groups of mice measured in an interleaved fashion. NER_{plaque} (determined on inversion-recovery fast spin echo images) remained high (~2) until 48 hours after injection of CB2-R targeted micelles, whereas NER_{plaque} decreased after 36 hours in the control group. The inter-scan variability and relation between NER_{plaque} and gadolinium (assessed with Inductively Coupled Plasma- Mass Spectrometry) were compared between inversion-recovery fast spin echo and fast spin echo. Inter-scan variability was higher for inversion-recovery fast spin echo than for fast spin echo. Although gadolinium and NER_{plaque} correlated well for both techniques, the NER of plaque was higher for inversion-recovery fast spin echo than for fast spin echo.

Conclusions

In mice injected with CB2-R targeted micelles, NER_{plaque} can be best evaluated at 36-48 hours post-injection. Because NER_{plaque} was higher for inversion-recovery fast spin echo than for fast spin echo, but with high inter-scan variability, repeated inversion-recovery fast spin echo imaging and averaging of the obtained NER_{plaque} values is recommended

INTRODUCTION

Noninvasive imaging of atherosclerotic disease could facilitate serial studies to investigate the important issue of plaque stabilization and destabilization. There is an urgent need for surrogate measures of progression of the disease and new biomarkers are needed that can be applied to test drug efficacy with the objective to stabilize the atherosclerotic process. Magnetic Resonance Imaging (MRI) has important advantages in this perspective: it provides the possibility of contrast-enhanced molecular or cellular imaging combined with anatomic detail and it does not involve ionizing radiation.

Atherosclerotic plaques have been visualized using various carrier platforms of gadolinium (Gd) aimed at different molecular targets.[1-15] Pharmacokinetics of these carriers and the resultant concentration gradient between blood and plaque will determine the wash-in and washout kinetics and the time of maximum contrast enhancement of the plaque.[16] Clearance of untargeted agents from tissues, e.g. vulnerable plaques, is likely to be faster when compared to specifically targeted agents. Contrast-enhanced MRI of mouse atherosclerotic plaque is performed typically at baseline and at discrete time-points with large intervals, like 24, 48 and 72 hours after injection of micelles.[1, 5, 6, 9, 17] These time points are likely based on practical considerations related with the timing of the MRI procedure. However, it is largely unknown when enhancement ratios after injection of untargeted and targeted agents exactly diverge.[9, 17]

In addition, molecular MR imaging of atherosclerotic plaques is often performed with single measurements and limited time frames. The knowledge on reproducibility of single measurements using targeted contrast is limited. Localization of contrast enhancement may suffer from inter-scan variability (ISV) when contrast-enhanced MRI is executed. Another complicating factor is that even with an in-plane spatial resolution of 100 μm^2 it is not straightforward to differentiate between contrast uptake by peri-aortic lymph nodes and aortic wall in mice (unpublished data).

The peripheral cannabinoid receptor (CB2-R) has been reported to be expressed in advanced human and murine atherosclerotic plaque.[18] CB2-R has an important immuno-modulatory function in atherosclerosis which is mediated by endogenous cannabinoids.[19] Activation of CB2-R by a synthetic agonist led to a decrease of the amount of atherosclerosis.[18] We have reported on the efficacy of T1 contrast generation of CB2-R targeted micelles, containing this synthetic lipophilic CB2-R agonist, after binding to the CB2 receptor in an *in vitro* cell system.[20] *In vitro* dose dependence of binding of CB2-R targeted micelles has been shown and successful *in vivo* experiments have also been performed in an atherosclerotic mouse model, demonstrating *in vivo* enhancement of plaque corresponding with CB2-R targeted micelles co-localizing with macrophages (Figures 1 and 2, online Supplement).

Additionally, in general, non-prepared T1-weighted sequences are used for visualization of the plaque with T1 contrast agents. However, theoretically, one would expect that inversion recovery (IR) prepared sequences are capable to generate larger T1 contrast than traditionally used non-prepared T1 weighted sequences.[21]

In this study, we aim to optimize MRI procedures for detection of atherosclerotic plaque enhancement in mice. CB2-R targeting Gd containing micelles or control Gd containing micelles are injected intravenously in $ApoE^{-/-}/eNOS^{-/-}$ mice. These mice are known to develop atherosclerotic plaque in the abdominal aorta.[22] MRI data of murine atherosclerotic aorta are collected using an inversion recovery sequence every 15 minutes from pre- up to 48 hours after injection. We explore the post-injection time window, in which MR contrast of plaque caused by atherosclerosis targeting micelles exceeds MR contrast of plaque caused by control micelles. In a subset of animals both IR-Fast Spin Echo (IR-FSE)

and FSE (modified from Briley-Saebo et al.[17]) are applied every 15 minutes and Gd-content will be measured *ex vivo* with Inductively Coupled Plasma-Mass Spectrometry (ICP-MS). We will evaluate the relation between increase of plaque signal intensity and Gd-content, for IR-FSE and FSE. Furthermore, we will examine the ISV for these scanning procedures.

MATERIALS & METHODS

Materials

Di-stearoyl-polyethylene glycol-phosphatidylethanolamine (DSPE) with a polyethylene glycol (PEG) residue of 2000 Da (DSPE-PEG2000), Lissamine-rhodamine-di-oleoyl-phosphatidylethanolamine (Liss-rhod-PE) were purchased from Avanti Polar Lipids (Alabaster, AL, USA). Gd-DTPA-bisstearylamide was purchased from Gateway chemical Technology Inc (St Louis, USA). A synthetic very potent selective agonist of the peripheral cannabinoid-2 receptor (CB2-R), 4-(4-(1,1-Dimethylheptyl)-2,6-dimethoxyphenyl)-6,6-dimethyl-bicyclo(3.1.1)hept-2-ene-2-methanol)) (HU-308) was purchased from Alexis Biochemicals (San Diego, USA). NaCl, Na_2HPO_4 and NaH_2PO_4 were purchased from Merck (Darmstadt, Germany). Phosphate buffered saline (PBS, containing 8.2 g/L NaCl and 3 g/L Na_2HPO_4 and 0.33 g/L NaH_2PO_4 (pH 7.4)) was prepared. Magnevist (Gd-DTPA) (dimegluminegadopentetaat 469.01 mg/ml) was purchased from Schering Nederland B.V. (Weesp, Netherlands).

Preparation of micelles

CB2-R targeted and non-conjugated micelles

A mixture of the appropriate amounts of lipids (DSPE-PEG2000 (35M%), Gd-DTPA-bisstearylamide (50M%), Liss-rhod-PE (5M%) and HU-308 (10M%)), dissolved in chloroform, was dried by rotary evaporation at 55˚C. The lipid film was subsequently hydrated in 1 ml PBS, yielding a total lipid concentration of 10 mM, and Gd-DTPA-bisstearylamide concentration of 5 mM. HU-308 has a lipophilic chain of 7 carbon atoms which has avidity for the micelle core, whereas the more hydrophilic methoxyphenyl and methanol groups will be located in the micelle corona (non-covalent bonds). The more hydrophilic groups of HU-308 harbor the binding region for the CB2-R, however data published so far do not allow a detailed structure-activity relationship.[23] A scheme of the structure of the micelles is provided in figure 1. Control micelles were made similarly (DSPE-PEG2000 (45 M%)/Gd-DTPA-bisstearylamide (50 M%)/Liss-rhod-PE (5M%)). Both, CB2-R targeted and control micelles had a size of ~19.0 nm (unpublished data).

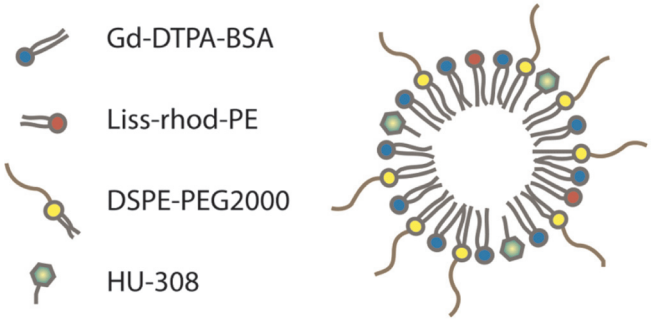

Figure 1 | *Scheme of the structure of the CB2-R targeted micelle. Control micelles have a similar structure but lack HU-308.*

Animal protocol and study setup

Experimental protocols were reviewed and approved by the Institutional Animal Care and Use Committee at Utrecht University Medical Center (Utrecht, the Netherlands) and were carried out in accordance with the standards established by the Dutch Animal Welfare Acts.

All knockout mice were backcrossed for 10 generations to the C57BL/6J genetic background. ApoE$^{-/-}$- and eNOS$^{-/-}$ mice (Jackson Laboratories, Bar Harbor, Me) were crossed to generate double heterozygous mice. These mice were then crossed and the offspring was genotyped for eNOS and for ApoE by polymerase chain reaction. Male ApoE$^{-/-}$/eNOS$^{-/-}$ animals (aged 9-12 months) were used for experiments. They were fed for 4 weeks a high-fat high-cholesterol diet containing 2.5% cholesterol (Arie Blok, Woerden, Netherlands).

Group 1 (4 teams of ~2 mice: n=9); targeted micelles

The mouse was positioned in a cradle and vital functions (heart rate and breathing frequency) were continuously recorded. Pre-injection MRI of the aorta of team members was followed by injection of 200 µl (~67 µmol/kg) CB2-R targeted micelles via the tail vein in the mouse which was measured last. MRI measurements were continued in this animal from t=8 minutes up to 24 hours, unless vital functions significantly deteriorated after which the experiment ended. One hour after injection of this animal, its team member in which pre-injection MRI had been performed, had been injected. Post-injection MRI measurements were executed from the time-point at the end of the MRI experiment in the team member till 48 hours post-injection. Finally, each of 4 teams covered an episode of 48 hours. For a scheme of study setup, see figure 2. One of the 4 teams was completed with a third mouse to cover the episode of 48 hours.

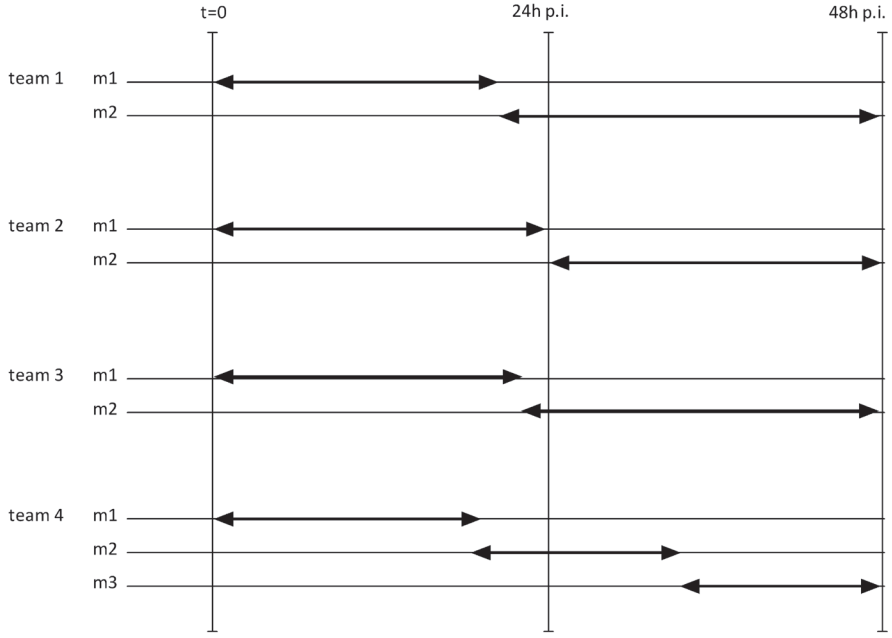

Figure 2 | *Scheme of study setup for group 1 or 2:*
One group contains three teams of two mice (m1 and m2) and one team of three mice, which cover four episodes of 48 hours per group. Horizontal arrows indicate start, duration and end of pre-and post-injection MRI measurements. At t=0 micelles are injected.

Group 2 (4 teams of ~2 mice: n=9); control micelles
Group 2 was treated similar to group 1, but instead of CB2-R targeted micelles control micelles were injected. Also in this group, one team was completed with a third mouse to cover the episode of 48 hours.

Group 3 (n=3); Gd-DTPA
Group 3 was treated similar to groups 1 and 2, except that 60 µl Magnevist (Gd-DTPA, 4.69 mg/ml ~ 5.0 mM) were injected and the follow-up MRI duration was up to 6 hours. This group served as a control group for the control micelles. So, the effect of the carrier, the micelle, on plaque uptake and residence time could be evaluated.

MRI protocol

Animal preparation and anesthesia
Mice were imaged in a vertical 9.4T, 89mm bore size magnet equipped with 1500 mT/m gradients and connected to an Avance 400 MR system (Bruker BioSpin, Germany) using a quadrature-driven birdcage coil with an inner diameter of 3 cm. Monitoring of and triggering on respiratory and cardiac motions were performed with a respiratory pad connected to a trigger unit (Rapid Biomedical, Rimpar, Germany). Induction and maintenance of anesthesia was provided with isoflurane by inhalation. Animals were suffering only minimally from these experiments because they were not allowed to recover after induction of anesthesia. An intravenous catheter was inserted into the tail vein. A small Eppendorf centrifuge tube filled with Magnevist (Gd-DTPA 5.0 mM) as an external reference was positioned left-sided to the mouse in the cradle (at the level of the right renal artery).

Scout images
Fast Spin Echo (FSE) technique was used for axial scout images. Subsequently, coronal and saggital scout images of the suprarenal abdominal aorta were acquired. Twenty contiguous axial slices, perpendicular to coronal and saggital scout images, were planned from 4 mm below the right renal artery branch up to 5 mm above this branch.

Optimization of trigger delay
Signal acquisition was planned at the moment of maximal flow through the abdominal aorta. Because cardiac action was sensed by a respiratory pad instead of by ECG, trigger delay (TD) had to be adjusted for each individual mouse. Hereto, axial T1 weighted FSE (cardiac and respiratory gated) at a level 1 mm above the right renal artery was repeated with varying trigger delays. Images were checked for laminar flow artifacts (bright vessel rims as a result of slow flow) and the diameter of the aortic lumen. TD corresponding with the image, which lacked flow artifacts and had the largest aortic diameter was chosen (optimized TD) for other scans as described below (see: “IR-FSE and FSE pre-injection images”).

Reference images for recognition of anatomic landmarks: small vessels, lymph nodes, plaque
Anatomic T2 weighted FSE axial reference images from 4 mm below the right renal artery branch up to 5 mm above were acquired. Diffusion weighted imaging sequence was used with diffusion gradient (b=400 s/mm^2) and with the same acquisition modules but zero diffusion (b=0 s/mm^2). These images were used for discrimination of peri-aortic lymph nodes (having low diffusion) usually found at 5 levels

around the right renal artery branch (-1 up to +3 mm). A time-of-flight (gradient echo (GE)) technique was used for acquisition of non-triggered bright-blood images.

IR-FSE and FSE pre-injection images

For mice in which only IR-FSE was applied (group 1: n=4; group 2: n=6; group 3: n=3), this sequence was applied 5 times in order to define the standard deviation (SD) of the pre-injection signal intensity of plaque. For mice in which both IR-FSE and FSE were used (group 1: n=5; group 2: n=3), both sequences were applied 5 times in an interleaved fashion. For IR-FSE the acquisition scheme was started at a trigger with an inversion pulse followed by the inversion time, which is much longer than 1 cardiac cycle. The chosen TD for IR-FSE was chosen in a way, that the equation (inversion time + TD)/(cardiac cycle duration) = integer + optimized TD was satisfied.

Contrast injection and post-injection IR-FSE and FSE

The cradle was removed from the magnet, contrast agent was injected via the intravenous catheter and the animal was repositioned in the magnet (or recovered from anesthesia). Scout scans were repeated to register a shift of the position of the aorta. An axial slice package (20 slices) was oriented parallel to the transverse scout images of the aorta. T1 weighted scans were acquired every 15 minutes (interleaved IR-FSE and FSE or only IR-FSE). Duration of post-injection follow-up MRI has been mentioned before. The delay from injection of the contrast agent up to the start of post-injection MRI was 8-10 minutes.

MRI parameters

Anatomic T2 weighted FSE reference images

2D SE, TR/TE=3500/28.9 ms, rare factor=8, sinc3 pulse 450 µs, excitation/refocusing flip angle=90˚/180˚, Spectral width=75757 Hz, Field of view (FOV)=30x30 mm^2, matrix=400x400 resulting in pixel dimension=75x75 μm^2, 20 consecutive axial slices, thickness=0.5 mm, chemical shift selective fat suppression, Number of Averages (NA)=15, zero fill acceleration factor 1.34, total acquisition time 32m22s.

Diffusion weighted images

2D SE, TR/TE=2000/13.2 ms, hermite pulse 1.0 ms, excitation/refocusing flip angle=90˚/180˚, b value (longitudinal/z-axis) 0 or 400 s/mm^2, diffusion gradient duration 1.40 ms, separation 5.0 ms, Spectral width=50000 Hz, FOV=30x30 mm^2, matrix=256x256 resulting in a pixel dimension=117x117 μm^2, 1 axial slice, thickness=0.5 mm (at five levels around the right renal artery: -1 up to +3 mm), chemical shift selective fat suppression, NA=1, zero fill acceleration factor 1.9, total acquisition time 4m20s. Lymph nodes were discerned by calculation of the apparent diffusion coefficient: ADC=ln(S1-S2)/ΔB. S1 and S2 are the mean signal intensities on the image with b=0 and the image with b=400 s/mm^2, respectively, while $\Delta b = 400\text{-}0=400$ s/mm^2. If ADC was less than 1.8, the structure was identified as a lymph node.

Bright-blood images (TOF)

2D GE, TR/TE=150/1.75 ms, gauss pulse 500 µs, flip angle=90˚, Spectral width=166667 Hz, FOV=30x30 mm^2, Matrix =256x256 resulting in a pixel dimension=117x117 μm^2, 20 consecutive axial slices, thickness=0.5 mm, NA=5, zero fill acceleration factor 1.34, total acquisition time 2m24s.

IR-FSE images

2D IR-FSE, TR/TE=4000/15.14 ms, inversion time=1150 ms, rare factor=10, excitation/refocusing pulse gauss 1 ms, flip angle=90˚/180˚, Spectral width=75757 Hz, FOV=30x30 mm^2, matrix=200x200 resulting in a pixel dimension=150x150 μm^2, 20 consecutive axial slices, thickness=0.5 mm, chemical shift selective fat suppression, 2 inflow saturation slices (1 cranial (saturation of arterial inflow) and 1 caudal (saturation of venous inflow)), thickness 10 mm, NA=10, zero fill acceleration factor 1.7, total acquisition time 7m20s.

FSE images:

2D FSE, TR/TE=1200/8.0 ms, rare factor=4, excitation/refocusing pulse hermite 1.2 ms, flip angle=90˚/180˚, Spectral width=200000 Hz, FOV=30x30 mm^2, matrix=256x256 resulting in a pixel dimension=117x117 μm^2, 20 consecutive axial slices, thickness=0.5 mm, chemical shift selective fat suppression, 2 inflow saturation slices (1 cranial (saturation of arterial inflow) and 1 caudal (saturation of venous inflow)), thickness 10 mm, NA=11, zero fill acceleration factor 1.92, total acquisition time 7m15s.

Harvesting and preparation of aortas

After 24 hours follow-up MRI or when vital functions deteriorated the animal was taken out of the magnet. Anesthesia was continued with a mixture of medetomidine (6%)/ketamine (5%) (0.1 mL per 10 gram). The imaged part of the aorta was harvested after perfusion with PBS/formaldehyde 4% (9:1) within 15 minutes after the MRI experiment ended. The samples were stored in aluminium vials at -20 ºC until the ICP-MS procedure (2-3 weeks after harvesting).

Quantification of Gd: ICP-MS

Gd-content was assessed in aortic samples (group1, n=8; group 2, n=8; group3, n=2). For technical reasons 3 aortic samples could not be analyzed. The samples were transferred to clean glass tubes. Tissue was digested in nitric acid. The amount of Gd was determined using ICP-MS (Philips Research, MiPlaza, Eindhoven, Netherlands). The amount of Gd present was determined by comparison with the intensities produced by standard solutions. The maximum inaccuracy in the amount of Gd is expected to be between 3-5%.

MRI data analysis

Aortic wall contours were manually traced on pre-injection T2 weighted images using software for data acquisition and processing (Paravision 4.0, Bruker-Biospin, Germany) (see figure 2 for example). Also circular regions of interest in representative areas of kidney, spleen, liver, lymph node and pre-vertebral skeletal muscle were drawn. These regions were copied to the five pre-injection and post-injection images and, when needed, slightly rotated and translated to fit relative distances to anatomic landmarks like right renal artery branch, vertebral spine, pre-vertebral muscle and peri-aortic lymph nodes.

Relative signal intensities of plaque on pre- and post-injection images were defined as the signal intensity of plaque divided by the external reference. The values for the 5 baseline images were averaged. Normalized Enhancement Ratio (NER) was calculated as relative signal intensity at a certain time point post-injection divided by averaged relative signal intensity pre-injection.

The plaques with highest NER were selected for further calculations. The NER after injection was averaged from 0 till 60 minutes, 60 till 120 minutes, and so on to obtain NER_{30min}, NER_{90min}, and so on

for the whole covered time span. Graphs with NER (and standard deviation of measurements covering 1 hour) as a function of time were made in Excel Microsoft 2002. Visual inspection of these graphs revealed the plaque with highest NER per mouse. Plaques with highest NER were selected for further calculations as described in the next section.

Statistical Analysis

CB2-R targeted versus control micelles

For each team in group 1 and 2, NER_{plaque} determined from IR FSE images from 3 hour periods 4-6, 10-12, 16-18, 22-24, 28-30, 34-36, 40-42 and 46-48 hours post-injection were averaged. Team values were averaged per time-point and differences of averaged NER_{plaque} between group 1 and 2 for each of these time points were tested with an independent samples t-test. Also differences between NER of organs (kidney, spleen, liver, lymph node and skeletal muscle) were likewise tested at time points 4-6, 10-12, 22-24, 34-36 and 46-48 hours. Moreover differences between NER of organs and plaque at mentioned time points and pre-injection value (NER=1) were tested. For FSE images statistical tests for differences between groups were not executed, because less than 4 measurements were available per time point.

Relation between NER_{plaque} and Gd in aortic plaque

NER_{plaque} was assessed at all 20 MRI levels. Correlation between highest NER_{plaque} (averaged in 1 hour), immediately before sacrificing the mouse, and corresponding Gd-content, assessed by ICP-MS, was measured for IR-FSE and FSE. Pearson correlation coefficients were tested one-tailed. The higher the slope, the more sensitive the technique is to an increase in Gd-content.

Secondly, for each mouse for which both IR-FSE and FSE were performed, the plaque with highest NER with IR-FSE and FSE was chosen and only the time point of 24 hours post-injection was analyzed. The pre-injection standard deviation (SD_0) was calculated as the standard deviation of the value for NER_{plaque} of the 5 pre-injection images. When we assume a standard normal distribution of these values, the 95% confidence interval of the pre-injection value for NER_{plaque} is characterized by the mean value (=1 by definition) ± 2xSD0 of a set of measurements of this value for NER_{plaque}. Before concluding that the post-injection value for NER_{plaque} is higher than the pre-injection value (at p=0.05, type I error (false positive increase)= 5%), the post-injection value should be higher than $1+2xSD_0$. $NER_{24h}/(2xSD_0+1)$ was calculated for both imaging techniques. A value for the latter ratio of more than 1 indicated that the NER at 24 hours was outside the 95% confidence interval of pre-injection NER. A higher averaged value for $NER_{24h}/(2xSD_0+1)$ for one of both techniques suggested a higher sensitivity of this technique to a particular amount of Gd in that plaque. However, there was no external *ex vivo* validation. The number of plaques with $NER_{24h}/(2xSD_0+1)>1$ according to IR-FSE and FSE was assessed. A difference in this number suggested also a difference between the *in vivo* detection limits of Gd for these techniques.

Inter-Scan Variability (ISV)

Standard deviation of 4 consecutive measurements at 24 hours post-injection (SD_{24h}) was calculated. SD_{24h}/NER_{24h} is a measure of inter-scan variability (ISV) of NER_{plaque} scaled to the size of NER_{plaque}. A higher ratio indicated higher ISV. Differences in $NER_{24h}/(2xSD_0+1)$, SD_{24h}/NER_{24h}, SD_0 and SD_{24h} were tested with a paired samples t-test. Significance was tested two-tailed. Moreover for each technique the number of mice with $NER_{24h}/(2xSD_0+1)>1$ was assessed.

RESULTS

Both CB2-R targeted and control micelles accumulated in plaque within 15 minutes after injection as observed by MRI. After a few hours also lymph node and liver enhancement were observed, whereas kidney, spleen and pre-vertebral muscle did not show enhancement. Comparison of IR-FSE and FSE images with differences in NER, as a result of the difference in T1 contrast generating effect between the two techniques, is shown in Figure 3. Clearly seen is the lower overall plaque enhancement with the FSE technique when compared with the IR-FSE technique. Importantly, the FSE pre-injection images show higher signal than the IR-FSE pre-injection images (Figure 3, upper and third row).

Careful inspection of anatomic T2 weighted reference images suggested presence of peri-aortic lymph nodes at levels -1 up to +3 mm with respect to the right renal artery branch. Regions of interest drawn on this image were copied to the diffusion weighted image. For healthy lymph nodes an ADC of $1.15x10^{-3}$ mm^2/s has been reported.[24] In this study, we found ADC values of obvious mouse lymph nodes between $0.70x10^{-3}$ mm^2/s and $1.50x10^{-3}$ mm^2/s, whereas plaque regions had ADC higher than 2.5x10-3 mm2/s. We think diffusion weighted imaging is a good technique for discrimination between aortic wall and peri-aortic lymph nodes.

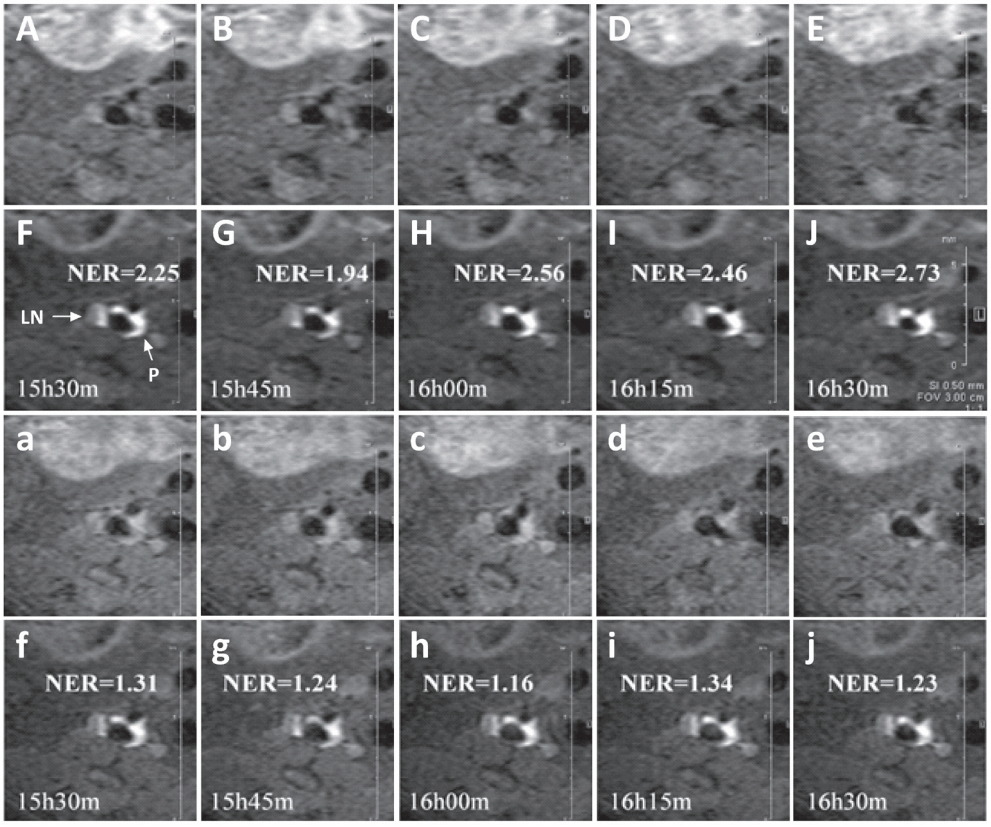

Figure 3 | *Variation in NERplaque around 16 hours after injection of CB2-R targeted micelles. Five IR-FSE images pre-contrast (A-E) as well as post contrast (F-J) and five FSE images pre-contrast (a-e) and post contrast (f-j) were acquired in an inter-leaved fashion. LN: lymph node; P: plaque; NER: normalized enhancement ratio (1 is baseline).*

CB2-R targeted versus control micelles

For IR-FSE images, differences of NER_{plaque} and NER_{organ} between targeted micelles and control micelles were tested. Figure 4 shows IR-FSE images of the aortic plaque pre-injection and at different time-points post-injection of CB2-R targeted micelles in two mice of the same team. The NER^{plaque} remained stable around 1.9 after injection of targeted micelles, whereas NER_{plaque} decreased around 36 hours after injection of control micelles to achieve pre-injection values at t= 42 hours post-injection (42 hours: 1.95±0.29 versus 1.13±0.18 ($p<0.05$); 48 hours: 1.90±0.33 versus 1.22±0.15 ($p<0.01$), respectively) (Figure 5). NER_{plaque} was higher than pre-injection values for all time points after injection of targeted micelles. NER_{plaque} seemed to be higher than pre-injection values up to 36 hours after injection of control micelles, however with a large standard deviation. NER_{plaque} increased to a peak level of 1.57±0.12 at 1.5 hours after injection of Gd-DTPA, returning to baseline level at 2.5 hours. $NER_{lymph\ node}$ increased after injection of CB2-R targeted micelles to ~1.3 at 12 hours post-injection and decreased to pre-injection

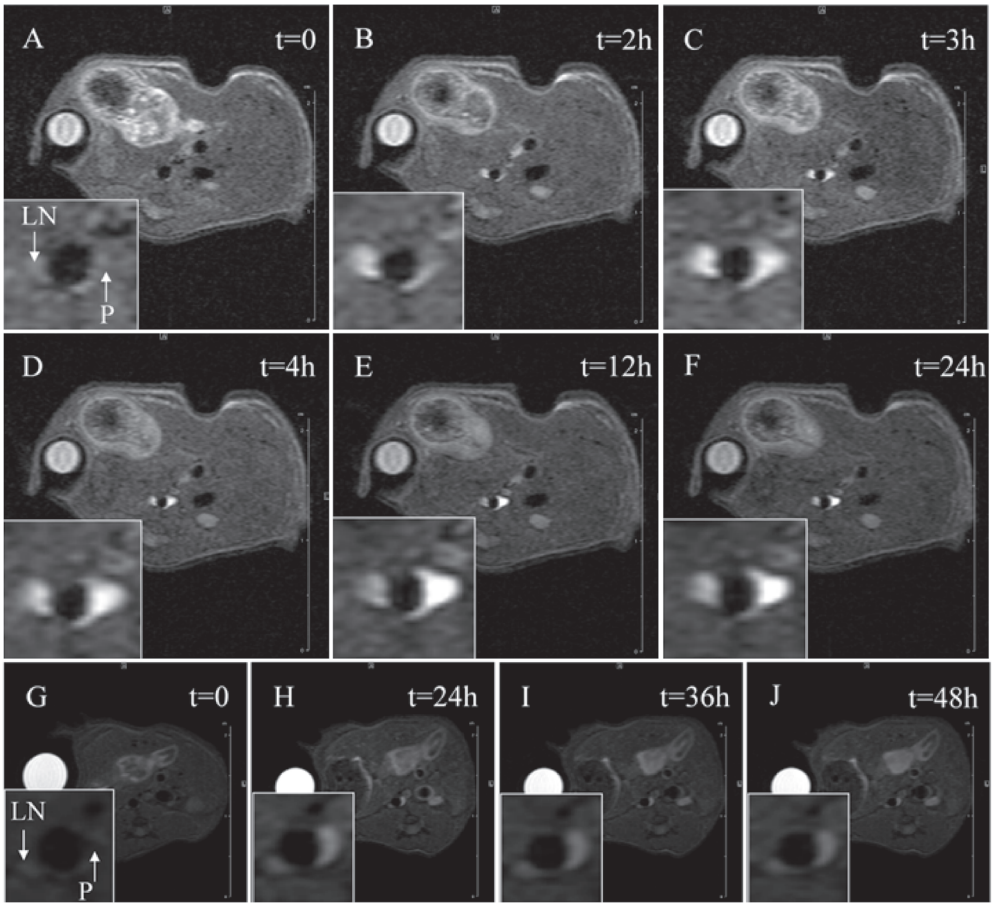

Figure 4 | *IR-FSE images of murine abdominal aortic plaque.*
Pre- and post-injection of CB2-R targeted micelles at various time-points until 24 hours in one mouse (A-F) and in another mouse of the same team pre- and post-injection from 24 hours until 48 hours (G-J). The inserts show zoomed peri-aortic regions.

values afterwards (Figure 6). $NER_{lymph\ node}$ did not increase after injection of control micelles. NER_{liver} increased to ~1.5 at 24 hours after injection of CB2-R targeted micelles and decreased to pre-injection values later. Also after injection of control micelles NER_{liver} seemed to increase a little bit with a peak level at 24 hours (~1.25). However, only at 12 and 24 hours after injection of CB2-R targeted micelles, NER_{liver} was significantly higher than pre-injection. NER of kidney, spleen and pre-vertebral muscle did not show a change after injection of CB2-R targeted or control micelles (Figure 6).

Relation between NER_{plaque} and Gd in aortic plaque

Aortic Gd content of mice, at 24 hours after injection of targeted and control micelles, was 4.38 ± 8.34 and 3.63 ± 2.50 µg/g respectively. Aortic Gd content of mice, at 48 hours after injection of targeted and control micelles, was 3.31 ± 1.57 and 1.61 ± 0.45 µg/g, respectively ($p<0.05$). Correlation between Gd content and final highest NER_{plaque} (averaged from 4 measurements) was highly significant for both IR-FSE images (Pearson correlation coefficient=0.837; $p<0.001$) and FSE images (Pearson correlation coefficient=0.663; $p<0.05$). The slope of the regression line was approximately 10 times higher for the

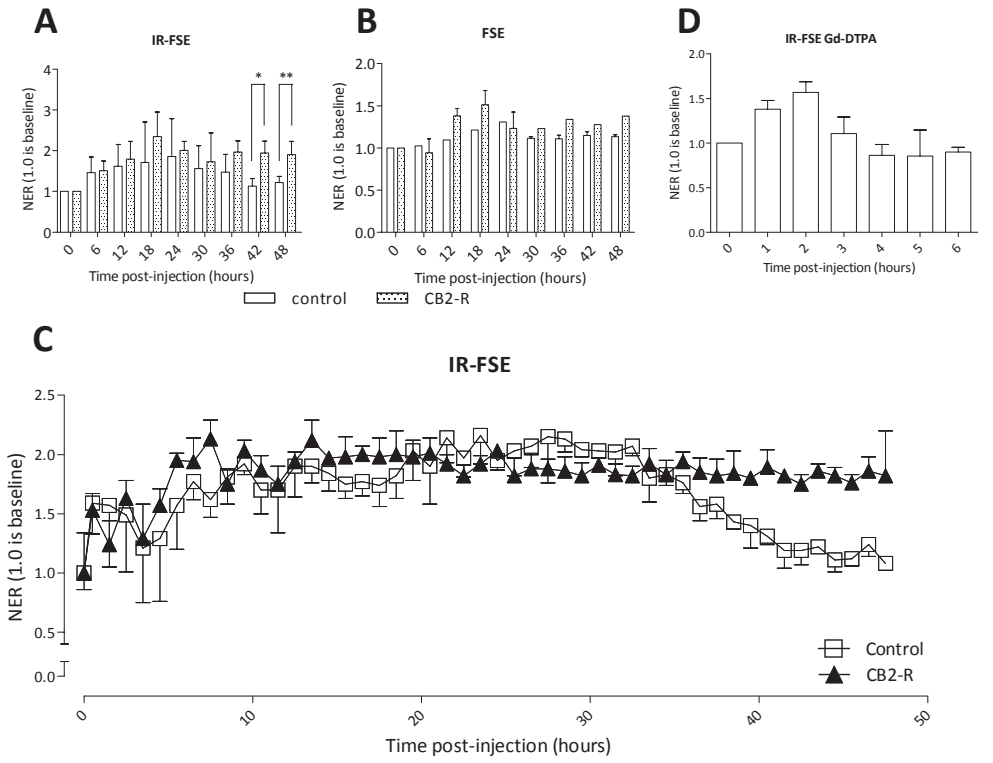

Figure 5 | *NER of murine abdominal aortic plaque.*
*NER determined after injection of CB2-R targeted and control micelles on IR-FSE images (A), and determined on FSE images (n=1 or n=2) (B). Additionally, typical examples of the course of NER are shown, determined on IR-FSE images in a team, between 0 and 48 hours after injection of CB2-R targeted or control micelles (C). NER of murine abdominal aortic plaques during the first hour after injection of Gd-DTPA (Magnevist) is also shown (n=3) (D). Whiskers show SD. *p<0.05; **p<0.01. NER: normalized enhancement ratio.*

IR-FSE technique when compared to the FSE technique (0.20 versus 0.022, with estimated standard errors of 0.03 and 0.015 respectively), indicating that the IR-FSE technique is more sensitive to an increased amount of Gd (Figure 7).

This was supported by calculations of $NER_{24h}/(2xSD_0+1)$, which is only a surrogate measure of the sensitivity of the technique. IR-FSE showed higher ratios when compared to FSE, however differences were not significant (IR-FSE: 1.30±0.36; FSE: 1.07±0.25) (p=0.146) (Table 1). At 24 hours highest NER_{plaque} represented a significant increase of plaque signal intensity ($NER_{24h}/(2xSD_0+1)>1$) in 6 of 8 mice with IR-FSE, while only in 4 of 8 mice highest NER_{plaque} with FSE represented a significant increase of plaque signal intensity. This observation supports the findings with *ex vivo* Gd measurements and point to a lower *in vivo* detection limit of gadolinium for IR-FSE when compared to FSE.

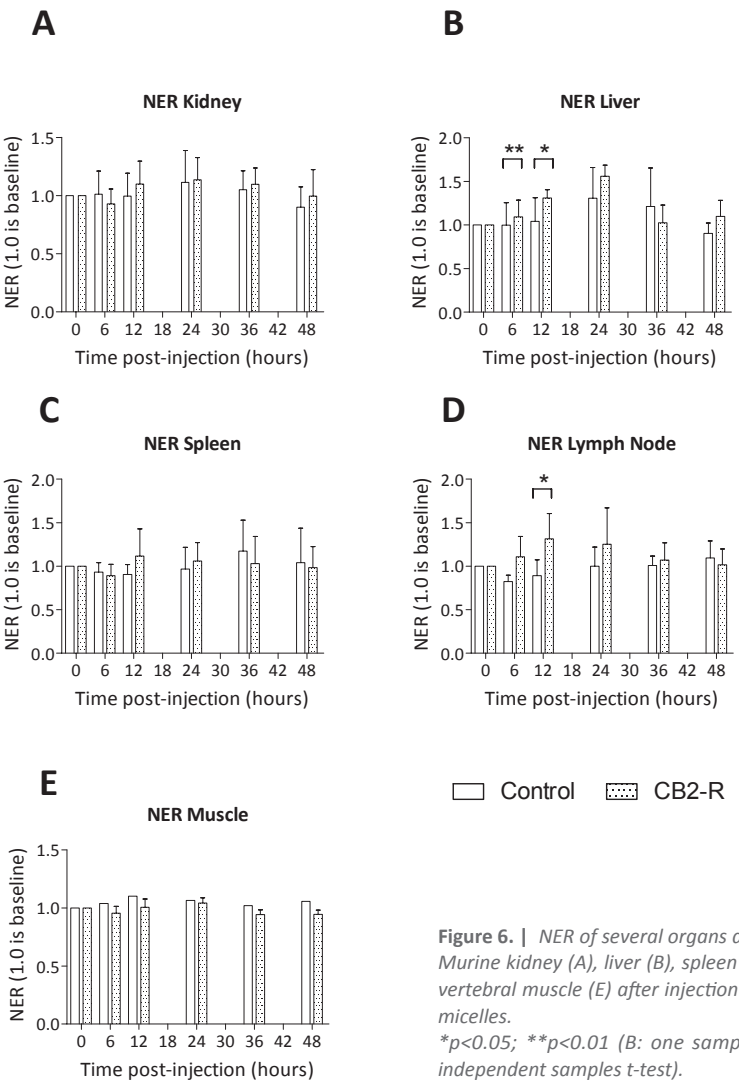

Figure 6. | *NER of several organs determined on IR-FSE images. Murine kidney (A), liver (B), spleen (C), lymph node (D) and pre-vertebral muscle (E) after injection of CB2-R targeted or control micelles.*
**p<0.05; **p<0.01 (B: one samples t-test (test value=1); D: independent samples t-test).*

Inter-Scan Variability (ISV)

The ISV may be best examined by calculation of SD24h/NER_{24h}. SD_0 and SD_{24h} were significantly lower with FSE technique than with IR-FSE (SD_0: 0.08±0.04 versus 0.17±0.08, respectively; SD_{24h}: 0.08±0.05 versus 0.15±0.10, respectively ($p<0.05$)). There was a tendency to a lower SD_{24h}/NER_{24h} measured with FSE when compared to IR-FSE (9±7 % versus 6±4%) (p=0.169). An example of the large ISV of plaque enhancement with IR-FSE is shown in Figure 8. In this case the ISV of the FSE technique is lower, but NER_{plaque} is hardly increased when compared to the pre-injection value (Figure 8B). The large ISV, when IR-FSE is applied, is not observed in larger organs like liver, muscle and kidney (Figure 8D-E). On the other hand, peri-aortic lymph nodes also revealed large ISV (Figure 8C).

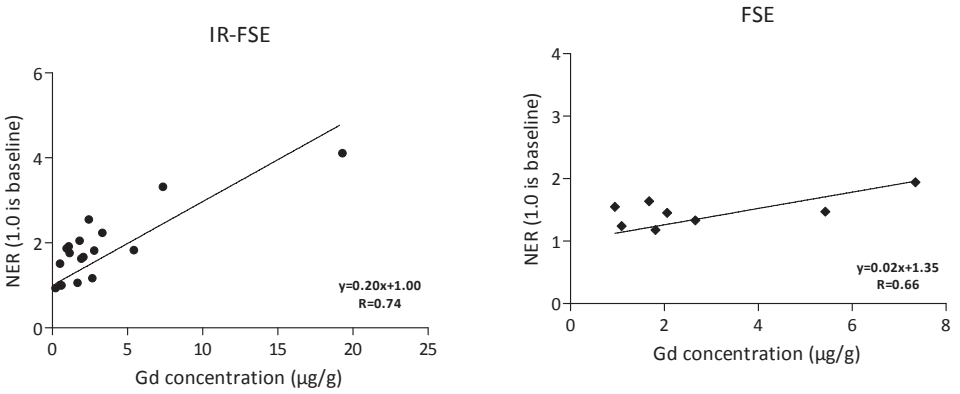

Figure 7 | *Correlation plot of Gd content.*
Murine aortas (group 1, n=7; group 2, n=9; group 3, n=2) assessed with ICP-MS and corresponding highest NERplaque on IR-FSE images (averaged from last hour alive). The correlation was also executed on highest NERplaque on FSE images when available (n=8). ICP-MS: Inductively coupled plasma mass spectroscopy.

Table 1 | NER_{plaque} and ISV at 24 hours post-injection and a surrogate measure of the sensitivity of IR-FSE and FSE for detection of enhancement of plaque in 8 individual mice.

	IR FSE					SE				
Micelle type	**NER_{24h}**	**SD_0**	**SD_{24h}**	**Sens**	**ISV**	**NER_{24h}**	**SD_0**	**SD_{24h}**	**Sens**	**ISV**
targeted		ISV	0.26	1.13	0.15	1.03	0.11	0.06	0.85	0.06
targeted	1.29	0.33	0.33	0.78	0.25	1.31	0.05	0.20	1.18	0.15
targeted	1.63	0.15	0.11	1.25	0.07	1.18	0.14	0.02	0.92	0.02
targeted	1.63	0.14	0.05	1.28	0.03	0.96	0.08	0.08	0.83	0.08
targeted	2.11	0.15	0.12	1.63	0.05	1.36	0.02	0.08	1.31	0.06
control	1.07	0.09	0.11	0.90	0.11	1.32	0.08	0.05	1.13	0.04
control	1.93	0.08	0.13	1.65	0.07	1.61	0.04	0.05	1.50	0.03
control	2.28	0.14	0.07	1.78	0.03	0.99	0.08	0.08	0.85	0.08
Avg± SD	1.71± 0.39	0.17± 0.08*	0.15± 0.10*	1.30± 0.36	0.09± 0.07	1.22± 0.22	0.08± 0.04*	0.08± 0.05*	1.07± 0.25	0.06± 0.04

*Avg: average; Sens: surrogate measure of the sensitivity of the technique to detect uptake of contrast agent = $NER_{24h}/(2xSD_0+1)$; ISV: Inter-Scan Variability= SD_{24h}/NER_{24h}. *Differences between groups 1 and 2: $p<0.05$.*

High ISV of NER_{plaque} is also visible on the IR-FSE images (Figure 3). A large difference between lowest NER_{plaque} and highest NER_{plaque} is observed for IR-FSE images (Figure 3, post IR-FSE row second panel and fifth panel, respectively).

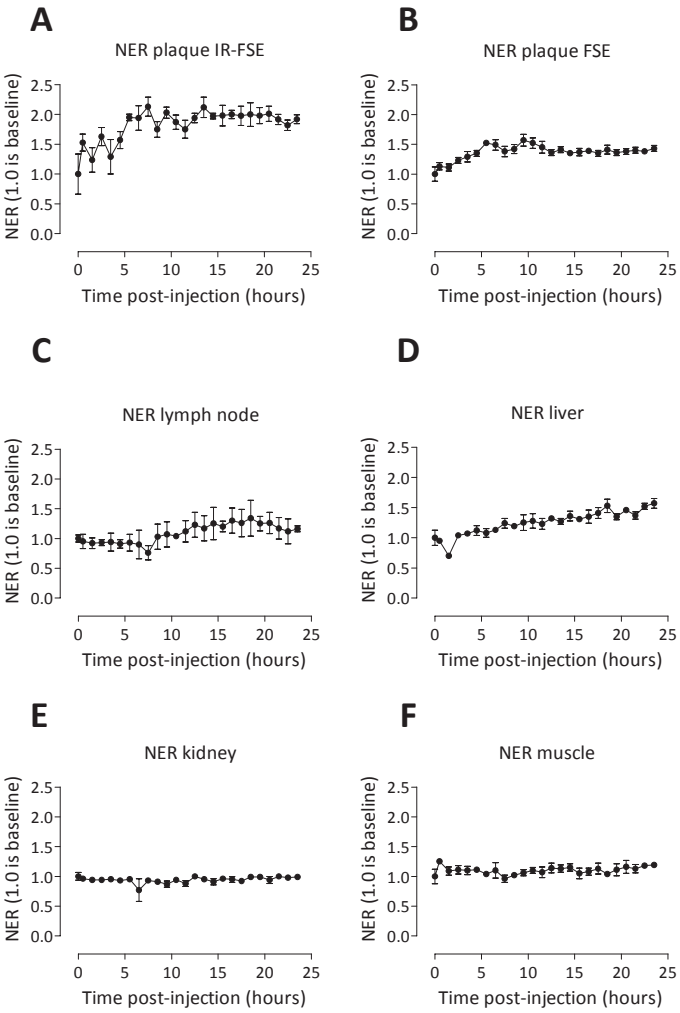

Figure 8 | *NERplaque determined by IR-FSE and FSE as a function of time. A typical example (also shown in Fig. 1C) of higher ISV of NERplaque for IR-FSE (A) than for FSE (B) is shown. For IR-FSE images also NER of some organs during time after injection of CB2-R targeted micelles is shown. Notice the higher ISV of NERlymph node (C) when compared to ISV of NERliver (D), NERkidney (E) and NERpre-vertebral muscle (F). ISV: Inter-scan variability*

DISCUSSION

The main findings of this study are: 1; CB2-R targeted micelles show enhancement for a longer period in ApoE$^{-/-}$/eNOS$^{-/-}$ mouse atherosclerotic plaque than control micelles, as shown by magnetic resonance IR-FSE imaging, 2; the increase of plaque signal intensity at similar increase of Gd content measured with IR-FSE is higher than the increase of plaque signal intensity measured with FSE, 3; the ISV was higher for IR-FSE than for FSE. The results of this study are highly relevant to the design of future studies concerning molecular MRI of atherosclerotic plaque in mice with targeted paramagnetic micelles or other targeted paramagnetic probes. Plaque enhancement did not differ between mice treated with atherosclerosis-targeted and control micelles until 36 hours post-injection. At 36 hours post-injection, plaque enhancement diverged between control and positive targeted micelles, and became more evident and consistent at 42 and 48 hours post-injection. However, at earlier time points, NER did not differ consistently between mice treated with CB2 targeted micelles and mice treated with control micelles. Another *in vivo* MRI study reported a higher NER_{plaque} at 1 hour after injection of macrophage targeting micelles when compared to control micelles.[1] Also 24 hours after injection of targeted molecular probes which recognize oxidation-specific epitopes, plaque enhancement was reported to be increased compared to non-targeted micelles.[17] We used micelles which target another epitope on plaque macrophages. We cannot exclude that temporal signal enhancement may vary among molecular targets.

In this study, the variability of NER_{plaque} between mice within groups, treated with CB2-R targeted and control micelles, was remarkably large during the first 30 hours. An explanation for this variability could be large biological differences of inflammation within the group. This may lead to varying endothelial fenestration sizes leading to faster or slower wash-in kinetics of plaque. NER_{plaque} in mice treated with control micelles apparently decreased 30 hours post-injection, accompanied by decreasing variability. The concentration of micelles in the blood decays and so does the concentration gradient of micelles between blood and plaque. Non-conjugated micelles containing the same lipid components and having a similar size as the non-conjugated micelles in this study have been found to have a plasma half-life of 22 hours.[25] Micelles to which CNA35, a collagen targeting protein, was attached, were found to have a plasma half-life of 17 hours.[25] An intermediate plasma half-life (17-22h) for micelles, in which HU-308 is incorporated, is suggested, because the CB2-R agonist is smaller and has a synthetic origin with lower expected immunogenicity. Below a critical blood concentration, no more net plaque uptake will take place, whereas the wash-out process prevails. The decrease of NER_{plaque} after 36 hours in mice injected with control micelles corresponds with the results of van Bochove et al.. In mice treated with CB2-R targeted micelles, one would expect that NER_{plaque} remains stable for a longer period when compared to mice treated with control micelles. Because highly variable wash-in kinetics does not contribute to the NER anymore, variability of NER_{plaque} decreases after the blood concentration has decreased below a critical value. Further insights in general pharmacokinetics and biodistribution of nanoparticles are found in literature.[16] The long blood circulation time of these micelles is clinically not convenient and will necessitate two separate imaging days.

In our study, peak NER_{plaque} in mice, treated with Magnevist (Gd-DTPA), was attained at 1.5 hours and returned to pre-injection values at 2.5 hours post-injection. In contrast with NER_{plaque} in mice treated with Magnevist, NER_{plaque} in mice treated with control micelles showed a prolonged stay up to 36 hours post-injection. The early drop to pre-injection value of NER_{plaque} in mice, treated with Magnevist, is in accordance with earlier reported results.[1] Measurement of Gd was used for quantification of uptake of micelles in plaque. In an earlier study in our laboratory, fluorescence microscopy of lissamine-

rhodamine has been used for localization of CB2-R targeted micelles (unpublished data). These micelles colocalized with macrophages in the plaque.

The increase of plaque signal intensity accompanied by the same increase of aortic Gd content was higher for IR-FSE when compared to FSE. Approximately only 66% of the plaques with a NER value significantly higher than the pre-injection value according to IR-FSE images, had a NER value which was higher than pre-injection according to FSE images. The slope of the regression line of the correlation plot between aortic Gd content and NER_{plaque} was approximately ten times higher for IR-FSE images than for FSE images. Though data in this study fitted best to a linear function, relation between NER_{plaque} and Gd does not need to be linear. However, a linear relation is expected to exist between inverse T1 and Gd. Effective decrease of the MR signal of non-enhanced aortic wall by choosing a suitable inversion time determines the efficiency of IR-FSE for depiction of T1 contrast between tissues. In contrast to our results, Briley-Saebo *et al*. reported nice enhancement ratios with the FSE technique, similar to the FSE technique in this study, after injection of micelles, which were similar to the micelles used in this study, however targeting oxidation-specific epitopes.[17] The difference in injection dose could explain the different observations. Briley-Saebo *et al*. injected 0.075 mmol Gd/kg whereas in this study 0.033 mmol Gd/kg was injected. The modifications of the FSE technique in this study are: TR=1200 ms and FA=90˚ instead of TR=600 ms and FA=30˚,[17] but these differences will lead to approximately comparable T1 contrast.

Another explanation could be a difference in quenching of the relaxation enhancement of contrast agent after internalization in the macrophage.[26, 27] With in vitro fluorescence microscopy we showed that CB2-R targeted micelles were internalized by CB2-R over-expressing CHO cells.[20] Other studies have shown that intracellular compartmentalization of Gd (vesicle compartments) could lead to quenching of relaxivity of the Gd containing contrast agent.[26, 27] However, the intracellular destiny of neither the CB2-R targeted nor the oxidation-specific epitope targeting micelles is known.

Also the difference in pixel dimensions between IR-FSE and FSE (150x150 μm^2 and 117x117 μm^2, respectively) could create a bias in comparison of NER. In this study IR-FSE parameters were chosen in a way that the acquisition time was similar to that of FSE.[28] Because inversion recovery is less time-efficient, this adjustment leads to reduced signal-to-noise-ratio or to reduced pixel dimensions, as was chosen in this study. When this is added to the higher ISV for IR-FSE, one could easily conclude that FSE would be the method of choice. However, IR-FSE showed a better correlation of NER with Gd content at 24 and 48 hours after injection than FSE. In addition, IR-FSE was more sensitive to an increase of Gd-content when compared to FSE. Molecular MRI is generally hampered by a low sensitivity for the presence of molecular markers.[29] Successful contrast-enhanced MRI needs µM-mM concentrations of the molecular marker of interest.[29] So, the most sensitive technique for visualization of a molecular plaque marker, often in the nM-µM range, is desirable. The better performance of IR-FSE in this study is relevant for studies focused on molecular MRI of any disease process using any type of targeted Gd containing probe.

In this study, the FSE technique tended to have lower ISV. An explanation for the tendency of a lower ISV for FSE when compared to IR-FSE could be complication of the “real trigger delay”. The use of cardiac-gated MRI for visualization of abdominal aortic wall has not been reported so far, to our knowledge. However, our data suggest that triggering on vessel motion is important for better image quality and recognition of lymph nodes. The position and dilation of the aorta and small organs embedded together with the aorta in connective tissue (like peri-aortic lymph nodes) will be influenced by pulsating flow. Therefore, in this study not only NER_{plaque} but also $NER_{lymph\ node}$ values show larger inter-scan variability.

Further, inadequacy in setting the real trigger delay for the IR-FSE technique could lead to higher ISV. The long inversion time may cause this inadequacy. For IR-FSE the inversion time was 1150ms. The next trigger

is followed by this inversion time + echo time, which is much longer than 1 cardiac cycle. The cardiac cycle duration could vary during this long inversion time, which will lead to some shift of the acquisition within the cardiac cycle. For FSE the next trigger is followed by the echo time, which is much shorter than 1 cardiac cycle. So no shift of the acquisition within the cardiac cycle will occur. Actually, during the experiments we observed minor arrhythmias that caused variation of cardiac cycle duration. The IR-FSE images suffered more from these arrhythmias than FSE images, which is in support of the mentioned explanation. From this theory we can understand also that averaging IR-FSE images before calculation of NER_{plaque} will not solve the problem of the larger ISV. However, averaging NER_{plaque} calculated on repeated scans will decrease the chance of false positive and false negative results.

Immunomicelles are made by conjugation of specific antibodies to the micellar corona (of PEG for example).[2, 30] We expect that biodistribution and pharmacokinetics of antibody-conjugated micelles highly depend on immunogenic response elucidated by the bound protein. Activation of macrophages in the reticulo-endothelial system of spleen and liver by the conjugated protein may lead to increased filtering from the blood. So, clearance of antibody-conjugated micelles from the blood is expected to be faster than for non-conjugated micelles. As a result of the prolonged circulation time, residence of non-conjugated micelles in micelle-excreting organs will be prolonged. However, the residence time of non-conjugated micelles in the plaque is expected to be lower due to lack of specific binding. We have used a small lipophilic agonist, which is non-covalently bound to the lipophilic core without modification of PEG groups forming the corona. Therefore, targeted micelles used in this study are expected to have similar immunogenicity when compared to non-conjugated micelles. We found a significant elevation of NER_{liver} at 12 and 24 hours after injection of CB2-R targeted micelles. Antibody-conjugated micelles, targeting oxidation-specific epitopes in plaque, and non-conjugated micelles were also found to be predominantly cleared by the liver, however with peak accumulation of gadolinium at 48 hours after injection.[17] In the mentioned study, however, the concentration of gadolinium in the liver was measured with ICP-MS, whereas we measured NER_{liver} changes post-injection.

Study Limitations

We were only able to find a tendency to a larger ISV in IR-FSE images when compared to FSE images. Probably a statistic significant difference was found, when more animals would be studied with both techniques. We have only measured NER until 48 hours after injection of micelles. Therefore we may have missed further contrast enhancement due to cellular processing and intracellular de-compartmentalization of the contrast agent.[26, 27, 31] Also extensive pre-clinical pharmacokinetic and safety testing will be required before clinical implementation may take place.

Conclusions

The present study shows *in vivo* aortic plaque enhancement after injection of specific plaque targeted and control Gd containing micelles in an atherosclerotic mouse model. In mice treated with CB2-R targeted micelles aortic plaque enhancement was significantly higher at 42 and 48 hours post-injection than in mice treated with control micelles. Plaque signal intensity increase accompanied by the same increase of aortic Gd content was higher for IR-FSE when compared to FSE. On the other hand, ISV tended to be higher with IR-FSE due to complication of triggered acquisition when compared to FSE. Therefore, we recommend the acquisition of repeated IR-FSE scans and averaging of NER_{plaque} for optimization of contrast enhancement of atherosclerotic plaque.

1. Amirbekian V, Lipinski MJ, Briley-Saebo KC, Amirbekian S, Aguinaldo JG, Weinreb DB, Vucic E, Frias JC, Hyafil F, Mani V, Fisher EA, Fayad ZA. Detecting and assessing macrophages in vivo to evaluate atherosclerosis noninvasively using molecular MRI. Proc Natl Acad Sci U S A 2007 January 16;104(3):961-6.

2. Lipinski MJ, Amirbekian V, Frias JC, Aguinaldo JG, Mani V, Briley-Saebo KC, Fuster V, Fallon JT, Fisher EA, Fayad ZA. MRI to detect atherosclerosis with gadolinium-containing immunomicelles targeting the macrophage scavenger receptor. Magn Reson Med 2006 September;56(3):601-10.

3. Lancelot E, Amirbekian V, Brigger I, Raynaud JS, Ballet S, David C, Rousseaux O, Le GS, Port M, Lijnen HR, Bruneval P, Michel JB, Ouimet T, Roques B, Amirbekian S, Hyafil F, Vucic E, Aguinaldo JG, Corot C, Fayad ZA. Evaluation of matrix metalloproteinases in atherosclerosis using a novel noninvasive imaging approach. Arterioscler Thromb Vasc Biol 2008 March;28(3):425-32.

4. Cormode DP, Briley-Saebo KC, Mulder WJ, Aguinaldo JG, Barazza A, Ma Y, Fisher EA, Fayad ZA. An ApoA-I mimetic peptide high-density-lipoprotein-based MRI contrast agent for atherosclerotic plaque composition detection. Small 2008 September;4(9):1437-44.

5. Mulder WJ, Strijkers GJ, Briley-Saboe KC, Frias JC, Aguinaldo JG, Vucic E, Amirbekian V, Tang C, Chin PT, Nicolay K, Fayad ZA. Molecular imaging of macrophages in atherosclerotic plaques using bimodal PEG-micelles. Magn Reson Med 2007 December;58(6):1164-70.

6. Briley-Saebo KC, Amirbekian V, Mani V, Aguinaldo JG, Vucic E, Carpenter D, Amirbekian S, Fayad ZA. Gadolinium mixed-micelles: effect of the amphiphile on in vitro and in vivo efficacy in apolipoprotein E knockout mouse models of atherosclerosis. Magn Reson Med 2006 December;56(6):1336-46.

7. Cornily JC, Hyafil F, Calcagno C, Briley-Saebo KC, Tunstead J, Aguinaldo JG, Mani V, Lorusso V, Cavagna FM, Fayad ZA. Evaluation of neovessels in atherosclerotic plaques of rabbits using an albumin-binding intravascular contrast agent and MRI. J Magn Reson Imaging 2008 June;27(6):1406-11.

8. Winter PM, Morawski AM, Caruthers SD, Fuhrhop RW, Zhang H, Williams TA, Allen JS, Lacy EK, Robertson JD, Lanza GM, Wickline SA. Molecular imaging of angiogenesis in early-stage atherosclerosis with alpha(v)beta3-integrin-targeted nanoparticles. Circulation 2003 November 4;108(18):2270-4.

9. Frias JC, Ma Y, Williams KJ, Fayad ZA, Fisher EA. Properties of a versatile nanoparticle platform contrast agent to image and characterize atherosclerotic plaques by magnetic resonance imaging. Nano Lett 2006 October;6(10):2220-4.

10. Lobbes MB, Miserus RJ, Heeneman S, Passos VL, Mutsaers PH, Debernardi N, Misselwitz B, Post M, Daemen MJ, van Engelshoven JM, Leiner T, Kooi ME. Atherosclerosis: contrast-enhanced MR imaging of vessel wall in rabbit model--comparison of gadofosveset and gadopentetate dimeglumine. Radiology 2009 March;250(3):682-91.

11. Chen W, Vucic E, Leupold E, Mulder WJ, Cormode DP, Briley-Saebo KC, Barazza A, Fisher EA, Dathe M, Fayad ZA. Incorporation of an apoE-derived lipopeptide in high-density lipoprotein MRI contrast agents for enhanced imaging of macrophages in atherosclerosis. Contrast Media Mol Imaging 2008 November;3(6):233-42.

12. Zheng J, Ochoa E, Misselwitz B, Yang D, El N, I, Woodard PK, Abendschein D. Targeted contrast agent helps to monitor advanced plaque during progression: a magnetic resonance imaging study in rabbits. Invest Radiol 2008 January;43(1):49-55.

13. Kawahara I, Morikawa M, Honda M, Kitagawa N, Tsutsumi K, Nagata I, Hayashi T, Koji T. High-resolution magnetic resonance imaging using gadolinium-based contrast agent for atherosclerotic carotid plaque. Surg Neurol 2007 July;68(1):60-5.

14. Sirol M, Itskovich VV, Mani V, Aguinaldo JG, Fallon JT, Misselwitz B, Weinmann HJ, Fuster V, Toussaint JF, Fayad ZA. Lipid-rich atherosclerotic plaques detected by gadofluorine-enhanced in vivo magnetic resonance imaging. Circulation 2004 June 15;109(23):2890-6.

15. Barkhausen J, Ebert W, Heyer C, Debatin JF, Weinmann HJ. Detection of atherosclerotic plaque with Gadofluorine-enhanced magnetic resonance imaging. Circulation 2003 August 5;108(5):605-9.

16. Neubauer AM, Sim H, Winter PM, Caruthers SD, Williams TA, Robertson JD, Sept D, Lanza GM, Wickline SA. Nanoparticle pharmacokinetic profiling in vivo using magnetic resonance imaging. Magn Reson Med 2008 December;60(6):1353-61.

17. Briley-Saebo KC, Shaw PX, Mulder WJ, Choi SH, Vucic E, Aguinaldo JG, Witztum JL, Fuster V, Tsimikas S, Fayad ZA. Targeted molecular probes for imaging atherosclerotic lesions with magnetic resonance using antibodies that recognize oxidation-specific epitopes. Circulation 2008 June 24;117(25):3206-15.

18. Steffens S, Veillard NR, Arnaud C, Pelli G, Burger F, Staub C, Karsak M, Zimmer A, Frossard JL, Mach F. Low dose oral cannabinoid therapy reduces progression of atherosclerosis in mice. Nature 2005 April 7;434(7034):782-6.

19. Mach F, Steffens S. The role of the endocannabinoid system in atherosclerosis. J Neuroendocrinol 2008 May;20 Suppl 1:53-7.

20. te Boekhorst BC, Bovens SM, Rodrigues-Feo J, Sanders HM, van de Kolk CW, de Kroon AI, Cramer MJ, Doevendans PA, ten HM, Pasterkamp G, van Echteld CJ. Characterization and in vitro and in vivo testing of CB2-receptor- and NGAL-targeted paramagnetic micelles for molecular MRI of vulnerable atherosclerotic plaque. Mol Imaging Biol 2010 December;12(6):635-51.

21. Mitchell DG. MRI principles. 2004 ed. Philadelphia, Pennsylvania, USA: Saunders; 2011.

22. Kuhlencordt PJ, Gyurko R, Han F, Scherrer-Crosbie M, Aretz TH, Hajjar R, Picard MH, Huang PL. Accelerated atherosclerosis, aortic aneurysm formation, and ischemic heart disease in apolipoprotein E/endothelial nitric oxide synthase double-knockout mice. Circulation 2001 July 24;104(4):448-54.

23. Hanus L, Breuer A, Tchilibon S, Shiloah S, Goldenberg D, Horowitz M, Pertwee RG, Ross RA, Mechoulam R, Fride E. HU-308: a specific agonist for CB(2), a peripheral cannabinoid receptor. Proc Natl Acad Sci U S A 1999 December 7;96(25):14228-33.

24. Kwee TC, Takahara T, Luijten PR, Nievelstein RA. ADC measurements of lymph nodes: inter- and intra-observer reproducibility study and an overview of the literature. Eur J Radiol 2010 August;75(2):215-20.

25. van Bochove GS, Paulis LE, Segers D, Mulder WJ, Krams R, Nicolay K, Strijkers GJ. Contrast enhancement by differently sized paramagnetic MRI contrast agents in mice with two phenotypes of atherosclerotic plaque. Contrast Media Mol Imaging 2011 January;6(1):35-45.

26. Terreno E, Geninatti CS, Belfiore S, Biancone L, Cabella C, Esposito G, Manazza AD, Aime S. Effect of the intracellular localization of a Gd-based imaging probe on the relaxation enhancement of water protons. Magn Reson Med 2006 March;55(3):491-7.

27. Kok MB, Hak S, Mulder WJ, van der Schaft DW, Strijkers GJ, Nicolay K. Cellular compartmentalization of internalized paramagnetic liposomes strongly influences both T1 and T2 relaxivity. Magn Reson Med 2009 May;61(5):1022-32.

28. Briley-Saebo KC, Shaw PX, Mulder WJ, Choi SH, Vucic E, Aguinaldo JG, Witztum JL, Fuster V, Tsimikas S, Fayad ZA. Targeted molecular probes for imaging atherosclerotic lesions with magnetic resonance using antibodies that recognize oxidation-specific epitopes. Circulation 2008 June 24;117(25):3206-15.

29. Massoud TF, Gambhir SS. Molecular imaging in living subjects: seeing fundamental biological processes in a new light. Genes Dev 2003 March 1;17(5):545-80.

30. Mulder WJ, Strijkers GJ, van Tilborg GA, Griffioen AW, Nicolay K. Lipid-based nanoparticles for contrast-enhanced MRI and molecular imaging. NMR Biomed 2006 February;19(1):142-64.

31. Strijkers GJ, Hak S, Kok MB, Springer CS, Jr., Nicolay K. Three-compartment T1 relaxation model for intracellular paramagnetic contrast agents. Magn Reson Med 2009 May;61(5):1049-58.

4

Molecular MRI of murine atherosclerotic plaque targeting NGAL: a protein associated with unstable human plaque characteristics

Published
Cardiovasc Res. 2011 Feb 15;89(3):680-8

Sandra M. Bovens[1,2]*, Bernard C.M. te Boekhorst[1,2]*, Willem E. Hellings[3], Petra H. van der Kraak[4], Kees W.A. van de Kolk[1], Aryan Vink[4], Frans L. Moll[3], Matthijs F. van Oosterhout[5], Jean P. de Vries[6], Pieter A.F. Doevendans[1,2], Marie-Jose Goumans[7], Dominique P.V. de Kleijn[1,2], Cees J.A. van Echteld[1], Gerard Pasterkamp[1], and Joost P.G. Sluijter [1,2]

1 Department of Cardiology, University Medical Center Utrecht, the Netherlands
2 Netherlands Heart Institute (ICIN), Utrecht, the Netherlands
3 Department of Vascular Surgery, University Medical Center Utrecht, Utrecht, the Netherlands
4 Department of Pathology, University Medical Center Utrecht, Utrecht, the Netherlands
5 Department of Pathology, St Antonius Hospital, Nieuwegein, the Netherlands
6 Department of Vascular Surgery,St Antonius Hospital, Nieuwegein, the Netherlands
7 Department of Molecular Cell Biology, Leiden University Medical Center, Leiden, the Netherlands

* Authors contributed equally to this study

ABSTRACT

Aims

Neutrophil gelatinase-associated lipocalin (NGAL) is an effector molecule of the innate immune system. One of its actions is the prolongation of matrix metalloproteinase-9 (MMP-9) activity by the formation of a degradation-resistant NGAL/MMP-9 complex. We studied NGAL in human atherosclerotic lesions and we examined whether NGAL could act as a target for molecular imaging of atherosclerotic plaques.

Methods and Results

Increased levels of NGAL and the NGAL/MMP-9 complex were associated with high lipid content, high number of macrophages, high interleukin-6 (IL-6) and IL-8 levels, and low smooth muscle cell content in human atherosclerotic lesions obtained during carotid endarterectomy (n = 122). Moreover, plaque levels of NGAL tended to be higher when intra-plaque haemorrhage (IPH) or luminal thrombus was present (n = 77) than without the presence of IPH or thrombus (n = 30). MMP-9 and -8 activities were strongly related to NGAL levels. The enhancement on magnetic resonance (MR) images of the abdominal aorta of $ApoE^{-/-}/eNOS^{-/-}$ mice was observed at 72 h after injection of NGAL/24p3-targeted micelles. The specificity of these results was validated by histology, and co-localization of micelles, macrophages, and NGAL/24p3 was observed.

Conclusion

NGAL is highly expressed in atheromatous human plaques and associated with increased MMP-9 activity. NGAL can be detected in murine atherosclerotic arteries using targeted high-resolution MR imaging. Therefore, we conclude that NGAL might serve as a novel imaging target for the detection of high-risk plaques.

INTRODUCTION

In vivo imaging of proteins which are associated with atherosclerotic disease progression and plaque destabilization is a major challenge. Magnetic resonance imaging (MRI) provides both a high anatomical detail and the option of molecular MRI of plaque proteins. Molecular MRI, using gadolinium (Gd) loaded nanoparticles, of macrophage and cholesterol metabolism related targets in early to intermediate plaques has revealed promising results.[1-5] Micelles are lipid-based nanoparticles, in the nm range, and may be coated with PEG (poly-ethylene-glycol) to extend plasma half-lives.[6] The possibility to bind antibodies to PEG and to incorporate Gd and fluorescent probes, makes these particles very suitable for targeted MRI of the high-risk atherosclerotic plaque.

Neutrophil gelatinase-associated lipocalin (NGAL) is a 25 kD glycoprotein which was first discovered in human neutrophils.[7, 8] NGAL is an effector molecule of the innate immune system through inhibition of bacterial iron uptake by binding bacterial siderophores.[9] Moreover, it mediates inflammatory activity through binding to formyl-methionyl-leucyl-phenylalanine (fMLP; a chemotactic peptide), leukotriene B4 and platelet activating factor.[10-12] Production of NGAL is induced via nuclear factor kappa B (NFκB), and high levels are found in inflammatory conditions.[11, 13] NGAL is able to form a stable, biologically active complex with matrix metalloproteinase 9 (MMP-9), preventing its degradation, and thereby prolonging MMP-9 activity.[14] In addition, NGAL is involved in the allosteric activation of MMP-8 and MMP-9.[15]

MMPs are key players in atherosclerotic disease. They are capable of degrading a broad spectrum of extracellular matrix components and held responsible for vascular remodeling and breakdown of the fibrous cap of atherosclerotic lesions.[16] Especially MMP-9 is implicated to play a crucial role in atherosclerotic plaque destabilization, both in human studies and experimental models.[17-21] The mouse analogue of NGAL, called 24p3 (SIP24, lipocalin-2, uterocalin), was present in murine atherosclerotic lesions, as demonstrated by Hemdahl *et al*.[22] Considering the function of NGAL in the innate immune system and its effect on MMP-9 activity, NGAL might play an important role in atherosclerotic plaque destabilization.

We studied whether NGAL is associated with histological characteristics of high-risk human atherosclerotic lesions and whether MRI of micelles, targeting NGAL, is feasible in the ApoE$^{-/-}$/eNOS$^{-/-}$ mouse model[23] and thereby could serve as a novel target to visualize high-risk atherosclerotic lesions.

METHODS

Human carotid atherosclerotic specimen

Carotid plaques were obtained from a consecutive series of patients undergoing CEA (n=122), participating in the Athero-Express biobank.[24] This ongoing biobank is running in two Dutch Hospitals: The University Medical Center Utrecht and the St. Antonius Hospital Nieuwegein. These patients all suffered from high grade (>70%) carotid stenosis. Indications for CEA were based on recommendations from the NASCET, ECST, ACAS and ACST trials.[25-28] The investigations conformed to the principles outlined in the Declaration of Helsinki. The study was approved by the institutional review boards of both participating hospitals and all patients provided written informed consent.

Carotid plaque characterization

The CEA specimens were divided in segments of 5 mm thickness along the longitudinal axis of the vessel. The segment with greatest plaque burden was embedded in paraffin for further histological characterization. Staining for macrophages, endothelial cells, smooth muscle cells and NGAL was performed. Semi-quantitative analysis of plaque for macrophages, smooth muscle cells, collagen, lipid content, calcifications and overall phenotype followed. Additionally, presence of intra-plaque hemorrhage (IPH) or luminal thrombus was scored by checking for (remnants of) erythrocytes and fibrin strands on HE stainings. The directly adjacent segment was used for protein extraction. Interleukin-6 (IL-6) and IL-8, MMP-2, -8 and -9 activities in the protein extracts were measured with an activity assay. See online appendix for further details.

Detection of NGAL in carotid plaques

For immunohistochemical detection of NGAL/MMP-9 complex in carotid plaques, see online appendix. NGAL/MMP-9 complex activity was determined using gelatin zymography (N=122) (see online appendix). Additionally, NGAL concentration in protein extracts of the tissue specimens was measured with a NGAL Enzyme-Linked Immunosorbent Assay (ELISA) kit (N=107), according to the manufacturer's protocol (Antibodyshop, Gentofte, Denmark). This assay has no cross-reactivity with NGAL/MMP-9 complexes. The measurements were standardized for total protein concentration of the protein extracts.

Release of NGAL and NGAL/MMP-9 complex from carotid plaques

To assess release of NGAL or NGAL/MMP-9 complexes from plaques into the systemic circulation, we applied a novel model comparable to the system applied by Maier *et al*[29]. A blood sample obtained at the site of the plaque was compared to a peripheral blood sample for the concentration of NGAL and NGAL/MMP-9 complex in 9 consecutive patients undergoing CEA. The difference in concentration between the local and peripheral obtained samples is a measure of secretion of the protein by the plaque. During CEA, the blood sample at the plaque site ("plaque-related blood") was drawn directly from the already exposed common carotid artery. This was done after the blood had been halted for 2 minutes at the plaque site during test-clamping, which is routinely performed in our hospital before incision of the carotid artery. At exactly the same time, a peripheral blood sample was drawn from the indwelling arterial line in the radial artery. NGAL was measured by ELISA as described above. Levels of the NGAL/MMP-9 complex were determined by ELISA (R&D Systems, Minneapolis, MN).

Animals

Animal experiments conformed to the Guide for the Care and Use of Laboratory Animals published by the US National Institutes of Health (NIH Publication No. 85-23, revised 1996) and they were approved by the animal experimental committee of the Utrecht University. Old (between 9-12 months) male ApoE/eNOS double knockout mice (generated in our lab by crossing the offspring of $ApoE^{-/-}$ and $eNOS^{-/-}$ mice, genotype confirmed by PCR) were fed a western type diet (Harlan) for 12 weeks. In group A1 (n=6), mice were injected with NGAL-targeted micelles and imaged at baseline and t=24 hours. In group A2 (n=8), mice were injected with NGAL targeted micelles and imaged at baseline, t=24 hours and t=72 hours. In group B1 (n=4) mice were injected with isotype-conjugated micelles (control) and imaged at baseline and t=24 hours. In group B2 (n=6) mice were injected with isotype-conjugated micelles (control) and imaged at baseline, t=24 hours and t=72 hours.

Validation of the unstable plaque mouse model

The histology from abdominal aortic plaques in ApoE$^{-/-}$/eNOS$^{-/-}$ mice was compared to histology from an in literature well-accepted unstable plaque mouse model [30] (brachiocephalic artery plaque of an apoE knockout mouse on an atherogenic diet).

Micelles

A mixture of the appropriate amounts of lipids (DSPE-PEG2000 (43M%), Gd-DTPA-bisstearylamide (50M%), Liss-Rhod-PE (5M%) and Mal-PEG2000-DSPE (2M%); all purchased from Avanti Polar Lipids Inc., Alabaster, USA), dissolved in chloroform, was dried by rotary evaporation at 55 °C. The lipid film was subsequently hydrated in 1 ml PBS, yielding a total lipid concentration of 3 mM. Rat anti-mouse 24p3 antibodies (3mg/ml) (MAB1857, R&D systems, Minneapolis, USA) and rat IgG isotype antibodies (Invitrogen, Carlsbad, USA) were conjugated via SATA-modification as described previously.[31] The modified antibody was added to the micelles and incubated overnight at 4°C. According to size exclusion chromatography >95% of antibodies was bound to mal-PEG (data not shown). Given that the molar antibody to lipid ratio was 0.7:100 and the percentage of mal-PEG was 2%, ~35% of mal-PEG should be occupied by antibody. Assuming that these micelles are composed of ~100 lipid monomers, nearly all micelles were occupied by antibodies. Rat isotype and 24p3 antibody-conjugated micelles had a size of ~23.0 nm determined by dynamic light scattering (data not shown).

Animal preparation and anesthesia

Mice were imaged in a vertical 9.4T, 89mm bore size magnet equipped with a 1500 mT/m gradient set and connected to an Avance 400 MR system (Bruker BioSpin, Germany) in a quadrature-driven birdcage coil with an inner diameter of 3 cm. ParaVision 4.0 software was used for MR acquisition and reconstruction.

Mice were anesthetized with 5 vol% isoflurane in a 2:1 mixture of air (0.3 L/min) and oxygen (0.15 L/min) and maintained with 1.5-2.5 vol% isoflurane to keep the respiratory rate stable. An intravenous catheter was inserted into the tail vein. The cardiac- and respiratory motion were monitored using a respiratory pad linked to an ECG/respiratory unit.

Baseline and follow-up MRI procedure

After scout imaging was performed, twenty contiguous axial slices were planned from 4 mm below the right renal artery branch up to 5 mm above this branch. Inversion Recovery-Fast Spin Echo (IR-FSE) images and anatomic reference images for lymph nodes and peri-aortic blood vessels were made. See online appendix for further details.

Contrast injection, harvesting and preparation of aortas:

After the baseline MRI procedure, 200 µL of contrast agent (3mM lipid 24p3-targeted or isotype-conjugated micelles) was injected via an intravenous catheter, the catheter was removed and the animal recovered from anesthesia until the next MRI procedure. After the last MRI procedure, anesthesia was continued with a mixture of medetomidine (6%)/ketamine (5%) (0.1 mL/10 gram). The imaged parts of the aortas were harvested after perfusion with nitroglycerin/PBS (1:10), perfusion-fixated with formaldehyde 4%/PBS (1:10) and embedded in paraffin or perfused with OCT compound/PBS (1:10) and embedded in OCT compound and stored at -20°C.

Histology of murine atherosclerotic specimens

From 4mm caudal to 5mm cranial of the right renal artery branch, sections were made at every 0.5mm. Staining for lipids, macrophages, 24p3 and micelles was performed. See online appendix for further details. In case of validation of the plaque mouse model, carotid arteries and aortas were stained for smooth muscle cells (buried fibrous caps[30]), iron (intra-plaque hemorrhage[32]) and NGAL.

MRI and Histological review

MRI data were reviewed independently (B.B. and S.B), and regions of interest (ROIs) representing pre-vertebral (pv) muscle and plaque were drawn on pre- and post-injection images. The normalized enhancement ratio (NER) was derived from the signal intensity (SI) of plaque and pv muscle (SIplaque and SIpv muscle) using the next formula:

$(SI_{plaque} / SI_{pv\ muscle(post\text{-}injection)})/(SI_{plaque} / SI_{pv\ muscle\ (pre\text{-}injection)})$.

Data analysis

All measurements are presented as mean +/- SEM. Associations between carotid plaque composition parameters and NGAL or NGAL/MMP-9 complex levels in the plaque were tested by Mann-Whitney U test or Spearman's non-parametric correlation where appropriate. Wilcoxon's signed rank test was used to test significance for the carotid plaque secretion experiments. To adjust the relation between MMP-9 and NGAL for the presence of macrophages, a linear regression model was constructed in which "NGAL" and "number of plaque macrophages" were entered as determinants and MMP-9 as the predicted variable. Differences of NER between mouse groups were tested with the independent samples t-tests. P-values ≤ 0.05 were considered statistically significant.

RESULTS

Association between NGAL and MMP levels in atherosclerotic carotid plaques

In atherosclerotic carotid plaques, a strong positive correlation was observed between total NGAL content and total MMP-9 (Figure 1A; R=0.528; p<0.001) and MMP-8 activity (Figure 1B, R=0.654; p<0.001) as determined by the activity assay. No association with MMP-2 activity could be observed (Figure 1C). MMP-9 activity correlated with NGAL/MMP-9 levels in the plaques (Supplement Figure 1A) and NGAL appears to preserve MMP-9 activity (Supplement Figure 2).

We investigated whether the strength of the association between NGAL and MMP-9 levels might be influenced by the number of macrophages in the plaque. Therefore, we rectified the relation between NGAL and MMP-9 levels for the extent of macrophage infiltration and put these variables in a linear regression model. This model demonstrated that NGAL levels were associated with MMP-9 levels, independently on the presence of macrophages (β=0.43; p<0.001).

Interaction of NGAL and MMP-9 in atherosclerotic carotid plaques

Gelatinolytic activity of NGAL/MMP-9 complexes (Suppl. Figure 1B) was detected at 125 kD (NGAL/MMP-9) and 150 kD (NGAL-dimer/MMP9) as previously described by Yan *et al*.[14] This was confirmed via Western Blotting: specific NGAL bands were detected at 125 kD and 150 kD, corresponding to the two bands observed in zymography (Suppl. Figure 1B). In addition, free NGAL was detected by Western blotting at 25 kD (monomer) and 50 kD (dimer; data not shown). The NGAL/MMP-9 complexes could

be reconstructed in vitro by incubation of MMP-9 and NGAL recombinants (Suppl. Figure 2). Gelatinolytic activity of the NGAL/MMP-9 complex was significantly higher in carotid artery plaques compared to the control mammary arteries (Suppl. Figure 1C). Moreover, as can be appreciated in suppl. Figure 1C, an important part of total gelatinolytic activity in the plaques was attributable to the NGAL/MMP-9 complexes (6.75 A.U.) compared to free MMP-9 (15.3 A.U.), which was confirmed by quantification of the NGAL/MMP-9 complex levels via ELISA in a subset of samples (0.60ng/g vs. 2.51 ng/g, respectively). Gelatinolytic activity of the NGAL/MMP-9 complex was strongly related to NGAL concentration (R=0.310; p=0.001) and MMP-9 activity (Suppl. Figure 1A; R=0.315; p=0.005), whereas NGAL/MMP-9 gelatinolytic activity was not associated with MMP-8 or MMP-2 activity levels (data not shown).

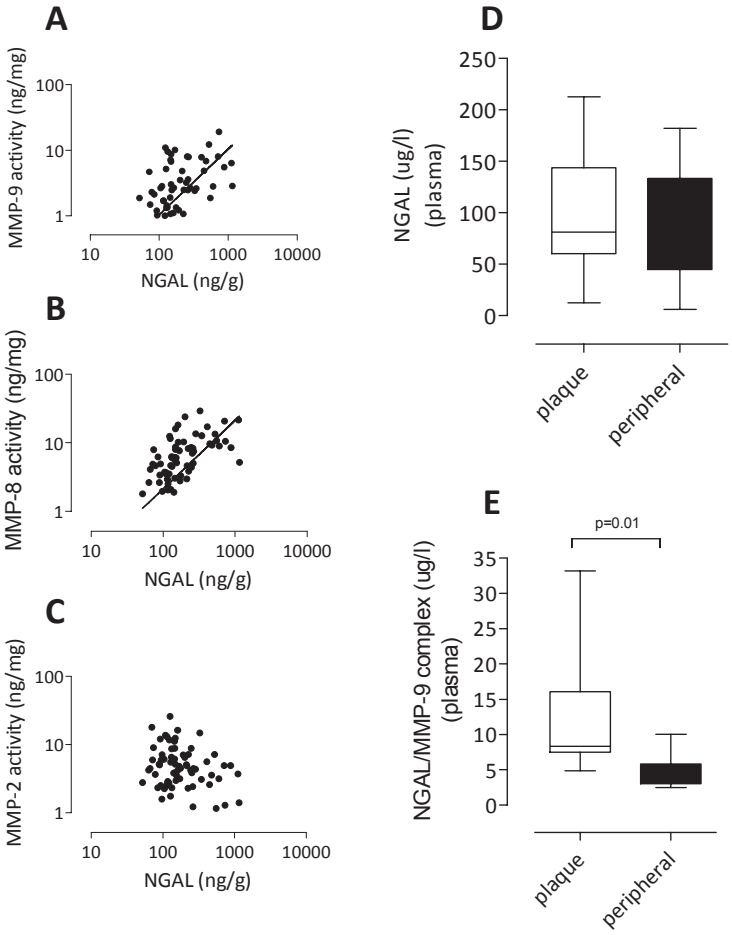

Figure 1 | *Association between NGAL and MMP activity; blood and plaque levels of NGAL and NGAL/MMP-9 in humans.*

A: Association between plaque NGAL concentration and plaque MMP-9 activity (ELISA) (R=0.528; P<0.001). B: Association between plaque NGAL concentration and plaque MMP-8 activity (ELISA) (R=0.654; P<0.001). C: Association between plaque NGAL concentration and plaque MMP-2 activity (ELISA) (P: n.s.). D: NGAL concentrations: local plaque-related blood vs. peripheral blood (n=9; P=0.06). E: NGAL/MMP-9 concentrations: local plaque-related blood vs. peripheral blood (n=9; P=0.007).

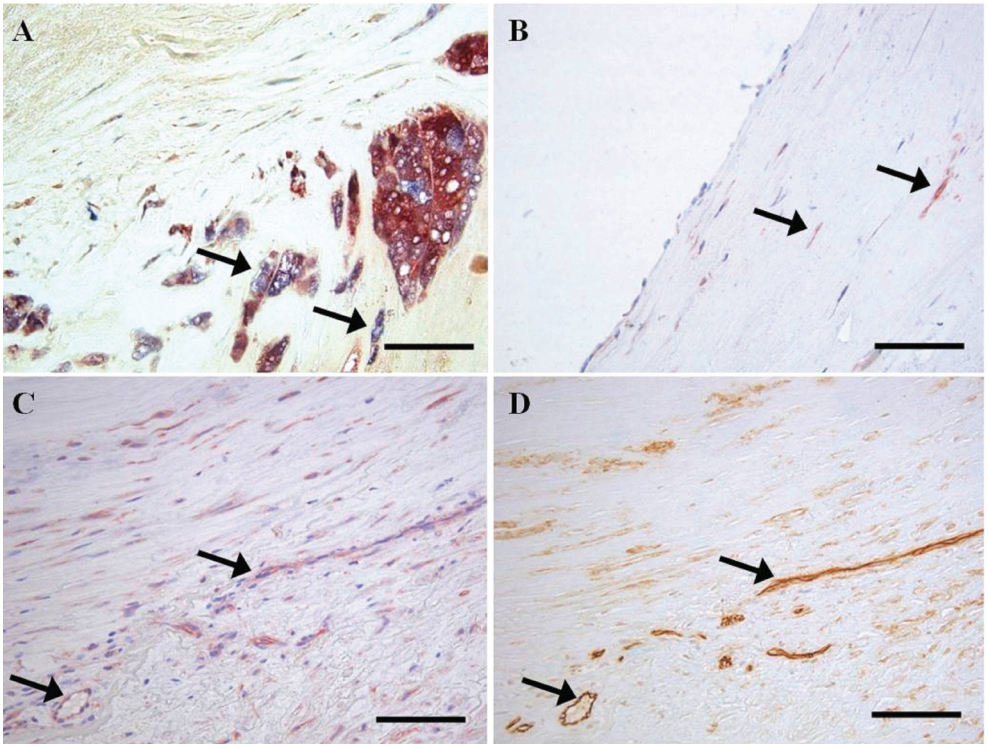

Figure 2 | *Histology of human atherosclerotic plaques.*
A: Double staining of NGAL (blue) and macrophages (CD68; red) reveals co-localization (purple). B: NGAL staining observed in SMCs (arrows) but not in inactive endothelium. C: NGAL staining observed in active endothelial cells aligning neovessels, and SMCs. D: CD34+ staining of the same endothelial cells aligning neovessels as in C.
Scale bar: 100 mm (original magnification: ×100).

Association between NGAL and unstable plaque phenotype

NGAL levels were higher in plaques with an unstable phenotype (Table 1). Fibro-atheromatous plaques had higher NGAL content and atheromatous plaques had higher NGAL/MMP-9 activity and NGAL content when compared to fibrous plaques. Plaques with more macrophages demonstrated higher NGAL/MMP-9 activity and plaques with high levels of pro-inflammatory cytokines IL-6 and IL-8 had higher NGAL content and demonstrated higher NGAL/MMP-9 activity than stable plaques that are fibrous and have higher smooth muscle cell content. Further, plaque NGAL/MMP-9 activity was higher with minor staining for smooth muscle cells when compared to heavy staining (p=0.03). Additionally, plaque levels of NGAL tended to be higher when IPH or luminal thrombus were present (N=77) than without presence of IPH or thrombus (N=30) (p=0.069). Together, these findings indicate an association of NGAL with unstable plaque characteristics. Immunohistochemistry demonstrated expression of NGAL in smooth muscle cells, macrophages and endothelial cells (Figure 2A-D). High NGAL expression was mainly observed in macrophages, and although NGAL expression was observed in smooth muscle cells and endothelial cells in the carotid plaques, their number was limited. Figure 2B shows an example of luminal endothelium with absent staining for NGAL. Additionally, neutrophils were examined as a possible source of NGAL within the plaques, however, none or very few neutrophils could be observed. Therefore, neutrophils are probably not an important source of NGAL in carotid atherosclerotic plaques.

Release of NGAL from atherosclerotic plaques

In blood, drawn directly from the carotid artery containing the atherosclerotic plaque (n=9), NGAL levels tended to increase when compared to NGAL levels in peripheral blood samples drawn at the same time (Figure 1D; p=0.06). Comparison of NGAL/MMP-9 complex levels (ELISA) in the plaque related to peripheral blood samples revealed a statistically significant increase of NGAL/MMP-9 complex level in the plaque related blood samples (Figure 1E, p=0.007).

Table 1 | Relation between plaque characterization and expression of NGAL

Plaque characteristics		NGAL/MMP-9 gelatinolytic activity (A.U.)	*P*	NGAL (ng/mg)	*P*
n		122		107	
Overall	Fibrous	4.6 +/- 1.0		158 +/- 20	
	Fibr-Ath	7.0 +/- 0.8		314 +/- 51	0.05
	Atheromatous	7.4 +/- 0.9	0.043	255 +/- 30	0.004
MO	Minor	6.2 +/- 0.8	0.1	247 +/- 44	0.9
	Heavy	7.2 +/- 0.7		195 +/- 30	
SMC	Minor	7.6 +/- 0.9	0.03	288 +/- 46	0.1
	Heavy	6.1 +/- 0.6		209 +/- 49	
MO/SMC	SMC dominant	6.0 +/- 0.7	0.03	280 +/- 36	0.8
	MO dominant	8.4 +/- 0.3		245 +/- 50	
Collagen	Minor	7.6 +/- 1.0	0.08	262 +/- 37	0.3
	Heavy	6.3 +/- 0.6		239 +/- 56	
Calcifications	Minor	7.0 +/- 0.7	0.6	379+/- 72	0.1
	Heavy	6.5 +/- 0.8		180 +/- 22	
IL-6	Low +	5.8 +/- 0.8	0.1*	207 +/- 27	0.02*
	High &	6.9 +/- 0.8		304 +/- 39	
IL-8	Low +	4.5 +/- 0.6	<0.001*	147 +/- 11	<0.001*
	High &	8.6 +/- 0.8		384 +/- 45	

*All values are presented as mean +/- standard error of the mean. Fibr-Ath: Fibro-Atheromatous; MO: macrophage infiltration; SMC: smooth muscle cell infiltration; IL: interleukin. * Spearman's correlation; +: <median; &: >= median. Significance level: p≤0.05*

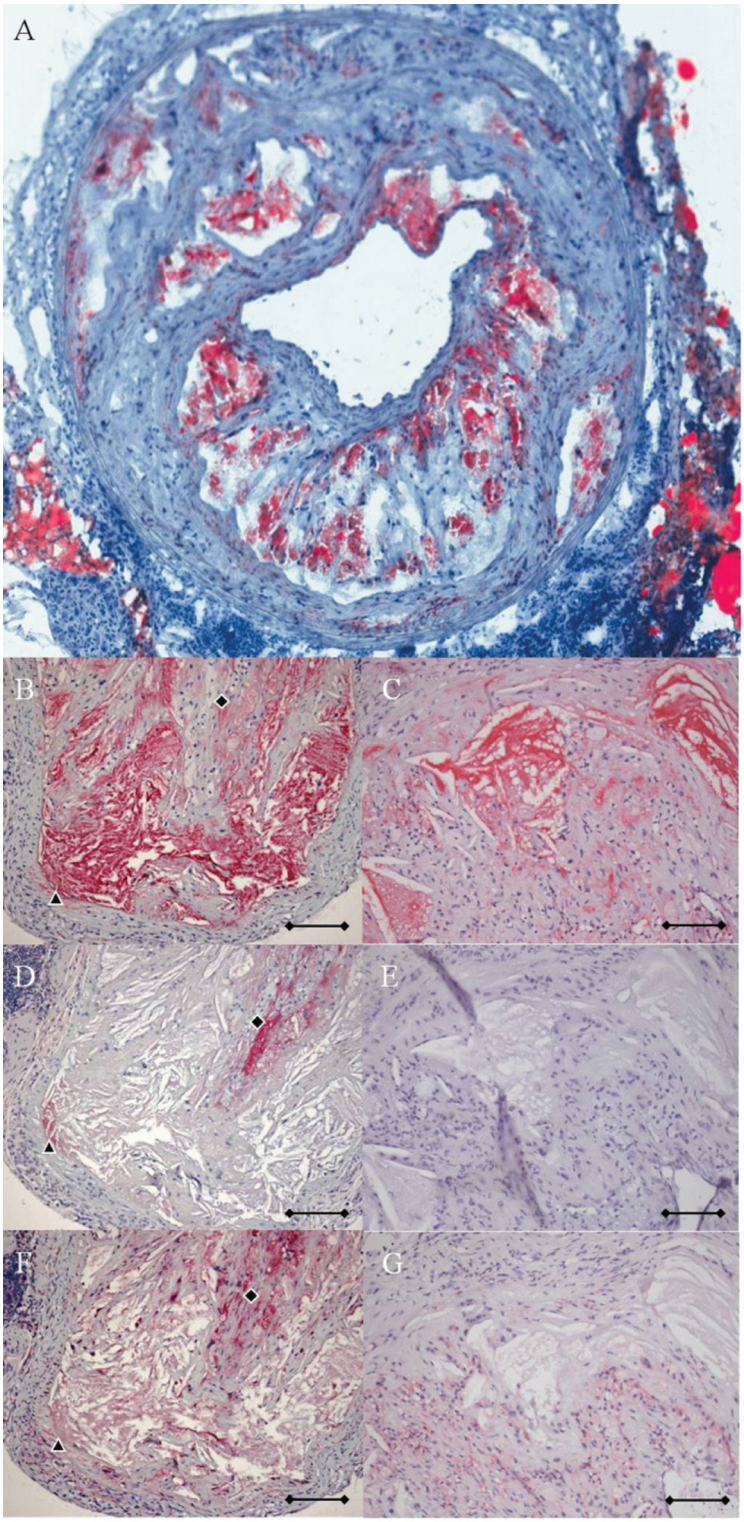

Figure 3 | *Histology of murine atherosclerotic plaques.*
A: Oil red O staining of a representative large aortic plaque with a large lipid core (cryo-section). NGAL/24p3 staining (B and C), micelle staining (D and E), and macrophage staining (MAC-3; F and G) of aortic plaque in an ApoE$^{-/-}$/eNOS$^{-/-}$ mouse injected with NGAL targeted micelles (B, D, and F) and an non injected ApoE$^{-/-}$/eNOS$^{-/-}$ mouse (C, E, and G). Micelles co-localize partially with macrophages (black diamond) and partially with extracellular NGAL/24p3 (black triangle). Scale bar: 100 mm (original magnification: ×100).

Mice/MRI

Positive NGAL staining and signs suggestive for buried fibrous caps (positive SMC staining (α-SMA)) were observed in the brachiocephalic artery of an ApoE$^{-/-}$ mouse (online appendix supplement Figure 3B and 3C, respectively) and in aortic plaques of ApoE$^{-/-}$/eNOS$^{-/-}$ mice after an atherogenic diet (online appendix supplement Figure 4A and 4B, respectively). ApoE$^{-/-}$/eNOS$^{-/-}$ mice showed large atherosclerotic plaques in the abdominal aorta with large lipid cores and many macrophages (Figure 3A and 3D).

MR images showed enhancement at 24 hours post-injection both in mice injected with NGAL/24p3-targeted and isotype-conjugated control micelles (Figure 4: NER=1.45 ± 0.14 and 1.31 ± 0.10, respectively). However, at 72 hours post-injection we observed that mice injected with NGAL/24p3-targeted micelles showed more enhancement than mice injected with isotype-conjugated control micelles (Figure 4: NER=1.67 ± 0.12 and 1.21 ± 0.06, respectively ($p<0.05$)).

Via immunohistochemistry, the specificity of the observed enhancement and detected micelles, macrophages and NGAL/24p3 was validated. The increase of NER at 72 hours in the NGAL/24p3-targeted mice was accompanied by micelle staining which co-localized with NGAL/24p3 expression and presence of macrophages (Figure 3B-D). As expected, micelles were also found in the glomeruli of the kidneys (data not shown), possibly as a consequence of body clearance.

DISCUSSION

MRI shows the most promise for imaging of atherosclerotic plaque vulnerability due to the combined information about anatomic detail and molecular expression. NGAL is a potential novel plaque target for visualization with molecular MRI. The current study reports several new findings regarding the expression of NGAL in human atherosclerotic lesions and its interaction with MMP-9. Moreover a successful *in vivo* visualization of NGAL/24p3 within murine atherosclerotic plaques was achieved with molecular MRI. Expression levels of NGAL are associated with unstable plaque characteristics, such as inflammation, and presence of thrombus or IPH. Previously, these histological characteristics of unstable atherosclerotic plaques have been found to correlate with symptoms in our carotid endarterectomy (CEA) patients.[33] Both free NGAL and associated with MMP-9 are present in plaques and able to form a NGAL/MMP-9 complex thereby preserving MMP-9 activity (see supplementary methods and results).

The role of NGAL in the plaque

Besides the interaction with MMPs, other functions of NGAL could be important in atherosclerotic plaques. NGAL is implicated to regulate inflammation, because it binds fMLP, leukotriene B4 and platelet activating factor.[10-12] In addition, NGAL is proposed to be involved in cell survival, but it is disputed if its function is pro- or anti-apoptotic.[34-36] In kidney ischemia, NGAL protects renal damage by preventing cell death via induction of haem-oxygenase.[37] Since inflammation, cell death and ischemia are key processes in atherosclerosis, free NGAL could play a role in atherosclerotic lesions via these functions but are not addressed in the present study. Here, we focused on the interaction between NGAL and MMP-9 as an important effector mechanism of NGAL in atherosclerotic plaques. In atherosclerotic carotid lesions, NGAL/MMP-9 complex levels were below ELISA detection limits and therefore gelatinolytic activity of the NGAL/MMP-9 complex was measured (see supplementary methods and results). This demonstrated similar associations with plaque characteristics as free NGAL. The current

study is the first to show the coupling of NGAL and MMP-9 in human atherosclerotic plaques, as confirmed by gelatin zymography and western blotting (see supplementary methods and results), potentially leading to prolonged protease activity (see supplementary methods and results). The strong association between NGAL plaque levels and MMP-8 activity levels is expected since NGAL was previously shown to be involved in activation of MMP-8.[15]

Features of plaque vulnerability like IPH and buried fibrous caps have been found in plaques of the ApoE$^{-/-}$/eNOS$^{-/-}$ mice, similar as can be observed in another animal model of atherosclerosis, the

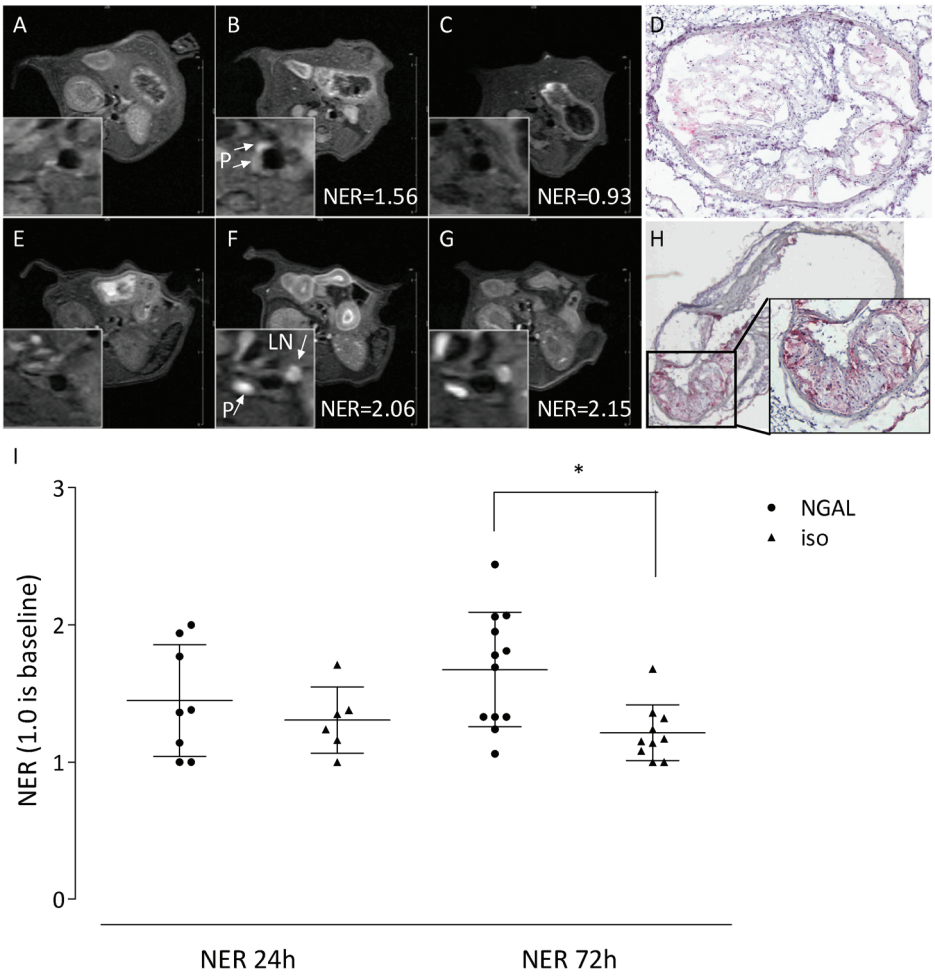

Figure 4 | *MR images and micelle staining on corresponding levels.*
Pre- and post-injection (0, 24, and 72 hours) MR images of the aortic wall in ApoE$^{-/-}$/eNOS$^{-/-}$ mice injected with control (A–C) and NGAL/24p3-targeted (E–G) micelles. Histology on murine aorta (72 hours after injection) showed no micelle staining after injection with control micelles (D) and extensive red staining after injection of NGAL/24p3-targeted micelles (H). The post-injection MR images show the enhancement of a lymph node, which was removed during harvesting of the aorta. Scale bar: 100 mm (original magnification: ×100). I: NER at 24 hours and 72 hours after injection of targeted and isotype-conjugated micelles. P: plaque; LN: lymph node.

brachiocephalic artery in ApoE knockout mice.[30, 32] In addition, in both animal models similar levels of NGAL staining were observed in the brachiocephalic artery.

In order to test whether NGAL deficiency could be associated with reduced incidence of cardiovascular events, we have checked if SNPs are present in NGAL (Affymetrix Genome-Wide Human SNP Array 5). Unfortunately, this analysis did not include SNPs, directly or indirectly available, that meet the query criteria (European descent and a LD r^2 >0.8). Therefore we could not assess the relationship between human genetic variation leading to NGAL deficiency and reduced incidence of cardiovascular events within our dataset. A causal link between NGAL deficiency and reduced incidence of athero-thrombosis could be investigated in an $ApoE^{-/-}/NGAL^{-/-}$ mouse model. Visualization of atherosclerotic plaques in this model using (molecular) MRI would provide the opportunity to find a link between more stable plaques and the lack of NGAL.

The association between NGAL and an unstable plaque phenotype, suggested NGAL to be a potential candidate for molecular imaging of high-risk atherosclerotic lesions. The number of macrophages was not associated with NGAL and NGAL/MMP-9 levels in human atherosclerotic plaques, which is rather unexpected. However, Ronald *et al*.[38] have described the presence of different subpopulations of macrophages (dormant and active) and probably only a part of these active macrophages contribute to the production of NGAL, as we can also observe in the presented staining of macrophages in human atherosclerotic plaque (Figure 2). In addition, NGAL (in complex or not) is secreted into the extracellular matrix and stored. This might lead to a relation between unstable plaque phenotypes and increasing levels of NGAL, but without a direct relation with macrophage content.

Some molecular atherosclerotic imaging studies have focused on targets available on macrophage membranes[39], while other studies have targeted ox-LDL, fibrin or MMPs[1, 40, 41], which have extra-cellular distributions. We may expect that a lot of extra-cellular targets in atherosclerotic plaque are also present in circulating blood. This could hamper the application of molecular MRI with micelles directed against these targets in patients, because they could bind to the circulating marker before arrival in the plaque. Indeed, in another study regarding the same patient group mean NGAL concentration in the plasma was 80 ng/ml, in contrast to the mean plaque NGAL concentration, which was ~120 times higher (unpublished data). We generated gadolinium loaded micelles targeting NGAL specifically and observed an increased plaque NER after injection of NGAL/24p3-targeted micelles as compared to isotype-conjugated micelles at 72 hours. At 24 hours, we could not observe a difference between the two types of micelles, suggesting an early and unspecific uptake of micelles due to the concentration gradient between blood and plaque. However, the level of micelle staining was very diverse among the groups injected with NGAL targeted micelles. Selection of histological slices and dependency of accumulation of micelles on degree of plaque neovasculature could be reasons for this diversity. A non-specific uptake of labeled micelles, probably due to a concentration gradient between the plaque and blood, is seen short after injection (24hours). However, an increased signal between NGAL-targeted and control micelles is present 72 hours post injection.

Although an earlier study revealed a difference in NER at 24 hours after injection of targeted versus non-conjugated micelles, their control micelles lacked an antibody and targeted the macrophage scavenger receptor.[39] Also maximum uptake of micelles targeting oxidation-specific epitopes was reported at 72 hours after injection, but isotype-conjugated micelles did not show significant enhancement at any earlier time points.1 These findings plead for more extended investigation of the MRI timing window for each nanoparticle-target combination.

Generally, fluorescence microscopy is used for *ex vivo* detection of fluorescently labeled paramagnetic

micelles. Because of extensive auto-fluorescence of plaque lipids at various emission wavelengths, we used immuno-histochemistry on micelle-conjugated rat antibodies. Via immunohistochemistry, we could not observe a difference after injection of targeted and isotype micelles at 24 hours, however, the observed enhancement at 72 hours post-injection was due to NGAL-targeted micelles since control targeted micelles could no longer be observed via histology. Micelles of isotype-conjugated and 24p3-targeted micelles were found in glomeruli, suggesting clearance by kidneys. This in contrast to earlier reported predominant clearance of immunomicelles by the liver.[1]

Conclusions

NGAL is highly expressed in atheromatous human plaques and associated with increased MMP-9 activity. The high plaque to blood ratio of this target in patients and successful visualization of NGAL/24p3 in atherosclerotic plaque of $ApoE^{-/-}/eNOS^{-/-}$ mice provides a basis for molecular MRI-based risk stratifications.

Funding

This work was supported by the Netherlands Organisation for Scientific Research (NWO) (grant number 016.056.319); the BSIK program (Dutch Program for Tissue Engineering, grant number UGT.6746); and the Netherlands Heart Foundation (grant numbers 2005T102, 2003B249, 2006T106).

Acknowledgements

We thank Petra van der Kraak, Els Busser, Chaylendra Strijder, Krista den Ouden, Kees van de Kolk and Sander van der Laan for their excellent technical support.

Conflict of Interest

None declared.

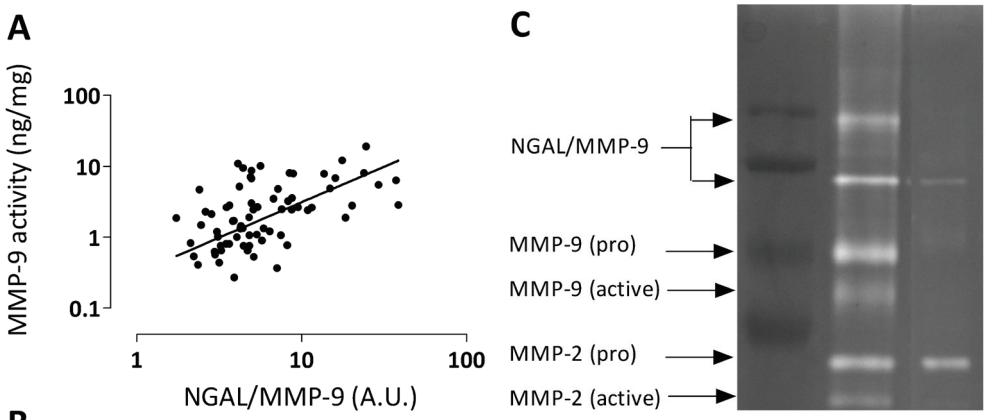

Supplement Figure 1 | *Association between NGAL and MMP activity.*
***A**: MMP-9 activity (Biotrak) is strongly related to gelatinolytic activity of the NGAL/MMP-9 complex (r=0.315; p=0.005) in carotid plaques. **B**: Representative zymogram (ZY) and NGAL Western Blot (WB), demonstrating that the gelatinolytic bands at 125 and 150 kD contain NGAL. **C**: representative zymogram detecting NGAL/MMP-9 complex at 125 kD and NGAL-dimer/MMP-9 complex at 150 kD.*

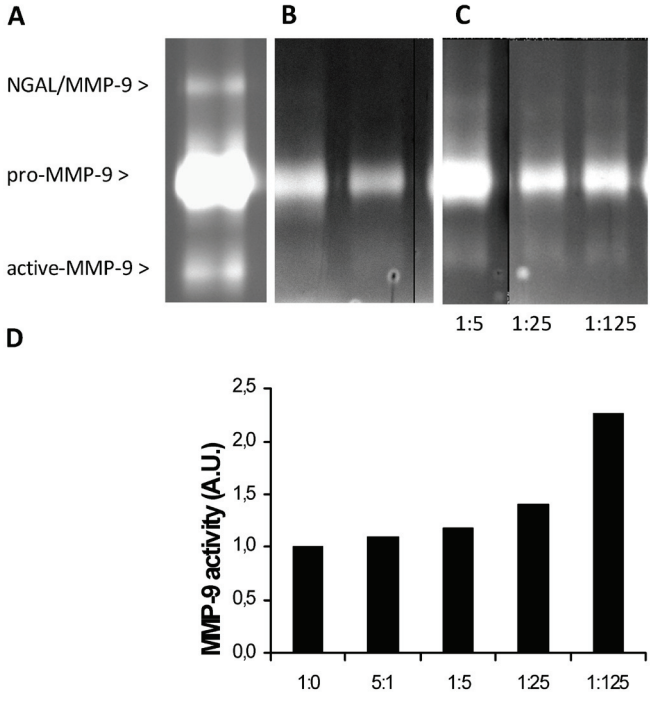

Supplement Figure 2 | *NGAL preserves MMP-9 activity.*
*Quantification of in vitro experiments by gelatin zymography. **A**: In vitro reconstruction of NGAL/MMP-9 complexes by combining recombinant NGAL and MMP-9. **B**: MMP-9 activity diminishes after 30 minutes incubation at 37°C (left lane: no incubation, right lane: 30 minutes incubation). **C**: Increasing addition of NGAL prevents the autodegradation of MMP-9, (MMP-9:NGAL molar ratio 1:5-1:125). **D**: Quantification of C.*

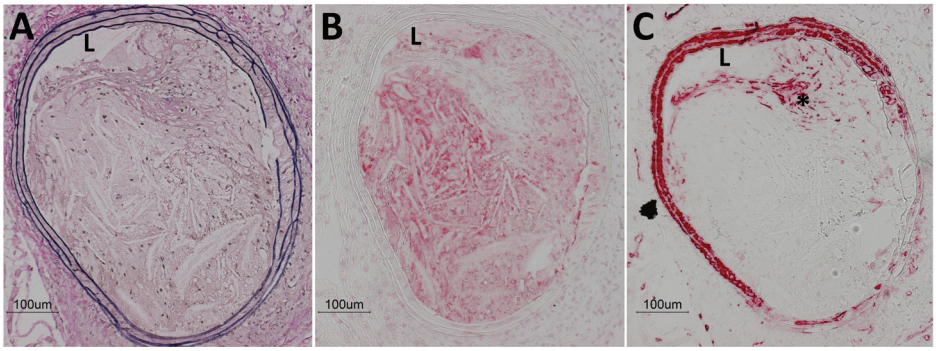

Supplement Figure 3 | *Histology of brachiocephalic artery atherosclerosis in apoE$^{-/-}$ mouse.*
***A**: Elastin von Giesson (EvG) staining. **B**: NGAL staining. **C**: smooth muscle cell (alpha-SMA) staining. *: buried fibrous cap suggested by an intra-plaque layer of smooth muscle cells. L: lumen; SMA: smooth muscle actin.*

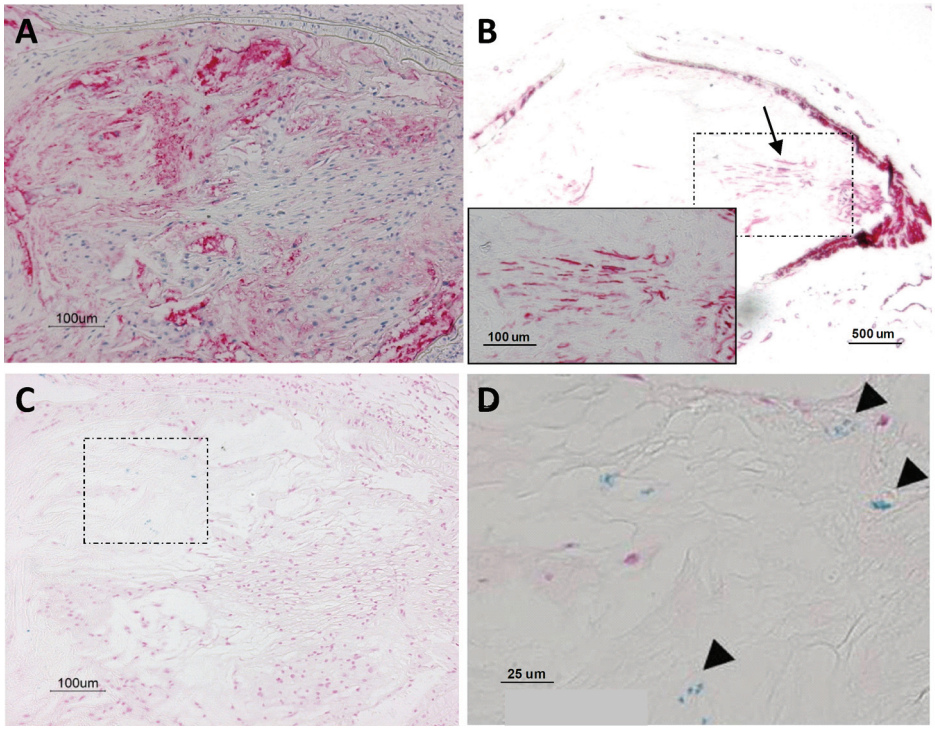

Supplement Figure 4 | *Histology of murine aortic atherosclerosis in apoE$^{-/-}$/eNOS$^{-/-}$ mouse.*
***A**: NGAL staining. **B**. smooth muscle cell (alpha-SMA) staining, smooth muscle cell layers suggesting buried fibrous cap (arrow) with enlarged view of indicated region. **C**: iron staining (Prussian Blue). Dashed region with positive iron staining is zoomed in **D**.*
Arrowheads: intra-plaque hemorrhage represented by blue iron staining.
SMA: smooth muscle actin.

1. Briley-Saebo KC, Shaw PX, Mulder WJ, Choi SH, Vucic E, Aguinaldo JG, Witztum JL, Fuster V, Tsimikas S, Fayad ZA. Targeted molecular probes for imaging atherosclerotic lesions with magnetic resonance using antibodies that recognize oxidation-specific epitopes. Circulation 2008 June 24;117(25):3206-15.

2. Briley-Saebo KC, Geninatti-Crich S, Cormode DP, Barazza A, Mulder WJ, Chen W, Giovenzana GB, Fisher EA, Aime S, Fayad ZA. High-relaxivity gadolinium-modified high-density lipoproteins as magnetic resonance imaging contrast agents. J Phys Chem B 2009 May 7;113(18):6283-9.

3. Cormode DP, Chandrasekar R, Delshad A, Briley-Saebo KC, Calcagno C, Barazza A, Mulder WJ, Fisher EA, Fayad ZA. Comparison of Synthetic High Density Lipoprotein (HDL) Contrast Agents for MR Imaging of Atherosclerosis. Bioconjug Chem 2009 April 20.

4. Mulder WJ, Strijkers GJ, Briley-Saboe KC, Frias JC, Aguinaldo JG, Vucic E, Amirbekian V, Tang C, Chin PT, Nicolay K, Fayad ZA. Molecular imaging of macrophages in atherosclerotic plaques using bimodal PEG-micelles. Magn Reson Med 2007 December;58(6):1164-70.

5. Stary HC, Chandler AB, Dinsmore RE, Fuster V, Glagov S, Insull W, Jr., Rosenfeld ME, Schwartz CJ, Wagner WD, Wissler RW. A definition of advanced types of atherosclerotic lesions and a histological classification of atherosclerosis. A report from the Committee on Vascular Lesions of the Council on Arteriosclerosis, American Heart Association. Circulation 1995 September 1;92(5):1355-74.

6. Lukyanov AN, Torchilin VP. Micelles from lipid derivatives of water-soluble polymers as delivery systems for poorly soluble drugs. Adv Drug Deliv Rev 2004 May 7;56(9):1273-89.

7. Kjeldsen L, Johnsen AH, Sengelov H, Borregaard N. Isolation and primary structure of NGAL, a novel protein associated with human neutrophil gelatinase. J Biol Chem 1993 May 15;268(14):10425-32.

8. Triebel S, Blaser J, Reinke H, Tschesche H. A 25 kDa alpha 2-microglobulin-related protein is a component of the 125 kDa form of human gelatinase. FEBS Lett 1992 December 21;314(3):386-8.

9. Goetz DH, Holmes MA, Borregaard N, Bluhm ME, Raymond KN, Strong RK. The neutrophil lipocalin NGAL is a bacteriostatic agent that interferes with siderophore-mediated iron acquisition. Mol Cell 2002 November;10(5):1033-43.

10. Bratt T, Ohlson S, Borregaard N. Interactions between neutrophil gelatinase-associated lipocalin and natural lipophilic ligands. Biochim Biophys Acta 1999 October 18;1472(1-2):262-9.

11. Nielsen BS, Borregaard N, Bundgaard JR, Timshel S, Sehested M, Kjeldsen L. Induction of NGAL synthesis in epithelial cells of human colorectal neoplasia and inflammatory bowel diseases. Gut 1996 March;38(3):414-20.

12. Sengelov H, Boulay F, Kjeldsen L, Borregaard N. Subcellular localization and translocation of the receptor for N-formylmethionyl-leucyl-phenylalanine in human neutrophils. Biochem J 1994 April 15;299(Pt 2):473-9.

13. Cowland JB, Sorensen OE, Sehested M, Borregaard N. Neutrophil gelatinase-associated lipocalin is up-regulated in human epithelial cells by IL-1 beta, but not by TNF-alpha. J Immunol 2003 December 15;171(12):6630-9.

14. Yan L, Borregaard N, Kjeldsen L, Moses MA. The high molecular weight urinary matrix metalloproteinase (MMP) activity is a complex of gelatinase B/MMP-9 and neutrophil gelatinase-associated lipocalin (NGAL). Modulation of MMP-9 activity by NGAL. J Biol Chem 2001 October 5;276(40):37258-65.

15. Tschesche H, Zolzer V, Triebel S, Bartsch S. The human neutrophil lipocalin supports the allosteric activation of matrix metalloproteinases. Eur J Biochem 2001 April;268(7):1918-28.

16. Galis ZS, Khatri JJ. Matrix metalloproteinases in vascular remodeling and atherogenesis: the good, the bad, and the ugly. Circ Res 2002 February 22;90(3):251-62.

17. de Nooijer R, Verkleij CJ, der Thusen JH, Jukema JW, van der Wall EE, van Berkel TJ, Baker AH, Biessen EA. Lesional overexpression of matrix metalloproteinase-9 promotes intraplaque hemorrhage in advanced lesions but not at earlier stages of atherogenesis. Arterioscler Thromb Vasc Biol 2006 February;26(2):340-6.

18. Galis ZS, Sukhova GK, Lark MW, Libby P. Increased expression of matrix metalloproteinases and matrix degrading activity in vulnerable regions of human atherosclerotic plaques. J Clin Invest 1994 December;94(6):2493-503.

19. Gough PJ, Gomez IG, Wille PT, Raines EW. Macrophage expression of active MMP-9 induces acute plaque disruption in apoE-deficient mice. J Clin Invest 2006 January;116(1):59-69.

20. Loftus IM, Naylor AR, Goodall S, Crowther M, Jones L, Bell PR, Thompson MM. Increased matrix metalloproteinase-9 activity in unstable carotid plaques. A potential role in acute plaque disruption. Stroke 2000 January;31(1):40-7.

21. Sluijter JP, Pulskens WP, Schoneveld AH, Velema E, Strijder CF, Moll F, de Vries JP, Verheijen J, Hanemaaijer R, de Kleijn DP, Pasterkamp G. Matrix metalloproteinase 2 is associated with stable and matrix metalloproteinases 8 and 9 with vulnerable carotid atherosclerotic lesions: a study in human endarterectomy specimen pointing to a role for different extracellular matrix metalloproteinase inducer glycosylation forms. Stroke 2006 January;37(1):235-9.

22. Hemdahl AL, Gabrielsen A, Zhu C, Eriksson P, Hedin U, Kastrup J, Thoren P, Hansson GK. Expression of neutrophil gelatinase-associated lipocalin in atherosclerosis and myocardial infarction. Arterioscler Thromb Vasc Biol 2006 January;26(1):136-42.

23. Kuhlencordt PJ, Gyurko R, Han F, Scherrer-Crosbie M, Aretz TH, Hajjar R, Picard MH, Huang PL. Accelerated atherosclerosis, aortic aneurysm formation, and ischemic heart disease in apolipoprotein E/endothelial nitric oxide synthase double-knockout mice. Circulation 2001 July 24;104(4):448-54.

24. Verhoeven BA, Velema E, Schoneveld AH, de Vries JP, de Bruin P, Seldenrijk CA, de Kleijn DP, Busser E, van der GY, Moll F, Pasterkamp G. Athero-express: differential atherosclerotic plaque expression of mRNA and protein in relation to cardiovascular events and patient characteristics. Rationale and design. Eur J Epidemiol 2004;19(12):1127-33.

25. Beneficial effect of carotid endarterectomy in symptomatic patients with high-grade carotid stenosis. North American Symptomatic Carotid Endarterectomy Trial Collaborators. N Engl J Med 1991 August 15;325(7):445-53.

26. Endarterectomy for asymptomatic carotid artery stenosis. Executive Committee for the Asymptomatic Carotid Atherosclerosis Study. JAMA 1995 May 10;273(18):1421-8.

27. Randomised trial of endarterectomy for recently symptomatic carotid stenosis: final results of the MRC European Carotid Surgery Trial (ECST). Lancet 1998 May 9;351(9113):1379-87.

28. Halliday A, Mansfield A, Marro J, Peto C, Peto R, Potter J, Thomas D. Prevention of disabling and fatal strokes by successful carotid endarterectomy in patients without recent neurological symptoms: randomised controlled trial. Lancet 2004 May 8;363(9420):1491-502.

29. Maier W, Altwegg LA, Corti R, Gay S, Hersberger M, Maly FE, Sutsch G, Roffi M, Neidhart M, Eberli FR, Tanner FC, Gobbi S, von Eckardstein A, Luscher TF. Inflammatory markers at the site of ruptured plaque in acute myocardial infarction: locally increased interleukin-6 and serum amyloid A but decreased C-reactive protein. Circulation 2005 March 22;111(11):1355-61.

30. Jackson CL, Bennett MR, Biessen EA, Johnson JL, Krams R. Assessment of unstable atherosclerosis in mice. Arterioscler Thromb Vasc Biol 2007 April;27(4):714-20.

31. Mulder WJ, Strijkers GJ, van Tilborg GA, Griffioen AW, Nicolay K. Lipid-based nanoparticles for contrast-enhanced MRI and molecular imaging. NMR Biomed 2006 February;19(1):142-64.

32. Cheng C, Tempel D, van HR, van der BA, Grosveld F, Daemen MJ, Krams R, de CR. Atherosclerotic lesion size and vulnerability are determined by patterns of fluid shear stress. Circulation 2006 June 13;113(23):2744-53.

33. Verhoeven B, Hellings WE, Moll FL, de Vries JP, de Kleijn DP, de BP, Busser E, Schoneveld AH, Pasterkamp G. Carotid atherosclerotic plaques in patients with transient ischemic attacks and stroke have unstable characteristics compared with plaques in asymptomatic and amaurosis fugax patients. J Vasc Surg 2005 December;42(6):1075-81.

34. Tong Z, Wu X, Ovcharenko D, Zhu J, Chen CS, Kehrer JP. Neutrophil gelatinase-associated lipocalin as a survival factor. Biochem J 2005 October 15;391(Pt:2):2-8.

35. Tong Z, Wu X, Kehrer JP. Increased expression of the lipocalin 24p3 as an apoptotic mechanism for MK886. Biochem J 2003 May 15;372(Pt:1):1-10.

36. Caramuta S, De Cecco L, Reid JF, Zannini L, Gariboldi M, Kjeldsen L, Pierotti MA, Delia D. Regulation of lipocalin-2 gene by the cancer chemopreventive retinoid 4-HPR. Int J Cancer 2006 October 1;119(7):1599-606.

37. Mori K, Lee HT, Rapoport D, Drexler IR, Foster K, Yang J, Schmidt-Ott KM, Chen X, Li JY, Weiss S, Mishra J, Cheema FH, Markowitz G, Suganami T, Sawai K, Mukoyama M, Kunis C, D'Agati V, Devarajan P, Barasch J. Endocytic delivery of lipocalin-siderophore-iron complex rescues the kidney from ischemia-reperfusion injury. J Clin Invest 2005 March;115(3):610-21.

38. Ronald JA, Chen JW, Chen Y, Hamilton AM, Rodriguez E, Reynolds F, Hegele RA, Rogers KA, Querol M, Bogdanov A, Weissleder R, Rutt BK. Enzyme-sensitive magnetic resonance imaging targeting myeloperoxidase identifies active inflammation in experimental rabbit atherosclerotic plaques. Circulation 2009 August 18;120(7):592-9.

39. Amirbekian V, Lipinski MJ, Briley-Saebo KC, Amirbekian S, Aguinaldo JG, Weinreb DB, Vucic E, Frias JC, Hyafil F, Mani V, Fisher EA, Fayad ZA. Detecting and assessing macrophages in vivo to evaluate atherosclerosis noninvasively using molecular MRI. Proc Natl Acad Sci U S A 2007 January 16;104(3):961-6.

40. Botnar RM, Perez AS, Witte S, Wiethoff AJ, Laredo J, Hamilton J, Quist W, Parsons EC, Jr., Vaidya A, Kolodziej A, Barrett JA, Graham PB, Weisskoff RM, Manning WJ, Johnstone MT. In vivo molecular imaging of acute and subacute thrombosis using a fibrin-binding magnetic resonance imaging contrast agent. Circulation 2004 April 27;109(16):2023-9.

41. Lancelot E, Amirbekian V, Brigger I, Raynaud JS, Ballet S, David C, Rousseaux O, Le GS, Port M, Lijnen HR, Bruneval P, Michel JB, Ouimet T, Roques B, Amirbekian S, Hyafil F, Vucic E, Aguinaldo JG, Corot C, Fayad ZA. Evaluation of matrix metalloproteinases in atherosclerosis using a novel noninvasive imaging approach. Arterioscler Thromb Vasc Biol 2008 March;28(3):425-32.

5

Lactate measured with NMR spectroscopy in atherosclerotic plaques is a marker for local hypoxia

Submitted

Sandra M. Bovens[1,2], Gijsbert Zomer[3], Wouter J.M. Derksen [1,4], Frans L. Moll[4], Dominique P.V. de Kleijn[1], Aryan Vink[5], and Gerard Pasterkamp[1]

1 Department of Cardiology, University Medical Center, Utrecht, the Netherlands.
2 Netherlands Heart Institute (ICIN), Utrecht, the Netherlands
3 National Institute of Public Health and the Environment (RIVM), Bilthoven, the Netherlands
4 Department of Vascular Surgery, University Medical Center Utrecht, Utrecht, the Netherlands
5 Department of Pathology, University Medical Center Utrecht, Utrecht, the Netherlands

ABSTRACT

Background

It has been suggested that hypoxia and subsequent inflammatory cell infiltration promote neovascularization of atherosclerotic plaques. In these inflamed and hypoxic areas new vasculature may be fragile with local leakage and extravasation of blood derived cells. These fragile and leaking vessels could be the primary source of intra-plaque hemorrhage and therefore increase the risk of rapid plaque expansion and plaque rupture. One of the metabolites associated with hypoxia is lactate, which can be detected with ^{1}H-NMR spectroscopy. We hypothesized that the detection of lactate with ^{1}H-NMR spectroscopy is associated with increased plaque vessel density as well as hypoxia-inducible factor (HIF)-1α expression and could therefore serve as a local marker for (rupture-prone) hypoxic plaques.

Methods and Results

^{1}H-NMR spectra analysis at 400 MHz was performed in 50 atherosclerotic femoral artery plaques which were obtained during vascular surgical interventions. NMR spectra were analyzed and peak integration curves were used for analysis as a substitute for metabolite concentration. Vessel density and HIF-1α were determined in histological slides of adjacent plaque sections. We observed that vessel density in atherosclerotic plaques was positively correlated with lactate concentrations ($p=0.006$, $r=0.383$). Additionally, femoral plaques with high lactate levels revealed significantly higher HIF-1α expression ($p=0.015$) as well as presence of intra-plaque hemorrhage ($p=0.023$).

Conclusion

Lactate concentration (determined by ^{1}H-NMR spectroscopy) is associated with hypoxia, intra-plaque hemorrhage and vessel density in the atherosclerotic plaque. This observation supports the view that lactate measurements could potentially serve as a marker for hypoxia related intra-plaque vessel formation.

INTRODUCTION

The natural history of atherosclerotic disease progression is still unknown. Currently, it is well recognized that ischemic events due to athero-thrombosis often originate from thin capped atheromatous plaques.[1] The presence of microvessels in atherosclerotic lesions has been associated with intra-plaque hemorrhage (IPH) as well as plaque rupture due to the extravasation of inflammatory cells and red blood cells.[2-6] In addition, more recently we showed that increased vessel density and the presence of local plaque hemorrhage are predictive for the occurrence of future cardiovascular events.[7] For these reasons, there is an increasing interest in the pathogenetic mechanisms leading to plaque neovessel formation and bleeding [2] since insight in these mechanisms may give rise to new surrogate biochemical and imaging markers that reflect atherosclerotic disease progression.

Advanced atherosclerotic lesions often have macrophage-rich areas characterized by hypoxia[8, 9], which can provoke the formation of microvessels in the plaque. This process is accelerated by the local increase of hypoxia-inducible factor-1α (HIF-1α). In normal oxygen conditions, the transcription factor HIF-1α is rapidly degraded so that it cannot form a heterodimer with HIF-1β. Once HIF-1 is activated, it induces expression of (amongst others) vascular endothelial growth factor (VEGF) with subsequent plaque neovascularization.[10] Hypoxia leads to increased levels of lactic acid, which is an hydroxy carboxylic acid. *In vitro* experiments with macrophage cell lines demonstrated that lactate promotes angiogenic activity via the activation of the VEGF gene.[11, 12] Hypothetically, lactate levels in atherosclerotic lesions could be detected via non-invasive methods and serve as a marker for plaque hypoxia and subsequently for the risk of plaque rupture. Previously, an *in situ* study assessing hypoxia in atherosclerotic plaques was performed in rabbits. This study was evaluated with bioluminescence on snap frozen aortas and showed hypoxia with high lactate levels in plaques >500µm.[13]

To test whether lactate is an appropriate marker for plaque hypoxia and intra-plaque vessel density we examined human femoral plaque specimens by means of ^{1}H-NMR spectroscopy *ex vivo*. ^{1}H-NMR spectroscopy is a non-invasive technique that is widely used for the detection and quantification of metabolites in e.g. urine, cerebrospinal fluid, blood, and plasma.[14, 15] It could also be applicable as a non invasive technique to detect metabolites of interest in atherosclerotic plaques.

MATERIALS AND METHODS

Athero-Express Biobank

Athero-Express is an ongoing longitudinal study that includes patients undergoing carotid endarterectomy (CEA) as well as femoral (tromb)endarterectomy (TEA). The study design has been reported earlier.[16] Plaques are collected during surgery and processed according to a standardized protocol. After surgery, patients undergo a 3-year clinical follow-up. All patients undergoing CEA or TEA in the two participating centers (St. Antonius Hospital Nieuwegein and University Medical Center Utrecht) are asked to participate in the Athero-Express study. With respect to femoral endarterectomy, patients underwent a sole endarterectomy of the common femoral artery or remote endarterectomy of the superficial femoral artery to treat severe intermittent claudication, critical ischemia or tissue loss (Fontain classification IIb–IV).[17] The medical ethics board of both participating hospitals approved the study and all participants of the study provided written informed consent. For the present study, we randomly selected 50 femoral artery plaques from patients operated between July 4, 2002 and April 21, 2008

Determination of plaque phenotype

According to a standardized protocol, the plaque was divided into segments of 5 mm along the longitudinal axis. The segment with the largest plaque burden was considered as the culprit lesion and subjected to histological examination.[16] Paraffin sections of the plaques were stained and analyzed. Macrophage infiltration (CD68) and smooth muscle cell infiltration (α-actin) were quantitatively scored (average percentile positively stained area of total plaque area) using computerized analyses (AnalySIS 3.2, Soft Imaging Systems GmbH, Münster, Germany) as well as semi-quantitatively as 'no', 'minor', 'moderate' or 'heavy' staining.[18] Collagen (Sirius red), calcifications (hematoxylin and eosin (HE)) and overall phenotype were scored semi-quantitatively. The size of the lipid core was visually estimated as a percentage of total plaque area using HE and Sirius red stains, with a division in three categories: no, < 40% and >40% lipid of the total plaque area. Intra-plaque hemorrhage, including both luminal thrombosis and intra-plaque hematoma, were examined in HE and fibrin stainings and rated as 'absent' or 'present'.

^{1}H-NMR spectroscopy

Frozen plaque segments adjacent to the culprit lesion were grinded and dissolved in PBS. After vortexing, the samples were centrifuged and the supernatant filtered. The filtered solution was analyzed by ^{1}H-NMR-spectroscopy at 400 MHz (JEOL JNM-ECP400FT, Tokyo, Japan). Spectra were analyzed with JEOL Delta software (Peabody, MA, USA) and peak integration curves used for statistical analysis.

HIF-1α staining

Immunohistochemical staining for HIF-1α was performed as described previously.[10] In short, sections were pretreated with target retrieval solution (DakoCytomation, Glostrup, Denmark) and incubated with mouse anti-human HIF-1α monoclonal antibody (1:500; BD Biosciences, San Diego, CA) for 30 minutes. Thereafter, the catalyzed signal amplification system (Dako) was used and HIF-1α signal visualized using diaminobenzidine (DAB). Only macrophages with completely and darkly stained nuclei were regarded as positive. Sections were arranged in four groups: negative (no), absent nuclear staining or staining in <10 cells per mm^2; minor, staining in 10–50 cells; moderate, staining in 50–100 cells; heavy, staining in >100 cells.

Vessel density

Plaque vessel density was determined by the average number of CD34 positive intra-plaque vessels from three hotspots within every single plaque as described previously.[7] A hotspot was defined as one high-power field at x40 magnification. For each hotspot we used an overlying grid (100x100 μm). Vessel density was determined by counting vessels when they crossed a bar of the grid, when one vessel crossed two bars it was counted twice, by doing so we compensated for vessel size. Data was expressed as the average count/mm^2.

Data analysis

All patients were included in all analyses. Lactate peak integration curves (doublet present at 1.32ppm) were determined as a substitute for concentration and expressed as arbitrary units (a.u.). All measurements are presented as mean +/- standard deviation (SD). Parameters were related with lactate levels by using the non-parametrical Kruskal-Wallis and Mann-Whitney-U test (SPSS 17.0, Chicago, USA). For the correlation between lactate levels and vessel density, macrophages and smooth muscles cells a Spearman correlation was used. P-values < 0.05 were considered statistically significant.

RESULTS

Patient characteristics

In table 1, patient characteristics are listed. In our patient population we included 44 patients (88%) who suffered from a stenosis of 90-100%, and 6 patients (12%) who suffered from a stenosis of 65-89%. A significant difference in lactate levels was found between males and females (p=0.006). In this study population females showed higher contents of collagen and smooth muscle cells and lower content of intra-plaque hemorrhage (data not shown).

Plaque characteristic

In figure 1 an example of an ^{1}H-NMR spectrum is shown, with at 1.3ppm the lactate doublet. In all patients lactate peaks were detectable. The height of the peaks revealed significant variation with some patients that had peaks which were just above baseline. In table 2, general plaque characteristics are listed. Femoral arterial segments that are selected for endarterectomy are often locally occluded. These plaques mostly reveal stable, non inflammatory and calcified characteristics. The quantitative and

Table 1 | Patient characteristics

Patient characteristics	mean ± SD (range)	Lactate concentration		P-value
Age (years)	67 ± 9 (45-83)			
		No (n)	Yes (n)	
Smoker at time surgery		0.062 ± 0.015 (28)	0.052 ± 0.008 (19)	0.298
Diabetic		0.051 ± 0.011 (32)	0.070 ± 0.017 (18)	0.097
Hypertension		0.034 ± 0.006 (8)	0.063 ± 0.011 (42)	0.266
Hypercholesterolemia		0.058 ± 0.015 (20)	0.057 ± 0.012 (28)	0.754
History peripheral intervention		0.069 ± 0.016 (27)	0.043 ± 0.008 (22)	0.154
History myocardial infarction		0.063 ± 0.011 (41)	0.035 ± 0.005 (9)	0.306
History stroke		0.065 ± 0.012 (38)	0.035 ± 0.007 (12)	0.084
CAD event during follow-up		0.062 ± 0.010 (44)	0.028 ± 0.006 (6)	0.073
Stroke during follow-up		0.050 ± 0.007 (47)	0.179 ± 0.080 (3)	0.043*
Statin use		0.062 ± 0.017 (17)	0.055 ± 0.011 (32)	0.215
Aspirin use		0.059 ± 0.011 (40)	0.049 ± 0.012 (9)	0.918
Oral anti-coagulant use		0.045 ± 0.005 (39)	0.103 ± 0.039 (10)	0.372
Gender		Male (n)	Female (n)	
		0.077 ± 0.015 (28)	0.033 ± 0.004 (22)	0.006*
BMI		<25	>25	
		0.037 ± 0.006 (17)	0.073 ± 0.016 (26)	0.074
Serum levels				
C-reactive protein	11.6 ± 17.6 (0.64-77.1)			
HDL	1.27 ± 0.3 (0.74-2.08)			
LDL	2.66 ± 1.0 (1.20-4.50)			

*All values are presented as mean +/- standard deviation. * p<0.05*
CAD: coronary artery disease, BMI: body mass index, HDL: high density lipoprotein, LDL: low density lipoprotein

Table 2 | Atherosclerotic plaque characteristics

Plaque characteristics		Lactate concentration (A.U.)	n	P-value
Lipid content	No	0.053 ± 0.01	27	
	<40%	0.058 ± 0.02	18	
	>40%	0.078 ± 0.03	5	0.399$
MO	Minor	0.048 ± 0.01	36	
	Heavy	0.082 ± 0.02	14	0.342
SMC	Minor	0.073 ± 0.02	12	
	Heavy	0.053 ± 0.01	37	0.306
Collagen	Minor	0.057 ± 0.02	6	
	Heavy	0.057 ± 0.01	44	0.834
Calcifications	Minor	0.068 ± 0.02	23	
	Heavy	0.048 ± 0.01	27	0.748
Intra-plaque hemorrhage	Absent	0.046 ± 0.01	32	
	Present	0.079 ± 0.02	17	0.023*

*Macrophages and SMC infiltration were also quantitatively scored, no significant correlations were found with lactate concentrations. All values are presented as mean +/- standard deviation. * p<0.05. MO: macrophage infiltration, SMC: smooth muscle cell infiltration.*

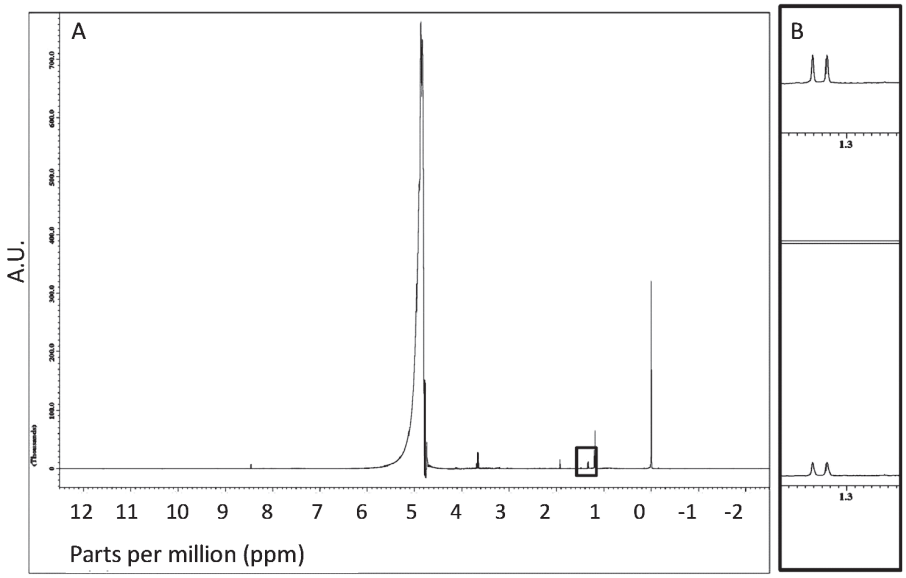

Figure 1 | *NMR spectrum of metabolites extracted from atherosclerotic plaque material.*
Due to the chemical formula of lactate it can be detected as a doublet at a location of 1.32 ppm (chemical shift compared to the internal reference at 0ppm; TMSP).
A: example of a full spectrum with within the black square the lactate doublet.
B: zoomed spectrum of lactate doublets from two separate atherosclerotic plaques with a high and a low lactate level. TMSP: Trimethylsilyl propanoic acid; A.U.: Arbitrary Units

semi-quantitative analysis of macrophage, calcification, collagen, and smooth muscle cell (SMC) staining were divided in two groups: a group revealing no or minor staining and a group with moderate or heavy staining of a specific characteristic. A significant increase of lactate levels was found within sections where intra-plaque hemorrhage was present (p=0.023). In the semi-quantitative macrophage group no/minor staining showed lactate concentrations of 0.048 ± 0.01 (a.u.) and in the moderate/heavy group concentrations were 0.082 ± 0.02 (a.u.), although these numbers suggest higher lactate levels with heavier macrophage staining, the difference is not significant due to the wide confidence intervals. This was confirmed by correlating the computerized quantified analyses of macrophages, no significant correlations were found. Additionally, the degree of staining of SMC, collagen and the percentage of lipid in atherosclerotic plaques were not significantly associated with lactate content (table 1).

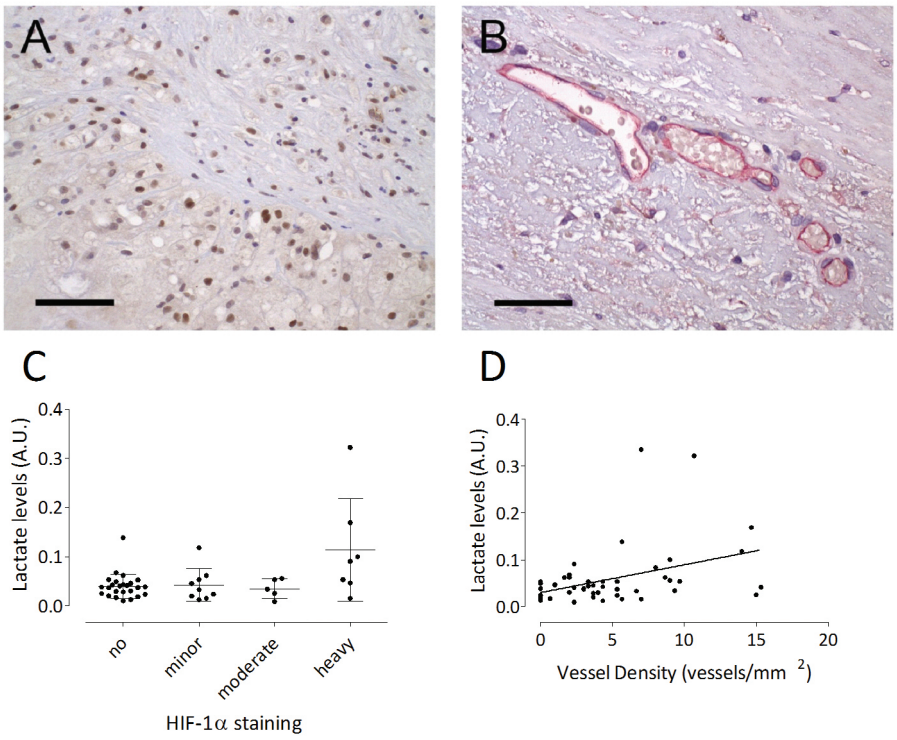

Figure 2 | *Lactate levels expressed against HIF-1α staining and vessel density (CD34 staining)*
A/B: Microscopic examination and immunohistochemical staining of femoral endarterectomy specimens. A: HIF-1α staining showing positive nuclear staining (in brown) in cells in the atherosclerotic plaque. Bar = 100 µm. B, microvessels (in red) in the shoulder of a femoral atherosclerotic plaque. CD34 immunostain, bar = 50 µm.
C: Lactate levels at different degrees of HIF-1α staining, a significant difference between the lactate levels in heavy staining and no staining is found (p=0.015). Heavy staining tended to be correlated with higher lactate levels when compared to minor and moderate staining (p=0.081 and p=0.123, respectively).
D: Spearman correlation plot between lactate levels and vessel density showing a significant correlation (p=0.006) with a moderate correlation coefficient (r=0.383). Vessel density is expressed as average number of vessels/mm2.
HIF-1α: Hypoxia Inducible Factor-1α

HIF-1α and Vessel density in plaques

HIF-1α staining was present in 21 sections, 25 sections were negative and 4 sections were excluded from analysis due to poor quality. The positive sections were classified as minor (n=9), moderate (n=5), and heavy (n=7) HIF-1α stained sections. We observed an association between HIF-1α staining (Figure 2A) and lactate levels. Heavy HIF-1α staining was associated with a significant increase in lactate levels (Figure 2C, p=0.015). This difference was mainly evident comparing the sections with no and heavy staining for HIF- 1α. Lactate levels in minor or moderately stained HIF-1α sections did not differ significantly compared to sections with strong HIF-1α staining, although a tendency was observed (p=0.081 and p=0.123, respectively). In each plaque we assessed vessel density and an example of representative staining is shown in figure 2B. Intraplaque vessels were present in 41 sections, 7 sections were negative and 2 sections were excluded from analysis due to poor quality. The mean vessel density was 4.76 ± 4.17 (range 0-15.33) vessels/mm2. Plaque vessel density correlated significantly with lactate levels (Figure 2D, p=0.006, r=0.383).

DISCUSSION

This study showed that plaque lactate levels correlate with intra-plaque microvessel density as well as expression levels of the hypoxia marker; HIF-1α. Atherosclerotic plaque hypoxia may induce plaque angiogenesis. These new microvessels are formed in an inflammatory proteolytic environment and are often leaky, giving the opportunity for erythrocytes and macrophages to extravasate into the plaque, which may lead to intra-plaque hemorrhage (IPH).[2] IPH is a major risk factor for cerebrovascular ischemic events as well as other cardiovascular events, including myocardial infarction.[7, 19] The (early) detection of plaque hypoxia could therefore be of great importance. This is supported by the imaging studies which have been focusing on the visualization of IPH, in carotid and coronary arteries.[19-22]
In the present study we explored a surrogate marker, lactate, which could reflect plaque hypoxia and consequently predict the occurrence of IPH. Under hypoxic conditions, anaerobic glycolysis is maintained by conversion of pyruvate to lactate, a reaction catalysed by lactate dehydrogenase.[23] Active inflammatory cells, macrophages in particular, have a high metabolism and foam cells need even more energy, causing hypoxia and increased lactate production.[24] We did not find a correlation between the number of macrophages and lactate levels, however this may be due to the low number of plaques with significant macrophage staining. The low number of inflammatory plaques is explained by the fact that many of the femoral artery plaques have been occluded prior to surgery. Occlusion is often associated with fibrosis, collagen deposition and less inflammatory cell infiltration.

High lactate levels can instigate increased production of HIF-1α and VEGF, leading to the formation of intra-plaque microvessels.[25] Our results tend to support this theory: high expression of HIF-1α in histological cross-sections correlated with high lactate levels.
In a previous study we have shown that increased plaque vessel density was related to higher event rates during follow-up.[7] In the present study we were not able to find a correlation between event rates and either increased vessel density or lactate levels, likely due to the fact that we included a low number of patients and these were all femoral plaques. In the previous study 818 carotid artery plaques were included. A larger study would be needed to show whether lactate levels could serve as a surrogate for plaque neovascularisation and subsequently predict the occurrence of adverse events.

Our study may have suffered from some limitations. First, our atherosclerotic plaques were analyzed after surgery. During surgery the plaque may have been subjected to trauma (traction, ischemia) which could have resulted in increased lactate levels. However, the procedure within the Athero-Express is standardized and plaque segments are stored in nitrogen directly after excision, this would limit increased hypoxia and the effect would be similar for every plaque. Additionally, Sluimer *et al*. showed that there was no increase in plaque hypoxia/pimonidazole due to the clamping of the artery.[8] Nevertheless, we cannot exclude the possibility that (slightly) higher lactate levels were found when compared to the *in vivo* situation, especially since every patient plaque had a detectable lactate peak. Secondly, this is a descriptive study and a causal relation between lactate, HIF-1α and plaque neovascularization cannot be proven. Thirdly, as mentioned most vessels were occlusive and showed only moderate inflammation. It is therefore unclear whether the results can be extrapolated to patient atherosclerotic vessels that are normally observed in carotid and coronary segments.

There are some issues to resolve before considering the application of ^{1}H-NMR spectroscopy *in vivo*. The biggest hurdle might be that the lactate peak can be obscured by the spectrum of fat. Lactate concentrations are, under normal aerobic metabolism, very low, thus a reasonably big voxel has to be placed over the area of interest, chances are that lipids from within the plaque as well as perivascular fat are included in the voxel.[26] There are some strategies to circumvent this problem[26], and with the rise of high field MRI scanners (such as the 7 Tesla) this problem may be eluded.

Conclusion

^{1}H-NMR spectroscopy may be a valuable tool to identify hypoxic atherosclerotic plaques and could act as a surrogate for plaque vessel density. Since vessel density and intra-plaque hemorrhage have previously been associated with adverse events it could be of interest to consider lactate measurements in follow up studies to assess the value of lactate measurements as a marker for plaque vulnerability.

Funding

This study was funded by Grant NHS2006T106 from the Dutch Heart Foundation.

Conflict of interest

None declared.

1. Michel JB, Virmani R, Arbustini E, Pasterkamp G. Intraplaque haemorrhages as the trigger of plaque vulnerability. Eur Heart J 2011 March 12.

2. Sluimer JC, Kolodgie FD, Bijnens AP, Maxfield K, Pacheco E, Kutys B, Duimel H, Frederik PM, van H, V, Virmani R, Daemen MJ. Thin-walled microvessels in human coronary atherosclerotic plaques show incomplete endothelial junctions relevance of compromised structural integrity for intraplaque microvascular leakage. J Am Coll Cardiol 2009 April 28;53(17):1517-27.

3. Bot I, de Jager SC, Zernecke A, Lindstedt KA, van Berkel TJ, Weber C, Biessen EA. Perivascular mast cells promote atherogenesis and induce plaque destabilization in apolipoprotein E-deficient mice. Circulation 2007 May 15;115(19):2516-25.

4. Kockx MM, Cromheeke KM, Knaapen MW, Bosmans JM, De Meyer GR, Herman AG, Bult H. Phagocytosis and macrophage activation associated with hemorrhagic microvessels in human atherosclerosis. Arterioscler Thromb Vasc Biol 2003 March 1;23(3):440-6.

5. Kolodgie FD, Gold HK, Burke AP, Fowler DR, Kruth HS, Weber DK, Farb A, Guerrero LJ, Hayase M, Kutys R, Narula J, Finn AV, Virmani R. Intraplaque hemorrhage and progression of coronary atheroma. N Engl J Med 2003 December 11;349(24):2316-25.

6. de NR, Verkleij CJ, von der Thusen JH, Jukema JW, van der Wall EE, van Berkel TJ, Baker AH, Biessen EA. Lesional overexpression of matrix metalloproteinase-9 promotes intraplaque hemorrhage in advanced lesions but not at earlier stages of atherogenesis. Arterioscler Thromb Vasc Biol 2006 February;26(2):340-6.

7. Hellings WE, Peeters W, Moll FL, Piers SR, van SJ, Van der Spek PJ, de Vries JP, Seldenrijk KA, De Bruin PC, Vink A, Velema E, de Kleijn DP, Pasterkamp G. Composition of carotid atherosclerotic plaque is associated with cardiovascular outcome: a prognostic study. Circulation 2010 May 4;121(17):1941-50.

8. Sluimer JC, Gasc JM, van Wanroij JL, Kisters N, Groeneweg M, Sollewijn G, Cleutjens JP, van den Akker LH, Corvol P, Wouters BG, Daemen MJ, Bijnens AP. Hypoxia, hypoxia-inducible transcription factor, and macrophages in human atherosclerotic plaques are correlated with intraplaque angiogenesis. J Am Coll Cardiol 2008 April 1;51(13):1258-65.

9. Hulten LM, Olson FJ, Aberg H, Carlsson J, Karlstrom L, Boren J, Fagerberg B, Wiklund O. 15-Lipoxygenase-2 is expressed in macrophages in human carotid plaques and regulated by hypoxia-inducible factor-1alpha. Eur J Clin Invest 2010 January;40(1):11-7.

10. Vink A, Schoneveld AH, Lamers D, Houben AJ, van der GP, van Diest PJ, Pasterkamp G. HIF-1 alpha expression is associated with an atheromatous inflammatory plaque phenotype and upregulated in activated macrophages. Atherosclerosis 2007 December;195(2):e69-e75.

11. Xiong M, Elson G, Legarda D, Leibovich SJ. Production of vascular endothelial growth factor by murine macrophages: regulation by hypoxia, lactate, and the inducible nitric oxide synthase pathway. Am J Pathol 1998 August;153(2):587-98.

12. Constant JS, Feng JJ, Zabel DD, Yuan H, Suh DY, Scheuenstuhl H, Hunt TK, Hussain MZ. Lactate elicits vascular endothelial growth factor from macrophages: a possible alternative to hypoxia. Wound Repair Regen 2000 September;8(5):353-60.

13. Leppanen O, Bjornheden T, Evaldsson M, Boren J, Wiklund O, Levin M. ATP depletion in macrophages in the core of advanced rabbit atherosclerotic plaques in vivo. Atherosclerosis 2006 October;188(2):323-30.

14. Imamura A, Matsuo N, Ariki M, Horikoshi H, Hattori T. MR imaging and 1H-MR spectroscopy in a case of cerebral infarction with transient cerebral arteriopathy. Brain Dev 2004 December;26(8):535-8.

15. Teul J, Ruperez FJ, Garcia A, Vaysse J, Balayssac S, Gilard V, Malet-Martino M, Martin-Ventura JL, Blanco-Colio LM, Tunon J, Egido J, Barbas C. Improving metabolite knowledge in stable atherosclerosis patients by association and correlation of GC-MS and 1H NMR fingerprints. J Proteome Res 2009 December;8(12):5580-9.

16. Verhoeven BA, Velema E, Schoneveld AH, de Vries JP, de Bruin P, Seldenrijk CA, de Kleijn DP, Busser E, van der GY, Moll F, Pasterkamp G. Athero-express: differential atherosclerotic plaque expression of mRNA and protein in relation to cardiovascular events and patient characteristics. Rationale and design. Eur J Epidemiol 2004;19(12):1127-33.

17. Norgren L, Hiatt WR, Dormandy JA, Nehler MR, Harris KA, Fowkes FG. Inter-Society Consensus for the Management of Peripheral Arterial Disease (TASC II). J Vasc Surg 2007 January;45 Suppl S:S5-67.

18. Peeters W, Moll FL, Vink A, Van der Spek PJ, de Kleijn DP, de Vries JP, Verheijen JH, Newby AC, Pasterkamp G. Collagenase matrix metalloproteinase-8 expressed in atherosclerotic carotid plaques is associated with systemic cardiovascular outcome. Eur Heart J 2011 February 2.

19. Singh N, Moody AR, Gladstone DJ, Leung G, Ravikumar R, Zhan J, Maggisano R. Moderate carotid artery stenosis: MR imaging-depicted intraplaque hemorrhage predicts risk of cerebrovascular ischemic events in asymptomatic men. Radiology 2009 August;252(2):502-8.

20. Oei ML, Ozgun M, Seifarth H, Bunck A, Fischbach R, Orwat S, Heindel W, Botnar R, Maintz D. T1-weighted MRI for the detection of coronary artery plaque haemorrhage. Eur Radiol 2010 December;20(12):2817-23.

21. Zhao X, Underhill HR, Zhao Q, Cai J, Li F, Oikawa M, Dong L, Ota H, Hatsukami TS, Chu B, Yuan C. Discriminating Carotid Atherosclerotic Lesion Severity by Luminal Stenosis and Plaque Burden: A Comparison Utilizing High-Resolution Magnetic Resonance Imaging at 3.0 Tesla. Stroke 2010 December 23.

22. King-Im JM, Fox AJ, Aviv RI, Howard P, Yeung R, Moody AR, Symons SP. Characterization of carotid plaque hemorrhage: a CT angiography and MR intraplaque hemorrhage study. Stroke 2010 August;41(8):1623-9.

23. Wigfield SM, Winter SC, Giatromanolaki A, Taylor J, Koukourakis ML, Harris AL. PDK-1 regulates lactate production in hypoxia and is associated with poor prognosis in head and neck squamous cancer. Br J Cancer 2008 June 17;98(12):1975-84.

24. Naghavi M, John R, Naguib S, Siadaty MS, Grasu R, Kurian KC, van Winkle WB, Soller B, Litovsky S, Madjid M, Willerson JT, Casscells W. pH Heterogeneity of human and rabbit atherosclerotic plaques; a new insight into detection of vulnerable plaque. Atherosclerosis 2002 September;164(1):27-35.

25. Hunt TK, Aslam R, Hussain Z, Beckert S. Lactate, with oxygen, incites angiogenesis. Adv Exp Med Biol 2008;614:73-80.

26. Vinitski S, Griffey RH, Szumowski J, Matwiyoff NA. Lactate observation in vivo by spectral editing in real time. Magn Reson Imaging 1988 November;6(6):707-11.

6

PLACD-7T Study: Atherosclerotic Carotid Plaque Components Correlated with Cerebral Damage at 7 Tesla Magnetic Resonance Imaging

Published in part
Current Cardiology Reviews 2011; feb 7: 1: 28-3

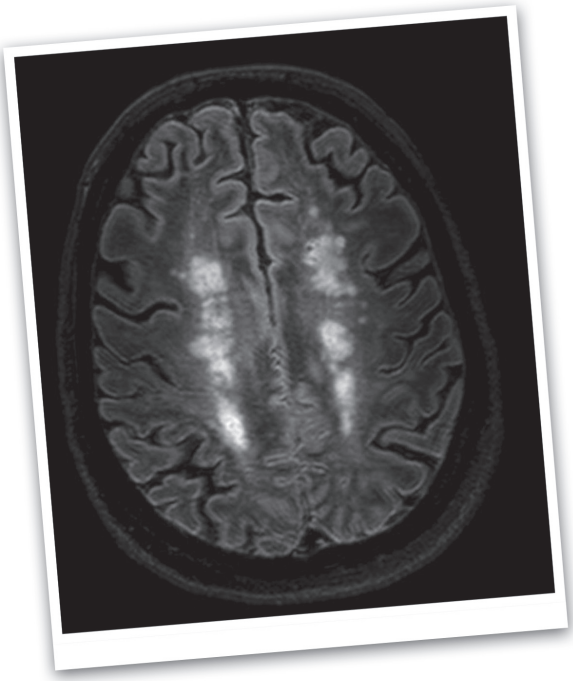

S.M. Bovens[1, 2]*, A.G. den Hartog[3]*, W. Koning[4], F.L. Moll[3], G. Pasterkamp[1], G.J. de Borst [3]*

1 Department of Cardiology, University Medical Center, Utrecht, the Netherlands.
2 Netherlands Heart Institute (ICIN), Utrecht, the Netherlands
3 Department of Vascular Surgery, University Medical Center Utrecht, Utrecht, the Netherlands
4 Department of Radiology, University Medical Center Utrecht, Utrecht, the Netherlands.

* Authors contributed equally to this study

ABSTRACT

Introduction

In patients with carotid artery stenosis plaque composition is associated with plaque stability and with presenting symptomatology. Vulnerable plaque phenotype, composed of inflammatory cell infiltrates, thin fibrous cap and intraplaque hemorrhage is related to higher event rates, due to an increased risk of rupture. Preferentially, plaque vulnerability should be taken into account in pre-operative work-up of patients with severe carotid artery stenosis, to stratify high and low risk plaques and their chance to cause events. However, currently no appropriate and conclusive (non-)invasive technique to differentiate between the high and low risk carotid artery plaque *in vivo* is available. We propose that 7 Tesla human high resolution MRI scanning will visualize carotid plaque characteristics more precisely and will enable correlation of these specific components with cerebral damage.

Study objective

The aim of the PlaCD-7T study is to correlate 7T imaging with carotid plaque histology (gold standard). In addition, we correlated plaque characteristics with cerebral damage, reflected by clinically silent cerebral (micro) infarcts or bleeds, on 7 Tesla high resolution (HR) MRI.

Design

We propose a single center prospective study for either symptomatic or asymptomatic patients with haemodynamic significant (≥70%) stenosis of at least one of the carotid arteries. The Athero-Express (AE) biobank histological analysis will be derived according to standard protocol. Patients who are included undergo a pre-operative 7 Tesla HR-MRI scan of both the head and neck area.

Preliminary results

In this ongoing study, we were able to visualize the plaques in the T2w images in the first included patients. T1w (FLAIR) brain images clearly depicted infarcted areas. Quantitative and semi-quantitative analysis have not been performed yet. Histology showed visualization of several plaque components, such as lipid-rich necrotic core (LRNC), collagen, calcifications, and thrombus. Correlation studies of histology and MR images have to be performed to evaluate the value of 7 Tesla MR imaging of atherosclerotic lesion.

Discussion

We hypothesize that the 7 Tesla MRI scanner will allow early identification of high risk carotid plaques being associated with micro infarcted cerebral areas, and will thus be able to identify patients with a high risk of peri-procedural stroke, by identification of surrogate measures of increased cardiovascular risk.

BACKGROUND

Ipsilateral carotid stenosis of 50% or more is found in approximately 10% of carotid territory ischemic strokes and approximately 15% of transient ischemic attacks (TIAs). Additionally, it is associated with a high risk of recurrent stroke.[1, 2] Current treatment of symptomatic patients with carotid stenosis is based on stenosis grade alone, where stenosis ≥70% is an indication for carotid endarterectomy (CEA). Plaque morphology is not yet included in this clinical decision, although it plays an important role as it is found to be directly correlated with the risk of embolism and progression to occlusion, thus resulting in cerebral ischaemia.[3] Patients with a stenosis <70% are generally not eligible for surgery although they might have a plaque phenotype which is at risk for rupture. Thrombo-embolic events, caused by (a) (ruptured) atherosclerotic carotid plaque(s), can cause a TIA or ischemic stroke. Carotid plaque phenotype is a major independent determinant of the clinical outcome after CEA, while plaque composition is related to clinical presentation, gender, age and time interval between most ischemic symptoms and CEA.[4-9]

Athero-Express[10] (AE; plaque biobank) studies have previously shown that certain compositions of the atherosclerotic plaque are associated with pre- and postoperative cerebral embolisation measured with Trans Cranial Doppler (TCD). Clinically, patients with a more inflamed plaque showed more embolisation[11], and the composition of the atherosclerotic plaque was associated with repeated cerebral infarcts after surgery.[12] In addition, patients with a fibrotic plaque had a lower risk for recurrent TIA or stroke than patients with a more lipid-rich plaque.[3] In the same study during three years follow-up it was found that a high rate of neovasculature with intraplaque hemorrhage (IPH) was a strong predictor for cardiovascular events elsewhere in the vascular tree. Thus, the classically defined measures for plaque vulnerability (plaque bleeding, large lipid cores and local inflammation) were all related with adverse outcomes peri-operatively as well as during follow up.

These plaque components were all found in patients who underwent CEA to remove the atherosclerotic plaque. However, the data suggest that plaque phenotype is of utmost importance to identify patients with high-risk plaques, regardless of the degree of stenosis.

Identification of these high-risk patients, preferably with minimally invasive techniques such as MRI, could lead to different peri- and postoperative monitoring of CEA patients as well as the monitoring of patients who are not eligible for CEA. In the future this could lead to a different selection of patients who will benefit from plaque removal.

MRI has the capability to visualize plaque characteristics in the stenotic carotid artery. Several preliminary studies, both *ex vivo* and *in vivo*, have been performed to assess the possibility of plaque imaging with MRI.[13-20]

Ultimately we aim that HR 7 Tesla diagnostic accuracy will be valuable in clinical decision making by differentiating low risk and high risk patients and thereby determining which patients benefit most from revascularization. This prognostic study could ultimately lead to the addition of a 7 Tesla HR-MRI scan to differentiate low risk and high risk patients.

Ex vivo MRI plaque studies

In an *ex vivo* study using dissected human carotid arteries (autopsy material), plaque components were evaluated using different HR-MRI weightings at 9.4 Tesla (vertical Bruker system). The outcome of this study suggested that HR-MRI is able to visualize several plaque characteristics, which were previously related with increased embolisation and repeated stroke. Multi-weighted MRI sequences could identify

calcified regions, lipid area, foam cell area, IPH, neovasculature and the fibrous cap.[21] Although this study was performed on autopsy material (no flow effects of blood) and in a high magnetic field, it gives information regarding components that can be visualized with the 7 Tesla human MRI scanner, whereas this might be more challenging if not impossible in a lower field MRI scanner. Several other *ex vivo* studies on human MRI scanners (1.5 Tesla) have been performed on atherosclerotic plaques obtained from CEA.[13, 14] Both studies found sensitivity values ranging from 60-97% to 72-98% for fibrous tissue, necrosis, calcification and for loose connective tissue. Specificity varied from 75%-98% to 74%-99% in the same plaque characteristics.

In vivo MRI plaque studies

Several human *in vivo* studies investigated 1.5 and 3 Tesla MRI as a tool to accurately determine plaque components, sometimes with histology as a reference.[15-20] For example, one study revealed sensitivity and specificity of 84%, a negative predictive value of 70%, and a positive predictive value of 93% of direct thrombus imaging with MRI, with histology as the gold standard. This would suggests that MRI can accurately determine plaque components with an 1.5 Tesla MRI scanner.[17] However, these studies merit careful consideration. The resolution of the 1.5 Tesla scanner is very limited and although the 3 Tesla scanner already has a higher resolution, for example imaging of large IPH and thin/ruptured fibrous cap is possible[17], moderate IPH is difficult to detect. In addition, up to now it has not been possible to discriminate between IPH and intra-plaque lipid. The latter is of great interest since recent studies have shown that IPH and not intra-plaque lipid is related with adverse events during follow up.[3]
In summary, appreciating the limitations of the above reported study methods and lower resolution of the current MRI scanners, it is valuable to perform an *in vivo* study with the 7 Tesla scanner to optimize the relevance of plaque characterization. In the present article we describe the protocol of our study designed to determine the relation between carotid plaque characteristics and cerebral damage by 7 Tesla HR-MRI. To our knowledge this is the first study that investigates the association between MR imaging features and histological characteristics relation with a 7 Tesla MRI scanner.

Study objective

We are conducting a single center, prospective, observational study, using a 7 Tesla MRI scanner (Philips Healthcare, Cleveland, OH, USA). The primary objective of PlaCD-7T is to compare 7T HR-imaging with carotid plaque histology (gold standard). Our secondary objective is to correlate plaque characteristics with cerebral damage ((clinically silent) cerebral (micro) infarcts or bleeds) on 7 Tesla HR-MRI.
Histology is being performed to compare the *ex vivo* specimen with the *in vivo* images. Only one pre-operative HR-MRI scan is added to the standard work-up of CEA patients in our hospital.

MRI 7.0 Tesla scanner

Seven Tesla MRI benefits from a high intrinsic Signal-to-Noise Ratio (SNR) compared to MRI with lower field strengths. The gain in SNR can be expressed in shorter scan times as well as higher resolution. Above that, different contrast mechanisms due to changed magnetic parameters in the tissues may lead to higher sensitivities for certain contrasts. For example, susceptibility differences are greater at 7 Tesla as well as the differences in chemical shift and relaxation times between different tissues. Also, higher resolution imaging suffers less from partial volume effects, enabling the visualization of more detailed structures. More and more research is being done to explore this potential of 7 Tesla MRI.[22, 23] High field MR (plaque) imaging with 7 Tesla may allow plaque

characterization and localization of cerebral damage with a higher resolution and more detail than imaging at lower field strengths. For instance, not only obvious cerebral ischemic lesions can be found, but also micro-bleeds, micro-infarcts and clinically silent ischemic lesions can also be visualized, currently not possible with 1.5 Tesla or 3 Tesla MRI.[23]

The main reason for imaging patients scheduled for CEA at 7 Tesla is the high resolution and high contrast brain scan. Since we would like to correlate cerebral damage to specific plaque components it is of importance to have superior image quality of the brain. At the moment a few human studies at 7 Tesla have successfully been performed and published. [24-27] In addition, hypothetically, plaque imaging with 7 Tesla MRI could provide more detailed images of the plaque components. The 1.5 and 3 Tesla MRI may lack some discriminative power to assess plaque characteristics that correlate with risk for future manifestations of the disease. However, even if 7 Tesla MRI is not capable of discriminating more components in plaque compared to 3 Tesla MRI, the addition of the 7 Tesla brain imaging will provide new insights into the pathogenesis of cerebral damage as a result of plaque composition. Apart from these new insights, when this study shows that micro-infarctions, micro-embolisations or plaque characteristics can be visualized with these 7 Tesla MRI scans, then subsequent studies might be performed to establish the value of non-invasive MRI scanning in pre-operative work-up in patients with carotid artery stenosis.

Study design

This is an observational study. First of all, patients with a stenosis ≥70% of the carotid artery visit the vascular surgeon or neurologist in our hospital. Subsequently these patients are discussed in our multidisciplinary vascular meeting (vascular surgeons, neurologists, radiologists). When eligible for CEA, the patient are included via the vascular surgeon in the AE study as well as the PlaCD-7T study. The majority of the patients will be symptomatic (TIA or stroke). However, a minority of asymptomatic patients with a haemodynamically significant stenosis >80% of the carotid artery and planned to be scheduled for a CEA will be eligible for inclusion in this study as well. Pre-operative (~1 day) the included patients are scheduled for an MRI scan of the brain and carotid artery in the 7 Tesla MRI scanner. Anatomical scans of the brain are evaluated for the presence of cerebral damage. In the carotid artery, MRI images with several contrast weightings are acquired for plaque visualization and characterization. A contrast agent (gadolinium (Gadovist®)) will be injected to assess neovascularisation, intra-plaque hemorrhage and inflammation, In future patients, after the correct sequences have been evaluated. The investigation takes approximately 75 minutes. Images are stored and during off line analyses the bifurcation of the carotid artery is used as an anatomical landmark.

Patient Population

All indications for surgery are reviewed by a multidisciplinary vascular team.[10] All patients are examined by a neurologist pre-operatively and postoperatively to document cerebrovascular symptom status and to record any new neurological deficits after CEA. Percentage stenosis of both carotid arteries is recorded with duplex ultrasound pre-operatively following internationally accepted guidelines.[28] A flowchart of the study protocol is shown in Figure 1. Baseline characteristics of included patients is collected by the AE investigators and include standard baseline characteristics together with known risk factors of cardiovascular disease. It is important to state that besides one MRI scan, patients receive the regular work-up, treatment, and follow-up according to the current guidelines for treatment of carotid artery disease.

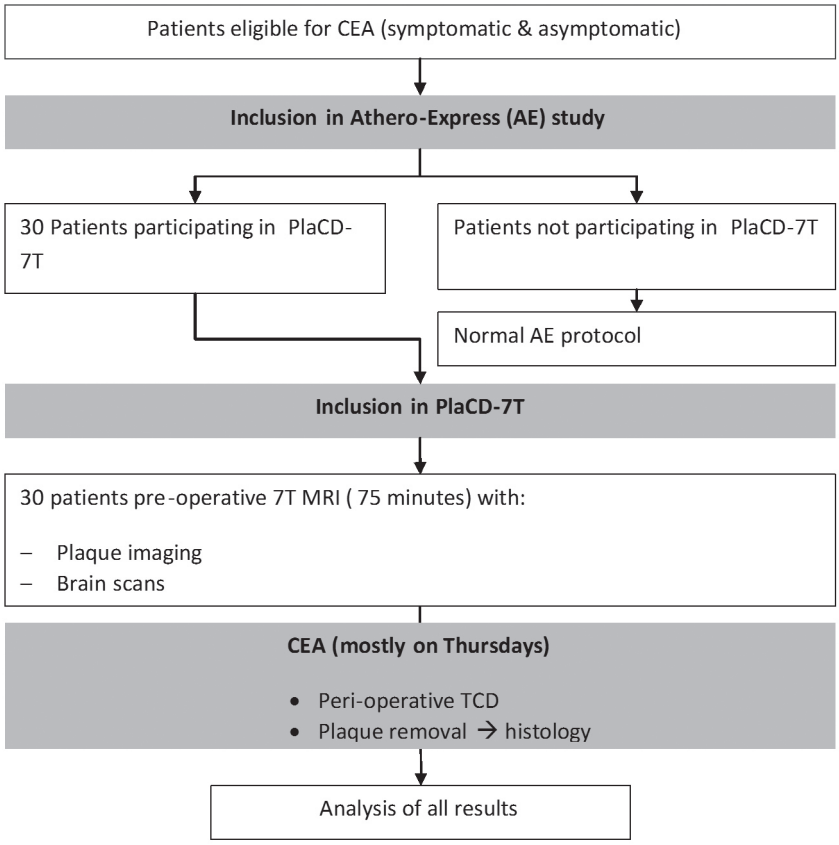

Figure 1 | *Simplified flowchart of study protocol.*

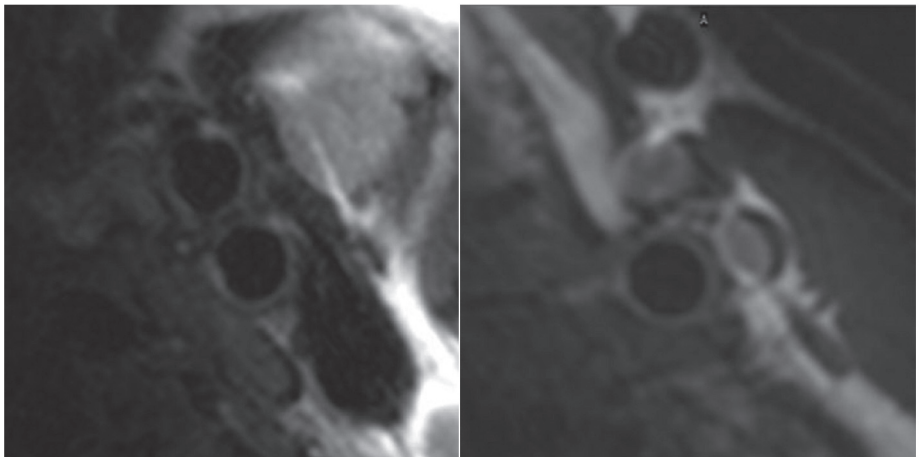

Figure 2 | *Imaging examples of the carotid artery.*
Images made with 7 Tesla MRI in a healthy individual, acquired with a 4 channel transceiver coil (Machnet B.V., Eelde, The Netherlands).

Athero-Express Biobank

AE is an ongoing longitudinal study that includes patients undergoing CEA. The study design has been reported earlier.[10] In our study gold standard for plaque characterization is the histopathological analysis of the removed carotid artery plaque according to the standardized AE protocol. The segment with the largest plaque burden (the culprit lesion) is located and fixated in formalin for histological analysis. This analysis is routinely performed and intra- and inter-observer analyses are excellent and have been reported in international literature previously.[29] After surgery, the patients undergo normal clinical follow-up with duplex to assess procedural restenosis and to fill out questionnaires addressing the occurrence of relevant cardiovascular symptoms. All patients undergoing CEA in one participating center (University Medical Center Utrecht) are asked to participate in this study. The medical ethics board of the University Medical Center Utrecht approved the study, and all participants of this study must provide written informed consent.

Scan protocol

The total MRI examination including MR plaque imaging and anatomical MRI of the brain takes approximately 75 minutes. A dedicated RF coil is used for imaging of the carotid bifurcation. This coil allows for sub-millimeter resolution imaging of the carotid lumen, vessel wall and atherosclerotic plaque. First, the carotid bifurcation is identified by means of MR angiography without contrast material enhancement. Subsequently, several transverse images are obtained from several millimeters caudal to several millimeters cranial of the carotid bifurcation, imaging the complete plaque. This area is imaged using specific sequences to obtain different contrast weightings for optimal discrimination of plaque components. Next, post-contrast images after intravenous injection of gadolinium will be obtained, in future patients, when the sequences are evaluated. Additionally, anatomical MR brain imaging of cerebral damage is performed; 3D FLAIR and T2w images are acquired using the head coil. Two MRI readers blinded to the histo-pathological results and clinical data score the MRI plaque status independently.

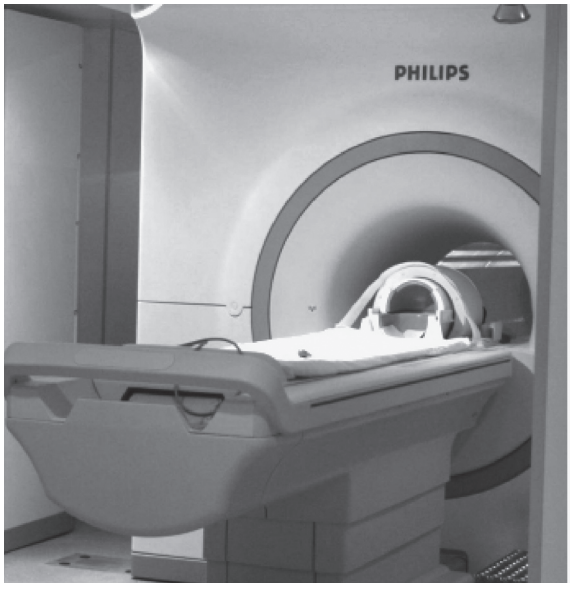

Figure 3 | *Procedural set-up in 7 Tesla scanner.*

Carotid Endarterectomy

Pre-operatively, patients start with aspirin, except those patients taking already oral anticoagulants for other indications. For these patients dipyridamol 2dd200mg is be added. Patients with aspirin intolerance receive plavix 75mg. Before exposure of the carotid artery, patients receive 5000 U of heparin intravenously. With the use of a standardized CEA technique, the plaque is carefully dissected and removed *in toto*, without procedure-related complications. Immediately after dissection, the plaque will is transferred to the laboratory.

Histology

The atherosclerotic plaque is first decalcified in an EDTA solution (2 weeks), sliced at several loci, embedded in paraffin, and stained for presence of collagen (Sirius red), macrophages (CD68), smooth muscle cells (α-actin), lipid, thrombus and endothelium (CD34, microvessels or neovasculature).
This analysis is routinely performed and intra- and inter-observer analyses are excellent and have been reported in international literature previously.[28] Histology is assessed by an experienced pathologist blinded to the MRI results.

Sample size

In a previous study we observed a >100% increase in peri-operative stroke when a lipid rich plaque was obtained compared to plaques that were fibrous.[3] A major endpoint was reached in 9% when a lipid rich lesion was evident but 2.5% when a fibrous lesion was present. We expect to observe cerebral micro-infarcted areas in 33% of the patients. This data is based on the article of Verhoeven *et al*.[11] In this study TCD was used to measure micro embolism. In 27% of the patients an event was registered before or during surgery. We expect the 7 Tesla system to be sensitive enough to find micro infarcts as a result of micro embolism. The power analysis is based on the calculation of the differences between two groups of a continuous variable. A 3-fold detection increase from 1 to 3 micro embolisms or 1 versus 3 micro infarcts with an SD of 2, an α of 0.05 and β of 0.80 we calculate that we will need 2 groups of 14 patients. Therefore we asked and received permission to include 30 patients. We do not expect a normal distribution.

Data analysis

MR images are processed with dedicated software, with this software component size and intensity on images can be calculated. Histology is semi-quantitatively scored as previously described.[3, 10] Cerebral damage ((clinically silent) cerebral (micro) infarcts or bleeds) are depicted as a semi-quantitative measure (no, small, major defects). Micro-embolisation are assessed as a continuous variable.
The different identified plaque components are correlated with cerebral damage by calculating the regular parameters for diagnostic testing (positive predictive value, negative predictive value, sensitivity, specificity).

Ethical consideration

This study has been approved by the local Medical Ethics Committee of the University Medical Center in Utrecht.

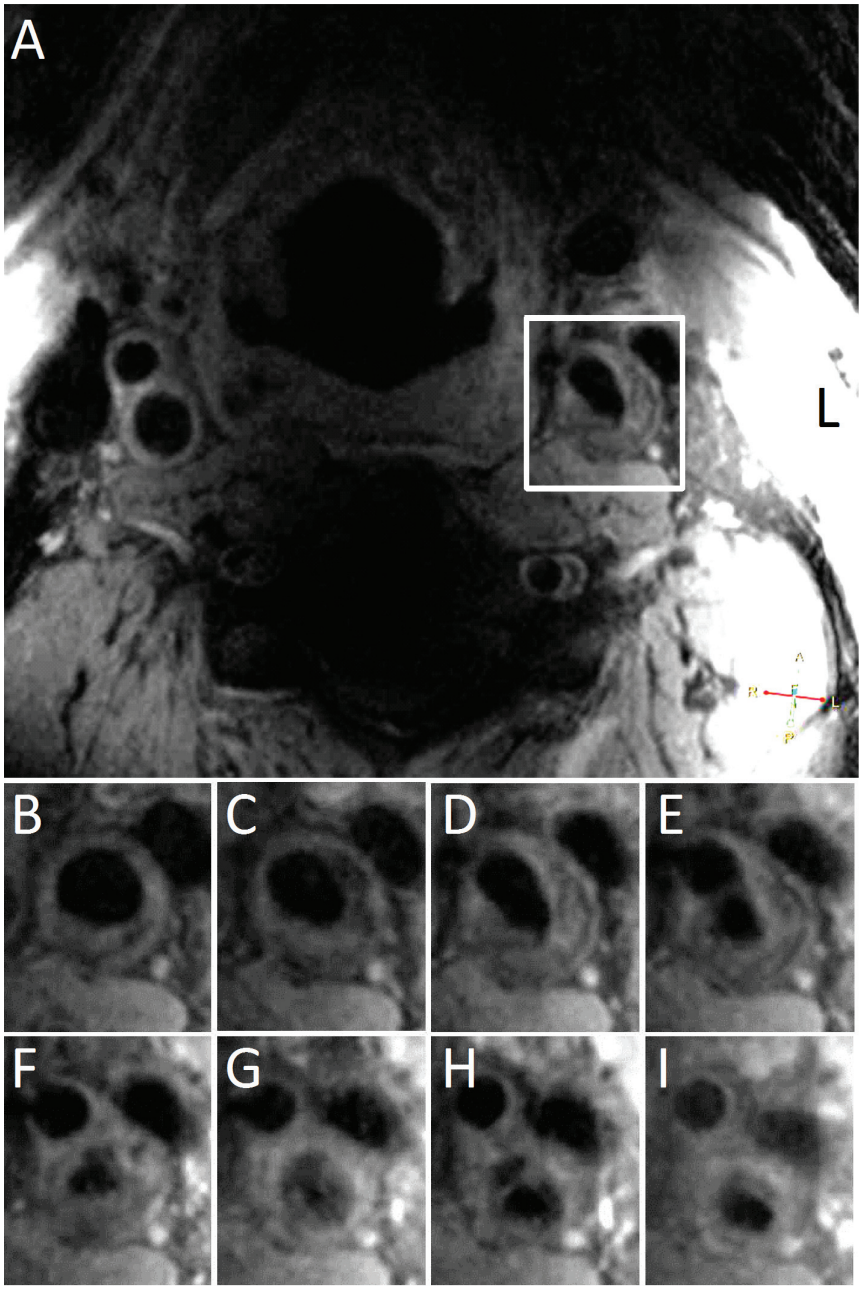

Figure 4 | *Imaging examples of an atherosclerotic plaque (T2W) in a patient*
Overview scan of neck area with the left carotid artery outlined in the white box (A). Zoomed images (B-I) of the left carotid artery at different levels showing plaque, from common carotid artery to bifurcation.

Preliminary results

So far, 7 patients have been included in this study and in all patients T1w 3D FLAIR brain scans as well as T2w/PDW carotid artery scans have been acquired. From patient 6 on, an additional T1w sequence for the carotid artery was included in the standard MR protocol. In Figure 4 T2w scans of an atherosclerotic lesion in the left carotid artery are shown, Figure 4A illustrates the culprit lesion and from Figure 4B to 4I the entire plaque is shown, proximal to distal. Figure 5 shows examples of 2 different patients with major (A+B) and minor (C+D) cerebral infarctions. This is an ongoing study and therefore cerebral damage has not been correlation with atherosclerotic plaque components yet.

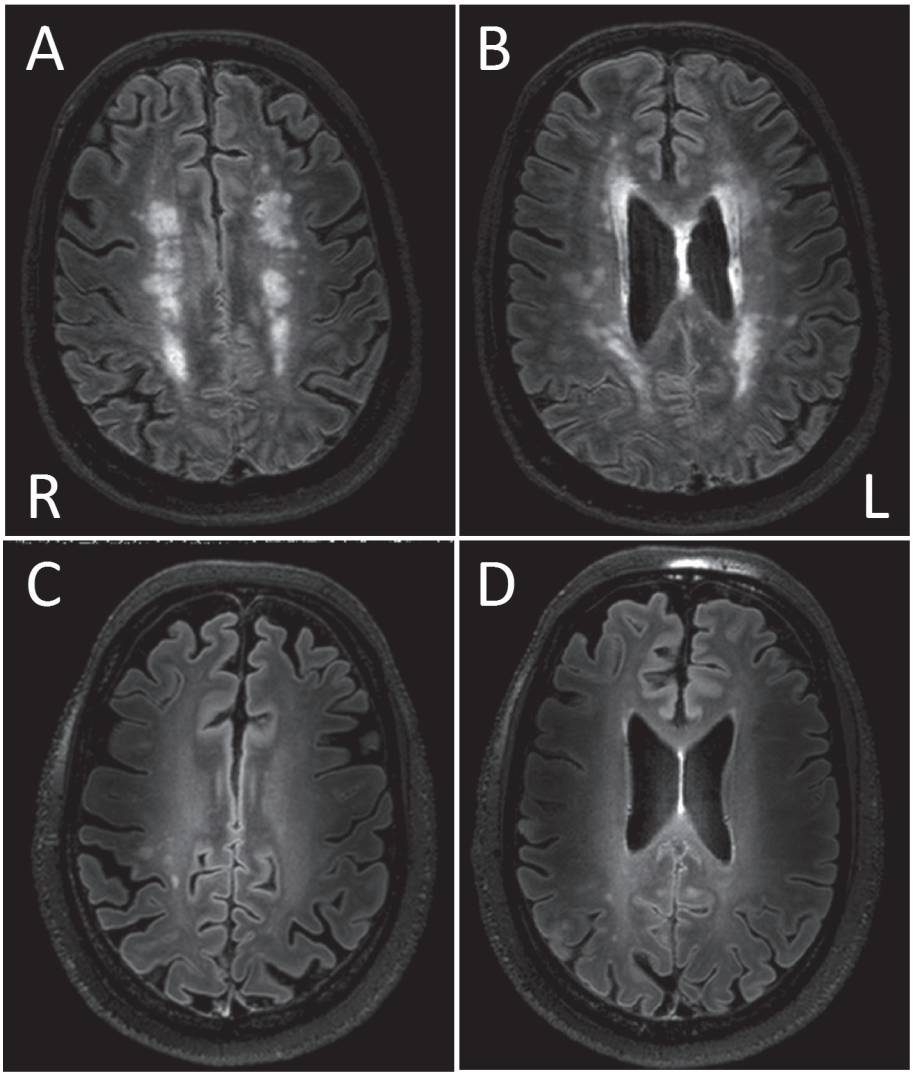

Figure 5 | *Imaging examples of the brain in 2 different patient*
A/B: throughout the entire brain infarcted areas can be seen (in white). C/D: another patient only has a few small infarcted areas

DISCUSSION

We present the protocol and first preliminary results of a single center, observational study to determine the relation of plaque characteristics with cerebral damage ((clinically silent) cerebral (micro) infarcts or bleeds) with 7 Tesla HR-MRI. As gold standard histology of the plaques is obtained according to the protocol of the AE biobank.

The interpretation of outcome in earlier studies imaging the carotid plaque and using histology as reference standard is complicated by the differences in histology methods, difference in the magnetic field strength of the MRI scanners and in scanning protocols (sequences).

In previous *ex vivo* studies some limitation are apparent when translation their results to *in vivo* MRI. First, there is no blood flow, thus no triggering is needed and no flow artifacts are seen. Additionally, artifacts caused by swallowing are also absent. Second, the RF coil is placed very close to the plaque, creating higher signal intensities compared to *in vivo* measurements.

There are also some limitations in current *in vivo* MR studies, mostly performed on lower field 1.5 Tesla and some on 3 Tesla scanners. First, it is difficult to discriminate between IPH and intraplaque lipid. Second, *in vivo*, the length of the neck and depth of the carotid artery are main determinants of image quality. Some sequences, which can give excellent contrast between components *ex vivo*, are not applicable *in vivo*, due to timing of the sequence or due to limited total scan time of the patient. Third, there are currently several studies performed, however, it is difficult to draw conclusions of all these studies together, mainly due to differences in MRI and histology protocols.

Some of these limitation will still stand, however, we believe the 7 Tesla MR scanner has some distinct advantages compared to the lower field scanners. First, is has been shown that the 7 Tesla has superior brain imaging.[27] Second, the possibility to increase the resolution when imaging the atherosclerotic plaque might reveal structures that are hidden by partial volume effects. Third, a higher sensitivity for certain contrast mechanisms (e.g. susceptibility weighted imaging or Ultra short TE imaging (UTE)) will possibly allow detection of plaque components that are hard to detect with lower field strengths, like IPH).

Several studies have focused on the identification of atherosclerotic plaque components by means of MRI to identify patients at risk for strokes or TIAs.[15-20] Components such as large lipid pools, thin fibrous caps, IPH are the main focus points due to the increased risk of plaque rupture. One of the components that is of importance and has been correlated with cardiovascular and cerebrovascular events is microvasculature in the plaque.[3] However, this component is very small (the same holds true for mild/moderate IPH) and needs an imaging modality with a high spatial resolution and anatomical detail such as the 7 Tesla scanner can provide. In addition, the 7 Tesla scanner is superior in the detection of micro-infacts and/or bleeds in the brain.[27] Combining this information with the HR-MRI of the atherosclerotic plaque, as described in this protocol, we believe this can give new insights and possibly lead to new standardized protocols for patient work-up before CEA.

Conclusion

We hypothesize that 7 Tesla HR-MRI will allow more detailed visualization of the brain, and is expected to determine the carotid plaque components more precisely. Therefore, in our opinion, this is the right modality to correlate brain imaging with carotid plaque characteristics. The AE biobank allows us to use histology as a validated reference according to standardized Athero-Express protocol.

The first patient was included on May 25th, 2011 in the University Medical Center in Utrecht.

Trial collaborators

Collaborators of this study (all located in the University Medical Center Utrecht, The Netherlands) are: (in alphabetical order):
G.J.de Borst, MD, PhD, vascular surgeon
S.M.Bovens, MSc, PhD student
A.G.den Hartog, MD, PhD student vascular surgery
J.Hendrikse, MD, PhD, radiologist
LJ Kappelle MD, PhD, Professor Neurology
D.J.W. Klomp, PhD, assistent professor Functional Medical Imaging
W.Koning, MSc, PhD student
P.Luijten, MD, PhD, Professor radiology
F.L.Moll, MD, PhD, Professor vascular surgery
G.Pasterkamp, MD, PhD, Professor experimental Cardiology
A.Vink, MD, PhD, pathologist
H.B. van der Worp, MD, PhD, neurologist

ABBREVIATIONS

CEA	carotid endarterectomy
HR	high resolution
AE	athero-express
DWI	diffusion weighted imaging
IPH	intra-plaque haemorrhage
FLAIR	fluid attenuation inversion recovery
MRI	magnetic resonance imaging
RF	radio frequency
SMC	smooth muscle cells
SWI	susceptibility weighted imaging
T1W	T1 weighted
TCD	Trans Cranial Doppler

Conflict of interest

None declared

Acknowledgments

S.M. Bovens' work was funded by the Netherlands Heart Foundation (2006T106 to SB).

1. Lovett JK, Coull AJ, Rothwell PM. Early risk of recurrence by subtype of ischemic stroke in population-based incidence studies. Neurology 2004 February 24;62(4):569-73.

2. Fairhead JF, Mehta Z, Rothwell PM. Population-based study of delays in carotid imaging and surgery and the risk of recurrent stroke. Neurology 2005 August 9;65(3):371-5.

3. Hellings WE, Peeters W, Moll FL, Piers SR, van SJ, Van der Spek PJ, de Vries JP, Seldenrijk KA, De Bruin PC, Vink A, Velema E, de Kleijn DP, Pasterkamp G. Composition of carotid atherosclerotic plaque is associated with cardiovascular outcome: a prognostic study. Circulation 2010 May 4;121(17):1941-50.

4. Carr S, Farb A, Pearce WH, Virmani R, Yao JS. Atherosclerotic plaque rupture in symptomatic carotid artery stenosis. J Vasc Surg 1996 May;23(5):755-65.

5. Hellings WE, Pasterkamp G, Verhoeven BA, de Kleijn DP, de Vries JP, Seldenrijk KA, van den BT, Moll FL. Gender-associated differences in plaque phenotype of patients undergoing carotid endarterectomy. J Vasc Surg 2007 February;45(2):289-96.

6. Peeters W, Hellings WE, de Kleijn DP, de Vries JP, Moll FL, Vink A, Pasterkamp G. Carotid atherosclerotic plaques stabilize after stroke: insights into the natural process of atherosclerotic plaque stabilization. Arterioscler Thromb Vasc Biol 2009 January;29(1):128-33.

7. Redgrave JN, Lovett JK, Gallagher PJ, Rothwell PM. Histological assessment of 526 symptomatic carotid plaques in relation to the nature and timing of ischemic symptoms: the Oxford plaque study. Circulation 2006 May 16;113(19):2320-8.

8. van Oostrom O, Velema E, Schoneveld AH, de Vries JP, de BP, Seldenrijk CA, de Kleijn DP, Busser E, Moll FL, Verheijen JH, Virmani R, Pasterkamp G. Age-related changes in plaque composition: a study in patients suffering from carotid artery stenosis. Cardiovasc Pathol 2005 May;14(3):126-34.

9. Verhoeven B, Hellings WE, Moll FL, de Vries JP, de Kleijn DP, de BP, Busser E, Schoneveld AH, Pasterkamp G. Carotid atherosclerotic plaques in patients with transient ischemic attacks and stroke have unstable characteristics compared with plaques in asymptomatic and amaurosis fugax patients. J Vasc Surg 2005 December;42(6):1075-81.

10. Verhoeven BA, Velema E, Schoneveld AH, de Vries JP, de Bruin P, Seldenrijk CA, de Kleijn DP, Busser E, van der GY, Moll F, Pasterkamp G. Athero-express: differential atherosclerotic plaque expression of mRNA and protein in relation to cardiovascular events and patient characteristics. Rationale and design. Eur J Epidemiol 2004;19(12):1127-33.

11. Verhoeven BA, de Vries JP, Pasterkamp G, Ackerstaff RG, Schoneveld AH, Velema E, de Kleijn DP, Moll FL. Carotid atherosclerotic plaque characteristics are associated with microembolization during carotid endarterectomy and procedural outcome. Stroke 2005 August;36(8):1735-40.

12. Verhoeven BA, Pasterkamp G, de Vries JP, Ackerstaff RG, de Kleijn D, Eikelboom BC, Moll FL. Closure of the arteriotomy after carotid endarterectomy: patch type is related to intraoperative microemboli and restenosis rate. J Vasc Surg 2005 December;42(6):1082-8.

13. Clarke SE, Hammond RR, Mitchell JR, Rutt BK. Quantitative assessment of carotid plaque composition using multicontrast MRI and registered histology. Magn Reson Med 2003 December;50(6):1199-208.

14. Fabiano S, Mancino S, Stefanini M, Chiocchi M, Mauriello A, Spagnoli LG, Simonetti G. High-resolution multicontrast-weighted MR imaging from human carotid endarterectomy specimens to assess carotid plaque components. Eur Radiol 2008 December;18(12):2912-21.

15. Alizadeh DR, Doornbos J, Tamsma JT, Stuber M, Putter H, van der Geest RJ, Lamb HJ, de RA. Assessment of the carotid artery by MRI at 3T: a study on reproducibility. J Magn Reson Imaging 2007 May;25(5):1035-43.

16. Kerwin W, Xu D, Liu F, Saam T, Underhill H, Takaya N, Chu B, Hatsukami T, Yuan C. Magnetic resonance imaging of carotid atherosclerosis: plaque analysis. Top Magn Reson Imaging 2007 October;18(5):371-8.

17. Ota H, Yu W, Underhill HR, Oikawa M, Dong L, Zhao X, Polissar NL, Neradilek B, Gao T, Zhang Z, Yan Z, Guo M, Zhang Z, Hatsukami TS, Yuan C. Hemorrhage and large lipid-rich necrotic cores are independently associated with thin or ruptured fibrous caps: an in vivo 3T MRI study. Arterioscler Thromb Vasc Biol 2009 October;29(10):1696-701.

18. Moody AR, Murphy RE, Morgan PS, Martel AL, Delay GS, Allder S, MacSweeney ST, Tennant WG, Gladman J, Lowe J, Hunt BJ. Characterization of complicated carotid plaque with magnetic resonance direct thrombus imaging in patients with cerebral ischemia. Circulation 2003 June 24;107(24):3047-52.

19. Cappendijk VC, Cleutjens KB, Kessels AG, Heeneman S, Schurink GW, Welten RJ, Mess WH, Daemen MJ, van Engelshoven JM, Kooi ME. Assessment of human atherosclerotic carotid plaque components with multisequence MR imaging: initial experience. Radiology 2005 February;234(2):487-92.

20. Yuan C, Kerwin WS, Ferguson MS, Polissar N, Zhang S, Cai J, Hatsukami TS. Contrast-enhanced high resolution MRI for atherosclerotic carotid artery tissue characterization. J Magn Reson Imaging 2002 January;15(1):62-7.

21. Te Boekhorst BC, van 't KR, Bovens SM, van de Kolk KW, Cramer MJ, van Oosterhout MF, Doevendans PA, van der Geest RJ, Pasterkamp G, van Echteld CJ. Evaluation of multicontrast MRI including fat suppression and inversion recovery spin echo for identification of intra-plaque hemorrhage and lipid core in human carotid plaque using the mahalanobis distance measure. Magn Reson Med 2011 October 13.

22. Snyder CJ, DelaBarre L, Metzger GJ, Van De Moortele PF, Akgun C, Ugurbil K, Vaughan JT. Initial results of cardiac imaging at 7 Tesla. Magn Reson Med 2009 March;61(3):517-24.

23. Zwanenburg JJ, Hendrikse J, Visser F, Takahara T, Luijten PR. Fluid attenuated inversion recovery (FLAIR) MRI at 7.0 Tesla: comparison with 1.5 and 3.0 Tesla. Eur Radiol 2010 April;20(4):915-22.

24. Pfeuffer J, Adriany G, Shmuel A, Yacoub E, Van De Moortele PF, Hu X, Ugurbil K. Perfusion-based high-resolution functional imaging in the human brain at 7 Tesla. Magn Reson Med 2002 May;47(5):903-11.

25. Yacoub E, Shmuel A, Pfeuffer J, Van De Moortele PF, Adriany G, Andersen P, Vaughan JT, Merkle H, Ugurbil K, Hu X. Imaging brain function in humans at 7 Tesla. Magn Reson Med 2001 April;45(4):588-94.

26. Vaughan JT, Garwood M, Collins CM, Liu W, DelaBarre L, Adriany G, Andersen P, Merkle H, Goebel R, Smith MB, Ugurbil K. 7T vs. 4T: RF power, homogeneity, and signal-to-noise comparison in head images. Magn Reson Med 2001 July;46(1):24-30.

27. Pfeuffer J, Van De Moortele PF, Yacoub E, Shmuel A, Adriany G, Andersen P, Merkle H, Garwood M, Ugurbil K, Hu X. Zoomed functional imaging in the human brain at 7 Tesla with simultaneous high spatial and high temporal resolution. Neuroimage 2002 September;17(1):272-86.

29. Hellings WE, Pasterkamp G, Vollebregt A, Seldenrijk CA, de Vries JP, Velema E, de Kleijn DP, Moll FL. Intraobserver and interobserver variability and spatial differences in histologic examination of carotid endarterectomy specimens. J Vasc Surg 2007 December;46(6):1147-54.

28. Grant EG, Benson CB, Moneta GL, Alexandrov AV, Baker JD, Bluth EI, Carroll BA, Eliasziw M, Gocke J, Hertzberg BS, Katanick S, Needleman L, Pellerito J, Polak JF, Rholl KS, Wooster DL, Zierler RE. Carotid artery stenosis: gray-scale and Doppler US diagnosis--Society of Radiologists in Ultrasound Consensus Conference. Radiology 2003 November;229(2):340-6.

7

Negative MR Contrast caused by USPIO uptake in lymph nodes may lead to false positive observations with in vivo visualization of murine atherosclerotic plaque

Published:
Atherosclerosis. 2010 May; 210(1): 122-9

Bernard C.M. te Boekhorst[1,2], Sandra M. Bovens[1,2], Marcel G.J. Nederhoff[1,2], Kees W.A. van de Kolk[1], Maarten J.M. Cramer[1], Matthijs F.M. van Oosterhout[3,4], Michiel ten Hove[1], Pieter A.F. Doevendans[1], Gerard Pasterkamp[1], Cees J.A. van Echteld[1]

1 Department of Cardiology, University Medical Center, Utrecht, the Netherlands.
2 Netherlands Heart Institute (ICIN), Utrecht, the Netherlands
3 Department of Pathology, University Medical Center Utrecht, Utrecht, the Netherlands
4 Department of Pathology, Antonius Medical Center, Nieuwegein, the Netherlands

ABSTRACT

Background

USPIO are used clinically as a contrast agent for magnetic resonance imaging (MRI) of lymph nodes, and in research settings for MRI of macrophages in atherosclerotic lesions. However, T2* weighted (T2*w) imaging can lead to "blooming" with overestimation of the area occupied by USPIO. In this study, plaque uptake of USPIO in atherosclerotic mice was investigated in the presence and absence of circulating monocytes. The influence of peri-aortic lymph node uptake on the interpretation of T2*w images of the aortic wall was studied.

Method

Atherosclerotic mice were fed an atherogenic diet and were randomized to total body irradiation or non-irradiation. After 2 days, T2*w MRI of the abdominal aorta was performed, followed by intravenous administration of 100 µmol/kg USPIO (t=0). At t=3 and 5 days MRI of the abdominal aorta was repeated. Animals were sacrificed and histological evidence for iron uptake by aortic wall and lymph nodes was compared with the degree of focal signal loss on *in vivo* MR images.

Results

Aortic walls in irradiated and non-irradiated mice, but also in healthy wild-type mice, showed signal loss on T2*w MRI. Signal loss, however, did not correspond with histological evidence of USPIO uptake by aortic wall but by peri-aortic lymph nodes.

Conclusions

The versatility of USPIO as a negative MR contrast agent for both lymph node staging and atherosclerosis may limit the use for detection of atherosclerotic lesions in vessels where lymph nodes are highly prevalent.

INTRODUCTION

Atherosclerosis is an inflammatory disease, which affects mid-sized arteries including the coronary arteries.[1, 2] Coronary angiography is the clinical diagnostic tool of choice, providing a silhouette of the lumen but it does not visualize the atherosclerotic plaque. Therefore, direct visualization of the atherosclerotic plaque using Magnetic resonance imaging (MRI) has gained interest. MRI offers both anatomic detail and the potential to image cellular and molecular tissue characteristics.

Ultra small superparamagnetic particles of iron oxide (USPIO) are used as a MR contrast agent with a strong T2* shortening effect. They have a diameter of 18-30 nm and are not immediately recognized by the hepatic and splenic mononuclear phagocytic system. The half-life of USPIO has been reported to be around 90 minutes which is comparable to that of small liposomes.[3] Because of their long half-life in blood, USPIO can be digested by macrophages throughout the whole body. USPIO have been used for detection of macrophage-rich atherosclerotic lesions in rabbit studies[4-6], and in some clinical studies which focused on carotid artery plaque in patients scheduled for carotid arterectomy.[7-11]

However, the use of USPIO as a contrast agent has some potential drawbacks. Firstly, the strong T2* effect can lead to focal signal loss of an area larger than corresponding with the location of the USPIO. This effect is called “blooming” and is concentration-dependent.[12]

Secondly, USPIO are not tissue-specific: they target macrophages, which may be active in various infective diseases and in healthy lymph nodes. Lymph nodes are distributed along the vascular tree[13] and are often located close to arterial sites of interest like the aortic wall. Blooming may impair the discrimination between signal loss due to homing in atherosclerotic plaques and signal loss due to close proximity of peri-aortic lymph nodes. To our knowledge, it is unknown whether iron uptake in lymph nodes may lead to false positive observations in atherosclerotic plaque imaging procedures.

We studied to what extent blooming of lymph nodes following USPIO uptake occurs near to the murine aortic atherosclerotic wall, which could easily lead to false positive observations.

MATERIALS AND METHODS

Animals and study setup:

Experimental protocols were reviewed and approved by the Institutional Animal Care and Use Committee at Utrecht University Medical Center.

All knockout mice were backcrossed for 10 generations to the C57BL/6J genetic background. eNOS knockout (eNOS$^{-/-}$) and apoE$^{-/-}$ mice (Jackson Laboratories, Bar Harbor, Me) were crossed to generate double heterozygous mice. These mice were then crossed and the offspring genotyped for eNOS and for apoE by polymerase chain reaction. ApoE$^{-/-}$/eNOS$^{-/-}$ animals (aged 5-7 months) were used for experiments. Mice were weaned at 21 days and fed a regular diet until entry in to the study protocol. In addition, old (age >1 year) apoE$^{-/-}$ mice were used. Wild-type mice (BALB/C) were used as controls.

Group A

Male apoE$^{-/-}$/eNOS$^{-/-}$ or apoE$^{-/-}$ mice (n=15) were fed a high fat, high cholesterol diet (42% of total calories from fat; 0.15% cholesterol added; Harlan-Teklad) for 16 weeks. After this diet period (t=-2 days), depletion of circulating monocytes was achieved with total body irradiation (TBI) of the animals with 7.0 Gray, in order to study whether signals in the vascular wall would originate from circulating

monocytes.[14] Two days later, baseline (t=0) MRI of the abdominal aorta was performed at the region from the right renal artery branch up to 9 mm above this branch. Immediately after MRI, a bolus injection of 75 µL (=100 micromole/kg) USPIO (Sinerem (dextran-coated), Laboratoire Guerbet, Aulnay-Sous-Bois, France) was administered via the tail vein. MRI measurements were repeated at t=3 and 5 days. Six mice did not survive until t=3 days and were kept out of analysis because no follow-up MRI was available. Five mice were terminated after the imaging procedure at t=3 days because of ruptured abdominal aortic aneurysm or because of severe hind limping, caused by aortic dissection. Before termination or after the measurements at 5 days, aortas of animals were perfusion-fixed in 4% formaldehyde and histology was performed. Blood samples were obtained from the tail vein of 5 mice at baseline and at 3 days. Analysis of white blood cell count and differentiation was performed for 3 of these animals at 5 days after TBI.

Group B

Male apoE$^{-/-}$/eNOS$^{-/-}$ or apoE$^{-/-}$ mice (n=7) were treated the same as the animals in group A, except that no TBI was applied. Two animals were sacrificed after the MRI examination at t=1 and 3 days respectively to study early plaque uptake. *Ex vivo* MRI of the aorta of these animals was performed before histology. These animals were excluded from the statistical analysis.

Negative control

In one mouse, saline was administered instead of USPIO as a negative control for blooming of the aorta. Otherwise, the animal was treated as the animals in group B.

Wild-type controls

Three adult wild-type (BALB/c) mice were treated as animals in group B, except that they were fed a standard chow diet and MRI was performed only at t=5 days. MR images of the healthy aortas were acquired at aortic bifurcation, renal artery branches and aortic arch. These locations are known for the presence of peri-aortic lymph nodes.[13]

Anaesthesia and MRI protocol

See on line supplement.

Histopathology and Immunohistochemistry

Aortas were perfusion-fixed, excised and stored in 4% formaldehyde. Transversely cut 5 µm sections were stained with hematoxylin/eosin and elastin von-Giesson (EvG). Prussian blue (PB) and MAC-3 stainings (R&D systems, Oxon, UK) were used for detection of iron particles and macrophages, respectively. The renal artery branches were used as landmarks for correspondence with MRI.

Comparison of MR images and histology

The degree of blooming on T2* weighted (T2*w) images was assessed semi-quantitatively using a "darkening index" (DI). Each MRI level was scored according to the degree of luminal signal loss of the aorta: 1. minimal (outside the lumen), 2. moderate (less than half the area), 3. severe (more than half the area) or 4. very severe (totally obscured lumen). The cumulative DI was defined as the sum of DI scores for the ten slice levels. Cumulative DI from group A was compared with cumulative DI from group B. The amount of iron uptake in the plaque and in the lymph node (PB-staining area) was quantified

by measurement of the absolute area of positive PB-staining per slice level (software package Image J 1.41). PB-staining area was correlated to DI at the corresponding MRI level. The relative cumulative PB-staining area was defined as the cumulative PB-staining area divided by total lymph node area. The cumulative PB-staining area and relative cumulative PB-staining area were compared between groups. T2*w and T2w images acquired at t=3 days were compared with the corresponding images acquired at t=5 days. Plaque area and number of plaque macrophages were determined per slice level and cumulatively to obtain the total plaque area (mm^2) and total number of macrophages. The relative number of macrophages per mouse is calculated as the number of macrophages divided by the total plaque area.

Statistics

Descriptive statistics show mean ± standard error of the mean (SEM). Kendall's tau_b (τ) was calculated to test the correlation between the DI and PB-staining area of corresponding histology.
Differences between groups A and B with regard to plaque area, number of macrophages in the plaque, cumulative DI and PB-staining area were analyzed by one-way analysis of variance (ANOVA) and Student's t-test where appropriate. If ANOVA revealed a significant difference or a strong tendency to a difference between the groups, post-hoc comparison of means was performed with a Bonferroni test (with 2-sided p value).

RESULTS

Plaque area, number of macrophages, cumulative darkening index and PB-stained area

The irradiation protocol led to a significant depletion of white blood cells at 2 days after TBI. The number of all blood cell types further decreased from 2 days after TBI up to 7 days after TBI (Table 1).
No differences in plaque area and number of macrophages were observed between old $apoE^{-/-}$ and 5-7 month old $apoE^{-/-}$/$eNOS^{-/-}$ mice (p=0.54) and between group A and B (Table 2). Histology sections of both irradiated (group A) and non-irradiated mice (group B) showed extensive plaques around the renal artery branches.
Only minor PB-staining was detected in atherosclerotic plaques. PB stained macrophages were predominantly observed in lymph nodes (Figure 1 and 2). No differences in cumulative DI were observed at t=3 days between groups A, B and controls. Interestingly, at t=5 days, PB stained macrophages were found in peri-aortic lymph nodes, but not in aortic plaque in the non-irradiated as well as the irradiated group (Figure 1 and 2 respectively). In all groups, one or two mice showed a few iron particles in the interstitium (around the vasa vasorum). In one mouse, from the irradiated group terminated at t=3 days, some PB-stained macrophages were found in the plaque. The amount of PB-staining of interstitium and plaque was negligible when compared to the amount of PB-staining of adjacent lymph nodes (Figure 2). The cumulative PB-staining area in group B was higher than in group A, but due to large variability this did not reach significance when compared to group A (Table 2; p=0.558). Importantly, despite the presence of strong focal signal loss, it was not possible to determine the exact location of iron uptake, *i.e.* in lymph nodes or plaque, based on the T2*w images. The T2w FSE images showed more confined signal loss. However, it was still not possible to locate this signal loss precisely. Retrospectively, it was often identified as a small lymph node, which approximated the outer aortic wall very closely (Figure 2).

Table 1 | The effect of TBI on depletion of white blood cells (WBC), lymphocytes, monocytes, and granulocytes (concentrations in 109/L).

Mouse	Before TBI (n=5)	Day 2 after TBI (n=5)	Day 7 after TBI (n=3)
WBC	12.1 ± 0.91*	1.16 ± 0.05*/**	0.57 ± 0.03*/**
Lymphocytes	8.94 ± 0.88*	0.84 ± 0.05*/**	0.37 ± 0.03*/**
Monocytes	1.64 ± 0.10*	0.10 ± 0.00*	0.10 ± 0.00*
Granulocytes	1.52 ± 0.08*	0.20 ± 0.03*	0.10 ± 0.00*

**p<0.001, differences between numbers of mentioned blood cell types before TBI and one of both time points after TBI. **p<0.001, differences between numbers of mentioned blood cell types at 2 days and 7 days after TBI.*

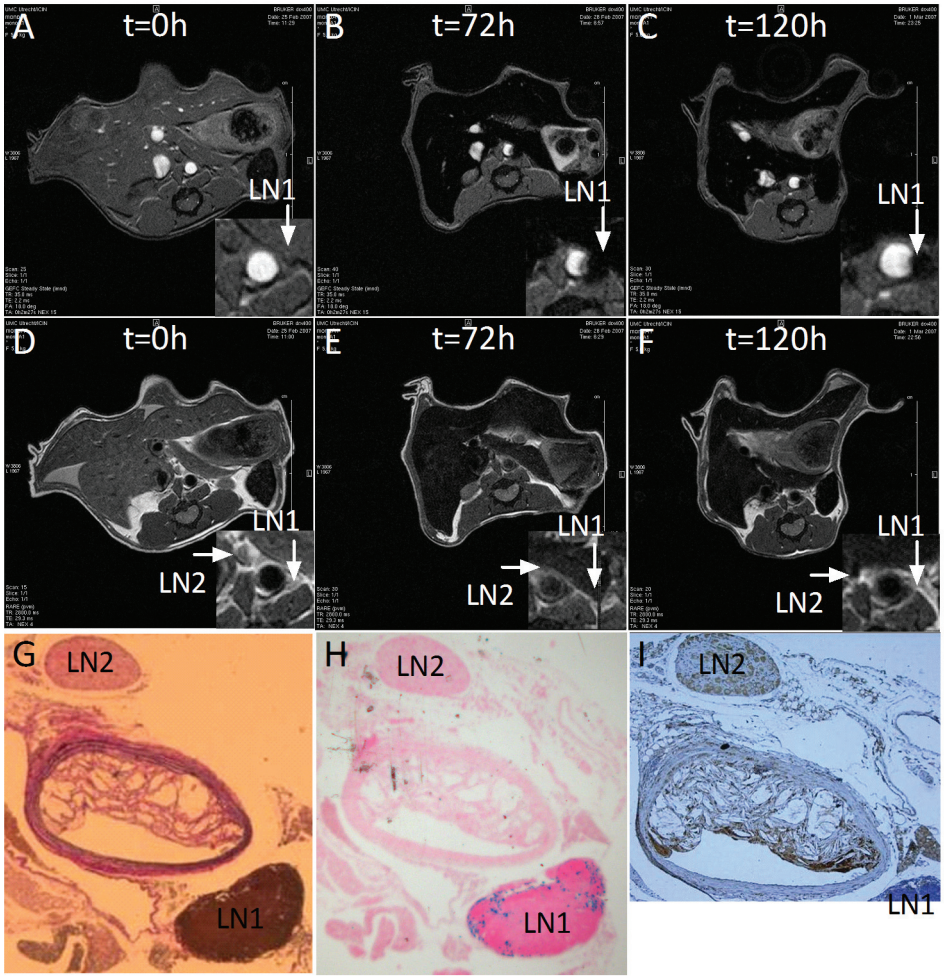

Figure 1 | *T2*w (A-C) and T2w (D-F) MR images of the aorta of an apoE$^{-/-}$/eNOS$^{-/-}$ mouse of group B at t=0 (A and D), t=3 days (B and E) and t=5 days (C and F); 3mm above the right renal artery branch. Corresponding histology sections stained; EvG (G), Prussian Blue (iron) (H) and MAC-3 (macophages) (I). Inserted panels: magnification of peri-aortic region. Bar = 500µm. LN: lymph nodes; EvG: Elastin von Giesson.*

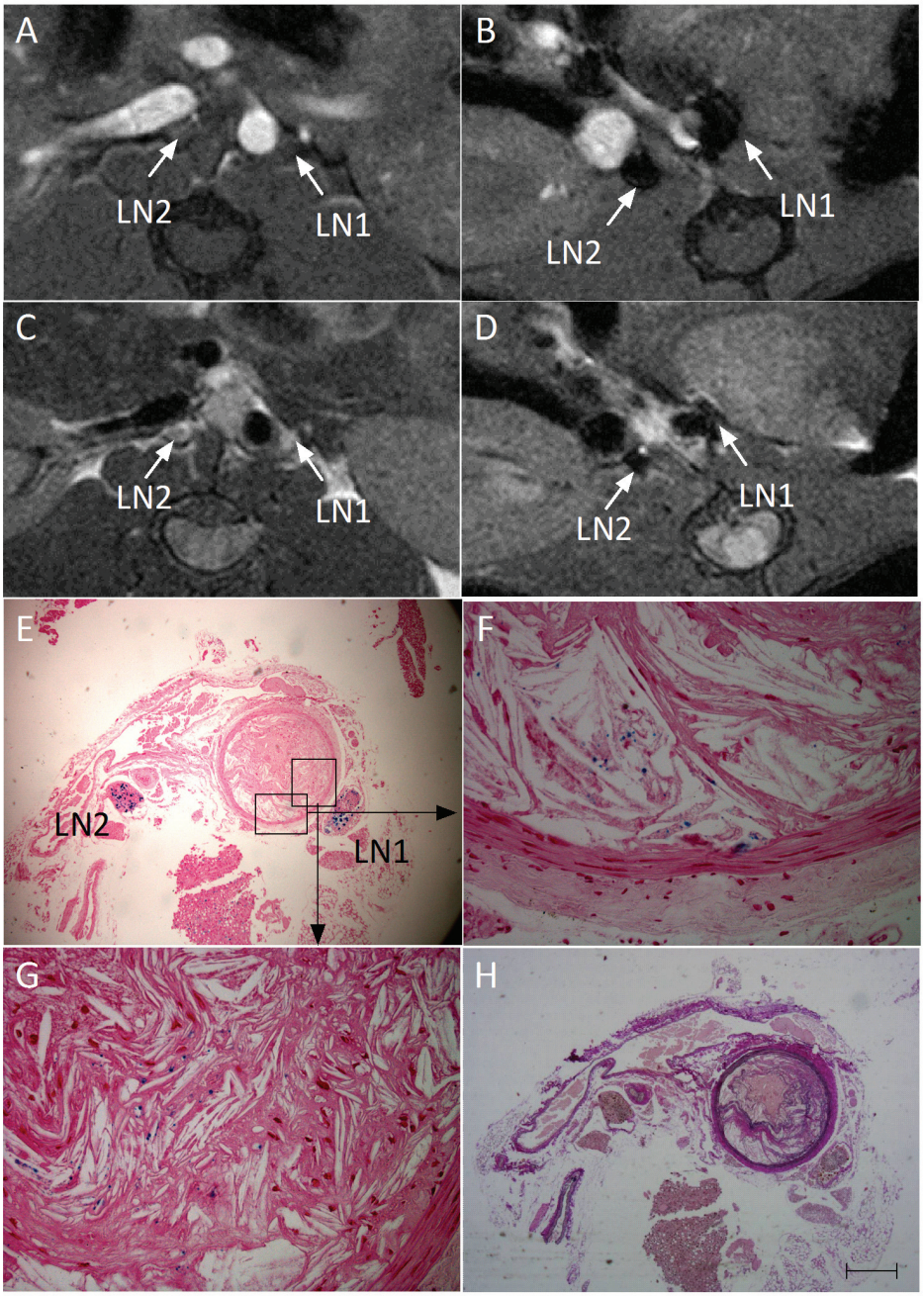

Figure 2 | *T2*w and T2w MR images of the aorta of an apoE$^{-/-}$/eNOS$^{-/-}$ mouse of group A at t=0 (A and C), and t=3 days (B and D); 1mm above the right renal artery branch. Corresponding ex vivo sections are stained with Prussian Blue (E) and EvG (H). Further magnification of two plaque regions (F and G) reveals intracellular uptake of USPIOs in plaque macrophages at 3 days after administration. For further explanation: see text. Bar = 500µm.*

Table 2 | Histology parameters and cumulative DI of all mice; mean ± SEM; Norm. Mϕ= normalized number of macrophages, PBSA= PB-staining area (iron), Relative Cumulative PBSA= cumulative PBSA divided by total lymph node area.

Group	Plaque area (mm^2)	Norm. Mϕ (mm^{-2})	Cumulative DI (t=72h)	Cumulative DI (t=120h)	Cumulative PBSA (mm^2)	Relative Cumulative PBSA (%)
A	1.74 ± 0.69	566 ± 100	10.67 ± 1.04	10.75 ± 1.11	0.26 ± 0.07	23.3 ± 4.7
B	2.46 ± 1.88	415.5 ± 95.1	11.40 ± 1.66	12.40 ± 1.97	0.39 ± 0.14	24.5 ± 4.7

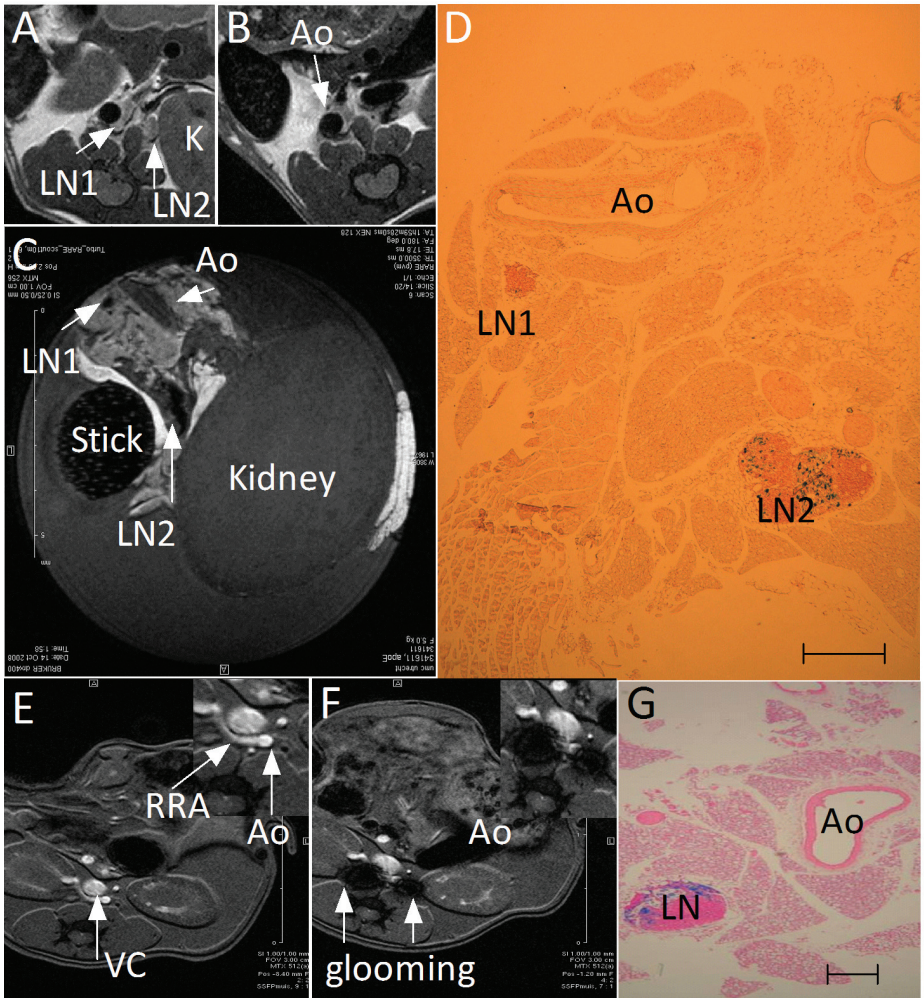

Figure 3 | *Comparison between in vivo/ex vivo MRI and histology in one ApoE$^{-/-}$ mouse and between in vivo MRI and histology in a healthy wild-type mouse after administration of USPIOs. In vivo T2w FSE images of the abdominal aorta of an old ApoE$^{-/-}$ mouse at t=0 (A) and 3 days (B), and ex vivo high-resolution T2w FSE image at 3 days (C). Corresponding histology section stained with Prussian Blue (D). In vivo T2*w MRI at t=0 (E) and t=5 days (F) in a wild-type mouse. Corresponding histology section stained with Prussian Blue (G). See text for explanation. Level: abdominal aorta, right renal artery branch.*
LN: lymph node; Ao: aorta; VC: vena cava; RRA: right renal artery. Bar = 500µm

To test whether MRI at higher resolution could better localize USPIO uptake, *in vivo* MRI of one mouse, treated as a non-irradiated mouse in group B and sacrificed at t=3 days instead of 5 days, was followed by *ex vivo* MRI. *In vivo* MRI showed a cumulative DI=11, which is similar to the mean cumulative DI in group A and B. High-resolution *ex vivo* MRI revealed that uptake of USPIO was confined to the peri-aortic lymph nodes, which was confirmed by histology (Figure 3). We treated another old apoE$^{-/-}$ mouse as group B, but performed MRI and harvested the aorta at 14 hours after administration of USPIO. Also in this mouse plaque uptake of USPIO was not observed despite reasonable plaque area and number of macrophages (data not shown).

Correlation between MRI and histology

DI at t=5 days correlated positively with PB-staining area (τ =0.347, p<0.001). Therefore, the results of T2*w MRI correlated well with the abundant presence of USPIO in peri-aortic lymph nodes. DI at t=3 days also correlated well with PB-staining area in group A and B (τ =0.428, p<0.001). As expected, DI at t=3 days correlated closely with DI at t=5 days in irradiated and non-irradiated mice that were imaged at both time points (τ =0.821, p<0.001).

Control experiments

In one mouse, saline was administered instead of USPIO. At t=5 days, MRI showed no focal signal loss on T2*w images. Corresponding PB-stained sections did not reveal any iron in plaque, or in peri-aortic lymph nodes, indicating that endogenous iron did not explain the findings in groups A and B.
The T2*w images of wild-type mice at t=5 days after injection of USPIO showed signal loss of the (peri)-aortic region. The extent of the signal loss was similar to the signal loss found on T2*w images of animals in all atherosclerotic mice groups (cumulative DI=11 ± 1). Histology revealed iron uptake in peri-aortic lymph nodes but not in the vessel wall (Figure 3).

DISCUSSION

We studied the effect of blooming of lymph nodes on *in vivo* MRI detection of USPIO uptake in murine aortic atherosclerotic wall. In addition, we studied plaque uptake of USPIO in plaque in the presence and absence of circulating monocytes. For this purpose, we used total body irradiation of apoE$^{-/-}$/eNOS$^{-/-}$ and apoE$^{-/-}$ mice, which are known to develop atherosclerotic lesions. Of five irradiated mice, only one (which died before t=5 days) had plaque stained minimally positive for iron. So, we were unable to draw any conclusions regarding the routing of USPIO into plaque. However, we did see blooming that originated from lymph nodes, in both irradiated and non-irradiated mice, suggesting that resident macrophages are responsible for uptake of the USPIO. The main finding of our study was that focal signal loss of the aortic lumen on the T2*w images was exclusively caused by the accumulation of USPIO in peri-aortic lymph nodes. Therefore, we conclude that *in vivo* MRI of the murine aorta at the resolution used in this study (100 μm^2), may be impaired by the uptake of USPIO by peri-aortic lymph nodes. The latter may complicate the discrimination between aortic plaques and surrounding lymph nodes and could lead to false positive observations. We found that focal signal loss of the aortic lumen on MR images, acquired at 3 and 5 days after USPIO administration, correlated with PB-staining. Endogenous iron did not cause positive iron staining. These results show that USPIO-enhanced MRI may differentiate between low and high uptake of exogenous iron.

In all mice, we found intense PB-staining of the lymph nodes, whereas only one irradiated mouse showed PB-stained plaque macrophages. However, in the latter, PB-staining of the lymph nodes was much more intense than PB-staining of the plaque. One may suggest that the time course of uptake and clearance of USPIO in mice is shorter than we anticipated and therefore t=5 days may be too late for histology assessment. This theory could explain why one mouse in the irradiated group, terminated at 3 days, showed some intracellular uptake by plaque macrophages, whereas none of the animals showed uptake at day 5. It could also account for the finding of some iron particles in the interstitial tissue at t=5 days. However, in old apoE$^{-/-}$ mice (treated as group B) at t=1 and 3 days after administration of USPIO, we found no evidence for plaque uptake of USPIO, despite reasonable plaque area and number of macrophages. In this study, USPIO were found particularly in macrophages. The avidity of macrophages for USPIO was shown by the fact that after *ex-vivo* incubation with USPIO, a reasonable amount of USPIO-loaded mouse peritoneal macrophages could be sorted with a magnetized column (data not shown). Other studies confirm in-vivo uptake of USPIO by macrophages.[15] However, USPIO uptake in sub-intimal arterial wall layers and in media (via neovasculature) has also been reported.[6, 16]

In contrast to our study, Litovsky *et al*.[17] found SPIO in the plaque 5 days after administration. These particles, however, are substantially larger than USPIO which impairs comparisons. To our knowledge, only one other study has used MRI to visualise USPIO uptake in atherosclerotic plaque in mice.[15] Morris *et al*. showed the presence of USPIO in the plaque 48 hours after administration. However, in that study atherosclerotic plaque in the aortic arch of apoE$^{-/-}$ mice was visualized after stimulation of vascular inflammation with chronic angiotensin II infusion and not "spontaneously" (diet) induced plaque. Angiotension II could result in plaque microruptures, facilitating USPIO invasion into the plaque, rather than USPIO uptake in intact plaques. Ruehm *et al*. showed that in rabbits, MRI performed 120 hours after administration of USPIO showed plaque enhancement. Imaging at earlier time-points led to susceptibility artifacts caused by USPIO in the circulating blood.[4] In patients who were scheduled for carotid endarterectomy, USPIO were found in atherosclerotic plaque 24 hours after administration.[8] Importantly, in all these studies, USPIO uptake in adjacent lymph nodes was not studied or at least not reported. Finally, the chosen animal model and patient condition could influence plaque uptake of USPIO by virtue of the density of macrophages in the plaque. However, this study shows that atherosclerotic plaques in these mouse models have a large number of macrophages. The number of macrophages in plaques is comparable to that in the large lymph nodes in close proximity, which showed abundant uptake of USPIO. The mechanisms which explain the difference in uptake of USPIO by macrophages between lymph nodes and plaque are unknown.

Focusing on the main finding of this study, local signal loss of the aortic lumen on the T2*w images was exclusively caused by the accumulation of USPIO in peri-aortic lymph nodes. Apparently, from the perspective of this study, the amount of iron uptake in the plaque is, at least at the assessed time-points, too low to overcome the signal from the lymph nodes. Schmitz *et al*. describe, in a review, that USPIO, need to occupy at least 5 adjacent layered cells to be visible as a local signal void.16 Indeed, in this study plaque uptake of USPIO did not span two or three adjacent cells ever, which could explain why intra-plaque USPIO was not detectable with MRI.

The ability to detect USPIO in atherosclerotic plaque is affected not only by the number of adjacent cells occupied, but also by the MRI method of choice. As expected, T2*w images showed higher contrast between USPIO-containing regions and surrounding tissues, while T2w images showed more confined signal loss and less blooming. However, T2w *in vivo* images still did not discriminate between presence of USPIO in the plaque and the lymph node.

We hypothesized that resolution in relation to lymph node and plaque size is the main problem in accurate localization. Indeed, in this study, *ex vivo* high-resolution MRI showed that exact localization of USPIO is possible when the spatial resolution is increased (pixel size 39x39 μm^2, slice thickness 0.25 mm). Based on these results, we can conclude that for discrimination between mouse aortic wall and peri-aortic lymph nodes with T2w USPIO-enhanced MRI, a pixel size much smaller than 100 μm^2 is required. Morris *et al*. also showed that *ex vivo* MRI with a spin echo sequence at a similar pixel size may accurately depict a confined area with signal loss caused by USPIO. As mentioned before, in that study the presence of USPIO in plaque in the aortic arch (using a non-spontaneous atherosclerotic plaque model) was demonstrated[15], in contrast to our results. In addition, they showed corresponding *in vivo* T2*w images with focal signal loss of the aortic wall expanding to the lumen with a pixel size of approximately 100μm^2, which is comparable to the *in vivo* pixel size in this study. Some human MRI studies[9-11] showed clear uptake of USPIO in carotid plaque. The local absence of lymph nodes, the large plaque size and relatively higher resolution could explain those results.

The lack of uptake of USPIO in this study could be due to the particle size in relation to the endothelial pore size. In an atherosclerotic rabbit model, fractionated SPIO (hydrodynamic diameter <15 nm) were observed in plaque whereas un-fractionated SPIO (hydrodynamic diameter ~120 nm) were not found in plaque.[6] In this mouse study USPIO were slightly larger than the fractionated SPIO used in the mentioned rabbit study, while the average rabbit aortic diameter is approximately 4 times larger than the average murine aortic diameter.[18, 19]

This study reveals some major limitations of dextran-coated USPIO, but PEG-lipid coated USPIO could avoid uptake by lymph node owing to lower immunogenicity. Also, antibodies or targeting peptides could be coupled to the PEG groups of these USPIO.[20] Targeted USPIO could remain in atherosclerotic plaque for a longer time or at a higher concentration. To address the blooming effect, gradient echo techniques that create positive signal enhancement in areas containing USPIO may increase the confidence of USPIO localization.[6]

Conclusions

Lymph node uptake may be misinterpreted as intra-plaque uptake of USPIO when visualized with MRI. Increased blooming on T2*w MR images may be prevented by T2w MR imaging at higher resolution because this strategy could lead to better discrimination between USPIO uptake in the plaque and the adjacent lymph nodes.

Funding

This work was supported by the Netherlands Heart Foundation (2003 B 249) and the Bekalis foundation.

Acknowledgments

The authors thank Laboratoire Guerbet (Aulnay-Sous-Bois, France) for providing Sinerem.

1. Lusis AJ. Atherosclerosis. Nature 2000 September 14;407(6801):233-41.

2. Vink A, Pasterkamp G. Atherosclerotic plaque burden, plaque vulnerability and arterial remodeling: the role of inflammation. Minerva Cardioangiol 2002 April;50(2):75-83.

3. Weissleder R, Elizondo G, Wittenberg J, Rabito CA, Bengele HH, Josephson L. Ultrasmall superparamagnetic iron oxide: characterization of a new class of contrast agents for MR imaging. Radiology 1990 May;175(2):489-93.

4. Ruehm SG, Corot C, Vogt P, Kolb S, Debatin JF. Magnetic resonance imaging of atherosclerotic plaque with ultrasmall superparamagnetic particles of iron oxide in hyperlipidemic rabbits. Circulation 2001 January 23;103(3):415-22.

5. Schmitz SA, Coupland SE, Gust R, Winterhalter S, Wagner S, Kresse M, Semmler W, Wolf KJ. Superparamagnetic iron oxide-enhanced MRI of atherosclerotic plaques in Watanabe hereditable hyperlipidemic rabbits. Invest Radiol 2000 August;35(8):460-71.

6. Briley-Saebo KC, Mani V, Hyafil F, Cornily JC, Fayad ZA. Fractionated Feridex and positive contrast: in vivo MR imaging of atherosclerosis. Magn Reson Med 2008 April;59(4):721-30.

7. Trivedi RA, Mallawarachi C, King-Im JM, Graves MJ, Horsley J, Goddard MJ, Brown A, Wang L, Kirkpatrick PJ, Brown J, Gillard JH. Identifying inflamed carotid plaques using in vivo USPIO-enhanced MR imaging to label plaque macrophages. Arterioscler Thromb Vasc Biol 2006 July;26(7):1601-6.

8. Kooi ME, Cappendijk VC, Cleutjens KB, Kessels AG, Kitslaar PJ, Borgers M, Frederik PM, Daemen MJ, van Engelshoven JM. Accumulation of ultrasmall superparamagnetic particles of iron oxide in human atherosclerotic plaques can be detected by in vivo magnetic resonance imaging. Circulation 2003 May 20;107(19):2453-8.

9. Kawahara I, Nakamoto M, Kitagawa N, Tsutsumi K, Nagata I, Morikawa M, Hayashi T. Potential of magnetic resonance plaque imaging using superparamagnetic particles of iron oxide for the detection of carotid plaque. Neurol Med Chir (Tokyo) 2008 April;48(4):157-61.

10. Tang TY, Howarth SP, Li ZY, Miller SR, Graves MJ, King-Im JM, Trivedi RA, Walsh SR, Brown AP, Kirkpatrick PJ, Gaunt ME, Gillard JH. Correlation of carotid atheromatous plaque inflammation with biomechanical stress: utility of USPIO enhanced MR imaging and finite element analysis. Atherosclerosis 2008 February;196(2):879-87.

11. Tang TY, Howarth SP, Miller SR, Graves MJ, King-Im JM, Li ZY, Walsh SR, Hayes PD, Varty K, Gillard JH. Comparison of the inflammatory burden of truly asymptomatic carotid atheroma with atherosclerotic plaques in patients with asymptomatic carotid stenosis undergoing coronary artery bypass grafting: an ultrasmall superparamagnetic iron oxide enhanced magnetic resonance study. Eur J Vasc Endovasc Surg 2008 April;35(4):392-8.

12. Qiu B, Gao F, Walczak P, Zhang J, Kar S, Bulte JW, Yang X. In vivo MR imaging of bone marrow cells trafficking to atherosclerotic plaques. J Magn Reson Imaging 2007 August;26(2):339-43.

13. Popesko P, Rajtova V, Horak J. Colour Atlas of Anatomy of Small Laboratory Animals. Saunders Ltd.; 2003.

14. Harrington NP, Chambers KA, Ross WM, Filion LG. Radiation damage and immune suppression in splenic mononuclear cell populations. Clin Exp Immunol 1997 February;107(2):417-24.

15. Morris JB, Olzinski AR, Bernard RE, Aravindhan K, Mirabile RC, Boyce R, Willette RN, Jucker BM. p38 MAPK inhibition reduces aortic ultrasmall superparamagnetic iron oxide uptake in a mouse model of atherosclerosis: MRI assessment. Arterioscler Thromb Vasc Biol 2008 February;28(2):265-71.

16. Schmitz SA. [Iron-oxide-enhanced MR imaging of inflammatory atherosclerotic lesions: overview of experimental and initial clinical results]. Rofo 2003 April;175(4):469-76.

17. Litovsky S, Madjid M, Zarrabi A, Casscells SW, Willerson JT, Naghavi M. Superparamagnetic iron oxide-based method for quantifying recruitment of monocytes to mouse atherosclerotic lesions in vivo: enhancement by tissue necrosis factor-alpha, interleukin-1beta, and interferon-gamma. Circulation 2003 March 25;107(11):1545-9.

18. Vernhet H, Demaria R, Perez-Martin A, Juan JM, Oliva-Lauraire MC, Marty-Double C, Senac JP, Dauzat M. Wall mechanics of the stented rabbit aorta: long-term study and correlation with histological findings. J Endovasc Ther 2003 June;10(3):577-84.

19. Knipp BS, Ailawadi G, Sullivan VV, Roelofs KJ, Henke PK, Stanley JC, Upchurch GR, Jr. Ultrasound measurement of aortic diameters in rodent models of aneurysm disease. J Surg Res 2003 June 1;112(1):97-101.

20. Li X, Du X, Huo T, Liu X, Zhang S, Yuan F. Specific targeting of breast tumor by octreotide-conjugated ultrasmall superparamagnetic iron oxide particles using a clinical 3.0-Tesla magnetic resonance scanner. Acta Radiol 2009 July;50(6):583-94.

PART II

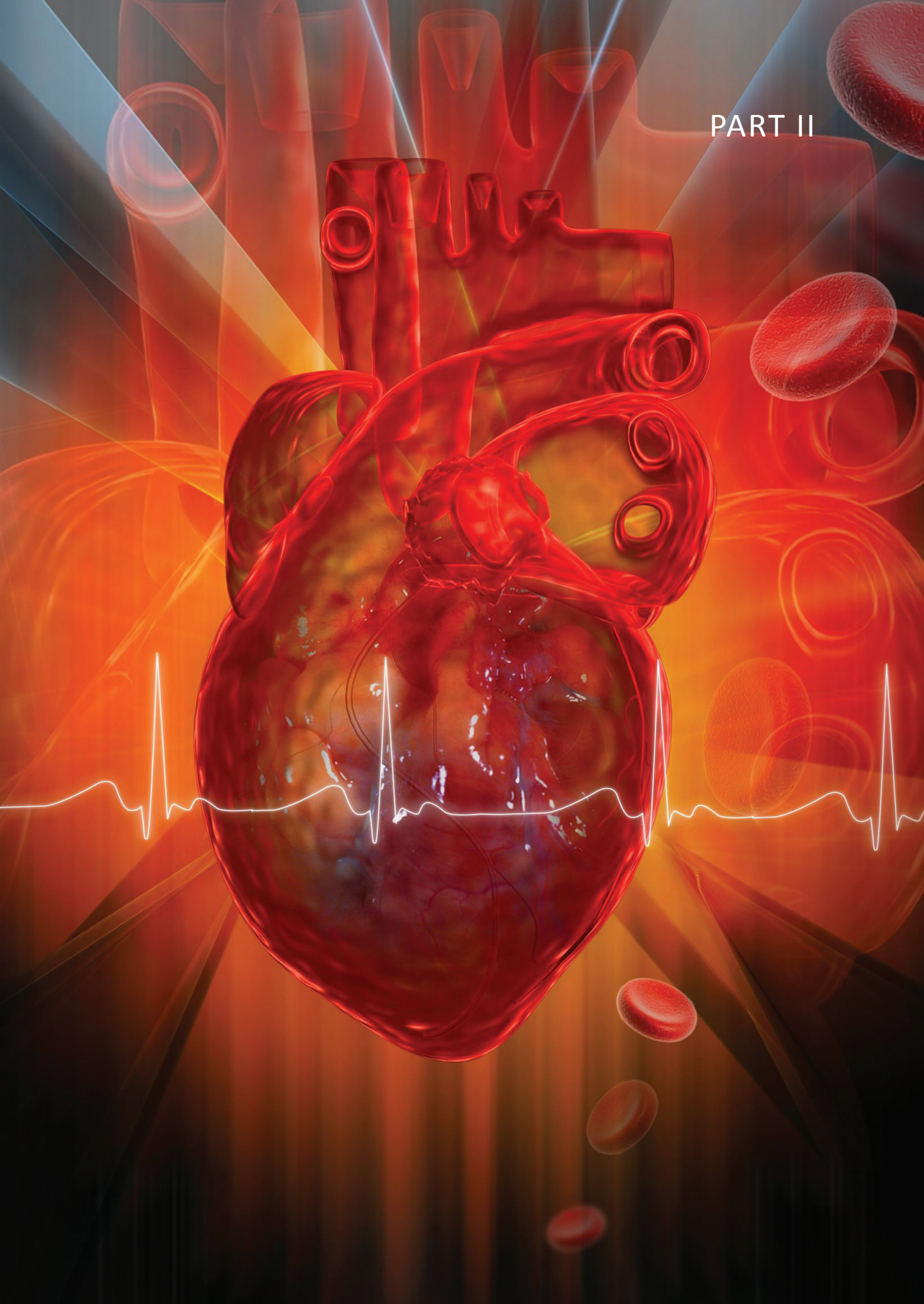

8

Evaluation of infarcted murine heart function: Comparison of prospectively triggered with self-gated MRI

Published
NMR in Biomed. 2011; 24: 307-31

Sandra M. Bovens [1,2*], Bernard C.M. te Boekhorst [1*], Krista den Ouden [1], Kees W.A. van de Kolk [1], Arno Nauerth [3], Marcel G.J. Nederhoff [1,2], Gerard Pasterkamp [1], Michiel ten Hove [1] and Cees J.A. van Echteld [1]

[1] Department of Cardiology, University Medical Center, Utrecht, the Netherlands.
[2] Interuniversity Cardiology Institute of the Netherlands (ICIN), Utrecht, the Netherlands
[3] Bruker BioSpin MRI GmbH, Ettlingen, Germany

[*] *Authors contributed equally to this study*

ABSTRACT

Background

Measurement of cardiac function is often performed in mice after, e.g., a myocardial infarction (MI). Cardiac magnetic resonance imaging (MRI) is often used, because it is noninvasive and provides high temporal and spatial resolution for the left- as well as the right ventricle. In animal cardiac MRI, the quality of the required ECG signal is variable and sometimes deteriorates over time, especially with infarcted hearts or cardiac hypertrophy. Therefore we compared the self-gated IntraGateFLASH method with a prospectively triggered FLASH method in mice with myocardial infarcts (MI) (n=16) as well as control mice (n=21).

Methods

Mice with an MI and control mice were imaged in a vertical 9.4T MR system. Images of contiguous 1mm slices were acquired from apex to base with prospective- and self-gated methods. Data were processed to calculate cardiac function parameters for the left-and right ventricle. Signal-to-noise ratio (SNR) and contrast-to-noise ratio (CNR) were calculated in mid-ventricular slices.

Results

The SNR and CNR of the self-gated data were higher than the SNR and CNR of the prospectively gated data. Differences between the two gating methods in the cardiac function parameters for both left- and right ventricle (e.g. end-diastolic volumes) did not exceed the inter-observer variability in the control mice or in the MI mice.

Conclusion

Both methods give comparable results with regard to the cardiac function parameters in both healthy control mice and mice with MIs. Moreover, the self-gated method provides better SNR and CNR when the acquisition time is equal. In conclusion, the self-gated method is suitable for routine use in cardiac magnetic resonance imaging in mice with an MI as well as in control mice and obviates the need for ECG triggering and respiratory gating. In both gating methods a number of frames higher than 10 per cardiac cycle is recommended.

INTRODUCTION

Cardiac magnetic resonance imaging (CMR) is often used to assess cardiac function following myocardial infarction (MI)[1, 2] in mice, because of its noninvasive nature and the ability to image with high temporal and spatial resolution.[3, 4]

Prospective ECG-triggering is performed by synchronizing the image sampling with the cardiac cycle and interrupting the image sampling during the respiratory period, thus reducing motion artifacts.[4, 5] However, in animal CMR, the quality of the ECG signal is variable and sometimes deteriorates over time, especially in mice with an MI or cardiac hypertrophy.

In retrospective gating the ECG and respiratory data are stored together with the MRI data. During retrospective reconstruction of the images, data can be sorted to a particular cardiac phase and excluded when acquired during a specific respiratory phase.[6] Recently, an alternative approach has been developed, which captures cardiac and respiratory motion measurements without sensors. The MR acquisition scheme of a FLASH sequence can be modified by postponing the read-out and phase-encoding gradients to the second echo; thus enabling the first echo for use as a navigator signal in the slice of interest. Due to cardiac and respiratory motion, different types of tissue move into the slice of interest, causing a change in MR signal.[4] The duration of the navigator echo, which is determined by the number of navigator points, will affect the sampling time of motion information. However, this comes with an important trade-off: the signal intensity of the eventual image will decrease due to T2* decay with longer navigator echo duration.

This 'wireless' cardiac MRI, also called self-gated MRI, has been applied in humans as well as in small rodents.[4, 7-9] The main benefit of this self-gated method is that electrodes or a respiratory pad are unnecessary for triggering purposes.

The goal of this study is to evaluate the quality of the self-gated method and whether this method can be used for routine cardiac cine MRI in healthy control mice and mice with an MI. Additionally, the influence of different navigator durations (number of navigator points) and number of cardiac frames will be evaluated.

EXPERIMENTAL

Animals

Group A: healthy male BALB/c mice (n=11, weight 29.7 ± 2.0 gram) were imaged with prospectively triggered and self-gated (long navigator) MRI. Group B: male non-obese, diabetic, severe combined immunodeficient (NOD-SCID) mice with 90 (± 2) day old MIs (n=11, weight 30.4 ± 3.1 gram) were imaged with prospectively triggered and self-gated (long navigator) MRI. Group C: healthy male BALB/c mice (n=5, weight 30.7 ± 1.8 gram) were imaged with prospectively triggered and self-gated (short navigator) MRI. Group D: healthy male C57Bl/6 mice (n=5, weight 24.0 ± 1.7) were imaged with prospectively triggered and self-gated (short navigator) MRI. Group E: male haptoglobin knockout mice (C57Bl/6 background) with 90 (±3) day old MIs (n=5, weight 30.9 ± 2.8 gram) were imaged with prospectively triggered and self-gated (short navigator) MRI. Groups D and E were used to compare SNR and CNR ratio between the two gating methods as well as to study the influence of the number of cardiac frames on left ventricular volumes (LVV) and right ventricular volumes (RVV).

Animal preparation

Mice were anesthetized with 5 vol% isoflurane in a 2:1 mixture of air (0.3 L/min) and oxygen (0.15 L/min) and transferred to a home-built cradle. Anesthesia was maintained with 1.5-2.5 vol% isoflurane to keep the respiratory rate stable. For cardiac triggering purposes a respiratory pad was placed under the chest, at the level of the heart without use of ECG electrodes. With this pad cardiac as well as respiratory motion was captured. This method is very robust; however, the first acquired frame in the heart cycle may differ between mice.

MRI measurements

Mice were imaged in a vertical 9.4T, 89mm bore size magnet equipped with 1500 mT/m gradients and connected to an Avance 400 MR system (Bruker BioSpin, Germany) using a quadrature-driven birdcage coil with an inner diameter of 3 cm. Due to unforeseen circumstances a different coil had to be used for the mice in group C. ParaVision 4.0 and IntraGate software (Bruker BioSpin, Germany) were used for cine MR acquisition and reconstruction. All MR parameters are listed in table 1. After orthogonal scout images, short axis (oriented roughly perpendicular to the septum) cardiac cine MR images were acquired. To cover the entire heart from apex to base, 8-9 slices (healthy mice) or 11-13 slices

Table 1 | Acquisition parameters of the prospectively triggered and self-gated MR methods.

	Prospective triggering	Self-gated	Self-gated (short nav)	Prospective triggering (group D/E)	Self-gated (group D/E)
TE (ms)	1,976	8,258	5,239	6,754	6,754
TR (ms)	Dependent on heart rate (HR) (~12-16ms)				
RF pulse (ms)	1.0	0.300	0.300	0.300	0.300
Flip angle	22˚	10˚	10˚	10˚	10˚
Spectr. Width (Hz)	101010.1	75757.6	75757.6	75757.6	75757.6
Echo position (%)	20	20	20	20	20
Acquisition matrix	256x128	256x128	256x128	256x128	256x128
Reconstructed matrix	256x256	256x256	256x256	256x256	256x256
In-plane resolution (µm)	117	117	117	117	117
Averages	4	~ 8	~ 17	8	Varying from 15-20 Depending on scan duration
Cardiac frames	10	10	10	Dependent on HR	Dependent on HR
Navigator points	NA	256	50	NA	50
Total acquisition time	Varying from 1m25s to 3m00s	2m20s	1m25s	Varying from 2m45s to 3m58s	Varying from 2m45s to 3m58s (per mouse equal to prospective)

(mice with MI) were needed. For groups A, B, and C 10 cardiac frames were acquired (prospectively triggered) or reconstructed (self-gated) per slice. The TR was equal in groups D and E and the number of frames (16-18 in group D and 18-24 in group E) were adjusted to the heart rate. Subsequently, acquisition time of the self-gated method was matched per mouse to the prospectively triggered experiment. In both methods the matrix was zero filled to 256x256. Shared-phase reconstruction was used in the self-gated method of each group. The total experiment time, including mouse preparation and scout images was approximately 65-90 minutes but never exceeded two hours. At the end of the experiment the mice with MI were sacrificed and the hearts were excised for further analysis.[2] The animal care committee of Utrecht University approved the experimental protocol.

FLASH and IntraGateFLASH

All MR sequences started with a steady-state preparation using dummy scans for at least 5 seconds and all cine MR images were acquired using a cine Fast Low Angle SHot (FLASH) sequence. A navigator echo was added in the self-gated sequence (IntraGateFLASH) to gather information on the cardiac- and respiratory motion. To achieve this, the read-out- and phase- dephase gradient were separated from the slice refocusing gradient in order to detect half an echo without phase encoding. The number of navigator points collected during the first echo determined the duration of the navigator. When a low number of navigator points was chosen, the TE became shorter, but less information about the cardiac- and respiratory motion was derived. The MR scheme of the IntraGateFLASH sequence, with a short (A) and long (B) navigator (nav.), is shown in figure 1. There was one phase-encoding step per TR independent of the heart rate (Figure 2). Retrospectively, four primary signals were calculated from the navigator echo by the IntraGate program and subsequently analyzed and weighted according to their contribution to a respiratory and a cardiac signal.[4] A mark was set on the minimum or maximum of the cardiac motion of every heart beat. The time between two marks was divided into the number of frames to reconstruct, for example 10 or 20 (figure 2: for simplification only four cardiac frames are shown). Data with different but contiguous k-space encodings were clustered and assigned to the correct frame. The data acquired during respiratory motion were excluded and a cine MR image was reconstructed. Additionally, the shared-phase option could be used. When using this option the time window per cardiac frame was chosen wider, resulting in a 50% overlap between each cardiac frame and the next, as well as an increase in number of averages.

Data Analysis

In all mice, dedicated, semi-automatic contour detection software (Qmass, MEDIS, Leiden, The Netherlands) was used for the determination of the end-diastolic volume (EDV) and end-systolic volume (ESV), in both the left (LV) and right ventricle (RV). The influence of the number of cardiac frames (groups D and E) on LVV and RVV was assessed. Stroke volume (SV), cardiac output (CO), and ejection fraction (EF) were calculated subsequently. Infarct size was calculated as the akinetic LV area as a percentage of the total LV area in the ED frame, which is recalculated to left ventricular mass. The SNR and CNR were calculated in the end-diastolic (ED) and end-systolic (ES) phase of mid-ventricular slices in groups D and E only. For the SNR and CNR the following formulas were used:

$$SNR = \frac{SI\ (myocardium\ or\ blood)}{SD_{noise}} \qquad CNR = \frac{SI_{blood} - SI_{myocardium}}{SD_{noise}}$$

Were SI is signal intensity and SD is standard deviation. The SD of the noise was determined in a square region of interest (ROI) outside the mouse and free from artifacts. The SI_{blood} was determined by drawing an ROI in the ES phase (consisting of the entire blood pool inside the LV) and copying to the ED phase. The $SI_{myocardium}$ was determined by drawing a circular ROI in a region of the myocardium minimally influenced by motion (typically near the septum).

Inter- and intra-observer variability

The data set of group A was analyzed twice by the same observer. The data sets of groups B, C, D, and E were analyzed three times, twice by the same observer and once by a second observer. Between the first and second analysis there was at least a six week time interval to avoid memory effects.

Statistics

Data are expressed as mean ± SD. Analysis of the differences between EDV and ESV measured with prospective triggering and self-gating was performed according to the technique of Bland and Altman.[10] The differences of EDV and ESV were expressed against the mean. For all cardiac function parameters absolute values of both positive and negative differences were used since no offset bias is expected. An independent t-test (SPSS 15.0, Chicago, USA) was used to test the intra- and inter-observer variability of EDV and ESV between prospectively triggered and self-gated data of all groups, between self-gated data of group A versus group C, and between data of group C versus group D. When the Levene's test for equality of variances had a significance of >0.10, equal variances were assumed. To test the differences between the prospectively triggered and self-gated CNR, SNR_{blood}, $SNR_{myocardium}$, EDV, and ESV a paired t-test was used. P-values of <0.05 were considered significant.

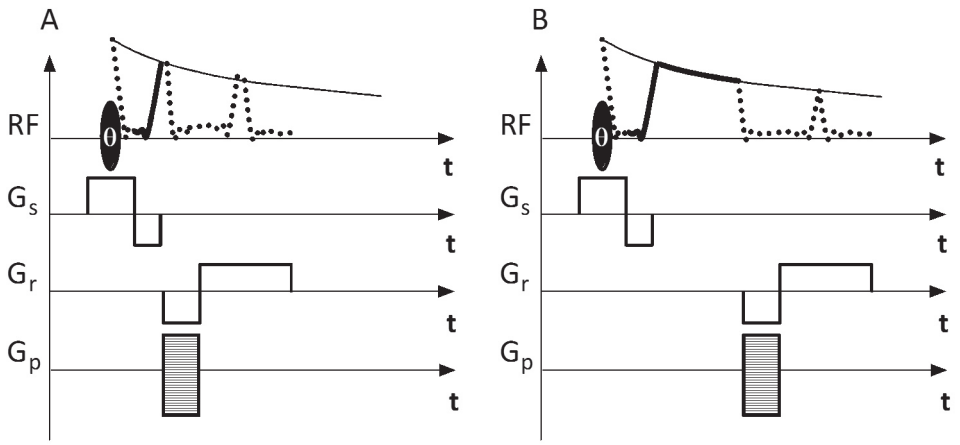

Figure 1 | *IntraGateFLASH sequence with a small number (A) or a large number (B) of navigator points. Black oval shape: RF pulse with flip angle ϑ; thick solid line: navigator; dotted line: echo; Gs: slice-selection gradient; Gr: read-out gradient; Gp: phase encoding gradient.*

Cardiac Parameters

The average heart rates (HR) were (in beats per minute): 440 ± 52 in group A, 390 ± 75 in group B, 380 ± 33 in group C, 503 ± 22 in group D, and 440 ± 47 in group E. The results of the cardiac function analyses in the different groups are shown in table 2. The mean infarct size, as determined from the MR images (in % of total LV mass), was 31.7 ± 4.0 in group B and 19.7 ± 7.3 in group E.

Prospective- versus Self-gated

In figure 3 mid-ventricular slices of a healthy control and a mouse with MI are shown in both the ED and ES phase. MR images acquired with the prospectively triggered and self-gated method are shown. There were no significant differences in LVV and RVV between the prospective and self-gated method in either group as shown in figures 4 and 5. Also, no offset bias was observed for one of the methods. As seen in figure 5 (mice with MI) the infarction areas in group E were smaller than in group B, leading to smaller LVV. Increasing the number of cardiac frames did not significantly change the LVV or RVV. In figure 6 all cardiac frames for both methods in a mid-ventricular slice are shown (Group C).

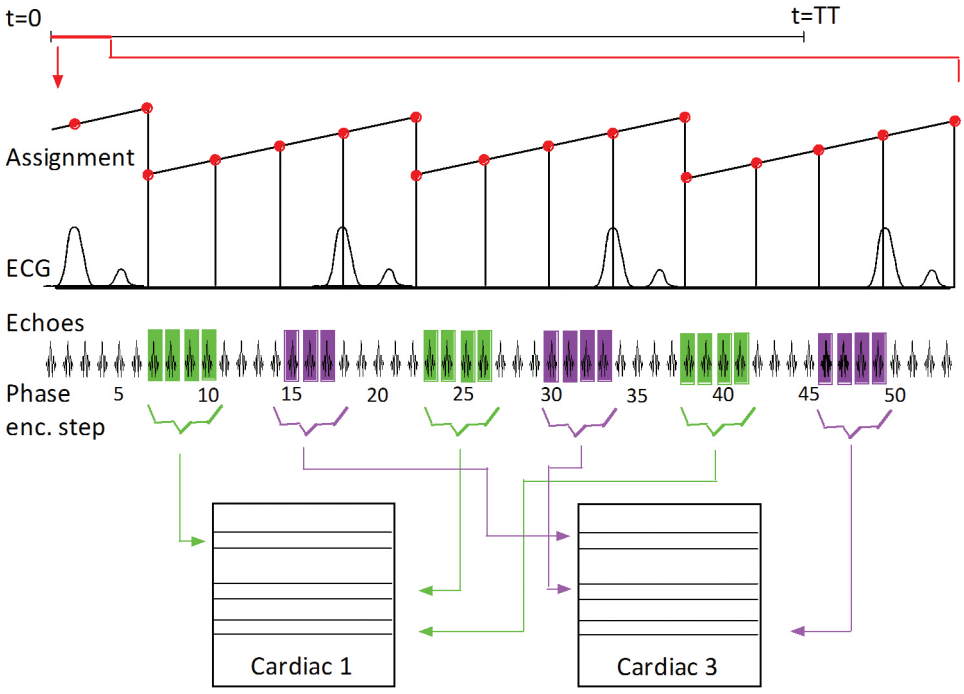

Figure 2 | *IntraGate reconstruction*
The start (t=0) of the total scan time (t=TT) is marked by a red line, and the assignment of the different phase encoding steps to the corresponding cardiac frame are shown. In this example 4 cardiac frames were reconstructed by IntraGate. The green phase encoding steps belong to the first cardiac frame; the purple phase encoding steps belong to the third cardiac frame.

SNR and CNR

The results of the SNR and CNR analyses are shown in table 3. A gradual variation in the SI of the blood was seen during the cardiac cycle, this was caused by darkened areas due to blood inflow during diastole. This was observed in both methods, causing a variation in CNR. Significantly higher SNR and CNR ratios were seen in ED as well as ES for the self-gated method when compared to the prospective method. This might be explained by the higher number of averages in the self-gated method, primarily as a result of the shared phase option, even though the acquisition time was equal for both methods.

Table 2 | Global cardiac function parameters and prospectively triggered vs. self-gated data in mean ± SD.

I	Group A Control n=11	Differences Group A n=11	Mean values Group B MI n=11	Differences Group B n=11	Mean values Group C Control Shortened nav. n=5	Differences Group C n=5
LVEDV (µl)	56.8 ± 12.8	1.9 ± 1.2 ns	237.7 ± 89.9	7.9 ± 6.2*	64.0 ± 7.6	1.6 ± 1.1 ns
LVESV (µl)	19.2 ± 7.5	1.8 ± 1.6 ns	207.6 ± 93.2	6.1 ± 4.0*	28.2 ± 7.3	2.9 ± 1.4 ns
LVSV (µl)	37.6 ± 6.6	2.8 ± 2.4	30.1 ± 5.1	4.1 ± 3.2	35.8 ± 3.0	1.3 ± 1.4
LVCO (ml/min)	16.6 ± 3.8	1.3 ± 1.2	11.6 ± 2.7	1.6 ± 2.1	13.8 ± 1.5	0.6 ± 0.1
LVEF (%)	67.1 ± 5.9	3.0 ± 2.6	14.9 ± 6.9	1.5 ± 1.6	56.5 ± 6.8	3.6 ± 1.8
RVEDV (µl)	42.6 ± 12.9	1.6 ± 1.3 ns	51.3 ± 13.5	7.0 ± 5.3 ns	45.7 ± 6.7	2.1 ± 0.9 ns
RVESV (µl)	13.4 ± 5.0	1.1 ± 1.6 ns	30.4 ± 11.8	3.9 ± 2.7 ns	15.5 ± 2.8	4.2 ± 3.4 ns
RVSV (µl)	29.2 ± 8.3	1.7 ± 0.7	21.0 ± 5.5	4.0 ± 3.0	30.2 ± 4.8	4.2 ± 2.2
RVCO (ml/min)	12.9 ± 3.9	0.7 ± 0.3	8.4 ± 3.1	1.6 ± 1.4	11.7 ± 1.9	2.0 ± 0.8
RVEF (%)	69.2 ± 4.5	2.4 ± 1.4	42.3 ± 11.7	4.1 ± 2.3	66.0 ± 3.4	8.6 ± 5.7

II	Mean values Group D Control n=5	Differences Group D n=5	Mean values Group E MI n=5	Differences Group E n=5
LVEDV (µl)	42.4 ± 5.2	2.8 ± 3.5 ns	111.6 ± 58.3	4.5 ± 3.2 ns
LVESV (µl)	17.1 ± 2.4	2.0 ± 0.8 ns	78.7 ± 60.5	4.5 ± 4.4 ns
LVSV (µl)	25.3 ± 3.4	2.7 ± 2.4	32.9 ± 5.1	4.5 ± 5.0
LVCO (ml/min)	12.7 ± 1.7	1.4 ± 1.2	14.5 ± 2.8	2.0 ± 2.2
LVEF (%)	59.6 ± 2.9	4.0 ± 1.1	35.0 ± 12.7	4.3 ± 4.9
RVEDV (µl)	30.1 ± 3.1	1.5 ± 1.6 ns	41.1 ± 7.1	1.4 ± 1.4 ns
RVESV (µl)	10.0 ± 1.6	0.7 ± 0.6 ns	15.6 ± 5.4	1.6 ± 1.4 ns
RVSV (µl)	20.1 ± 2.3	1.9 ± 1.8	25.5 ± 4.7	2.7 ± 1.1
RVCO (ml/min)	10.1 ± 1.3	1.0 ± 0.9	11.2 ± 2.3	1.2 ± 0.5
RVEF (%)	66.9 ± 3.7	3.5 ± 2.2	62.6 ± 9.2	4.8 ± 2.2

The global cardiac function parameters of the groups are averaged from the data of the two gating methods. (Table I: groups A, B, and C. Table II: groups D and E)
*The difference between prospectively triggered data and self-gated data expressed in µl (EDV, ESV, and SV), ml/min (CO), and % (EF).Left ventricular (LV), right ventricular (RV), end-diastolic volume (EDV), end-systolic volume (ESV), stroke volume (SV), cardiac output (CO), ejection fraction (EF). Comparison per group between prospectively- and self-gated LVEDV, LVESV, RVEDV, and RVESV * p<0.05. ns = not significant.*

Intra- and Inter-observer Variability

The intra-observer variability never exceeded 9 µl for LVV or RVV in healthy control mice (groups A, C, and E). The intra-observer variability of group C decreased compared to group A in the self-gated method. This decrease was not significantly different in the LVV, but both RVEDV and RVESV showed significant differences ($p<0.05$) between groups A and C: EDV; 8.5 ± 8.1 µl and 1.3 ± 1.9 µl, resp., as well as ESV; 7.0 ± 5.1 µl and 2.6 ± 1.2 µl, resp. This suggests that the use of a short navigator (group C) improves intra-observer variability. The inter-observer variability between the prospective method and the self-gated method was not significantly different in the healthy control mice. The intra-observer variability in groups B and E was not significantly different when using the prospective method compared to the self-gated method and never exceeded 4 µl for LVV or RVV when using either method. The inter-observer variability for LVV and RVV in groups B and E was also not significantly different between the prospective and the self-gated method and never exceeded 26 µl.

Table 3 | SNR ± SD and CNR ± SD of the prospectively triggered and self-gated methods and groups. Comparisons of prospective vs. self-gated with * $p<0.05$ ** $p<0.001$.

	Group D Control ED	Group D Control ES	Group E MI ED	Group E MI ES
CNR prospectively triggered	33.4 ± 3.8	24.3 ± 3.9	28.3 ± 4.3	24.0 ± 3.3
CNR self-gated	63.2 ± 10.9*	44.2 ± 10.0*	63.0 ± 12.3*	56.1 ± 8.7**
SNR blood prospectively triggered	66.2 ± 3.8	59.3 ± 3.3	61.2 ± 6.3	58.6 ± 3.9
SNR blood self-gated	108.2 ± 9.7**	93.0 ± 10.2*	107.2 ± 16.6*	103.2 ± 13.8*
SNR myocardium prospectively triggered	32.8 ± 1.9	35.1 ± 2.7	32.9 ± 4.0	34.5 ± 4.2
SNR myocardium self-gated	45.0 ± 4.6*	48.8 ± 2.8*	44.2 ± 6.3*	47.1 ± 5.9*

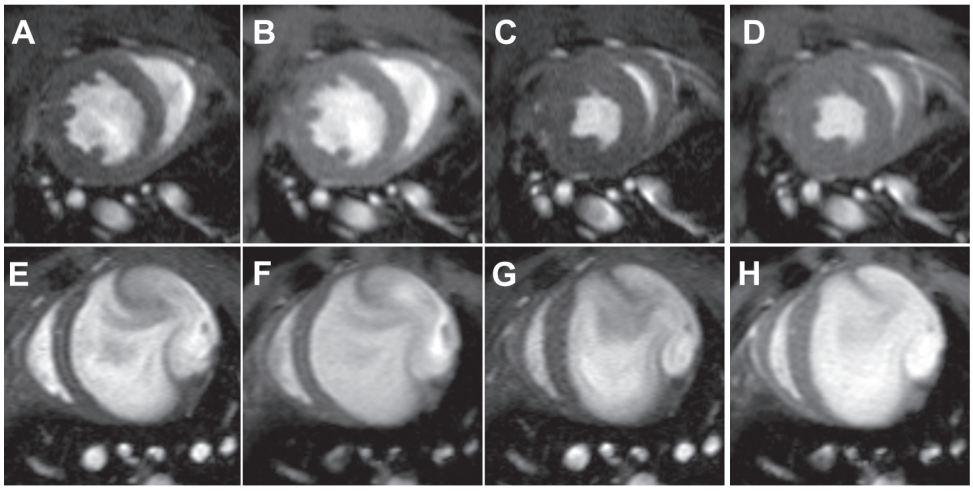

Figure 3 | *Mid-ventricular slice of a healthy murine heart (A-D) from group C, and a murine heart with an infarct (E-G) from group B; prospectively gated (A, C, E, G) and self-gated (B, D, F, H) in end-diastolic phase (A, B, E, F) and end-systolic phase (C, D, G, H).*

The higher inter-observer variability is in line with the larger mean volumes (ED and ES) due to post-MI LV dilatation. The intra-observer variability of LVESV, prospectively triggered, decreased significantly (p=0.02), when comparing group C and D; 3.3 ± 1.8 µl (10 frames) versus 0.5 ± 0.3 µl (16-18 frames). The inter-observer variability of RVESV, prospectively triggered, decreased significantly (p=0.05) when comparing group C and D; 5.0 ± 3.3 µl (10 frames) versus 1.0 ± 0.4 µl (16-18 frames).

DISCUSSION

In this study we compared prospectively triggered to self-gated cardiac cine MRI in healthy control mice and mice with MI. We found that in all mice the cardiac function parameters were similar in both methods.

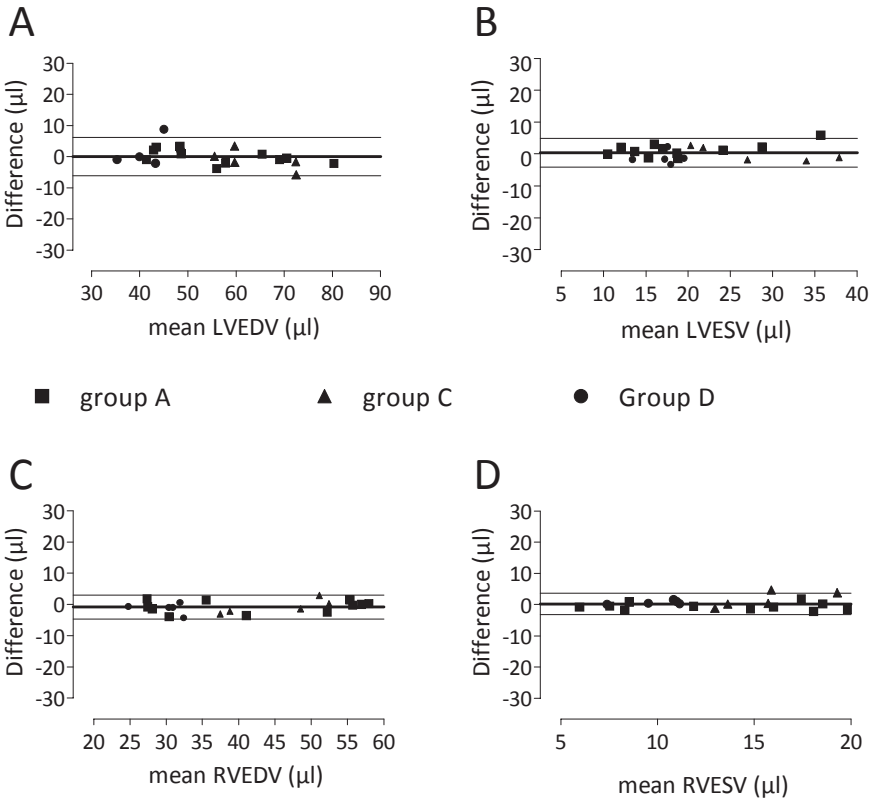

Figure 4 | *Bland Altman plots of prospectively triggered vs. self-gated data in healthy control mice. Left ventricular volumes (A+B) and right ventricular volumes (C+D).*
Prospective triggering vs. self-gated data is shown. The closed boxes indicate data from mice in group A. The closed triangles indicate data from mice in group C. The closed circles indicate data from mice in group D. The mean difference is indicated with the thick solid line; the 2SD lines are indicated as solid lines. All volumes are expressed in µl. A: Left ventricular end diastolic volume (LVEDV). B: Left ventricular end systolic volume (LVESV). C: Right ventricular end diastolic volume (RVEDV). D: Right ventricular end systolic volume (RVESV)

Cardiac Parameters

LV volumes of healthy mice found in this study were in line with values found in literature.[4] In this study a systematic difference was found between LV and RV stroke volumes. This difference could be explained by the asymmetrical shape of the RV, in particular the right ventricular outflow tract, which complicated the perpendicular orientation of the short axis MR slices. In a human study Sheehan *et al* used a 3D method to circumvent this problem.[11] This 3D method could be useful when studying diseases leading to RV dysfunction.

Schneider *et al* studied changes of cardiac function in mice during anesthesia, up to three hours.[12] They showed a limited, but significant, decrease in LVESV over time. This decrease was even more pronounced in failing murine hearts. In our study prospectively triggered imaging was performed before self-gated imaging. We did not observe any decrease in LVESV during a maximal examination time of two hours.

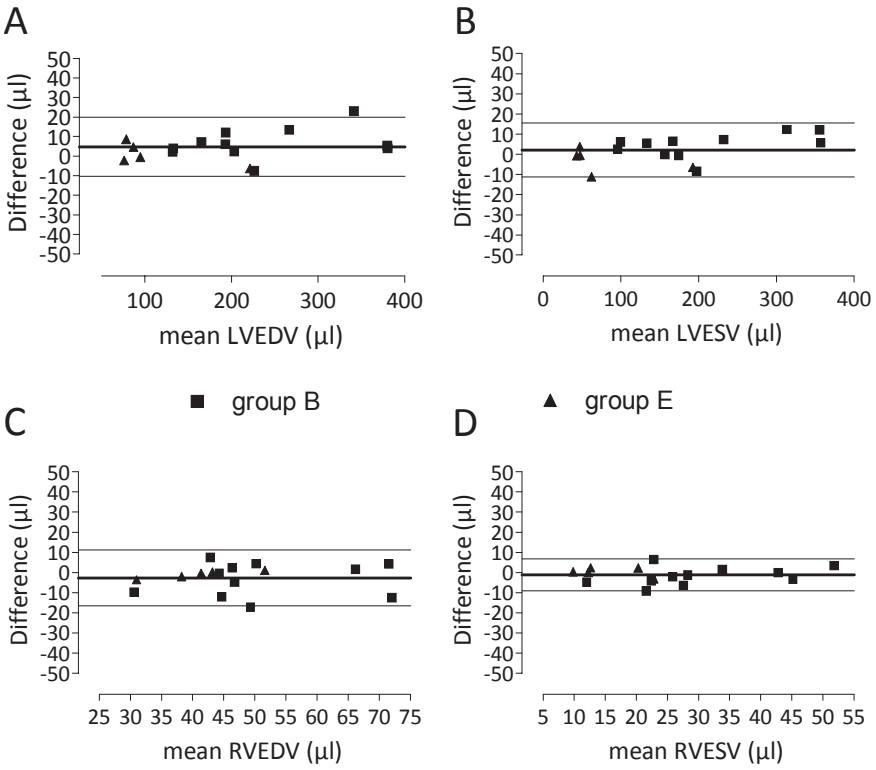

Figure 5 | *Bland Altman plots of prospectively triggered vs. self-gated data in mice with MIs. Left ventricular volumes (A+B) and right ventricular volumes (C+D).*
Prospective triggering vs. self-gated data is shown. The closed boxes indicate data from mice in group B. The closed triangles indicate data from mice in group E. The mean difference is indicated with the thick solid line; the 2SD lines are indicated as solid lines. All volumes are expressed in µl. A: Left ventricular end diastolic volume (LVEDV). B: Left ventricular end systolic volume (LVESV). C: Right ventricular end diastolic volume (RVEDV). D: Right ventricular end systolic volume (RVESV)

However, we could not exclude that a true difference between the prospectively triggered and the self-gated method was masked by a small decrease in LVESV.

Apart from obviating the need to record ECG or heart action and respiratory motion, the self-gated method has some additional distinct advantages over the prospectively triggered method. The self-gated cine showed a smoother transition from the last frame to the first, as seen in figure 6, even when the heart rate varies during the experiment, because the cardiac frames were assigned retrospectively. Also, the flow-artifacts, caused by fast inflow of blood during diastole, were less conspicuous in the self-gated method (Figure 6). Additionally, the self-gated method led to better delineation of the endocardial borders of the right ventricle.

Intra- and Inter-observer Variability

Our intra- and inter-observer variability was in line with other studies.[3, 13] Those studies provided intra- and inter-observer variability of LVV only, whereas we also determined intra- and inter-observer variability of RVV. No significant differences were found in the inter-observer variability between the two methods in either the healthy control mice or the mice with MI. A short navigator resulted in significantly improved intra-observer variability in healthy mice (group A versus group C). This might

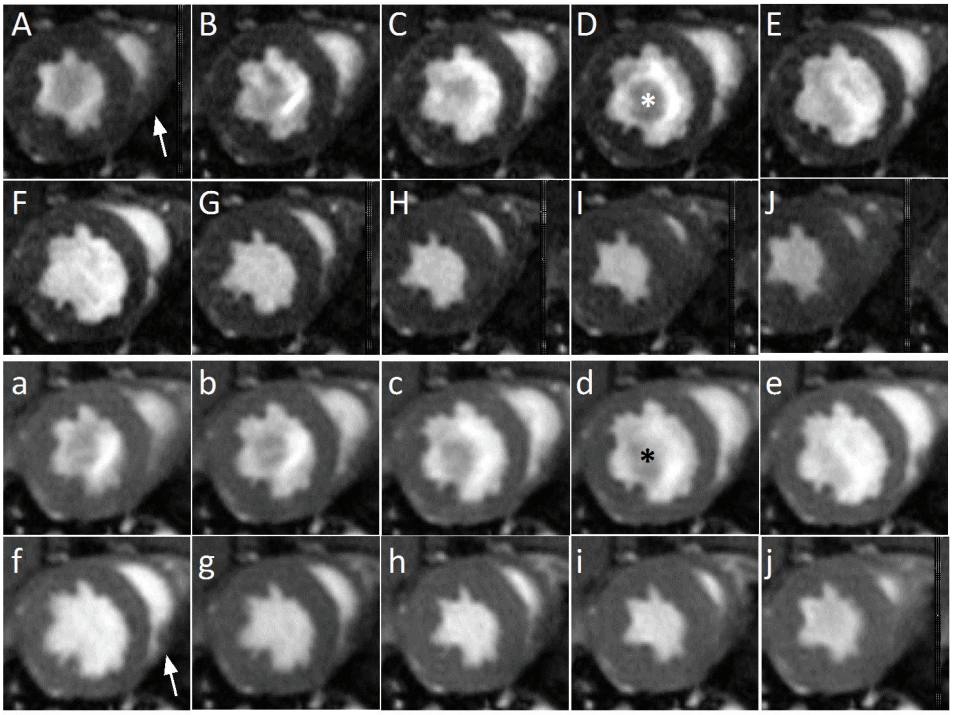

Figure 6 | *All 10 frames of prospectively triggered (A-J) and self-gated (a-j) images from a mid-ventricular slice of a healthy control mouse (group C)*
The white (D) and black (d) asterisks indicate flow artifacts, which are more conspicuous in the prospectively triggered image (D). In the right ventricle, white arrows (A and a) indicate the location of an artifact (in the RV) in the prospectively triggered image, which disappears in the self-gated method (a).

be caused by a 3 ms decrease in TE, resulting in higher SNR and better image quality. No comparison of SNR was made between group A and C due to the use of a different RF coil in group C.

Number of Cardiac Frames

Mice with a different background had to be used in groups D and E compared to groups A, B, and C (10 frames per cardiac cycle), due to limited availability of mice with MIs. This made it difficult to study the influence of the number of cardiac frames on ED and ES volumes. However, we observed during the data analysis of groups D and E that the ES phase was more easily detected. This could be explained due to the fact that it is more likely to catch the right frame at ES when using more frames per heart cycle.

SNR and CNR

In our study we observed higher SNR for blood and myocardium and higher CNR when using the self-gated method. The relevant MR parameters (TE, TR, spectral width, flip angle, and acquisition time) were equal, leading to a higher number of averages for the self-gated method, when using the shared-phase reconstruction. If this shared-phase reconstruction was not used, the SNR and CNR were comparable to the SNR and CNR of the prospective method (data not shown). However, the self-gated method could achieve a higher SNR and a higher quality of images in a similar time frame. When the number of averages would be lowered, resulting in an SNR equal to the SNR of prospectively triggered images, experiment time would be substantially shortened. On average $SNR_{myocardium}$ was 1.3 times higher for the self-gated method when compared to the prospectively triggered method, therefore the number of averages for the self-gated method could be 1.3^2 (=1.7) times lower to reach equal SNR.

As expected, the CNR varied slightly in the prospective method during cardiac cycle (as seen in Figure 6). The lowest CNR could be seen during the systolic phase. In the self-gated method there was also a lower CNR during the systolic phase, however no differences were found between the first and last reconstructed frame. This is most likely due to the steady-state the self-gated method can maintain, since the data were continuously recorded without a breathing pause.

In our study an inslice-navigator was used. With the self-gated method it is also possible to use a separate saturation navigator slice, which can be positioned independently of the imaged slice. This creates the possibility to perform multi-slice experiments (with or without blood saturation to achieve black or bright blood images). Because a separate slice will be used as a navigator, the TE becomes shorter and TR longer, which will most likely result in an even higher SNR.

A comparable study has been performed solely in healthy mice at a lower field strength.[4] The authors concluded that the SNR and CNR using the self-gated method were lower compared to the prospectively triggered method. At the time they performed their study the shared-phase reconstruction was not available yet, which could partially explain this contradictory observation.

Conclusion

The self-gated method can be used in routine cardiac cine MR measurements in mice with an MI as well as in healthy control mice and obviates the need for ECG triggering and respiratory gating. The self-gated method is more time-efficient compared to the prospectively triggered method. Regardless of the gating method it is recommended to use more than 10 frames per cardiac cycle,.

Acknowledgments

The authors would like to thank Linda van Laake (Department of Cardiology, University Medical Center

Utrecht, Utrecht, The Netherlands) and Fatih Arslan (Department of Experimental Cardiology, University Medical Center, Utrecht, The Netherlands) for the use of their MI mice, to be additionally evaluated with the self-gated method. Also the authors would like to thank Erich Treiber (Bruker BioSpin MRI GmbH, Ettlingen, Germany) for providing figure 2.

ABBREVIATIONS

CNR	=	contrast-to-noise ratio
CO	=	cardiac output
EDV	=	end diastolic volume(s)
EF	=	ejection fraction
ESV	=	end systolic volume(s)
HR	=	heart rate
LV	=	left ventricle/ventricular
LVV	=	left ventricular volume(s)
MI	=	myocardial infarction
Nav.	=	navigator
NOD-SCID	=	non-obese, diabetic, severe combined immunodeficient
RV	=	right ventricle/ventricular
RVOT	=	right ventricular outflow tract
RVV	=	right ventricular volume(s)
SD	=	standard deviation
SI	=	signal intensity
SNR	=	signal-to-noise ratio
SV	=	stroke volume
TT	=	total scan time

1. Timmers L, van Keulen JK, Hoefer IE, Meijs MF, van Middelaar B, den Ouden K, van Echteld CJ, Pasterkamp G, de Kleijn DP. Targeted deletion of nuclear factor kappaB p50 enhances cardiac remodeling and dysfunction following myocardial infarction. Circ.Res. 2009; 104: 699-706

2. van Laake LW, Passier R, Monshouwer-Kloots J, Nederhoff MG, Ward-van Oostwaard D, Field LJ, van Echteld CJ, Doevendans PA, Mummery CL. Monitoring of cell therapy and assessment of cardiac function using magnetic resonance imaging in a mouse model of myocardial infarction. Nat.Protoc. 2007; 2: 2551-2567.

3. Ruff J, Wiesmann F, Hiller KH, Voll S, von Kienlin M, Bauer WR, Rommel E, Neubauer S, Haase A. Magnetic resonance microimaging for noninvasive quantification of myocardial function and mass in the mouse. Magn Reson.Med. 1998; 40: 43-48.

4. Heijman E, de Graaf W, Niessen P, Nauerth A, van Eys G, de Graaf L, Nicolay K, Strijkers GJ. Comparison between prospective and retrospective triggering for mouse cardiac MRI. NMR Biomed. 2006; 20: 439-447.

5. Rose SE, Wilson SJ, Zelaya FO, Crozier S, Doddrell DM. High resolution high field rodent cardiac imaging with flow enhancement suppression. Magn Reson.Imaging. 1994; 12: 1183-1190.

6. Bishop J, Feintuch A, Bock NA, Nieman B, Dazai J, Davidson L, Henkelman RM. Retrospective gating for mouse cardiac MRI. Magn Reson.Med. 2006; 55: 472-477.

7. Hiba B, Richard N, Janier M, Croisille P. Cardiac and respiratory double self-gated cine MRI in the mouse at 7 T. Magn Reson.Med. 2006; 55: 506-513.

8. Crowe ME, Larson AC, Zhang Q, Carr J, White RD, Li D, Simonetti OP. Automated rectilinear self-gated cardiac cine imaging. Magn Reson.Med. 2004; 52: 782-788.

9. White RD, Paschal CB, Clampitt ME, Spraggins TA, Lenz GW. Electrocardiograph-independent, “wireless” cardiovascular cine MR imaging. J.Magn Reson.Imaging. 1991; 1: 347-355.

10. Bland JM, Altman DG. Statistical methods for assessing agreement between two methods of clinical measurement. Lancet. 1986; 1: 307-310.

11. Sheehan FH, Ge S, Vick GW, Urnes K, Kerwin WS, Bolson EL, Chung T, Kovalchin JP, Sahn DJ, Jerosch-Herold M, Stolpen AH. Three-dimensional shape analysis of right ventricular remodeling in repaired tetralogy of Fallot. Am.J.Cardiol. 2008; 101: 107-113.

12. Schneider JE, Hulbert KJ, Lygate CA, Ten Hove M, Cassidy PJ, Clarke K, Neubauer S. Long-term stability of cardiac function in normal and chronically failing mouse hearts in a vertical-bore MR system. MAGMA. 2004; 17: 162-169.

13. Schneider JE, Cassidy PJ, Lygate C, Tyler DJ, Wiesmann F, Grieve SM, Hulbert K, Clarke K, Neubauer S. Fast, high-resolution in vivo cine magnetic resonance imaging in normal and failing mouse hearts on a vertical 11.7 T system. J.Magn Reson.Imaging. 2003; 18: 691-701.

9

Diastolic dysfunction in type I diabetic mice evaluated with self-gated cardiac magnetic resonance imaging

Submitted

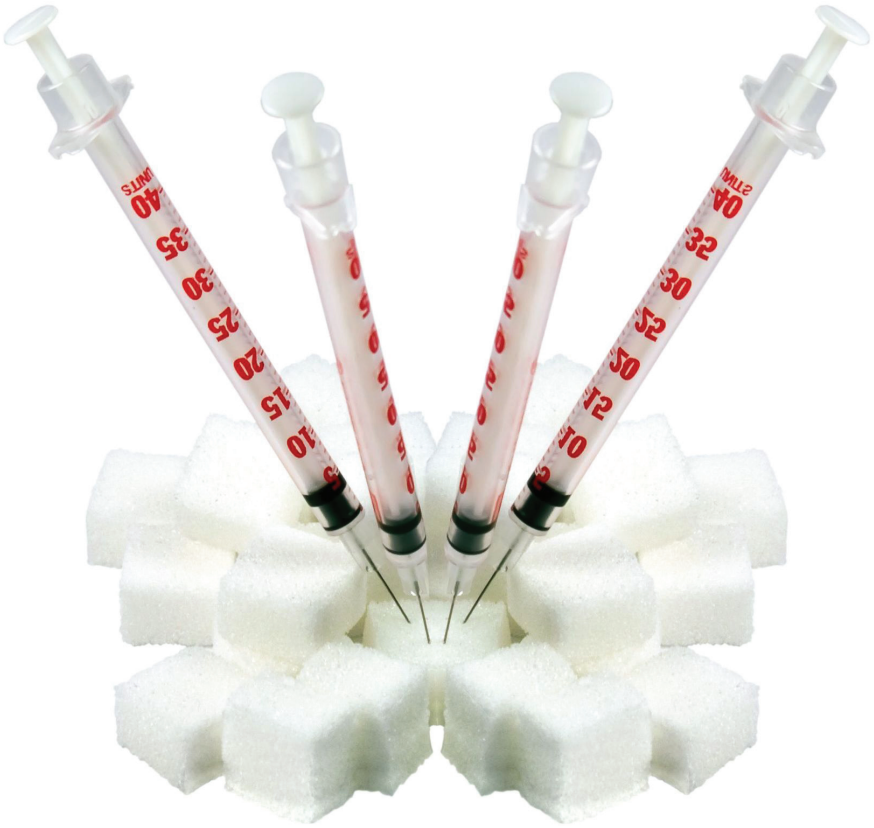

Sandra M. Bovens[1,2] , Bernard C.M. te Boekhorst[3], V. Maringa Emons[1], Petra H. van der Kraak[4], Cees J.A. van Echteld[1], Maarten J.M. Cramer[1] and Gerard Pasterkamp[1]

1 Department of Cardiology, University Medical Center Utrecht, Utrecht, the Netherlands.
2 Interuniversity Cardiology Institute of the Netherlands (ICIN), Utrecht, the Netherlands
3 Department of Biomedical Engineering, Eindhoven University of Technology (TUE), Eindhoven, the Netherlands
4 Department of Pathology, University Medical Center Utrecht, Utrecht, the Netherlands

ABSTRACT

Background

Diastolic dysfunction is an abnormality in the relaxation phase of the ventricles. Diabetes is a risk factor for development of diastolic dysfunction leading to systolic dysfunction. Mouse models facilitate the study on mechanisms and temporal development of diastolic dysfunction. However, Doppler ultrasound, which is clinically used to assess diastolic dysfunction, is difficult to perform in mice. Alternatively, cardiac MRI can be applied to assess cardiac function. We aimed to validate the use of high temporal resolution (HTR) MRI for the accurate detection of diastolic (dys)function in a murine diabetes model.

Methods and Results

Streptozotocin-induced diabetic BALB/c mice and controls (n=18) were imaged at baseline and 4, 8 and 12 weeks after confirmed diabetes (glucose > 15mmol/L) with self-gated HTR MRI. Data was processed to determine left ventricular cardiac function. The HTR scans revealed an increase in the number of frames per cardiac cycle in diabetic mice over time. In the early ventricular filling phase no differences in the percentile volume contribution were found between the controls and diabetic mice at all time points. However, in the late filling phase significant differences were found between controls and diabetic mice at 8 and 12 weeks ($p<0.001$). In the first 8 weeks no decline in systolic cardiac function was observed, however at 12 weeks a significant decline was found for end-diastolic volume, stroke volume and cardiac index compared to the control mice ($p=0.001$, $p=0.003$, and $p<0.001$, respectively). Additionally, in the diabetic mice a significant decline in peak filling rates, in the early as well as the late filling phase is seen as early as week 4 (E: $p<0.001$; A: $p=0.002$), this difference remains significant at week 8 (E: $p<0.001$; A: $p=0.012$) and week 12 (E: $p=0.002$; A: $p=0.02$).

Conclusion

HTR self-gated cardiac MRI is a suitable tool to detect changed left ventricular filling patterns, thus facilitating evaluation of early diastolic dysfunction in mice, even before systolic cardiac function declines.

INTRODUCTION

It is well known that diabetes is associated with cardiovascular diseases, such as atherosclerosis and heart failure.[1-3] Approximately 40% of patients with heart failure have preserved left ventricular systolic function with exhibiting diastolic heart failure (diastolic dysfunction). Several factors, like ischemia or valvular leakage, may contribute to the development of diastolic dysfunction, however, heart failure in diabetic patients may also develop without the presence of one of these causes. [4, 5] When diastolic dysfunction is present, the pressure in the left ventricle increases, giving rise to an increased pressure in the left atrium and the lung veins, which could possibly lead to an enlarged atrium and alveolar edema.[6] In addition, hypertrophy of the cardiomyocytes can be seen on histology, as well as an increase in interstitial collagen deposition and/or infiltration into the myocardium further deteriorating diastolic dysfunction.[6]

Murine models are frequently used to study cardiovascular diseases.[7, 8] To evaluate cardiac function in these small animals, e.g. after myocardial infarction, several imaging techniques are being applied, mainly echo and magnetic resonance imaging (MRI).[9-12] MRI is frequently used to assess cardiac systolic function in mice but the application to study diastolic function has been rare. The use of MRI to reproducibly assess diastolic function in mice would facilitate studies on the pathogenesis and treatment of diastolic dysfunction in small animal models. In earlier studies a self-gated MRI method was evaluated for the accurate determination of cardiac function in mice without the need for electrodes.[13, 14]

In this study we assessed a high temporal resolution (HTR) self-gated MRI scan for the accurate detection of (early) diastolic dysfunction in a murine type I diabetes model.

MATERIALS AND METHODS

Animals

Diabetes was induced in 9 male BALB/c mice (Charles River, Maastricht, the Netherlands) aged between 8-11 weeks, weighing 24-30 grams, via intraperitoneal streptozotocin (STZ, Sigma-Aldrich S0130) injections (single dose of 200mg/kg) dissolved in 100mM citrate buffer, pH 4.6. After three days blood glucose levels were determined using Accu-Chek Aviva Nano (Roche Diagnostics, Almere, the Netherlands) via mandibular vein punction. When glucose levels exceeded 15mmol/L mice were considered diabetic. When glucose levels did not exceed 15mmol/L, 7 days after STZ injections a second injection was given. All mice were diabetic after the first or second STZ injection. Control mice (n=9) received citrate buffer only. When diabetic mice lost 10-20% body weight within 48 hours a slow-release insulin pellet (LinBit, Linshin, Toronto, Canada) was placed subcutaneously, which was replaced after 4 weeks when needed. Mice were imaged at baseline (n=18) and 4 (n=17), 8 (n=17), and 12 weeks (n=15) after confirmed diabetes to determine systolic and diastolic left ventricular cardiac function. The animal care committee of Utrecht University approved the experimental protocol.

MRI preparation and measurement

Mice were anesthetized with 3-5 vol% isoflurane in a 2:1 mixture of air (0.3 L/min) and oxygen (0.15 L/min) and transferred to a home-built cradle. Anesthesia was maintained with 0.5-2.5 vol% isoflurane to keep the respiratory rate stable. For monitoring the cardiopulmonary physiology a respiratory pad was placed under the chest.

Mice were imaged in a vertical 9.4T, 89mm bore size magnet equipped with 1500 mT/m gradients and connected to an Avance 400 MR system (Bruker BioSpin, Germany) using a quadrature-driven birdcage coil with an inner diameter of 3 cm. ParaVision 4.0 and IntraGate software (Bruker BioSpin, Germany) were used for cine MR acquisition and reconstruction. After orthogonal scout images, self-gated short axis cardiac cine MR images were acquired. For accurate determination of diastolic left ventricular function a self-gated high HTR MRI scan was added, in which a cine of a mid-ventricular slice (slice thickness: 0.5mm) was acquired with a TR of 3.015ms, resulting in 45 to 90 frames per cardiac cycle (depending on the heart rate). At the end of the experiment mice were sacrificed and hearts excised. Left ventricular wet weight was determined and the left ventricle was fixated in 4% formaldehyde.

Histology

Paraffin sections of the left ventricles were stained and analyzed. Hematoxylin/Eosin (HE) staining and Picrosirius red staining were performed. The Picrosirius red staining was used to assess collagen content.

Data Analysis

In all mice, dedicated, automatic contour detection software (cmr42, Circle Cardiovascular Imaging, Calgary, Canada) was used to determine the end-diastolic volume (EDV) and end-systolic volume (ESV) in the left ventricle (LV). Stroke volume (SV), cardiac output (CO), and ejection fraction (EF) were calculated subsequently. Endocardial contours were drawn in each frame of the HTR scan to determine left ventricular volume in the mid-ventricular slice. Epicardial contours were drawn to determine left ventricular wall volume and subsequently left ventricular mass was calculated. Volume curves were used to determine the early ('E') and late/atrial ('A') filling phase. To correct for different left ventricular volumes, percentile contributions of total stroke volume in the slice were calculated for the E and A phase. Peak filling rates for the E and A filling phases were determined from the $\Delta V/\Delta t$ curves and the E/A ratio was calculated.

Statistics

Data are expressed as mean ± SD. For the comparison of different cardiac function parameters between groups the independent samples t-test was used. To determine correlation between left ventricular mass wet weight and weight determined by MRI a Pearson correlation was performed.

RESULTS

Animals

One diabetic mouse died after the first STZ injection and two mice (one diabetic and one control) were sacrificed at week 8 after the MRI scan to evaluate histology of the heart. At week 12 two diabetic mice showed macroscopic left ventricular hypertrophy, they were excluded from the analysis of diastolic function by MRI. In figure 1 an overview of general animal characteristics is given. Due to the diabetic status of the animals, the body weight decreased. The control mice, however, had an increase in body weight (figure 1A). The LV/body weight ratio is shown in figure 1B, since wet weight could only be determined when the mice were sacrificed an significant correlation between LV wet weight and LV weight according to MRI was found (figure 1C; $p<0.001$, $R=0.984$).

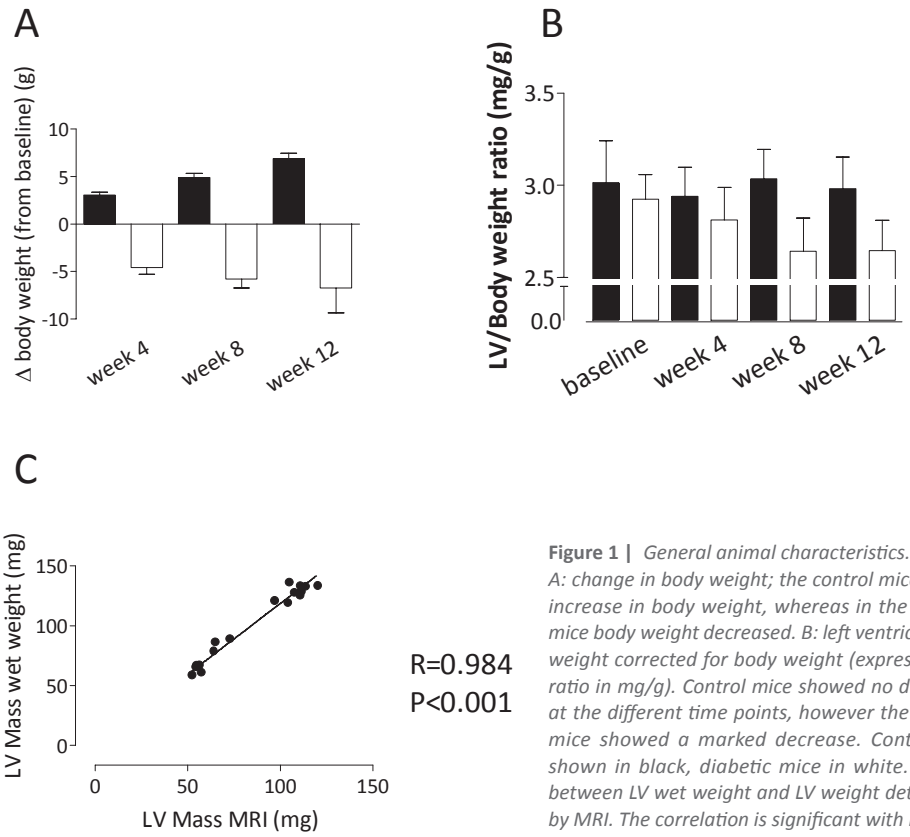

Figure 1 | *General animal characteristics. A: change in body weight; the control mice had an increase in body weight, whereas in the diabetic mice body weight decreased. B: left ventricular (LV) weight corrected for body weight (expressed as a ratio in mg/g). Control mice showed no difference at the different time points, however the diabetic mice showed a marked decrease. Controls are shown in black, diabetic mice in white. C: ratio between LV wet weight and LV weight determined by MRI. The correlation is significant with R=0.984.*

Overall Cardiac Function

The results of the cardiac function analyses are shown in table 1. To correct for the difference in body weight the end-diastolic volume (EDV), end-systolic volume (ESV) and stroke volume (SV) were divided by the body weight and expressed as µl/gram. Additionally, the cardiac index (CI) was also calculated, expressed as ml/min/gram. In figure 2 the graphs of the corrected data (figure 2A-C) as well as the original data (figure 2D-E) are shown. The corrected data revealed that systolic function (EDV and ESV) declined in the diabetic group at week 12. The EF increased at week 12 for the diabetic mice, this can most likely be explained by the relatively large decline of EDV and ESV compared to the smaller decline in SV. In the control mice the corrected EDV, ESV, SV and CI did not change significantly in time. In the diabetic mice however a decrease is observed at week 12. For EDV, SV and CI this decrease was significant when compared to the control mice ($p=0.001$, $p=0.003$, and $p<0.001$, respectively), suggesting that systolic dysfunction was only detectable after 12 weeks of diabetes.

Diastolic Cardiac Function

The HTR scans showed a higher frame number in diabetic mice over time; baseline: 52 ± 9 and 51 ± 4, week 4: 53 ± 4 and 67 ± 17, week 8: 51 ± 3 and 75 ± 14, and week 12: 51 ± 3 and 69 ± 10 frames per cardiac cycle for the control mice and diabetic mice, respectively. This difference is explained by the difference in heart rate, which is lower in the diabetic mice.

Table 1 | Cardiac function in control mice

	Controls			
	Baseline (n=9)	**w4 (n=9)**	**w8 (n=9)**	**w12 (n=8)**
EDV (µl)	62.69 ± 4.66	74.07 ± 6.05	80.92 ± 6.92	87.48 ± 3.26
ESV (µl)	26.62 ± 4.21	34.33 ± 5.00	38.56 ± 6.16	41.50 ± 3.33
SV (µl)	36.07 ± 2.17	39.74 ± 3.34	42.36 ± 3.89	45.98 ± 3.36
EF (%)	57.73 ± 4.37	53.80 ± 4.26	52.50 ± 4.68	52.57 ± 3.38
CO (ml/min)	14.61 ± 2.00	15.13 ± 2.35	17.03 ± 1.76	18.05 ± 2.07
LV Mass (mg)	NA	NA	121.2 (n=1)	129.69 ± 5.59
LV MRI Mass (mg)	90.13 ± 7.91	96.93 ± 6.96	105.62 ± 5.81	110.40 ± 5.12
BW (grams)	29.9 ± 1.4	32.96 ± 1.25	34.82 ± 1.43	37.06 ± 1.36
PFR 'E' (ml/sec)	0.118 ± 0.03	0.142 ± 0.03	0.140 ± 0.02	0.169 ± 0.03
PFR 'A' (ml/sec)	0.056 ± 0.01	0.059 ± 0.01	0.073 ± 0.02	0.083 ± 0.02
E/A ratio	2.21 ± 0.55	2.48 ± 0.54	2.02 ± 0.57	2.11 ± 0.57
HR	404 ± 38	379 ± 36	402 ± 24	392 ± 22
Values corrected for body weight				
EDV (µl/gram)	2.10 ± 0.12	2.25 ± 0.17	2.32 ± 0.19	2.36 ± 0.13
ESV (µl/gram)	0.89 ± 0.12	1.04 ± 0.16	1.11 ± 0.18	1.12 ± 0.12
SV (µl/gram)	1.21 ± 0.09	1.21 ± 0.08	1.21 ± 0.08	1.24 ± 0.08
CI (ml/min/gram)	0.49 ± 0.06	0.46 ± 0.06	0.49 ± 0.04	0.49 ± 0.05

EDV: end-diastolic volume; ESV: end-systolic volume; SV: stroke volume; EF: ejection fraction; CO: cardiac output; BW: body weight; PFR: peak filling rate; HR: heart rate; CI: cardiac index.

Table 2 | Cardiac function in diabetic mice

	Diabetics			
	Baseline (n=9)	**w4 (n=8)**	**w8 (n=8)**	**w12 (n=7)**
EDV (µl)	58.78 ± 5.94	58.12 ± 7.77	51.43 ± 6.65	44.25 ± 4.43
ESV (µl)	24.41 ± 5.70	28.33 ± 8.51	24.35 ± 3.85	18.62 ± 2.82
SV (µl)	34.37 ± 8.98	29.79 ± 6.85	27.07 ± 4.60	25.63 ± 4.52
EF (%)	57.98 ± 11.29	51.65 ± 11.36	52.52 ± 5.21	57.71 ± 6.27
CO (ml/min)	13.43 ± 3.46	8.43 ± 3.32	7.61 ± 2.53	6.46 ± 1.98
LV Mass (mg)	NA	NA	89.30 (n=1)	69.22 ± 9.87
LV MRI Mass (mg)	83.64 ± 4.40	67.45 ± 6.59	60.20 ± 8.10	57.69 ± 4.86
BW (grams)	28.6 ± 0.9	24.0 ± 1.7	22.8 ± 2.4	21.8 ± 1.8
PFR 'E' (ml/sec)	0.133 ± 0.03	0.079 ± 0.02*	0.075 ± 0.03*	0.082 ± 0.02*
PFR 'A' (ml/sec)	0.055 ± 0.01	0.040 ± 0.01*	0.047 ± 0.02*	0.044 ± 0.02*
E/A ratio	2.53 ± 0.78	2.01 ± 0.51	1.84 ± 0.93	1.95 ± 0.75
HR	391 ± 35	277 ± 55	277 ± 63	248 ± 38
Values corrected for body weight				
EDV (µl/gram)	2.05 ± 0.17	2.42 ± 0.27	2.27 ± 0.31	2.03 ± 0.18*
ESV (µl/gram)	0.85 ± 0.18	1.19 ± 0.36	1.08 ± 0.19	0.86 ± 0.16
SV (µl/gram)	1.21 ± 0.35	1.24 ± 0.23	1.19 ± 0.20	1.17 ± 0.15*
CI (ml/min/gram)	0.47 ± 0.13	0.35 ± 0.12	0.33 ± 0.10	0.30 ± 0.08*

**Significant decrease found compared to control mice: corrected EDV (w12: p=0.001), corrected SV (w12: p=0.003), CI (w12: p<0.001), PFR 'E' (w4: p<0.001; w8: p<0.001; w12: p=0.002), PFR 'A' (w4: p=0.002; w8: p=0.012; w12: p=0.02)*

EDV: end-diastolic volume; ESV: end-systolic volume; SV: stroke volume; EF: ejection fraction; CO: cardiac output; BW: body weight; PFR: peak filling rate; HR: heart rate; CI: cardiac index.

The early (E) and late/atrial (A) contributions were expressed as a percentile volume increase of total stroke volume in the mid-ventricular slice. In the E phase no differences were found between controls and diabetic mice, at none of the time points. However, an increase in atrial contribution was observed (figure 3A), with a significant difference ($p<0.001$) between controls and diabetic mice at 8 and 12 weeks. The data suggests that deterioration of diastolic function initiates at week 4. The diastolic dysfunction worsens between 8 weeks and 12 weeks together with a further decline in systolic function, which is observed at week 12. Additionally, some mice already developed cardiac hypertrophy at week 12.

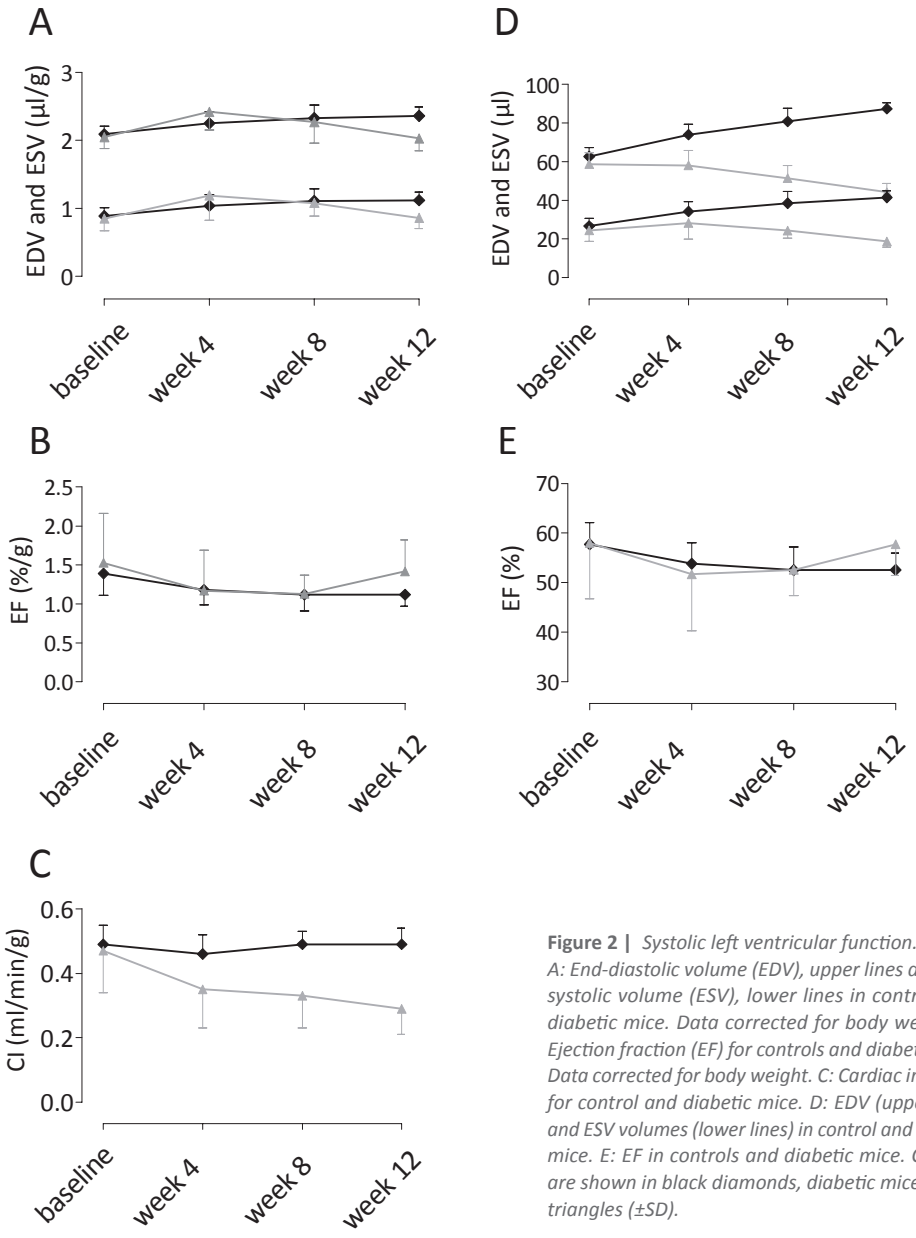

Figure 2 | *Systolic left ventricular function. A: End-diastolic volume (EDV), upper lines and end-systolic volume (ESV), lower lines in controls and diabetic mice. Data corrected for body weight. B: Ejection fraction (EF) for controls and diabetic mice. Data corrected for body weight. C: Cardiac index (CI) for control and diabetic mice. D: EDV (upper lines) and ESV volumes (lower lines) in control and diabetic mice. E: EF in controls and diabetic mice. Controls are shown in black diamonds, diabetic mice in grey triangles (±SD).*

The peak filling rates (PFR) of the E and A peaks are shown in figure 3B. In the diabetic mice a significant decline in PFR in the E phase as well as the A phase is seen as early as week 4 (E: p<0.001; A: p=0.002), this difference remains significant at week 8 (E: p<0.001; A: p=0.012) and week 12 (E: p=0.002; A: p=0.02). The E/A ratios showed a slight decrease in time in the diabetic group, whereas in the control group the E/A ratio remains the constant, however none of the differences are significant (figure 3C). In figure 4 the Sirius Red staining of a mid-ventricular slice is shown of a control mouse and a diabetic mouse. The polarized light picture shows more collagen in the diabetic mouse than the control mouse.

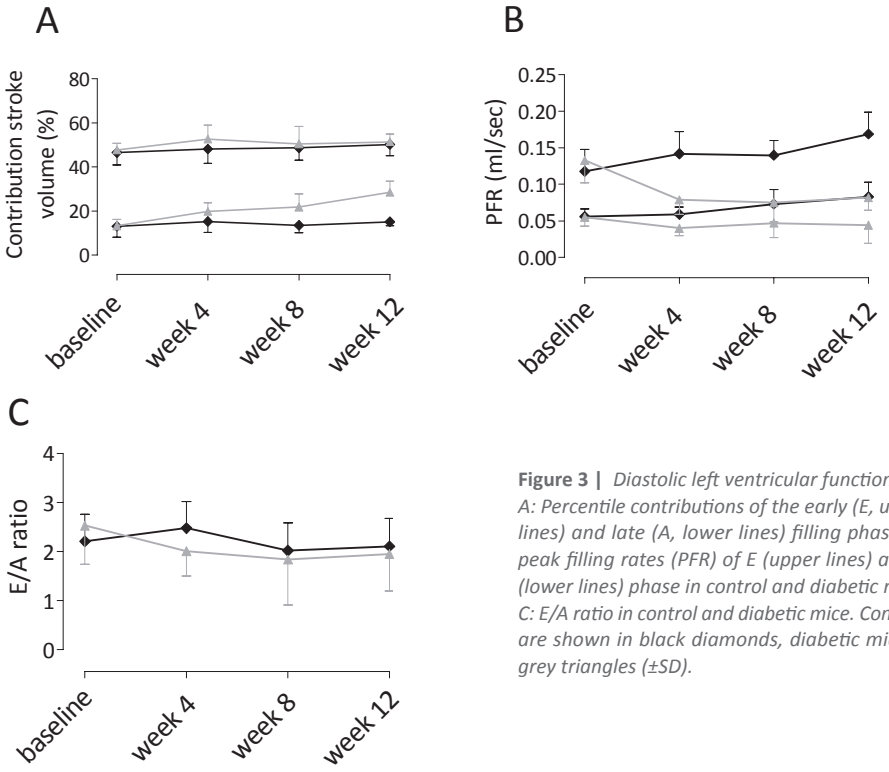

Figure 3 | *Diastolic left ventricular function. A: Percentile contributions of the early (E, upper lines) and late (A, lower lines) filling phase. B: peak filling rates (PFR) of E (upper lines) and A (lower lines) phase in control and diabetic mice. C: E/A ratio in control and diabetic mice. Controls are shown in black diamonds, diabetic mice in grey triangles (±SD).*

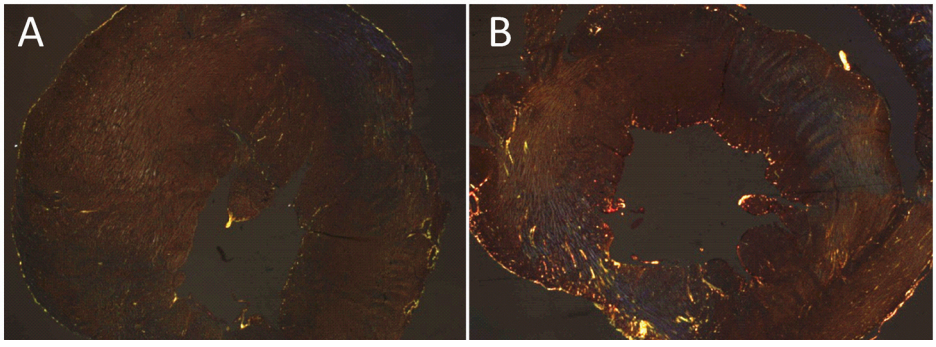

Figure 4 | *Collagen content mid ventricular slice.*
Polarized light photograph of a Sirius Red staining (collagen) in a control mouse (A) and a diabetic mouse (B).

DISCUSSION

Diabetes is a risk factor for cardiovascular diseases and especially diastolic heart failure is very common in diabetic patients.[4, 15] Since the prevalence of diabetes is increasing, mainly in the western countries, it would be useful to find a reliable, reproducible, non-invasive method to detect early diastolic dysfunction, so patients could be treated before systolic dysfunction develops.

It is important to understand the mechanisms of diastolic dysfunction. Murine models are needed to study the pathogenesis and possible pharmological interventions. To study the effect of e.g. pharmological interventions a reliable and reproducible method is needed to study diastolic function in this small animal model. At the moment several animal models of diabetes are available, with a differentiation in type I and type II diabetes. For type II diabetes mice with the leptin receptor mutation (leprdb) are often used.[16-18] For type I diabetes in mice a genetic mutated mouse is available, the Akita mouse, with a mutation in the insulin 2 gene.[19] Additionally, type I diabetes can be induced in every mouse strain (or any other animal model) by injection of streptozotocin (STZ), which is toxic to the insulin producing β-cells in the pancreas.[20-22] In our study we choose the STZ induced mouse model, because this made it possible to study the development of diabetic heart failure in time, whereas with a genetic model this might be more problematic. We show that self-gated MRI can be used to quantify E and A phase filling. We observed a marked decrease in the peak filling rate (PFR) of the E phase as early as 4 weeks after confirmed diabetes. When we calculated the E/A ratio, we did not find a significant reduction in the diabetic mice, however some mice did develop cardiac hypertrophy and no E/A ratio could be calculated, giving a high standard deviation and possible under powering at week 12. Stuckey *et al*.[17] showed similar results in a mouse model of type II diabetes. They observed a significant reduction in PFR in the E filling phase and no change in the A filling phase of diabetic mice.

Some studies used Doppler echo to evaluate diastolic dysfunction in mice with similar results.[19, 20, 22] Basu *et al*. used a genetic model of type I diabetes and found a reduction in the E phase when the mice where 3 months old.[19]

Reproducibility is an important factor in long term animal studies with possible pharmological interventions. In our study all of the diabetic mice revealed diastolic dysfunction. We also showed that in 12 weeks several stages of cardiac dysfunction were apparent. After 4 weeks of diabetes early, not significant, diastolic dysfunction had already developed which led to severe diastolic dysfunction after 8 weeks of diabetes without systolic dysfunction. And after 12 weeks of diabetes some mice developed cardiac hypertrophy while other mice developed systolic dysfunction. Thus the combination of this mouse model and self-gated MRI results in a reproducible setup to study different stages of cardiac dysfunction. For possible future evaluation of medications aimed at prevention of systolic dysfunction and possibly even reduction of diastolic dysfunction this model could be very useful. In the study of Katare *et al* they showed that the use of a vitamin B analogue can prevent diastolic dysfunction in a type I and type II diabetic mouse model.[20]

We found that self-gated MRI is a useful technique to study cardiac function in mice. With this technique it is possible to acquire frames every 3ms, which is needed to study diastolic function in the murine heart accurately due to the high heart rate (~400 beats per minute). Recently, Stuckey *et al*.[17] also used HTR MRI to evaluate diastolic function in a mouse model of type II diabetes and additionally also in a myocardial infarct model in rats. They used a high magnetic field and acquired frames every 2.4ms. However, they did not use self-gating, in which all the data is stored and reconstructed retrospectively. The benefit of self-gating, besides the fact that ECG electrodes become

obsolete, is that all the data is stored during the experiment, whereas with prospective gating data is only acquired after a trigger for a fixed time. When the heart rate changes during the experiment important information could be lost.

This study does have some limitations; the STZ injections create a type I diabetic model, as where type II diabetes is more common and many diabetic patients with heart failure suffer from type II diabetes. However, since diabetes related diastolic dysfunction is presumably partly explained by the stiffening of the cardiac muscle4, as a result of glycosylation[6, 23, 24], and this stiffening occurs in both types of diabetes we expect our data can be extrapolated to mice with type II diabetes. We also showed in our study that the diabetic mice had higher collagen contents in their hearts.

In our study the mice had very high glucose levels (>25mmol/L) during the entire study, which could have led to a more severe and accelerated model of diabetes and cardiac dysfunction.

Conclusion

In a streptozotocin induced murine model of type I diabetes diastolic dysfunction can be detected in an early phase, before apparent systolic dysfunction, by the addition of a high temporal resolution MRI scan.

ABBREVIATIONS

BPM	=	beats per minute
CI	=	cardiac index (ml/min/gram)
CO	=	cardiac output (ml/min)
EDV	=	end diastolic volume(s) (µl)
EF	=	ejection fraction (%)
ESV	=	end systolic volume(s) (µl)
HTR	=	high temporal resolution
HR	=	heart rate (bpm)
LV	=	left ventricle/ventricular
LVV	=	left ventricular volume(s)
PFR	=	peak filling rate (ml/sec)
SD	=	standard deviation
STZ	=	streptozotocin
SV	=	stroke volume (µl)

1. Yazici D, Yavuz DG, Toprak A, Deyneli O, Akalin S. Impaired diastolic function and elevated Nt-proBNP levels in type 1 diabetic patients without overt cardiovascular disease. Acta Diabetol 2010 November 12.

2. Marso SP, House JA, Klauss V, Lerman A, Margolis P, Leon MB. Diabetes mellitus is associated with plaque classified as thin cap fibroatheroma: an intravascular ultrasound study. Diab Vasc Dis Res 2010 January;7(1):14-9.

3. Shivu GN, Phan TT, Abozguia K, Ahmed I, Wagenmakers A, Henning A, Narendran P, Stevens M, Frenneaux M. Relationship between coronary microvascular dysfunction and cardiac energetics impairment in type 1 diabetes mellitus. Circulation 2010 March 16;121(10):1209-15.

4. Bronzwaer JG, Paulus WJ. Diastolic and systolic heart failure: different stages or distinct phenotypes of the heart failure syndrome? Curr Heart Fail Rep 2009 December;6(4):281-6.

5. Rodrigues B, McNeill JH. The diabetic heart: metabolic causes for the development of a cardiomyopathy. Cardiovasc Res 1992 October;26(10):913-22.

6. Allan L.Klein , Craig R.Asher. Diseases of the pericardium, restrictive cardiomyopathy, and diastolic dysfunction. In: Eric J.Topol, editor. Textbook of cardiovascular medicine. 3rd ed. Philadelphia: Lippincott Williams & Wilkins; 2007. p. 420-59.

7. Fabri DR, de Paula EV, Costa DS, nnichino-Bizzacchi JM, Arruda VR. Novel insights on the development of atherosclerosis in hemophilia A mouse models. J Thromb Haemost 2011 June 21.

8. Jin J, Zhao Y, Tan X, Guo C, Yang Z, Miao D. An improved transplantation strategy for mouse mesenchymal stem cells in an acute myocardial infarction model. PLoS One 2011;6(6):e21005.

9. Smits AM, van Laake LW, den OK, Schreurs C, Szuhai K, van Echteld CJ, Mummery CL, Doevendans PA, Goumans MJ. Human cardiomyocyte progenitor cell transplantation preserves long-term function of the infarcted mouse myocardium. Cardiovasc Res 2009 August 1;83(3):527-35.

10. Park JH, Yoon JY, Ko SM, Jin SA, Kim JH, Cho CH, Kim JM, Lee JH, Choi SW, Seong IW, Jeong JO. Endothelial progenitor cell transplantation decreases lymphangiogenesis and adverse myocardial remodeling in a mouse model of acute myocardial infarction. Exp Mol Med 2011 June 22.

11. Alsaid H, Bao W, Rambo MV, Logan GA, Figueroa DJ, Lenhard SC, Kotzer CJ, Burgert ME, Willette RN, Ferrari VA, Jucker BM. Serial MRI characterization of the functional and morphological changes in mouse lung in response to cardiac remodeling following myocardial infarction. Magn Reson Med 2011 June 10.

12. Arslan F, Smeets MB, O'Neill LA, Keogh B, McGuirk P, Timmers L, Tersteeg C, Hoefer IE, Doevendans PA, Pasterkamp G, de Kleijn DP. Myocardial ischemia/reperfusion injury is mediated by leukocytic toll-like receptor-2 and reduced by systemic administration of a novel anti-toll-like receptor-2 antibody. Circulation 2010 January 5;121(1):80-90.

13. Bovens SM, te Boekhorst BC, den OK, van de Kolk KW, Nauerth A, Nederhoff MG, Pasterkamp G, ten HM, van Echteld CJ. Evaluation of infarcted murine heart function: comparison of prospectively triggered with self-gated MRI. NMR Biomed 2011 April;24(3):307-15.

14. Heijman E, de GW, Niessen P, Nauerth A, van EG, de GL, Nicolay K, Strijkers GJ. Comparison between prospective and retrospective triggering for mouse cardiac MRI. NMR Biomed 2007 June;20(4):439-47.

15. Piccini JP, Klein L, Gheorghiade M, Bonow RO. New insights into diastolic heart failure: role of diabetes mellitus. Am J Med 2004 March 8;116 Suppl 5A:64S-75S.

16. Zhang H, Morgan B, Potter BJ, Ma L, Dellsperger KC, Ungvari Z, Zhang C. Resveratrol improves left ventricular diastolic relaxation in type 2 diabetes by inhibiting oxidative/nitrative stress: in vivo demonstration with magnetic resonance imaging. Am J Physiol Heart Circ Physiol 2010 October;299(4):H985-H994.

17. Stuckey DJ, Carr CA, Tyler DJ, Aasum E, Clarke K. Novel MRI method to detect altered left ventricular ejection and filling patterns in rodent models of disease. Magn Reson Med 2008 September;60(3):582-7.

18. Nielsen JM, Kristiansen SB, Norregaard R, Andersen CL, Denner L, Nielsen TT, Flyvbjerg A, Botker HE. Blockage of receptor for advanced glycation end products prevents development of cardiac dysfunction in db/db type 2 diabetic mice. Eur J Heart Fail 2009 July;11(7):638-47.

19. Basu R, Oudit GY, Wang X, Zhang L, Ussher JR, Lopaschuk GD, Kassiri Z. Type 1 diabetic cardiomyopathy in the Akita (Ins2WT/C96Y) mouse model is characterized by lipotoxicity and diastolic dysfunction with preserved systolic function. Am J Physiol Heart Circ Physiol 2009 December;297(6):H2096-H2108.

20. Katare R, Caporali A, Emanueli C, Madeddu P. Benfotiamine improves functional recovery of the infarcted heart via activation of pro-survival G6PD/Akt signaling pathway and modulation of neurohormonal response. J Mol Cell Cardiol 2010 October;49(4):625-38.

21. Rajesh M, Mukhopadhyay P, Batkai S, Patel V, Saito K, Matsumoto S, Kashiwaya Y, Horvath B, Mukhopadhyay B, Becker L, Hasko G, Liaudet L, Wink DA, Veves A, Mechoulam R, Pacher P. Cannabidiol attenuates cardiac dysfunction, oxidative stress, fibrosis, and inflammatory and cell death signaling pathways in diabetic cardiomyopathy. J Am Coll Cardiol 2010 December 14;56(25):2115-25.

22. Huynh K, McMullen JR, Julius TL, Tan JW, Love JE, Cemerlang N, Kiriazis H, Du XJ, Ritchie RH. Cardiac-specific IGF-1 receptor transgenic expression protects against cardiac fibrosis and diastolic dysfunction in a mouse model of diabetic cardiomyopathy. Diabetes 2010 June;59(6):1512-20.

23. Asbun J, Villarreal FJ. The pathogenesis of myocardial fibrosis in the setting of diabetic cardiomyopathy. J Am Coll Cardiol 2006 February 21;47(4):693-700.

24. van HL, Hamdani N, Handoko ML, Falcao-Pires I, Musters RJ, Kupreishvili K, Ijsselmuiden AJ, Schalkwijk CG, Bronzwaer JG, Diamant M, Borbely A, van d, V, Stienen GJ, Laarman GJ, Niessen HW, Paulus WJ. Diastolic stiffness of the failing diabetic heart: importance of fibrosis, advanced glycation end products, and myocyte resting tension. Circulation 2008 January 1;117(1):43-51.

10

The effect of leukotriene B4 inhibition on ventricular remodeling following myocardial infarction in mice

In preparation

Sandra M. Bovens[1,2], Pleunie van den Borne[1], Vince C. de Hoog[1], Aryan Vink[3], Cees J.A. van Echteld[1], Dominique P.V. de Kleijn[1,2], and Gerard Pasterkamp[1]

1 Department of Cardiology, University Medical Center Utrecht, Utrecht, the Netherlands.
2 Netherlands Heart Institute (ICIN), Utrecht, the Netherlands
3 Department of Pathology, University Medical Center Utrecht, Utrecht, the Netherlands

ABSTRACT

Background

Myocardial infarction (MI) is most commonly caused by atherosclerotic plaques in the coronary arteries. A sudden expansion or rupture of these plaques can cause a blockade in blood supply to the cardiac muscle, leading to necrosis. Inflammation plays an important role in the debris cleaning and scar formation. Leukotriene B4 (LTB4) is a strong chemoattractant for immune cells and blocking the specific receptor (BLT1) for this metabolite may reduce inflammatory cell infiltration into the myocardium after MI. Less inflammation after MI would have a beneficial effect on ventricular remodeling and subsequently improve cardiac function.

Methods and Results

In 24 healthy C57Bl6 mice LAD ligation was performed to induce an MI. Mice received a BLT1 receptor antagonist (n=12) or vehicle (n=12) via oral gavage for 7 days after MI. In the antagonist group significantly more animals died in the first 4 days after MI compared to the vehicle group (4 versus 0 mice). There was no difference in the numbers of neutrophils between control and treated mice at 3 days. However 3-4 days after MI macrophage content in the infarcted region was higher in the control animals. FACS analysis on peripheral blood, stimulated with LTB4 (7 days after MI), showed lower expression of CD11b on monocytes and neutrophils in the treated mice.

Conclusion

A specific BLT1 receptor antagonist effectively blocks LTB4 mediated immune cell chemotaxis, however the treatment resulted in an increased mortality rate. Further studies are necessary to unravel the mechanism and fine-tune the treatment.

INTRODUCTION

Ischemic heart disease and cerebrovascular disease are the leading causes of death globally, according to the World Health Organization (WHO).[1] Myocardial infarction (MI) is most commonly caused by atherosclerosis in the coronary arteries, where a sudden rupture or expansion of this atherosclerotic plaque blocks the artery and gives rise to myocardial cell death in the territory perfused downstream of the occlusion.[1] The necrotic tissue elicits an inflammatory cascade that will clear the debris and dead cells, and ultimately healing of the myocardium and scar formation.[2] This inflammatory response is necessary for the formation of a scar, however when inflammation is down-regulated cardiac function improves.[3] A strong chemo attractant upregulated in ischemic tissue is leukotriene B4 (LTB4). The receptor for LTB4 is present on macrophages and neutrophils, attracting them to sites of ischemia and it has been shown that LTB4 concentrations in ischemic myocardial tissue peak just before neutrophil infiltration.[4]

Leukotrienes are one of the downstream products of the 5-lypoxygenase (5-LO) pathway and most widely known for their actions during acute inflammation.[5, 6] Leukotriene A4 (LTA4) is one of these leukotrienes and can be converted to LTB4 via the enzyme LTA4 hydrolase. The 5-LO pathway is only present in a limited number of cells, amongst others in macrophages, neutrophils, and mast cells, and only these cells are able to produce and excrete LTA4. However, LTA4 hydrolase is present in other cells as well, such as vascular smooth muscle cells and endothelial cells in atherosclerotic plaques, and therefore, when LTA4 is excreted, they can produce LTB4 as well.[7] LTB4 is one of the most powerful pro-inflammatory products from the 5-LO pathway. There are two receptors known for LTB4, the BLT1 and BLT2 receptors, with BLT1 having high-affinity interactions with LTB4 and present on circulation peripheral blood leukocytes.[5] Binding of LTB4 to the BLT1 receptor results in promotion of leukocyte chemotaxis and the regulation of pro-inflammatory cytokines.[6] We hypothesized that treatment with a specific BLT1 receptor antagonist directly after the induction of an MI will limit the infiltration of inflammatory cells into the myocardium and thereby reduce infarct size and ventricular remodeling.

METHODS

Animals and experimental design

All experiments on 24 male C57Bl6 mice (Harlan, Horst, the Netherlands) were approved by the animal care committee of Utrecht University. Mice were divided into two groups; one group (n=12) received the BLT1 receptor antagonist (LSN2792613, Eli Lilly, Indianapolis, USA) dissolved in 10% w/v acacia (G-9752, Sigma) and 0.05% v/v antifoam (A8582, Sigma) in purified water via oral gavage, twice daily (50mg/kg) for 7 days after MI. The control mice (n=12) received the vehicle only, via oral gavage. At baseline and 7 days after MI blood was collected via mandibular vein puncture for fluorescence-activated cell sorting (FACS). Cardiac MRI was performed at baseline, 7 days and 28 days after MI. After the last experiment the mice were sacrificed and the hearts were excised for further (histological) analysis. Hearts of mice which died earlier (at 1, 4, 8, 15, and 26 days after MI) were excised post mortem and used for histological analysis. Histology of additional control mice (n=4) from a different study, which were terminated 3 days after MI, were used to compare histology of treated mice which died prematurely. These were also C57Bl6 mice operated by the same individual and received no treatment of any kind.

Surgery; myocardial infarction

All mice (10-12 weeks old) were anesthetized with a mixture of fentanyl (Jansen-Cilag; 0.05mg/kg), midazolam (Dormicum, Roche; 5mg/kg), and medetomidine (0.5mg/kg) via an intraperitoneal injection, intubated and ventilated (Harvard Apparatus Inc.) with 100% oxygen. Core body temperature was maintained round 37°C during surgery by continuous monitoring with a rectal thermometer and automatic heating blanket. The chest was opened in the third intercostal space and an 8-0 prolene suture was used to permanently ligate the left coronary artery. The chest was closed and the mice received subcutaneously atipamezole (Antisedan, Pfizer; 2.5mg/kg), flumazenil (Anexate, Roche; 0.5 mg/kg), and buprenorphine (Temgesic, Schering-Plough; 0.1 mg/kg) and allowed to recover from the surgery.

MRI measurements

Mice were anesthetized with 5 vol% isoflurane in a 2:1 mixture of air (0.3 L/min) and oxygen (0.15 L/min) and transferred to a home-built cradle. Anesthesia was maintained with 1.5-2.5 vol% isoflurane to keep the respiratory rate stable. Mice were imaged in a vertical 9.4T, 89mm bore size magnet equipped with 1500 mT/m gradients and connected to an Avance 400 MR system (Bruker BioSpin, Germany) using a quadrature-driven birdcage coil with an inner diameter of 3 cm. ParaVision 4.0 and IntraGate software (Bruker BioSpin, Germany) were used for cine MR acquisition and reconstruction. After orthogonal scout images, short axis cardiac cine MR images were acquired. To cover the entire heart from apex to base, 7-9 slices (baseline) or 8-10 slices (7 and 28 days post MI) were needed. Per slice 15 cardiac frames were reconstructed.

Histology

After the last experiment the mice were sacrificed, hearts rinsed with saline, the left ventricle fixated in 4% formaldehyde and embedded in paraffin. Paraffin sections were stained for Ly-6G (neutrophils, rat-anti-mouse Ly-6G 1:400, Abcam, United Kingdom) and MAC-3 (macrophages, rat-anti-mouse MAC3 1:200, eBioscience, the Netherlands). Sections were deparaffinized and endogenous peroxidase was blocked by 30 minutes incubation in methanol containing 1.5% H_2O_2. Antigen retrieval was performed by 15 minutes boiling in citrate buffer. Sections were pre-incubated with normal goat serum and incubated with the primary antibody for 1 hour at RT. Sections were then incubated for 1 hour (Ly-6G) or 45 minutes (MAC-3) at RT with a biotin labeled secondary antibody (Goat-anti-rat, Southern Biotech, Alabama, USA) followed by 1 hour (Ly-6G) or 30 minutes (MAC-3) incubation with streptavidin-horseradish peroxidase at RT and developed with AEC. Additionally, Hematoxylin/Eosin (HE) and Picrosirius red (PR, collagen) staining was also performed.

Fluorescence-activated cell sorting (FACS)

Blood was collected at baseline, 7 days and 28 days (during termination) after MI. Whole blood was stimulated with LTB4 (Sigma) or PBS (control) for 30 minutes at 37°C followed by staining with FACS antibodies: F4/80-647 (monocytes, eBioscience, the Netherlands), Ly-6G-PE (neutrophils, eBioscience, the Netherlands), CD11b-FITC (Bioconnect, the Netherlands), and CD62L-PE-Cy7 (L-selectin, Abcam, United Kingdom) for 45 minutes at RT in the dark. Erythrocytes were lysed by adding RBC lysis solution for 10 minutes at RT and FACS analysis performed on a Beckman-Coulter F500 (Beckman-Coulter inc). Scatterplots were analyzed with dedicated software (Kaluza, Beckman-Coulter).

Cardiac function analysis

In all mice, dedicated, semi-automatic contour detection software (Qmass, MEDIS, Leiden, The Netherlands) was used for the determination of the end-diastolic volume (EDV) and end-systolic volume (ESV) in the left ventricle (LV). Stroke volume (SV), cardiac output (CO), and ejection fraction (EF) were calculated subsequently.

Statistics

Data are expressed as mean ± SD. Non-parametric test were used to compare groups. P-values of <0.05 were considered significant.

RESULTS

Animals

Due to complications during surgery two mice died (treatment) and in two other mice (vehicle) no infarct was observed, probably due to technical failure. All these mice were excluded from analysis. An overview of all mice included in the study is shown in table 1. Summarized: in the treatment group two mice dead 1 day after MI, three died 4 days after MI, one died 8 days after MI and 1 died 26 days after MI. In the vehicle group only one mouse died, on day 15 after MI. The survival curves are shown in figure 1.

Cardiac Parameters

The results of the cardiac function analyses in the different groups are shown in table 2. Due to the limited number of mice which survived until 28 days after MI, of the treatment group, no valid comparisons can be made between vehicle and treated mice. At 7 days after MI no significant differences in cardiac function parameters can be observed between the treated and vehicle group.

Histology

Histological analysis showed collagen that was present in the infarcted region which was not observed in the remote tissue, present in both groups at day 28. Macrophages were found as early as 3 days after MI in both groups, in the control group more macrophages were present (Figure 2). Neutrophils were not observed or in very limited numbers in the mice which were treated (histology of mice that died prematurely at the time points; 1, 4, 8, and 26 days after MI) as well as the control mice (3 and 15 days after MI).

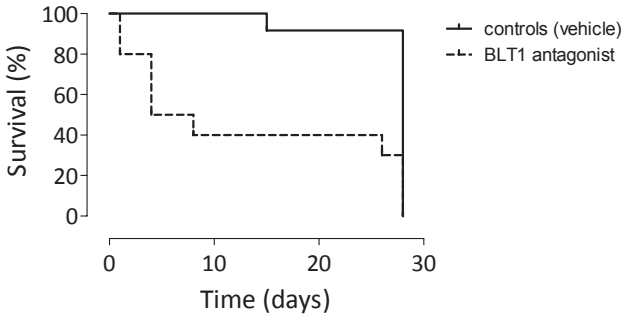

Figure 1 | *Survival plot.*
The mice treated with the BLT1 receptor antagonist are shown with an intermittent line, the mice receiving vehicle only are shown with a continuous line.

In figure 2 images of the macrophage staining of a treated mouse (died at 4 days after MI (A)) and a control mouse (B) are shown.

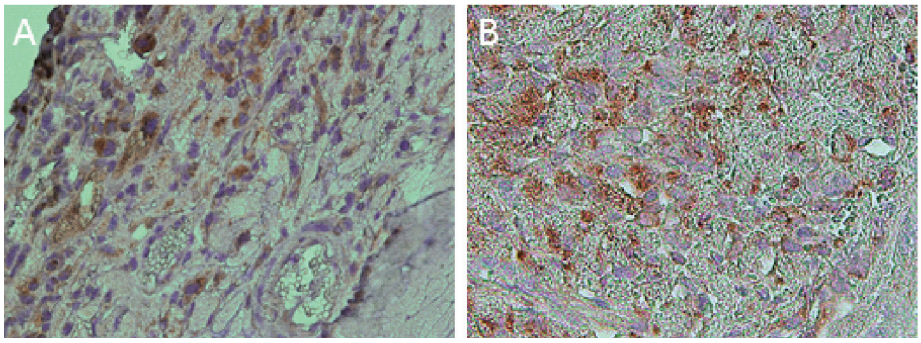

Figure 2 | *Macrophage staining.*
MAC-3 (macrophages) staining in brown/red (AEC) in the infarcted myocardium of a mouse treated with a BLT1 receptor antagonist (A; 4 days after MI) and of a control mouse (B; 3 days after MI).

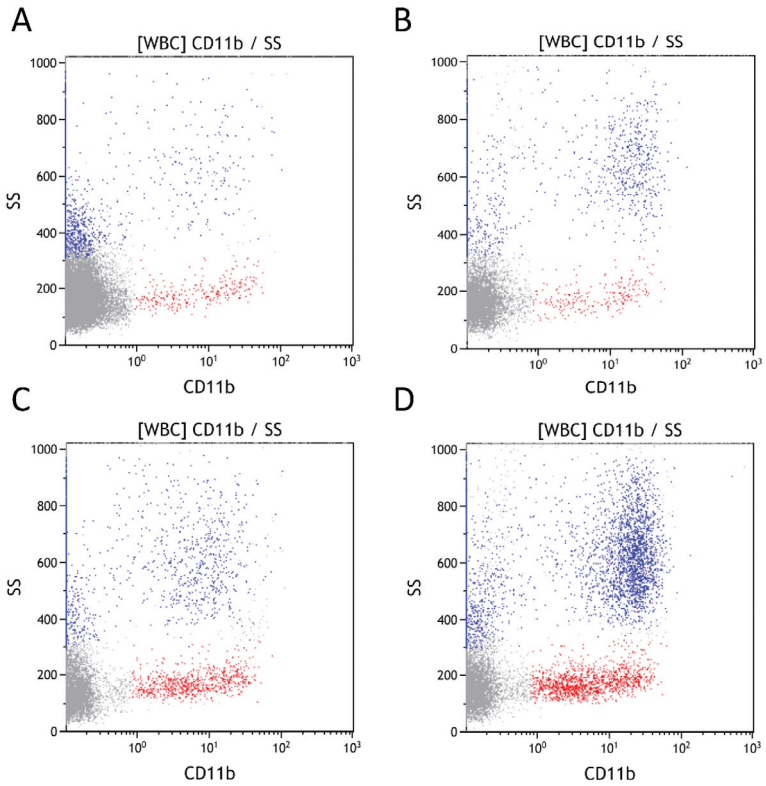

Figure 3 | *FACS analysis blood at 7 days after MI*
Stimulated blood of treated (A+B) and vehicle (C+D) mice, stimulation with PBS as a control shown in A and C, LTB4 stimulation is shown in B and D. It can be seen that a diminished response to LTB4 is present in mice treated with a BLT1 receptor antagonist when compared to untreated (vehicle) mice. y-axis: Sideward scatter, x-axis: CD11b expression, blue: neutrophils, red: monocytes

FACS

In figure 3 scatterplots (sideward scatter (y-axis) and CD11b (x-axis)) typical examples are shown of mice from the treated (A+B) and vehicle (C+D) group, stimulated with PBS (control, A+C) or LTB4 (B+D), measured at day 7 after MI. In the mouse from the vehicle group an increase in CD11b expression (activation marker) can be observed in the neutrophil as well as the monocyte population when the blood was stimulated with LTB4. In the mouse treated with the BLT1 receptor antagonist CD11b expression is only slightly increased, suggesting that the BLT1 receptor antagonist bound and LTB4 could no longer activate immune cells (monocytes and neutrophils).

Table 1 | Overview mice and survival

Mouse number	group	survival (in days)	COD	Mouse number	group	survival (in days)	COD
1	vehicle	15	MI	13	treatment	1	rupture MI
2	vehicle	28		14	treatment	1	rupture MI
3	vehicle	28		15	treatment	4	terminated
4	vehicle	28		16	treatment	4	rupture MI
5	vehicle	28		17	treatment	4	rupture MI
6	vehicle	28		18	treatment	8	terminated
7	vehicle	28		19	treatment	26	MI
8	vehicle	28		20	treatment	28	
9	vehicle	28		21	treatment	28	
10	vehicle	28		22	treatment	28	
11	vehicle	28	no infarct	23	treatment	0	OC
12	vehicle	28	no infarct	24	treatment	0	OC

All mice are shown, in both groups 2 mice were excluded due to no infarct (vehicle) or OR related death (vehicle), they are listed last per group. Mice which survived until day 28 were then terminated at the end of the MRI scan, no COD is listed. OC includes cardiac arrhythmia or heart failure due to the LAD ligation.
COD: cause of death; MI: myocardial infarction; terminated: humane endpoint termination; OC: operation complication; LAD: left anterior descending coronary artery.

Table 2 | Overall cardiac function

	Baseline (n=24)	Vehicle 7 days (n=10)	Treated 7 days (n=6)	Vehicle 28 days (n=9)	Treated 28 days (n=3)
EDV (µl)	45.00 ± 4.2	131.03 ±22.5	116.06 ± 36.5	152.42 ± 47.5	116.17 ± 48.0
ESV (µl)	16.22 ± 2.5	111.65 ± 23.7	96.51 ± 41.0	123.99 ± 53.3	87.73 ± 54.0
SV (µl)	28.78 ± 3.3	19.38 ± 3.9	19.55 ± 4.7	28.43 ± 11.1	28.45 ± 6.8
CO (ml/min)	13.65 ± 1.8	9.98 ± 2.6	9.08 ± 3.0	13.75 ±5.1	14.48 ± 3.1
EF (%)	63.97 ± 4.4	15.37 ± 5.3	19.79 ± 11.5	21.86 ± 16.5	28.21 ± 13.8
LV MRI Mass (mg)	64.51 ± 6.5	65.83 ± 15.7	59.38 ± 21.1	55.12 ± 22.4	63.04 ± 37.3
BW (grams)	23.51 ± 1.1	23.89 ± 1.1	21.93 ± 2.47	27.07 ± 1.1	26.93 ± 1.4
HR	476 ± 52	512 ± 50	463 ± 93	487 ± 22.4	511 ± 14.2

Cardiac function shown for baseline (n=24), 7 days after MI, and 28 days after MI for vehicle and treatment (BLT1 receptor antagonist) groups. At baseline all mice were pooled together. In both the treatment group and the vehicle group 2 mice were excluded from analysis. No significant differences were found between the groups.
EDV: end-diastolic volume; ESV: end-systolic volume; SV: stroke volume; CO: cardiac output; EF: ejection fraction; LV: left ventricular; BW: body weight; HR: heart rate.

DISCUSSION

In this study we showed that treatment with a specific BLT1 receptor antagonist is effectively blocking LTB4 mediated macrophage and neutrophil activation in peripheral blood from treated mice (FACS analysis), however the treatment resulted in an increased mortality.

After a myocardial infarction restoration of blood flow is essential, however, there is usually still an area of the myocardium which consists of dead cells, which cannot be revived by reperfusion. The size and location of this infarct area are determinants of cardiac function and ventricular remodeling, the immune systems plays an important role in both the formation of a scar as well as ventricular remodeling. Defects in the healing phase of an infarct can have detrimental effects, such as cardiac rupture and ventricular aneurysm development.[7] A treatment which could stimulate the healing phase and attenuate the adverse remodeling would be of great help in increasing cardiac function, since ventricular dilation is a predictor of mortality and adverse cardiac events, such as ventricular arrhythmias.[8-10] In our study we unfortunately may have blocked the inflammatory response either too early or too strongly. Neutrophils could not be observed in the myocardium of the treated mice that unexpectedly died during follow up or control mice. However, macrophages were observed, even in the treated mice, al be it in lower numbers, starting at 3-4 days after MI. It might be that the macrophages initiate debris cleaning and produce cytokines and growth factors necessary for scar formation. After 4 days the follow up of treated and non treated mice did not reveal further increases in unexpected major events.

We used a model with a permanent LAD ligation, there is no reperfusion restoration, which would often take place in the human setting. In another murine model, with cardiac ischemia/ reperfusion (I/R) injury, myocardial neutrophil infiltration can be observed quickly after reperfusion.[11] It might be that experiments with this model yield different results since LTB4 is a strong neutrophil chemo attractant and neutrophils play a more important role in I/R injury then in the permanent LAD ligation model.

At 7 and 28 days after MI no significant differences were observed between the treated and control group, this is most likely due to the low number in the treatment group, the infarcts of these mice were smaller, this is probably a biased results and might well be the reason for their survival until day 28.

Conclusion

An additional study, in which the mice will start treatment at 3 days after MI, will be necessary to evaluate whether blocking the BLT1 receptor has detrimental effects on the mortality rate. Maybe, in our study, the mice died due to the early start of the treatment and it might be that the treatment could be beneficial for ventricular remodeling when the initial inflammation is not disturbed and treatment is started after 3 days. Additional experiments with the BLT1 receptor antagonist in the I/R model could be used to study the effects of limited neutrophil infiltration on infarct size.

Acknowledgments

The authors would like to thank the following people for their excellent technical assistance: Ben van Middelaar, Maringa Emons and Petra van der Kraak. We would also like to thank Eli Lilly and Company for providing the BLT1 receptor antagonist (LSN2792613).

ABBREVIATIONS

CO	=	cardiac output
EDV	=	end diastolic volume(s)
EF	=	ejection fraction
ESV	=	end systolic volume(s)
HR	=	heart rate
LV	=	left ventricle/ventricular
LVV	=	left ventricular volume(s)
MI	=	myocardial infarction
SD	=	standard deviation
SV	=	stroke volume

1. Kim AS, Johnston SC. Global variation in the relative burden of stroke and ischemic heart disease. Circulation 2011 July 19;124(3):314-23.

2. Frangogiannis NG. The immune system and cardiac repair. Pharmacol Res 2008 August;58(2):88-111.

3. Arslan F, Smeets MB, O'Neill LA, Keogh B, McGuirk P, Timmers L, Tersteeg C, Hoefer IE, Doevendans PA, Pasterkamp G, de Kleijn DP. Myocardial ischemia/reperfusion injury is mediated by leukocytic toll-like receptor-2 and reduced by systemic administration of a novel anti-toll-like receptor-2 antibody. Circulation 2010 January 5;121(1):80-90.

4. Williams FM. Neutrophils and myocardial reperfusion injury. Pharmacol Ther 1996;72(1):1-12.

5. Li RC, Haribabu B, Mathis SP, Kim J, Gozal D. Leukotriene B4 receptor-1 mediates intermittent hypoxia-induced atherogenesis. Am J Respir Crit Care Med 2011 July 1;184(1):124-31.

6. Spite M, Hellmann J, Tang Y, Mathis SP, Kosuri M, Bhatnagar A, Jala VR, Haribabu B. Deficiency of the leukotriene B4 receptor, BLT-1, protects against systemic insulin resistance in diet-induced obesity. J Immunol 2011 August 15;187(4):1942-9.

7. Poeckel D, Funk CD. The 5-lipoxygenase/leukotriene pathway in preclinical models of cardiovascular disease. Cardiovasc Res 2010 May 1;86(2):243-53.

8. St John SM, Lee D, Rouleau JL, Goldman S, Plappert T, Braunwald E, Pfeffer MA. Left ventricular remodeling and ventricular arrhythmias after myocardial infarction. Circulation 2003 May 27;107(20):2577-82.

9. St John SM, Pfeffer MA, Plappert T, Rouleau JL, Moye LA, Dagenais GR, Lamas GA, Klein M, Sussex B, Goldman S, . Quantitative two-dimensional echocardiographic measurements are major predictors of adverse cardiovascular events after acute myocardial infarction. The protective effects of captopril. Circulation 1994 January;89(1):68-75.

10. White HD, Norris RM, Brown MA, Brandt PW, Whitlock RM, Wild CJ. Left ventricular end-systolic volume as the major determinant of survival after recovery from myocardial infarction. Circulation 1987 July;76(1):44-51.

11. Arslan F, de Kleijn DP, Timmers L, Doevendans PA, Pasterkamp G. Bridging innate immunity and myocardial ischemia/reperfusion injury: the search for therapeutic targets. Curr Pharm Des 2008;14(12):1205-16.

11

General Discussion

The objective of the research described in this thesis was to investigate new applications of (pre)-clinical cardiovascular (molecular) magnetic resonance imaging, in both mice and men. We focused on atherosclerotic plaque characterization and heart failure.

PART I
ATHEROSCLEROSIS AND (MOLECULAR) IMAGING

In part I we focused on atherosclerosis; we discussed studies concerning molecular imaging in mice and spectroscopy as well as high field imaging in humans.

Molecular imaging has gained increasing interest in the research field of cardiovascular diseases the last couple of years, mainly since atherosclerotic plaque composition seems to be important as a predictor for clinical events, even more so than the degree of stenosis.[1] In chapter 2 we showed the current status of carotid artery plaque imaging with MRI. We described that at present no consensus has been reached yet to standardize carotid artery plaque imaging, although this has been suggested earlier.[2] Most of the research described in chapter 2 aimed to improve specificity and sensitivity of component specific sequences. It has recently been shown that the presence of local intra-plaque hemorrhage or increased intra-plaque vessel formation is associated with an increased risk for cardiovascular events in other vascular plaques.[3] In contrast, the presence of local large lipid core, macrophages, collagen, smooth muscle cell infiltration, and calcifications did not show an increased risk for events originating from arterial plaques in other organs. Since intra-plaque hemorrhage is often diffusely present in large lipid cores and difficult to differentiate using imaging techniques, development of specific sequences aimed at the detection of components only present in intra-plaque hemorrhage have gained interest. Moody *et al*.[4] developed such a sequence which detects the methemoglobin present in subacute thrombus. In a more recent study they used this sequence to detect intra-plaque hemorrhage and related it to microembolic signals during dissection of the carotid plaque. The association between carotid intra-plaque hemorrhage and the presence of dissection phase microembolic signals was significant (p=0.007 with an odds ratio of 5.6).[5]

For the detection of intra-plaque vessel density a sequence combined with a contrast agent (Gadolinium) was evaluated[6, 7] and the rate of uptake of this contrast agent in the atherosclerotic plaque was related to the amount of microvessels present in the plaque. The use of contrast agents can add value to MR imaging, in chapter 2 we also discussed the development of testing several contrast agents (targeted and untargeted) in murine models of atherosclerosis. The evaluation of these new contrast agents is very important, however choosing the correct histological evaluation method might be of similar importance, to rule out false-positive results. Most contrast agents had a fluorescent label incorporated, which would result in detection of the contrast agent in histological slides, however, several problems arose. First, auto-fluorescence of the atherosclerotic plaque components could be observed in several wave lengths and switching to another fluorescent label at a different wavelength could solve this problem when using $ApoE^{-/-}$ mice. However, when using a more severe murine model of atherosclerosis, $ApoE^{-/-}/eNOS^{-/-}$ mice, auto-fluorescence could be observed in the whole spectrum, making tracing of contrast agents with fluorescent labels impossible. In chapter 4 we offered a solution for this problem, using a staining directed against the antibodies which were coated on the contrast agent (micelles). In this study we used antibodies to detect neutrophil gelatinase-associated lipocalin (NGAL), a marker for vulnerable/inflamed atherosclerotic lesions, since NGAL is mainly excreted by neutrophils and

macrophages and acts as a stabilizer for metalloproteinase-9 (MMP-9), which breaks down collagen.[8] When using (targeted) contrast agents it is important, for correct interpretation of the data, to know their pharmacokinetic and pharmacodynamic properties. There are enormous differences in half live of contrast agents, depending on their content, (ultra)small particles of iron oxide ((U)SPIO) which are used as a T2(*) contrast agent are cleared fairly quickly (~1.5 hours). In contrast, micelles and liposomes, which are usually coated with PEG-lipids, have longer blood circulation times (half life micelles ~22 hours, liposomes ~7 hours[9]). When contrast agents are coated with antibodies or (ant)agonists their blood circulation times would decline, this is most likely due to earlier recognition by the hosts immune system. Blood circulation times could potentially also differ between different atherosclerotic models; we therefore studied the behavior of untargeted and agonist-coated micelles in $ApoE^{-/-}$/$eNOS^{-/-}$ mice in chapter 3. We used a specific cannabinoid receptor 2 (CB_2) agonist, HU-308[10], which was incorporated into micelles. The untargeted and agonist-coated micelles were injected into $ApoE^{-/-}$/$eNOS^{-/-}$ mice and followed with MRI up to 48 hours after injection. Only after 42 and 48 hours a significant difference in uptake in the atherosclerotic plaque between the agonist-coated and untargeted micelles could be observed. This implied that imaging before 42 hours after injection could yield a false positive result since unbound micelles could still be present in the plaque before that time. For the translation into clinical practice this might pose a problem, since the patients would have to wait for 42 hours after their injection to receive the post-contrast scan while ideally imaging should be executed as fast as possible after injection. An alternative solution for this slow wash-out of unbound contrast agents was suggested by van Tilborg *et al*.[11] The authors incorporated a biotin-lipid into liposomes, which gave the opportunity to use a so-called avidin chase, leading to rapid clearance of unbound liposomes from the circulation. This created the possibility to perform the post-contrast image after a few hours. However, the authors tested their contrast agent in a tumor model, which would allow fast accumulation and good detection with MRI of the targeted contrast agent due to the large surface in which the contrast agent would be present. In atherosclerotic lesions the targets are usually present in smaller numbers and an increased accumulation of the contrast agent would be necessary to allow accurate detection with MRI.

The non-contrast applications with MRI in human atherosclerosis have been improved as well, since higher field MR scanners became more widely available, more sequences were, and still are, being developed, aimed at improvement of spatial resolution as well as the decrease in scan time. We described a study setup at the 7 Tesla MR scanner to evaluate MR images with histology and compare carotid artery atherosclerotic plaque components with brain damage. The 7 Tesla MR scanner already showed superior detection of micro-infarcts and micro-bleeds in the brain[12] and we suspected that 7 Tesla MRI could also provide additional information when imaging the carotid artery plaque. The preliminary results showed appropriate geometrical depiction of the atherosclerotic plaques, with T2W/PDW sequences. However, correlation with histology and a larger study group would be necessary to make any inferences on the benefit of a 7 Tesla scan to stratify patients eligible for carotid endarterectomy (CEA) surgery.

Another non-invasive method, using MR scanners, to evaluate atherosclerotic plaque was discussed in chapter 5. Using ^{1}H-NMR spectroscopy, metabolites present in atherosclerotic plaques could be evaluated. This technique has been used to detect and quantify metabolites in e.g. urine, cerebrospinal fluid, blood, and plasma.[13, 14] We used tissue homogenates of human atherosclerotic plaques, obtained during femoral endarterectomy, to evaluate the metabolite lactate as a surrogate marker for plaque

hypoxia. Atherosclerotic plaque hypoxia is the main drive for the formation of intra-plaque neovessels[15, 16] and subsequently a predictor for increased risk of plaque rupture. We showed that lactate is correlated with a histological marker of hypoxia, hypoxia inducible factor 1α (HIF-1α), and atherosclerotic plaque vessel density. Additional research will be necessary before this technique could be evaluated *in vivo*, mainly improvement of the technical aspects; for ^{1}H-NMR spectroscopy a voxel needs to be placed on the area of interest, these voxels need to have an adequate size to ensure a high enough signal of the metabolite of interest. Atherosclerotic plaques are relatively small and the placement of the voxel has to be completely inside the plaque, since perivascular fat can disturb the measurement of lactate due to the overlap in spectra.[17]

PART II
CARDIAC IMAGING

Part II focused on cardiac MRI in murine models of heart failure and myocardial infarction. Animal models are widely used as models of cardiovascular diseases, murine models in particular since they are relatively cheap and knock-out or knock-in models can be created to study specific gene involvement. To non-invasively determine cardiac function, with the possibility of long term follow-up, cardiac MRI is often used. High magnetic field scanners, such as 9.4 or even 11.7 Tesla, specifically designed for small animals, are widely available. In humans, ECG triggering is often used, this is very difficult in mice, due to their high heart rate and the disturbance created by the high magnetic field. We described an alternative for the use of ECG electrodes in mice, when performing MRI at 9.4 Tesla in chapter 8. We evaluated a so-called self-gated sequence, in this sequence a navigator was incorporated, the first echo was used to determine cardiac motion as well as breathing motion. The data was collected continuously and cardiac movies were reconstructed retrospectively. We tested the sequence in a model of murine myocardial infarction, in which the left coronary artery is ligated permanently as well as in healthy control mice and compared the results of cardiac function to the original prospectively gated sequence. The results in cardiac function were comparable in both sequences, however, the self-gated sequence proved to be more time efficient.[18] The self-gated sequence would also give the possibility to study not only systolic dysfunction, but also diastolic dysfunction. As a gold standard, diastolic dysfunction is evaluated with Doppler echocardiography; however, since MRI is often used a tool for the determination of cardiac function an MRI method to evaluate diastolic cardiac function could be useful. We decided to use a murine model in which we used streptozotocin (STZ) to induce diabetes. The main advantage of this model was that the exact day the mice became diabetic was known, giving the opportunity to start with baseline, non-diabetic, diastolic cardiac function measurements. Additionally, diastolic dysfunction developed slowly, so we could image mice suffering from early diastolic dysfunction up to cardiac hypertrophy. MRI showed to be able to detect early disturbed filling patterns at 4 weeks of diabetes, which resulted in cardiac hypertrophy at 12 weeks of diabetes in some mice. For possible future evaluation of pharmaceutical treatment aimed at prevention of systolic heart failure and possibly even reduction of diastolic dysfunction, this model could be very useful. For example, Katare *et al*. showed that the use of a vitamin B analogue can prevent diastolic dysfunction in type I and type II diabetic mouse models. [19]

Future perspectives

MRI is already frequently applied in all fields of cardiovascular research and in clinical evaluation. The increasing use is mainly due to its non-invasive nature and ability to differentiate between all sorts of tissues. The main drawback is the relatively low sensitivity for contrast agents, which is decreasing even more at higher magnetic fields. With the development of targeted contrast agents to visualize the vulnerable atherosclerotic plaque MRI will probably become even more important in the future, when clinical decision making is based on atherosclerotic plaque composition and not only on the degree of stenosis. There is a need to develop less toxic contrast agents, especially for patients with decreased kidney function and hopefully 'smarter' and more sensitive contrast agents will be developed for this purpose as well. An added value could most definitely be in combined imaging techniques, such as MRI/SPECT, in which the anatomical detail of MRI and high sensitivity of SPECT tracers can be combined.

Solutions to circumvent immunological problems with antibody-coated contrast agents that have already been developed, such as the llama-antibodies, which are very small compared to other antibodies, could be the future of targeted contrast agents, next to the synthetic ligands, which also have lower immunogenic properties.

The development of sequences to detect specific plaque components in humans without the need of contrast agents will hopefully continue to be improved as well, especially with the increasing availability of the promising higher magnetic field scanners, such as the 7 Tesla, and even the 9.4 Tesla human scanners.

Conclusions

The goal of this thesis was to address new applications of (pre)-clinical cardiovascular (molecular) magnetic resonance imaging, in mice and men. MRI is an imaging modality that undergoes a fast evolution and that will become more widely applied in preclinical and clinical cardiovascular science and diagnostic research. For vascular wall imaging some major hurdles still exist. Specifically standardization of imaging procedures and the development of non toxic contrast agents will be a major challenge for future research.

1. Wasserman BA, Wityk RJ, Trout HH, III, Virmani R. Low-grade carotid stenosis: looking beyond the lumen with MRI. Stroke 2005 November;36(11):2504-13.

2. Lovett JK, Gallagher PJ, Rothwell PM. Reproducibility of histological assessment of carotid plaque: implications for studies of carotid imaging. Cerebrovasc Dis 2004;18(2):117-23.

3. Hellings WE, Peeters W, Moll FL, Piers SR, van SJ, Van der Spek PJ, de Vries JP, Seldenrijk KA, De Bruin PC, Vink A, Velema E, de Kleijn DP, Pasterkamp G. Composition of carotid atherosclerotic plaque is associated with cardiovascular outcome: a prognostic study. Circulation 2010 May 4;121(17):1941-50.

4. Moody AR. Magnetic resonance direct thrombus imaging. J Thromb Haemost 2003 July;1(7):1403-9.

5. Altaf N, Beech A, Goode SD, Gladman JR, Moody AR, Auer DP, MacSweeney ST. Carotid intraplaque hemorrhage detected by magnetic resonance imaging predicts embolization during carotid endarterectomy. J Vasc Surg 2007 July;46(1):31-6.

6. Kerwin WS, O'Brien KD, Ferguson MS, Polissar N, Hatsukami TS, Yuan C. Inflammation in carotid atherosclerotic plaque: a dynamic contrast-enhanced MR imaging study. Radiology 2006 November;241(2):459-68.

7. Kerwin W, Hooker A, Spilker M, Vicini P, Ferguson M, Hatsukami T, Yuan C. Quantitative magnetic resonance imaging analysis of neovasculature volume in carotid atherosclerotic plaque. Circulation 2003 February 18;107(6):851-6.

8. te Boekhorst BC, Bovens SM, Hellings WE, van der Kraak PH, van de Kolk KW, Vink A, Moll FL, van Oosterhout MF, de Vries JP, Doevendans PA, Goumans MJ, de Kleijn DP, van Echteld CJ, Pasterkamp G, Sluijter JP. Molecular MRI of murine atherosclerotic plaque targeting NGAL: a protein associated with unstable human plaque characteristics. Cardiovasc Res 2011 February 15;89(3):680-8.

9. van Bochove GS, Paulis LE, Segers D, Mulder WJ, Krams R, Nicolay K, Strijkers GJ. Contrast enhancement by differently sized paramagnetic MRI contrast agents in mice with two phenotypes of atherosclerotic plaque. Contrast Media Mol Imaging 2011 January;6(1):35-45.

10. Hanus L, Breuer A, Tchilibon S, Shiloah S, Goldenberg D, Horowitz M, Pertwee RG, Ross RA, Mechoulam R, Fride E. HU-308: a specific agonist for CB(2), a peripheral cannabinoid receptor. Proc Natl Acad Sci U S A 1999 December 7;96(25):14228-33.

11. van Tilborg GA, Mulder WJ, van der Schaft DW, Reutelingsperger CP, Griffioen AW, Strijkers GJ, Nicolay K. Improved magnetic resonance molecular imaging of tumor angiogenesis by avidin-induced clearance of nonbound bimodal liposomes. Neoplasia 2008 December;10(12):1459-69.

12. van der Kolk AG, Hendrikse J, Zwanenburg JJ, Visser F, Luijten PR. Clinical applications of 7T MRI in the brain. Eur J Radiol 2011 September 19.

13. Teul J, Ruperez FJ, Garcia A, Vaysse J, Balayssac S, Gilard V, Malet-Martino M, Martin-Ventura JL, Blanco-Colio LM, Tunon J, Egido J, Barbas C. Improving metabolite knowledge in stable atherosclerosis patients by association and correlation of GC-MS and 1H NMR fingerprints. J Proteome Res 2009 December;8(12):5580-9.

14. Imamura A, Matsuo N, Ariki M, Horikoshi H, Hattori T. MR imaging and 1H-MR spectroscopy in a case of cerebral infarction with transient cerebral arteriopathy. Brain Dev 2004 December;26(8):535-8.

15. Sluimer JC, Gasc JM, van Wanroij JL, Kisters N, Groeneweg M, Sollewijn G, Cleutjens JP, van den Akker LH, Corvol P, Wouters BG, Daemen MJ, Bijnens AP. Hypoxia, hypoxia-inducible transcription factor, and macrophages in human atherosclerotic plaques are correlated with intraplaque angiogenesis. J Am Coll Cardiol 2008 April 1;51(13):1258-65.

16. Sluimer JC, Daemen MJ. [New understanding of the onset of atherosclerosis--angiogenesis and hypoxia play a crucial role]. Ned Tijdschr Geneeskd 2009;153:A847.

17. Vinitski S, Griffey RH, Szumowski J, Matwiyoff NA. Lactate observation in vivo by spectral editing in real time. Magn Reson Imaging 1988 November;6(6):707-11.

18. Bovens SM, te Boekhorst BC, den OK, van de Kolk KW, Nauerth A, Nederhoff MG, Pasterkamp G, ten HM, van Echteld CJ. Evaluation of infarcted murine heart function: comparison of prospectively triggered with self-gated MRI. NMR Biomed 2011 April;24(3):307-15.

19. Katare R, Caporali A, Emanueli C, Madeddu P. Benfotiamine improves functional recovery of the infarcted heart via activation of pro-survival G6PD/Akt signaling pathway and modulation of neurohormonal response. J Mol Cell Cardiol 2010 October;49(4):625-38.

12

Summary

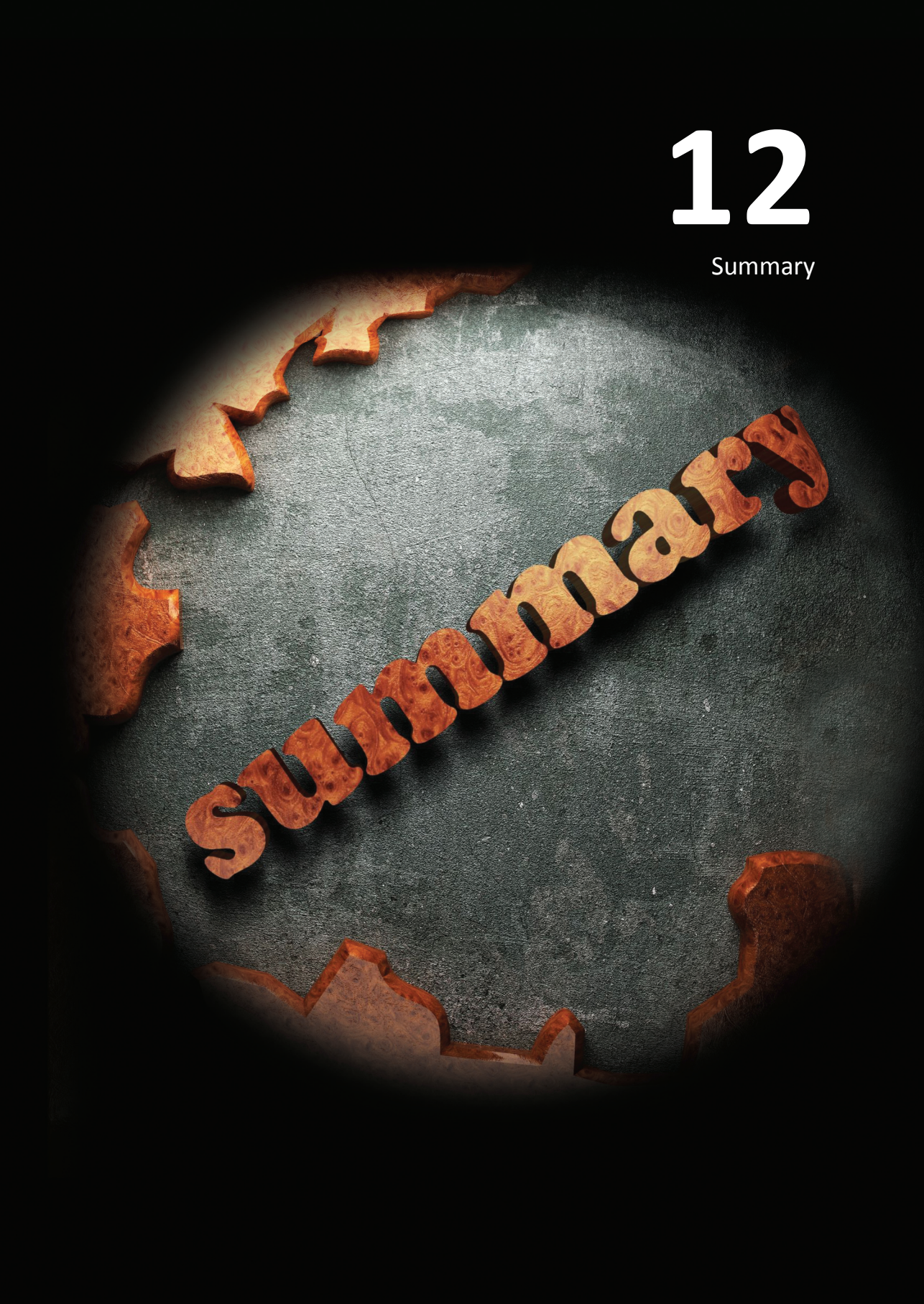

Magnetic resonance imaging (MRI) is one of the most applied imaging techniques in the medical world. This non-invasive technique is widely implemented in almost every medical specialty as well as in their respective fields of research, such as oncology, neurology, orthopedics, psychiatry, and cardiology, due to for example its ability to differentiate between several types of soft tissues and provide functional analysis of specific organs, like the brain and the heart.[1-6] Cardiac MRI (CMR) has many applications. It can be used to assess general cardiac function, for the left as well as the right ventricle, in which the heart is imaged by stacking a number of slices to cover the entire atrium and create cine images per slice with ECG triggering to calculate volumes.[6] The study of the right ventricle can be challenging due to the complex shape, however, some CMR sequences can be performed to create a 3D reconstruction, that facilitates a more accurate evaluation of right ventricular function and morphology.[7] Recently, several studies have been performed to visualize the geometry of the coronary arteries also by the use of 3D MRI.[8, 9]

The objective of the research described in this thesis was to investigate new applications of (pre)-clinical cardiovascular (molecular) magnetic resonance imaging, in both mice and men. We focused on atherosclerotic plaque characterization and heart failure.

PART I
ATHEROSCLEROSIS AND (MOLECULAR) IMAGING

In part I we focused on atherosclerosis; we discussed studies concerning molecular imaging in mice and spectroscopy as well as high field imaging in humans. Molecular imaging has gained increasing interest in the research field of cardiovascular diseases the last couple of years, mainly since atherosclerotic plaque composition seems to be important as a predictor for clinical events, even more so than the degree of stenosis.[10] In **chapter 2** we described the current state of carotid artery plaque imaging with MRI. At present no consensus has been reached yet to standardize carotid artery plaque imaging, although this has been suggested earlier.[11] It has recently been shown that the presence of local intra-plaque hemorrhage or increased intra-plaque vessel density is associated with an increased risk for cardiovascular events in other vascular plaques.[12] Since intra-plaque hemorrhage is often diffusely present in large lipid cores and difficult to differentiate using imaging techniques, development of specific sequences aimed at the detection of components only present in intra-plaque hemorrhage have gained interest. Moody *et al*. developed such a sequence which detects the methemoglobin present in subacute thrombus.[13]

For the detection of intra-plaque vessel density a sequence combined with a contrast agent (Gadolinium) was evaluated[14, 15] and the rate of uptake of this contrast agent in the atherosclerotic plaque was related to the amount of microvessels present in the plaque. The use of contrast agents can add value to MR imaging. In **chapter 2** we also discussed the development of testing several contrast agents (targeted and untargeted) in murine models of atherosclerosis. The evaluation of these new contrast agents is very important, however choosing the correct histological evaluation method might be of similar importance, to rule out false-positive results. In **chapter 4** we used antibodies to detect neutrophil gelatinase-associated lipocalin (NGAL), a marker for vulnerable/inflamed atherosclerotic lesions, since NGAL is mainly excreted by neutrophils and macrophages and acts as a stabilizer for metalloproteinase-9 (MMP-9), which breaks down collagen.[16] When using (targeted) contrast agents it is important, for correct interpretation of the data, to know their pharmacokinetic and pharmacodynamic properties.

There are enormous differences in half live of contrast agents, depending on their content. In **chapter 7** we used (ultra)small particles of iron oxide ((U)SPIO), mostly used as a T2(*) contrast agent, these are cleared fairly quickly (~1.5 hours). In contrast, micelles and liposomes, which are usually coated with PEG-lipids, have longer blood circulation times (half life micelles ~22 hours, liposomes ~7 hours[17]). When contrast agents are coated with antibodies or (ant)agonists their blood circulation times would decline, this is most likely due to earlier recognition by the immune system of the host. Blood circulation times could potentially also differ between different atherosclerotic models. We studied the behavior of untargeted and agonist-coated micelles in $ApoE^{-/-}$/$eNOS^{-/-}$ mice in **chapter 3**. We used a specific cannabinoid receptor 2 (CB2) agonist, HU-308[18], which was incorporated into micelles. The untargeted and agonist-coated micelles were injected into $ApoE^{-/-}$/$eNOS^{-/-}$ mice and followed with MRI up to 48 hours after injection. Only after 42 and 48 hours a significant difference in uptake in the atherosclerotic plaque between the agonist-coated and untargeted micelles could be observed. This implied that imaging before 42 hours after injection could yield a false positive result since unbound micelles could still be present in the plaque before that time.

The non-contrast applications with MRI in human atherosclerosis have been improved as well, since higher field MR scanners became more widely available, more sequences were, and still are, being developed, aimed at improvement of spatial resolution as well as the decrease in scan time. We described a study setup at the 7 Tesla MR scanner to evaluate MR images with histology and compare carotid artery atherosclerotic plaque components with brain damage. The 7 Tesla MR scanner already showed superior detection of micro-infarcts and micro-bleeds in the brain[19] and we suspected that 7 Tesla MRI could also provide additional information when imaging the carotid artery plaque.

In **chapter 6** the preliminary results showed appropriate geometrical depiction of the atherosclerotic plaques, with T2W/PDW sequences. However, correlation with histology and a larger study group would be necessary to make any inferences on the benefit of a 7 Tesla scan to stratify patients eligible for carotid endarterectomy (CEA) surgery.

Another non-invasive method, using MR scanners, to evaluate atherosclerotic plaque was discussed in **chapter 5**. Using ^{1}H-NMR spectroscopy, metabolites present in atherosclerotic plaques could be evaluated. This technique has been used to detect and quantify metabolites in e.g. urine, cerebrospinal fluid, blood, and plasma.[20, 21] We used tissue homogenates of human atherosclerotic plaques, obtained during femoral endarterectomy, to evaluate the metabolite lactate as a surrogate marker for plaque hypoxia. Atherosclerotic plaque hypoxia is the main drive for the formation of intra-plaque neovessels[22, 23] and subsequently a predictor for increased risk of plaque rupture. We showed that lactate is correlated with a histological marker of hypoxia, hypoxia inducible factor 1α (HIF-1α), and atherosclerotic plaque vessel density. Additional research will be necessary before this technique could be evaluated *in vivo*, mainly improvement of the technical aspects; for ^{1}H-NMR spectroscopy a voxel needs to be placed on the area of interest, these voxels need to have an adequate size to ensure a high enough signal of the metabolite of interest. Atherosclerotic plaques are relatively small and the placement of the voxel has to be completely inside the plaque, since perivascular fat can disturb the measurement of lactate due to the overlap in spectra.[24]

PART II
CARDIAC IMAGING

Part II focused on cardiac MRI in murine models of heart failure and myocardial infarction. Animal models are widely used as models of cardiovascular diseases, murine models in particular since they are relatively cheap and knock-out or knock-in models can be created to study specific gene involvement. To non-invasively determine cardiac function, with the possibility of long term follow-up, cardiac MRI is often used. High magnetic field scanners, such as 9.4 or even 11.7 Tesla, specifically designed for small animals, are widely available. In humans, ECG triggering is often used, this is very difficult in mice, due to their high heart rate and the disturbance created by the high magnetic field. We described an alternative for the use of ECG electrodes in mice, when performing MRI at 9.4 Tesla in **chapter 8**. We evaluated a so-called self-gated sequence, in this sequence a navigator was incorporated, the first echo was used to determine cardiac motion as well as breathing motion. The data was collected continuously and cardiac movies were reconstructed retrospectively. We tested the sequence in a model of murine myocardial infarction, in which the left coronary artery is ligated permanently, as well as in healthy control mice and compared the results of cardiac function to the original prospectively gated sequence. The results in cardiac function were comparable in both sequences, however, the self-gated sequence proved to be more time efficient.[25] The self-gated sequence would also give the possibility to study not only systolic dysfunction, but also diastolic dysfunction. As a gold standard, diastolic dysfunction is evaluated with Doppler echocardiography; however, since MRI is often used a tool for the determination of cardiac function an MRI method to evaluate diastolic cardiac function could be useful. In **chapter 9** we used streptozotocin (STZ) induced diabetic murine model. The main advantage of this model was that the exact day the mice became diabetic was known, giving the opportunity to start with baseline, non-diabetic, diastolic cardiac function measurements. MRI showed to be able to detect early disturbed filling patterns after 4 weeks of diabetes, which resulted in cardiac hypertrophy after 12 weeks of diabetes in some mice. For possible future evaluation of pharmaceutical treatment aimed at prevention of systolic heart failure and possibly even reduction of diastolic dysfunction, this model could be very useful. In **chapter 10** the preliminary results of a murine intervention study are shown. We studied ventricular remodeling with MRI in mice suffering from a myocardial infarction, which were treated with a BLT1 (B Leukotriene 1)receptor antagonist to reduce inflammation and consequently limit ventricular remodeling. The results of the first part of the study were surprising, by starting the treatment directly after the induction of a myocardial infarct the initial inflammatory response was most likely reduced too much and several mice died due to a rupture of the infarcted area. Due to these unexpected results we hypothesized that treatment should be started at 3 days after the induction of myocardial infarction, since the initial phase of inflammation, necessary for scar formation26, would then have occurred already. In **chapter 11** we discussed all results and speculated on the future perspectives of MRI in the cardiovascular field.

Conclusions

The goal of this thesis was to address new applications of (pre)-clinical cardiovascular (molecular) magnetic resonance imaging, in mice and men. MRI is an imaging modality that undergoes a fast evolution and that will become more widely applied in preclinical and clinical cardiovascular science and diagnostic research. For vascular wall imaging some major hurdles still exist. Specifically standardization of imaging procedures and the development of non toxic contrast agents will be a major challenge for future research.

1. Lebel RM, Eissa A, Seres P, Blevins G, Wilman AH. Quantitative high field imaging of sub-cortical gray matter in multiple sclerosis. Mult Scler 2011 October 27.

2. Fernandez-Seara MA, Mengual E, Vidorreta M, znarez-Sanado M, Loayza FR, Villagra F, Irigoyen J, Pastor MA. Cortical hypoperfusion in Parkinson's disease assessed using arterial spin labeled perfusion MRI. Neuroimage 2011 October 18.

3. Krivitzky LS, Roebuck-Spencer TM, Roth RM, Blackstone K, Johnson CP, Gioia G. Functional Magnetic Resonance Imaging of Working Memory and Response Inhibition in Children with Mild Traumatic Brain Injury. J Int Neuropsychol Soc 2011 October 12;1-10.

4. Chou D, Samartzis D, Bellabarba C, Patel A, Luk KD, Kisser JM, Skelly AC. Degenerative magnetic resonance imaging changes in patients with chronic low back pain: a systematic review. Spine (Phila Pa 1976) 2011 October 1;36(21 Suppl):S43-S53.

5. Budge LP, Salerno M. The role of cardiac magnetic resonance in the evaluation of patients presenting with suspected or confirmed acute coronary syndrome. Cardiol Res Pract 2011;2011:605785.

6. Nacif MS, Zavodni A, Kawel N, Choi EY, Lima JA, Bluemke DA. Cardiac magnetic resonance imaging and its electrocardiographs (ECG): tips and tricks. Int J Cardiovasc Imaging 2011 October 28.

7. Sheehan FH, Ge S, Vick GW, III, Urnes K, Kerwin WS, Bolson EL, Chung T, Kovalchin JP, Sahn DJ, Jerosch-Herold M, Stolpen AH. Three-dimensional shape analysis of right ventricular remodeling in repaired tetralogy of Fallot. Am J Cardiol 2008 January 1;101(1):107-13.

8. Chiribiri A, Ishida M, Nagel E, Botnar RM. Coronary imaging with cardiovascular magnetic resonance: current state of the art. Prog Cardiovasc Dis 2011 November;54(3):240-52.

9. Boffano C, Chiribiri A, Cesarani F. Native whole-heart coronary imaging for the identification of anomalous origin of the coronary arteries. Int J Cardiol 2009 September 11;137(1):e27-e28.

10. Wasserman BA, Wityk RJ, Trout HH, III, Virmani R. Low-grade carotid stenosis: looking beyond the lumen with MRI. Stroke 2005 November;36(11):2504-13.

11. Lovett JK, Gallagher PJ, Rothwell PM. Reproducibility of histological assessment of carotid plaque: implications for studies of carotid imaging. Cerebrovasc Dis 2004;18(2):117-23.

12. Hellings WE, Peeters W, Moll FL, Piers SR, van SJ, Van der Spek PJ, de Vries JP, Seldenrijk KA, De Bruin PC, Vink A, Velema E, de Kleijn DP, Pasterkamp G. Composition of carotid atherosclerotic plaque is associated with cardiovascular outcome: a prognostic study. Circulation 2010 May 4;121(17):1941-50.

13. Moody AR. Magnetic resonance direct thrombus imaging. J Thromb Haemost 2003 July;1(7):1403-9.

14. Kerwin WS, O'Brien KD, Ferguson MS, Polissar N, Hatsukami TS, Yuan C. Inflammation in carotid atherosclerotic plaque: a dynamic contrast-enhanced MR imaging study. Radiology 2006 November;241(2):459-68.

15. Kerwin W, Hooker A, Spilker M, Vicini P, Ferguson M, Hatsukami T, Yuan C. Quantitative magnetic resonance imaging analysis of neovasculature volume in carotid atherosclerotic plaque. Circulation 2003 February 18;107(6):851-6.

16. te Boekhorst BC, Bovens SM, Hellings WE, van der Kraak PH, van de Kolk KW, Vink A, Moll FL, van Oosterhout MF, de Vries JP, Doevendans PA, Goumans MJ, de Kleijn DP, van Echteld CJ, Pasterkamp G, Sluijter JP. Molecular MRI of murine atherosclerotic plaque targeting NGAL: a protein associated with unstable human plaque characteristics. Cardiovasc Res 2011 February 15;89(3):680-8.

17. van Bochove GS, Paulis LE, Segers D, Mulder WJ, Krams R, Nicolay K, Strijkers GJ. Contrast enhancement by differently sized paramagnetic MRI contrast agents in mice with two phenotypes of atherosclerotic plaque. Contrast Media Mol Imaging 2011 January;6(1):35-45.

18. Hanus L, Breuer A, Tchilibon S, Shiloah S, Goldenberg D, Horowitz M, Pertwee RG, Ross RA, Mechoulam R, Fride E. HU-308: a specific agonist for CB(2), a peripheral cannabinoid receptor. Proc Natl Acad Sci U S A 1999 December 7;96(25):14228-33.

19. van der Kolk AG, Hendrikse J, Zwanenburg JJ, Visser F, Luijten PR. Clinical applications of 7T MRI in the brain. Eur J Radiol 2011 September 19.

20. Teul J, Ruperez FJ, Garcia A, Vaysse J, Balayssac S, Gilard V, Malet-Martino M, Martin-Ventura JL, Blanco-Colio LM, Tunon J, Egido J, Barbas C. Improving metabolite knowledge in stable atherosclerosis patients by association and correlation of GC-MS and 1H NMR fingerprints. J Proteome Res 2009 December;8(12):5580-9.

21. Imamura A, Matsuo N, Ariki M, Horikoshi H, Hattori T. MR imaging and 1H-MR spectroscopy in a case of cerebral infarction with transient cerebral arteriopathy. Brain Dev 2004 December;26(8):535-8.

22. Sluimer JC, Gasc JM, van Wanroij JL, Kisters N, Groeneweg M, Sollewijn G, Cleutjens JP, van den Akker LH, Corvol P, Wouters BG, Daemen MJ, Bijnens AP. Hypoxia, hypoxia-inducible transcription factor, and macrophages in human atherosclerotic plaques are correlated with intraplaque angiogenesis. J Am Coll Cardiol 2008 April 1;51(13):1258-65.

23. Sluimer JC, Daemen MJ. [New understanding of the onset of atherosclerosis--angiogenesis and hypoxia play a crucial role]. Ned Tijdschr Geneeskd 2009;153:A847.

24. Vinitski S, Griffey RH, Szumowski J, Matwiyoff NA. Lactate observation in vivo by spectral editing in real time. Magn Reson Imaging 1988 November;6(6):707-11.

25. Bovens SM, te Boekhorst BC, den OK, van de Kolk KW, Nauerth A, Nederhoff MG, Pasterkamp G, ten HM, van Echteld CJ. Evaluation of infarcted murine heart function: comparison of prospectively triggered with self-gated MRI. NMR Biomed 2011 April;24(3):307-15.

26. Frangogiannis NG. The immune system and cardiac repair. Pharmacol Res 2008 August;58(2):88-111.

13

Nederlandse Samenvatting

Magnetische Resonantie Imaging (MRI) is één van de meest toegepaste beeldvormende technieken in de medische wereld. MRI is een niet invasieve techniek en wordt in bijna elk medisch specialisme gebruikt, zowel in de kliniek als in het onderzoek, zoals oncologie, neurologie, orthopedie, psychiatrie en cardiologie. De reden dat MRI vaak gebruik wordt is onder andere het goede onderscheidende vermogen van verschillende weefsels en de mogelijkheid om functionele analyses van specifieke organen uit te voeren (zoals het hart en het brein).[1-6] MRI van het hart wordt op verschillende manieren toegepast, meestal om de algemene hartfunctie te meten. Dit kan voor zowel de linker- als rechterkamer door van een stapel plakjes door het hart filmpjes te maken, met behulp van een ECG. Uit de verschillende fases van deze hartfilmpjes kunnen volumina berekend worden.[6] De studie van de rechterhartkamer is moeilijker door de asymmetrische vorm. Voor dit probleem zijn al een paar oplossingen bedacht, onder andere de toepassing van een 3D techniek. Met behulp van deze 3D techniek wordt de evaluatie van rechterhartfunctie en -vorm betrouwbaarder.[7] Recentelijk zijn er ook studies uitgevoerd die met behulp van de 3D techniek de kransslagaders in beeld hebben gebracht.[8, 9]

Arteriosclerose is de verkalking en vernauwing van slagaders, atherosclerose is een vorm van arteriosclerose waarbij er een atheroomplaat (plaque) vormt aan de binnenkant van de vaatwand. Deze plaque bestaat meestal grotendeels uit een ophoping van dode witte bloedcellen (met cholesterolvetten), ook wel de lipide rijke necrotische kern genoemd (in het Engels afgekort tot LRNC). Arteriosclerose en atherosclerose worden vaak door elkaar gebruikt, maar de problemen worden meestal veroorzaakt door atherosclerose, omdat als de plaque scheurt de inhoud in contact kan komen met de bloedstroom waarbij een bloedprop gevormd wordt welke verstoppingen kan veroorzaken. Deze verstoppingen kunnen lokaal tot zuurstoftekort in het weefsel leiden wat een hartaanval of een beroerte tot gevolg kunnen hebben. Plaques met een hoger risico op scheuren bevatten vaak veel witte bloedcellen (veel ontsteking, oftewel 'inflammatoir') en een dun laagje cellen (fibreuze cap) tussen de plaque en de bloedstroom.

Het doel van de verschillende studies beschreven in dit proefschrift was om nieuwe applicaties van MRI te onderzoeken in het veld van hart- en vaatziekten, zowel in muizen als in mensen. We hebben ons met name gericht op atherosclerose en hartfalen.

DEEL I
ATHEROSCLEROSE EN (MOLECULAIRE) MRI

In het eerste deel van dit proefschrift hebben we ons gericht op atherosclerose, studies gericht op moleculaire MRI in muizen, nucleair magnetische resonantie (NMR) spectroscopie en MRI met een sterke magneet in mensen.

Moleculaire MRI is gericht op het detecteren van specifieke moleculen/receptoren welke aanwezig zijn in atherosclerotische slagaders. De interesse hierin is de laatste jaren gestegen omdat er gebleken is dat de samenstelling van de plaque meer van belang is dan de mate van vernauwing.[10]

In **hoofdstuk 2.1** beschrijven we hoe MRI op het moment gebruikt wordt om de atherosclerotische plaques in de halsslagaders te visualiseren. Op dit moment is er nog geen standaard methode welke gebruikt wordt, hoewel dit wel al eerder gesuggereerd is.[11] Recentelijk is aangetoond dat de aanwezigheid van bloedingen in de plaque of een hoge dichtheid van kleine vaatjes in de plaque een verhoogd risico geven op het krijgen van bijvoorbeeld een hartaanval of een beroerte.[12] Omdat bloedingen in de plaque vaak diffuus aanwezig zijn in de LRNC is het moeilijk om met MRI een goed onderscheid te kunnen

maken tussen deze twee. De ontwikkeling van specifieke MRI sequenties die alleen bepaalde componenten in bloedingen zichtbaar maken zijn daarom van groot belang.[13]

Om de kleine vaatjes aanwezig in plaques zichtbaar te maken met MRI is een contrastmiddel nodig (Gadolinium). De snelheid waarmee dit contrastmiddel wordt opgenomen in de plaque is een mate voor de dichtheid/grootte van de vaatjes.[14, 15] Het gebruik van contrastmiddelen kan van toegevoegde waarde zijn, in **hoofdstuk 2.2** bespreken we het testen van nieuwe contrastmiddelen in diermodellen en waar rekening mee dient te worden gehouden als deze nieuwe middelen gevalideerd worden op weefsels van de dieren waarin ze getest zijn. In **hoofdstuk 4** hebben we een contrastmiddel met een antilichaam gericht tegen NGAL (een eiwit uitgescheiden door witte bloedcellen) getest. NGAL wordt door witte bloedcellen uitgescheiden en stabiliseert een eiwit (MMP-9)[16] welke verantwoordelijk is voor afbraak van collageen. NGAL is geassocieerd met een inflammatoire plaque, welke een hoger risico heeft op scheuren. Bij het gebruik van nieuwe contrastmiddelen is het ook belangrijk om te weten hoe lang deze circuleren in het bloed en via welke organen deze weer het lichaam verlaten. Er zijn enorme verschillen in circulatietijden van contrastmiddelen, wat afhankelijk is van hun samenstelling.

In **hoofdstuk 7** hebben gebruik gemaakt van kleine ijzeroxide deeltjes (USPIO), welke op een MRI afbeelding te zien zijn als zwarte plekken, en vrij snel weer verdwenen zijn uit het bloed na inspuiten (~1.5 uur). Daar staat tegenover dat contrastmiddelen bestaande uit lipiden, zoals micellen en liposomen, veel langer in het bloed circuleren (micellen ~22 uur, liposomen ~7 uur[17]). Deze contrastmiddelen zijn zichtbaar als witte plekken in een MRI afbeelding. De snelheid waarmee contrastmiddelen uit het bloed worden geklaard, heeft hoogstwaarschijnlijk te maken met de snelheid waarmee het immuunsysteem reageert. Wanneer contrastmiddelen antilichamen of iets dergelijks bevatten om specifieke receptoren te herkennen worden ze vaak sneller herkend door het immuunsysteem en daarom sneller geklaard uit het bloed. In **hoofdstuk 3** hebben we micellen met en zonder een deeltje om een receptor te herkennen (HU-308[18]) getest in $ApoE^{-/-}$/$eNOS^{-/-}$ muizen (deze muizen ontwikkelen atherosclerose). De resultaten lieten zien dat de micellen zonder HU-308 tot ongeveer 42 uur na injectie te traceren waren in de plaque. De micellen met HU-308 waren in ieder geval tot 48 uur na injectie nog te traceren. Dit suggereert dat er pas na 42 uur een specifieke detectie plaats kan vinden met MRI, te vroeg meten zou vals positieve resultaten opleveren.

De nieuwe contrastmiddelen worden nog getest in dieren, maar ook zonder het gebruik van contrastmiddelen wordt er vooruitgang geboekt bij de detectie van atherosclerotische plaques in mensen. Dit is mede te danken aan de verbetering van sequenties en de sterkere MRI magneten. We hebben in **hoofdstuk 6** een studie beschreven waarin de halsslagader van patiënten gescand werd met behulp van de 7 Tesla MRI scanner. De 7 Tesla is op het moment de sterkste magneet beschikbaar in Nederland. Patiënten bij wie een plaque verwijderd werd uit de halsslagader werden voor de operatie gescand met behulp van de 7 Tesla om zowel van de plaque als het brein MRI afbeeldingen te maken. Deze studie loopt nog en de eerste resultaten lieten zien dat de 7 Tesla MRI de plaque in de halsslagader goed zichtbaar kan maken. In de toekomst wordt er nog gekeken naar de verschillende componenten in de plaque op weefselniveau en dit wordt vergeleken met de MRI afbeeldingen. Hopelijk kan er dan in de toekomst beter voorspelt worden met behulp van een MRI scan welke patiënten een plaque hebben met een hoog risico op scheuren en geopereerd moeten worden.

Een andere niet-invasieve manier om atherosclerotische plaques te bestuderen wordt besproken in **hoofdstuk 5**. Hierbij is ook gebruik gemaakt van de magneet, maar er worden geen afbeeldingen gemaakt. NMR-spectroscopie visualiseert in dit geval protonen (^1H), welke in verschillende verhoudingen aanwezig zijn in eiwitten/metabolieten en hierdoor per eiwit/metaboliet een unieke 'vingerafdruk'

hebben.[19, 20] Wij hebben van deze techniek gebruik gemaakt om lactaatconcentraties in plaques te meten en te correleren aan hypoxie (zuurstoftekort) in de plaque. Hypoxie is verantwoordelijk voor de vorming van nieuwe vaatjes in plaques[21, 22] en creëert daarmee uiteindelijk een verhoogd risico op scheuren. In plaques uit de femorale (been) slagader waren lactaatconcentraties gecorreleerd aan een marker voor hypoxie (HIF-1α). Dit zou in de toekomst kunnen leiden tot een non-invasieve screening voor plaques met een hoog risico op scheuren.

DEEL II
MRI VAN HET HART

In het tweede deel van dit proefschrift hebben we onderzoek gedaan naar MRI van het hart in muizen, die ofwel aan een hartinfarct of aan hartfalen leden. MRI wordt vaak gebruikt om de hartfunctie te bepalen, met name in studies met meerdere meetpunten. Sterke MRI magneten, zoals 9.4 Tesla of zelfs 11.7 Tesla, welke speciaal zijn ontworpen om muizen (en andere kleine knaagdieren) te meten, zijn op veel plekken beschikbaar. Bij humane hartfunctiemetingen wordt vaak gebruik gemaakt van een ECG om te zorgen dat de hele hartcyclus in het MRI filmpje valt. Bij muizen is dit erg lastig omdat ze een hoge hartfrequentie hebben (ongeveer 500 hartslagen per minuut in vergelijking met 70 hartslagen per minuut in mensen) en door het sterke magnetische veld wordt het ECG signaal vaak verstoord. In **hoofdstuk 8** laten we de resultaten zien van een studie die gebruik maakt van een zogenoemde zelf-gating sequentie. Hierbij wordt er door de MRI sequentie zelf een hart- en ademhalingsbeweging afgeleid door de verschillen in contrast in de tijd. Deze data worden tegelijk opgeslagen met de afbeeldingen en nadat de meting is afgelopen wordt er retrospectief een filmpje van gemaakt. De hartfunctie werd bepaald in filmpjes verkregen met deze zelf-gating methode en de ECG methode. Er werden geen verschillen gevonden in hartfunctie tussen de methodes, in zowel gezonde muizen als muizen met een hartinfarct, maar de zelf-gating methode bleek sneller.[23] Deze zelf-gating sequentie werd vervolgens ook gebruikt in **hoofdstuk 9**, waar er in diabetische muizen werd gekeken naar de hartfunctie. Diabetes werd geïnduceerd na de eerste hartfunctiemetingen waardoor er in de tijd gekeken kon worden wat de invloed van diabetes was op de ontwikkeling van hartfalen. MRI metingen werden herhaald na 4, 8 en 12 weken. Na 4 weken werd er al een verstoorde vulling van het hart gezien en na 12 weken hadden sommige muizen een verdikte hartspier en hartfalen. Deze studie toont aan dat dit model en de MRI methode geschikt zijn om in de tijd de ontwikkeling van hartfalen te volgen, waardoor er in de toekomst mogelijk medicijnen getest kunnen worden. In **hoofdstuk 10** hebben we medicatie getest op muizen met een hartinfarct, welke zou moeten voorkomen dat er veel witte bloedcellen het hartinfarct ingaan. Als er minder witte bloedcellen het hartinfarct ingaan zou er op de lange termijn een minder slechte hartfunctie moeten zijn dan muizen die niet behandeld worden. De resultaten van de eerste studie zorgden verrassend genoeg voor het scheuren van het hartinfarct, hoogstwaarschijnlijk omdat de witte bloedcellen teveel geremd werden. Deze cellen zijn namelijk een noodzakelijk onderdeel om een litteken te vormen en het hartweefsel te stabiliseren tijdens het ontwikkelen van hartfalen na een hart infarct.[24] In een vervolgstudie zal de behandeling pas 3 dagen na het hartinfarct gestart worden, waardoor de littekenvorming wel plaats kan vinden.
In **hoofdstuk 11** worden alle resultaten van dit proefschrift bediscussieerd en toekomstperspectieven van de MRI binnen het hart- en vaatziekten onderzoek besproken.

Conclusies

Het doel van de verschillende studies beschreven in dit proefschrift was om nieuwe applicaties van MRI te onderzoeken in het veld van hart- en vaatziekten, zowel in muizen als in mensen. MRI is een beeldvormende techniek welke onderhevig is aan continue verbeteringen en toegepast wordt binnen bijna elk medisch specialisme. Om de vaatwand goed in beeld te brengen moeten er nog een paar hordes genomen worden. Er valt nog veel te winnen door de protocollen te standaardiseren en meer onderzoek te doen naar de ontwikkeling van minder toxische contrastmiddelen, welke een grote uitdaging is voor de toekomst.

1. Lebel RM, Eissa A, Seres P, Blevins G, Wilman AH. Quantitative high field imaging of sub-cortical gray matter in multiple sclerosis. Mult Scler 2011 October 27.

2. Fernandez-Seara MA, Mengual E, Vidorreta M, znarez-Sanado M, Loayza FR, Villagra F, Irigoyen J, Pastor MA. Cortical hypoperfusion in Parkinson's disease assessed using arterial spin labeled perfusion MRI. Neuroimage 2011 October 18.

3. Krivitzky LS, Roebuck-Spencer TM, Roth RM, Blackstone K, Johnson CP, Gioia G. Functional Magnetic Resonance Imaging of Working Memory and Response Inhibition in Children with Mild Traumatic Brain Injury. J Int Neuropsychol Soc 2011 October 12;1-10.

4. Chou D, Samartzis D, Bellabarba C, Patel A, Luk KD, Kisser JM, Skelly AC. Degenerative magnetic resonance imaging changes in patients with chronic low back pain: a systematic review. Spine (Phila Pa 1976) 2011 October 1;36(21 Suppl):S43-S53.

5. Budge LP, Salerno M. The role of cardiac magnetic resonance in the evaluation of patients presenting with suspected or confirmed acute coronary syndrome. Cardiol Res Pract 2011;2011:605785.

6. Nacif MS, Zavodni A, Kawel N, Choi EY, Lima JA, Bluemke DA. Cardiac magnetic resonance imaging and its electrocardiographs (ECG): tips and tricks. Int J Cardiovasc Imaging 2011 October 28.

7. Sheehan FH, Ge S, Vick GW, III, Urnes K, Kerwin WS, Bolson EL, Chung T, Kovalchin JP, Sahn DJ, Jerosch-Herold M, Stolpen AH. Three-dimensional shape analysis of right ventricular remodeling in repaired tetralogy of Fallot. Am J Cardiol 2008 January 1;101(1):107-13.

8. Chiribiri A, Ishida M, Nagel E, Botnar RM. Coronary imaging with cardiovascular magnetic resonance: current state of the art. Prog Cardiovasc Dis 2011 November;54(3):240-52.

9. Boffano C, Chiribiri A, Cesarani F. Native whole-heart coronary imaging for the identification of anomalous origin of the coronary arteries. Int J Cardiol 2009 September 11;137(1):e27-e28.

10. Wasserman BA, Wityk RJ, Trout HH, III, Virmani R. Low-grade carotid stenosis: looking beyond the lumen with MRI. Stroke 2005 November;36(11):2504-13.

11. Lovett JK, Gallagher PJ, Rothwell PM. Reproducibility of histological assessment of carotid plaque: implications for studies of carotid imaging. Cerebrovasc Dis 2004;18(2):117-23.

12. Hellings WE, Peeters W, Moll FL, Piers SR, van SJ, Van der Spek PJ, de Vries JP, Seldenrijk KA, De Bruin PC, Vink A, Velema E, de Kleijn DP, Pasterkamp G. Composition of carotid atherosclerotic plaque is associated with cardiovascular outcome: a prognostic study. Circulation 2010 May 4;121(17):1941-50.

13. Moody AR. Magnetic resonance direct thrombus imaging. J Thromb Haemost 2003 July;1(7):1403-9.

14. Kerwin WS, O'Brien KD, Ferguson MS, Polissar N, Hatsukami TS, Yuan C. Inflammation in carotid atherosclerotic plaque: a dynamic contrast-enhanced MR imaging study. Radiology 2006 November;241(2):459-68.

15. Kerwin W, Hooker A, Spilker M, Vicini P, Ferguson M, Hatsukami T, Yuan C. Quantitative magnetic resonance imaging analysis of neovasculature volume in carotid atherosclerotic plaque. Circulation 2003 February 18;107(6):851-6.

16. te Boekhorst BC, Bovens SM, Hellings WE, van der Kraak PH, van de Kolk KW, Vink A, Moll FL, van Oosterhout MF, de Vries JP, Doevendans PA, Goumans MJ, de Kleijn DP, van Echteld CJ, Pasterkamp G, Sluijter JP. Molecular MRI of murine atherosclerotic plaque targeting NGAL: a protein associated with unstable human plaque characteristics. Cardiovasc Res 2011 February 15;89(3):680-8.

17. van Bochove GS, Paulis LE, Segers D, Mulder WJ, Krams R, Nicolay K, Strijkers GJ. Contrast enhancement by differently sized paramagnetic MRI contrast agents in mice with two phenotypes of atherosclerotic plaque. Contrast Media Mol Imaging 2011 January;6(1):35-45.

18. Hanus L, Breuer A, Tchilibon S, Shiloah S, Goldenberg D, Horowitz M, Pertwee RG, Ross RA, Mechoulam R, Fride E. HU-308: a specific agonist for CB(2), a peripheral cannabinoid receptor. Proc Natl Acad Sci U S A 1999 December 7;96(25):14228-33.

19. Teul J, Ruperez FJ, Garcia A, Vaysse J, Balayssac S, Gilard V, Malet-Martino M, Martin-Ventura JL, Blanco-Colio LM, Tunon J, Egido J, Barbas C. Improving metabolite knowledge in stable atherosclerosis patients by association and correlation of GC-MS and 1H NMR fingerprints. J Proteome Res 2009 December;8(12):5580-9.

20. Imamura A, Matsuo N, Ariki M, Horikoshi H, Hattori T. MR imaging and 1H-MR spectroscopy in a case of cerebral infarction with transient cerebral arteriopathy. Brain Dev 2004 December;26(8):535-8.

21. Sluimer JC, Gasc JM, van Wanroij JL, Kisters N, Groeneweg M, Sollewijn G, Cleutjens JP, van den Akker LH, Corvol P, Wouters BG, Daemen MJ, Bijnens AP. Hypoxia, hypoxia-inducible transcription factor, and macrophages in human atherosclerotic plaques are correlated with intraplaque angiogenesis. J Am Coll Cardiol 2008 April 1;51(13):1258-65.

22. Sluimer JC, Daemen MJ. [New understanding of the onset of atherosclerosis--angiogenesis and hypoxia play a crucial role]. Ned Tijdschr Geneeskd 2009;153:A847.

23. Bovens SM, te Boekhorst BC, den OK, van de Kolk KW, Nauerth A, Nederhoff MG, Pasterkamp G, ten HM, van Echteld CJ. Evaluation of infarcted murine heart function: comparison of prospectively triggered with self-gated MRI. NMR Biomed 2011 April;24(3):307-15.

24. Frangogiannis NG. The immune system and cardiac repair. Pharmacol Res 2008 August;58(2):88-111.

14

Review Committee

Dankwoord

Publications

Curriculum Vitae

Prof. Dr. R. Goldschmeding
Department of Pathology
University Medical Center Utrecht

Prof. Dr. D.P.V. de Kleijn
Department of Experimental Cardiology
University Medical Center Utrecht

Prof. Dr. P. Luijten
Department of Radiology
University Medical Center Utrecht

Prof. Dr. R.E. Poelmann
Department of Anatomy and Embryology
Leiden University Medical Center

Prof. Dr. K. Nicolay
Department of Biomedical Engineering
Eindhoven University of Technology

DANKWOORD

Na vier jaar vol uitdagingen ligt hier dan eindelijk het resultaat, maar dit proefschrift zou niet zijn wat het is zonder de hulp van een aantal mensen. Het is een lange lijst waarbij er misschien een naam tussendoor is geglipt, dus hierbij wil ik graag [jou] (vul hier eigen naam in) bedanken voor je onmisbare bijdrage aan dit proefschrift!

Professor dr. Pasterkamp, beste Gerard, na het vertrek van Cees heb je me ondanks je overvolle bord volledig in het experimentele lab opgenomen. Ik heb erg veel van je geleerd, ook al lagen sommige studie topics niet direct binnen het veld van je expertise. Je weet altijd de juiste vragen te stellen en soms de vinger op de zere plek te leggen. Je hebt me altijd de vrijheid gegeven om eigen ideeën uit te werken en de experimenten uit te voeren. Dankzij je kritische en verfrissende blik zijn veel papers er sterker uit gekomen en ligt hier nu een divers gevuld proefschrift, hopelijk komen er in de toekomst ook uit de laatste studies nog een paar mooie papers!

Professor dr. van Echteld, beste Cees, ooit kwam ik als student bij jullie op het MRI lab binnenlopen waarbij ik erg enthousiast werd door alle studies die jullie uitvoerden. Hoe wonderbaarlijk is het ook om van een minuscuul muizenhartje filmpjes te kunnen maken waarbij zelfs de hartkleppen zichtbaar zijn, dit alles zonder de muis open te hoeven snijden. Na mijn studie heb je me de mogelijkheid gegeven om op het MRI lab mijn promotie onderzoek te starten, waar nu na vier jaar het resultaat van voor je ligt, ik wil je hiervoor dan ook erg bedanken.

Professor dr. de Kleijn, beste Dominique, vooral de laatste maanden zijn we elkaar vaker tegen gekomen en hebben we erg (voor mij) nuttige discussies gehad. Naast je expertise van het muizenhart en de immunologie heb ik veel gehad aan je nuchtere benadering van problemen, er is altijd een oplossing voor te bedenken!

Professors Poelmann en Nicolay, beste Rob en Klaas, dankzij de samenwerking binnen het project van de Nederlandse Hartstichting hebben we regelmatig gezamenlijke besprekingen gehad. Jullie hebben allebei duidelijk een eigen expertise en door de combinatie hiervan hebben we veel middagen goede discussies gehad met z'n allen. Ook konden we altijd op jullie labs langskomen om onder andere coupes te snijden of micellen te produceren, hiervoor wil ik jullie erg bedanken!

Daarnaast heb ik bij verschillende studies mogen samenwerking met verschillende mensen in het UMCU. Maarten Jan, ook jou wil ik graag bedanken, je enthousiasme en betrokkenheid hebben ervoor gezorgd dat er een mooi paper klaar ligt. Gert Jan en Anne, de opstart van onze gezamenlijke studie was een behoorlijke uitdaging, na een jaar was de METC goedkeuring dan eindelijk binnen! Ondertussen hebben we al 8 patiënten kunnen includeren en twee papers geschreven, hopelijk komen er in de toekomst nog een paar mooie aan! De mensen van de 7 Tesla; Wouter, Jaco, Anja, Jeroen, Dennis, ook jullie hebben alle hobbels van de PlaCD studie meegemaakt en we zijn er nog niet, maar ik ben ervan overtuigd dat we er uiteindelijk samen wat moois van kunnen maken. De pathologie; Aryan en Petra, vele kleuringen en coupes hebben we langs zien komen, bedankt voor alle hulp die jullie hierbij gegeven hebben.

Ook buiten het UMCU zijn er veel samenwerkingen geweest. Brigit en Roel, samen zijn we gestart binnen het NHS project. We hebben samen veel meetings en labmiddagen overleefd (welke erg gezellig waren!) en ik vind het erg leuk dat we ook samen een paar studies hebben opgezet. Heel veel succes nog met jullie laatste loodjes! Diederik en Dirk Jan, ook jullie wil ik bedanken voor de samenwerking en de gezellige ochtenden/middagen op de OK's. Verder wil ik ook de andere mensen uit Eindhoven en Leiden bedanken; Gustav, Louise, Linda en Bianca.

Op het experimentele cardio lab lopen ook een aantal mensen rond die ik wil bedanken. Arjan, in de eerste jaren durfde ik bijna niet bij je aan te kloppen, maar de laatste jaren heb ik wat meer moed gekregen. Dankzij jouw verhelderende inzichten zijn sommige 'mislukte' resultaten toch nog te gebruiken! Sander v.d. W, het zonnetje van het lab, dank voor je hulp bij het verwerken van de plaques en gezelligheid bij de borrels. Verder wil ik ook de andere mensen die ik vaker heb lastig gevallen met vragen op het lab graag bedanken voor hun geduld en gezelligheid, Loes, Noortje, Chaylendra, Joost S, Joost F, Bas, Esther, Roberto, Petra, Krista en Corina. And of course Hanna, although you already left the lab I would still like to thank you. We had some great 'koffiepraat' and our shopping and dinner sessions are still moments I enjoy a lot, hope you will drop by in London!

Daarnaast wil ik Marjolijn erg bedanken, het regelen van de koffie, fluorescerende gele stickers, de gezellige gesprekken 's ochtends vroeg om wakker te worden en alle andere dingen waardeer ik heel erg. Ook Ineke wil ik bedanken voor alle ondersteuning bij administratieve zaken, je bent altijd bereidt om extra moeite te doen als dit nodig is dankjewel!

Wendy, erg bedankt voor je hulp bij de lay-out van dit proefschrift.

Zonder mede promovendi (al gepromoveerd of nog niet) was het een stuk minder gezellig geweest de afgelopen jaren. Eissa en Bernard, samen waren we de AIO's van het MRI lab, veel gelachen en gedronken en tussendoor ook nog wel eens een experiment uitgevoerd, bedankt voor jullie gezelligheid! Ondanks dat ik pas wat later in m'n promotie ben binnengevallen bij het experimentele cardio lab heb ik nog heel wat gezelligheid kunnen meepikken. Ellen, Sanne, Geert en Marten, de AIO's van de 'zoete inval' kamer. Altijd gezellig om bij jullie een bakje te komen doen of gewoon een praatje te maken, ook de borrels op vrijdagmiddag, congressen en avonden waren erg leuk, soms te leuk! De andere AIO's die ook regelmatig bij borrels te vinden waren, en op het lab en GDL natuurlijk ook voor sfeer zorgen, Krijn, Alain, Claudia, Marish, Renate, Paul, Frebus, Diana, Olivier, Stefan en Hendrik, erg bedankt. Allemaal nog erg veel succes in het afronden van jullie eigen promotie! Ook de gezellige mensen die helaas eerder het lab hebben verlaten, René, Rob, Mihaela, Daphne, Fatih, Emrah, Vahideh, Wouter P, Wouter D, Leo, Anke, bedankt! De rest van de staf, Imo, Karlijn, Onno en Mirjam, jullie wil ik ook graag bedanken, jullie staan altijd klaar om vragen te beantwoorden en te helpen op het lab.

In het GDL heb ik ook behoorlijk wat tijd doorgebracht, als eerste wil ik dan ook de muisjes bedanken, vele dagen en nachten samen doorgebracht, het is toch fijn om te weten dat je in het GDL nooit alleen bent. Ook de mensen van de in vivo NMR wil ik graag bedanken voor de gezelligheid, borrels en verjaardagstaarten; Lisette, Geralda, Ivo, Maurits, Kajo, Rick, Mark en de rest. Ook de mensen van de CardioMR; Kees, Marcel en Michiel, bedankt voor de hulp, ervoor zorgen dat de scanner in de lucht bleef en alle andere dingen. Tamara, Helma, Sabine, Herma, Gerard, Kiki en anderen, bedankt voor

jullie hulp bij de verschillende muizenstudies. Ben, Maringa, Evelyn, Cees, Marlijn en Joyce, ook jullie wil ik bedanken voor al jullie hulp en vooral ook de gezelligheid in het GDL. Zonder jullie hulp waren de muizenstudies bijna onmogelijk geweest.

Daarnaast zijn er gedurende de afgelopen jaren ook vele studenten geweest die ik wil bedanken voor bijdrage aan de sfeer op de labs en kamers en hun inzet bij de verschillende studies; Meike, Niels, Suzanne, Danielle, Iris, Ayla, Michel, Bas, Jan Willem, Joyce, Verena, Mariam. Uiteraard wil ik Mark speciaal bedanken voor al het isoleer- en kleurwerk in de laatste weken van mijn promotie.

Daarnaast wil ik uiteraard de 'torenmensen' bedanken, Astrid, Kristy en Louise, thank you guys for the help when needed. De buren; Dave, bij jou kon ik altijd binnenvallen om moeilijke vragen te stellen, je hebt overal een antwoord op. Guus, Herman en Vincent, ook jullie wil ik bedanken voor de gezelligheid, de koffie die altijd klaarstond en de legendarische torenborrels!

Mijn (ex-) roomies!
Jullie ga ik nog het meest missen, de LuiCo meetings waren geweldig, ook nadat het labuitje al had plaatsgevonden! Ik hoop dat we die traditie in ere houden, jullie zijn altijd welkom in Londen.
Sander v.d. L, wat was ik blij dat jij in de toren bent aangeschoven, ik zat niet meer alleen op het kamertje. Je zorgt altijd voor gezelligheid, mede door je onuitputtelijke muziekcollectie en verhalen. Je hebt niet het simpelste promotieonderwerp en ik weet dat het niet altijd gemakkelijk is om mensen die met heel iets anders bezig zijn duidelijk te maken wat je nu eigenlijk uitspookt de hele dag. Ook buiten het werk hebben we gezellige etentjes en borrels gehad. Heel veel succes nog met de afronding van je eigen proefschrift, ik ben ervan overtuigd dat er iets heel moois uitkomt!
Vince, je bent pas een jaartje bezig, maar je hebt in dat jaar veel gezelligheid toegevoegd aan onze kamer. Ook jij hebt altijd tijd om even te kletsen of koffie te drinken, niet alleen op de kamer maar ook in het GDL en op het lab. Ik verbaas me er altijd over hoe jij dingen die ik als complex en problematisch zie zo gemakkelijk kunt versimpelen, hopelijk heb ik je niet te gek gemaakt met mijn soms, voor de buitenwereld, chaotische dagindeling en planning. Ik heb erg prettig met je samengewerkt en ook met de borrels en etentjes het erg gezellig gehad. Heel veel succes nog de komende jaren met je eigen promotie!

Mijn ex-roomie Pleunie, ik ben zo blij dat je mijn paranimf wil zijn! We hebben het altijd gezellig, heerlijke 'serie'avondjes, weekendjes in het buitenland, borrels en niet te vergeten ons dagelijkse koffiemomentje. Ik heb aan jou niet alleen een erg gezellige collega maar ook vriendin, je staat altijd klaar voor iedereen en we kunnen zowel over werk als over onzinnige dingen urenlang discussiëren. Je bent zelf nu ook over de helft van je promotie en over een paar jaar ligt er zeker weten een geweldig proefschrift! Ik ben erg blij dat je tijdens mijn verdediging aan mijn zijde staat en hoop je ook nog vaak in Londen te mogen verwelkomen!

Mijn tweede paranimf, Astrid, 'kleine' zus, hoe heerlijk is het om met je zusje te kunnen kletsen over wat je eigenlijk allemaal doet op je werk en dat ze het nog snapt ook. Ook al trokken we elkaar vroeger de haren uit, ik ben ontzettend blij dat ik een zusje heb met wie ik zo'n goede band heb. Ik ben erg benieuwd wat de toekomst ons gaat brengen en ben heel blij dat je naast me staat tijdens m'n verdediging! Hopelijk vind je zelf ook snel een promotieplek en kan ik over een aantal jaar aan jou zijde staan tijdens je verdediging.

Hoewel de afgelopen jaren het grootste deel van de week gevuld is geweest met werk was er ook altijd tijd om andere dingen te ondernemen. Ik ben erg blij dat ik vrienden heb die er altijd zijn, zelfs al dingen toch behoorlijk tegenzitten. Iris en Vincent, we kennen elkaar al meer dan tien jaar en nog steeds hebben we regelmatig onze 'VIS' avondjes. Iris, heel veel succes met de laatste maand van je eigen promotie! Er zijn nog veel meer familie en vrienden die ik graag wil bedanken voor de regelmatige en minder regelmatige, maar altijd gezellig avonden en dagen vol ontspanning, zeker goed te gebruiken na een lange werkweek! Chantal, Olger, Margot, Martijn, Roos, Mark, Mathijs, Carola, Inge, Wendy, Nadia, Allan, Christian, Shirley, Patrick, Marie-José, Tim, Eric en alle ooms en tantes en aanhang (sorry als ik iemand vergeten ben). Daarnaast wil ik mijn grootouders ook bedanken ondanks dat ze niet allemaal meer onder ons zijn. Jullie hebben altijd in me geloofd en ik zou niet zijn wie ik ben vandaag zonder jullie steun en wijsheden.

Ook pap en mam wil ik erg bedanken, zonder jullie had ik hier niet gestaan. Jullie hebben me altijd gesteund en ervoor gezorgd dat ik het beste uit mezelf haalde.

PUBLICATIONS

Bovens SM*, den Hartog AG*, Koning W, Hendrikse J, Pasterkamp G, Moll FL, de Borst GJ.
PLACD-7T Study: Atherosclerotic Carotid Plaque Components Correlated with Cerebral Damage at 7 Tesla.
Current Cardiology Reviews 2011 feb 7:1 (28-34).

Bovens SM*, te Boekhorst BC*, Hellings WE, van der Kraak PH, van de Kolk KW, Vink A, Moll FL, van Oosterhout MF, de Vries JP, Doevendans PA, Goumans MJ, de Kleijn DP, van Echteld CJ, Pasterkamp G, Sluijter JP.
Molecular MRI of murine atherosclerotic plaque targeting NGAL: a protein associated with unstable human plaque characteristics.
Cardiovasc Res. 2011 Feb 15;89(3):680-8

Bovens SM, te Boekhorst BC, Ouden KD, van de Kolk KW, Nauerth A, Nederhoff MG, Pasterkamp G, ten Hove M, van Echteld CJ.
Evaluation of infarcted murine heart function: comparison of prospectively triggered with self-gated MRI.
NMR Biomed. 2011 Apr;24(3):307-15.

te Boekhorst BC, **Bovens SM**, van de Kolk CW, Cramer MJ, Doevendans PA, ten Hove M, van der Weerd L, Poelmann R, Strijkers GJ, Pasterkamp G, van Echteld CJ.
The time window of MRI of murine atherosclerotic plaques after administration of CB2 receptor targeted micelles: inter-scan variability and relation between plaque signal intensity increase and gadolinium content of inversion recovery prepared versus non-prepared fast spin echo.
NMR Biomed. 2010 Oct;23(8):939-51.

te Boekhorst BC, **Bovens SM**, Rodrigues-Feo J, Sanders HM, van de Kolk CW, de Kroon AI, Cramer MJ, Doevendans PA, ten Hove M, Pasterkamp G, van Echteld CJ.
Characterization and in vitro and in vivo testing of CB2-receptor- and NGAL-targeted paramagnetic micelles for molecular MRI of vulnerable atherosclerotic plaque.
Mol Imaging Biol. 2010 Dec;12(6):635-51.

te Boekhorst BC, **Bovens SM**, Nederhoff MG, van de Kolk KW, Cramer MJ, van Oosterhout MF, Ten Hove M, Doevendans PA, Pasterkamp G, van Echteld CJ.
Negative MR contrast caused by USPIO uptake in lymph nodes may lead to false positive observations with in vivo visualization of murine atherosclerotic plaque.
Atherosclerosis. 2010 May;210(1):122-9. Epub 2009 Nov 3.

te Boekhorst BC, van 't Klooster R, **Bovens SM**, van de Kolk KW, Cramer MJ, van Oosterhout MF, Doevendans PA, van der Geest RJ, Pasterkamp G, van Echteld CJ.
Evaluation of multicontrast MRI including fat suppression and inversion recovery spin echo for identification of intra-plaque hemorrhage and lipid core in human carotid plaque using the mahalanobis distance measure.
Magn Reson Med. 2011 Oct 13.

Bovens SM, Zomer G, Derksen WJM, Moll FL, de Kleijn DPV, Vink A, Pasterkamp G.
Lactate measured with NMR spectroscopy in atherosclerotic plaques is a marker for local hypoxia.
Submitted

Bovens SM , te Boekhorst BCM, Emons VM, van der Kraak PH, van Echteld CJA, Cramer MJM, Pasterkamp G. Diastolic dysfunction in type I diabetic mice evaluated with self-gated cardiac magnetic resonance imaging.
Submitted

den Hartog AG, **Bovens SM**, Koning W, Hendrikse J, Luijten P, Moll FL, Pasterkamp G, de Borst GJ. Magnetic resonance imaging for determination of plaque characteristics confirmed by histology in patients with carotid artery stenosis: an overview of literature.
Submitted

** authors contributed equally*

CURRICULUM VITAE

Sandra Bovens was born on May 30, 1984 in Utrecht, the Netherlands. After graduating from secondary school in 2001 (O.R.S. Lek en Linge, Culemborg), she studied Biology and Medical Laboratory Sciences at the Hogeschool Utrecht. She obtained her Bachelor degree in Clinical Chemistry in 2005 after which she started her Master Biomedical Sciences at the VU in Amsterdam. During her Master, she completed her internships at the Department of Experimental Cardiology (CardioNMR) at the University Medical Center Utrecht (UMCU) and obtained her Master degree in 2008. In august 2007 she already started as a PhD candidate at the Department of Experimental Cardiology at the UMCU under the supervision of prof. dr. G. Pasterkamp and prof. dr. C.J.A. van Echteld. The results of her research are described in this thesis. Following her PhD training she started working as a postdoctoral researcher at the Department of Bioengineering at Imperial College London in the group of prof. dr. R. Krams.